

Measurement of the $e^+e^- \rightarrow \pi^+\pi^-\pi^+\pi^-$ Cross Section Using Initial State Radiation at *BABAR*.

Dissertation
zur Erlangung des Grades
“Doktor der Naturwissenschaften”
am Fachbereich Physik
der Johannes Gutenberg-Universität
in Mainz



Andreas Hafner

geb. in Wolfach
Mainz, den 7. Februar 2012

Andreas Hafner: *Measurement of the $e^+e^- \rightarrow \pi^+\pi^-\pi^+\pi^-$ Cross Section Using Initial State Radiation at BABAR*, 05.01.2012 Mainz
Tag der mündlichen Prüfung: 21.12.2011

Zusammenfassung

Das magnetische Moment des Myons, das dessen Kopplung an ein externes magnetisches Feld beschreibt, ist eine der am genauesten experimentell bestimmten Größen in der Teilchenphysik. Sie wird durch die Anomalie des magnetischen Momentes des Myons ausgedrückt, $a_\mu = (g - 2)_\mu / 2$, die mit einer relativen Genauigkeit von $0,5 \cdot 10^{-6}$ gemessen wurde. Die Messung zeigt eine Differenz von mehr als 3,5 Standardabweichungen zur Theorievorhersage im Rahmen des Standardmodells. Auf theoretischer Seite können die Beiträge der Quantenelektrodynamik sowie der schwachen Wechselwirkung mit sehr hoher Präzision mittels eines Störungsansatzes berechnet werden. Der hadronische Beitrag a_μ^{had} lässt sich bei niedrigen Energien nicht störungstheoretisch ermitteln. Es ist jedoch möglich, den führenden Beitrag, die hadronische Vakuumpolarisierung, in Form eines Dispersionsintegrals mit gemessenen hadronischen Wirkungsquerschnitten in der Elektron-Positron-Abschaffung in Verbindung zu setzen. Für eine präzise Standardmodellvorhersage von a_μ ist es deshalb essentiell, die experimentellen Unsicherheiten der hadronischen Wirkungsquerschnittsmessungen zu minimieren.

Zur Messung der hadronischen Wirkungsquerschnitte wird zusätzlich zu den traditionellen Energiescan-Experimenten die Methode der Photonabstrahlung im Anfangszustand (Initial State Radiation, ISR) verwendet. Hierbei werden Ereignisse untersucht, bei denen ein hochenergetisches Photon aus dem Eingangszustand des Elektron-Positron-Systems abgestrahlt wurde und somit die effektive Schwerpunktsenergie absenkt. Mit dieser Methode kann bei *BABAR* der Energiebereich von der hadronischen Produktionsschwelle bis zu ungefähr 4,5 GeV untersucht werden.

Der Wirkungsquerschnitt $e^+e^- \rightarrow \pi^+\pi^-$ hat mit ungefähr 70% den größten Beitrag zu a_μ^{had} und ist mit einer Präzision von besser als 1% bekannt. Durch diese Hochpräzisionsmessung kommt der führende Beitrag zur Unsicherheit von a_μ^{had} von dem Energiebereich zwischen 1 GeV und 2 GeV, in welchem die Kanäle $e^+e^- \rightarrow \pi^+\pi^-\pi^0\pi^0$ und $e^+e^- \rightarrow \pi^+\pi^-\pi^+\pi^-$ den inklusiven hadronischen Wirkungsquerschnitt dominieren. Die präziseste Messung des Prozesses $e^+e^- \rightarrow \pi^+\pi^-\pi^+\pi^-$ wird in dieser Doktorarbeit vorgestellt. Dieser Kanal wurde von *BABAR* bereits basierend auf 25% der Gesamtstatistik gemessen. Im Vergleich zur ersten Analyse werden detailliertere Studien des Untergrunds anderer ISR- wie auch nicht-radiativer-Kanäle durchgeführt. Zusätzliche umfangreiche Studien zur Spur- sowie zur Photon-Rekonstruktionseffizienz reduzieren die systematische Unsicherheit in der Peakregion des Wirkungsquerschnittes von 5% auf 2.4%.

Neben der Extraktion des Wirkungsquerschnittes $\sigma(e^+e^- \rightarrow \pi^+\pi^-\pi^+\pi^-)$ wird eine erste Analyse interner Strukturen durchgeführt, die Hinweise auf resonante Zwischenzustände $\rho(770)^0 f_2(1270)$, $\rho(770)^0 f_0(980)$ wie auch $a_1(1260)^{\pm}\pi^{\mp}$ ergibt. Schließlich werden in dieser Arbeit auch die Verzweigungsverhältnisse $\mathcal{B}_{J/\psi \rightarrow \pi^+\pi^-\pi^+\pi^-}$ sowie $\mathcal{B}_{\psi(2S) \rightarrow J/\psi \pi^+\pi^-}$ bestimmt.

Summary

One of the most precisely measured quantities in particle physics is the magnetic moment of the muon, which describes its coupling to an external magnetic field. It is expressed in form of the anomalous magnetic moment of the muon $a_\mu = (g - 2)_\mu/2$ and has been determined experimentally with a precision of 0.5 parts per million. The current direct measurement and the theoretical prediction of the standard model differ by more than 3.5 standard deviations. Concerning theory, the contribution of the QED and weak interaction to a_μ can be calculated with very high precision in a perturbative approach. At low energies, however, perturbation theory cannot be used to determine the hadronic contribution a_μ^{had} . On the other hand, a_μ^{had} may be derived via a dispersion relation from the sum of measured cross sections of exclusive hadronic reactions. Decreasing the experimental uncertainty on these hadronic cross sections is of utmost importance for an improved standard model prediction of a_μ .

In addition to traditional energy scan experiments, the method of Initial State Radiation (ISR) is used to measure hadronic cross sections. This approach allows experiments at colliders running at a fixed centre-of-mass energy to access smaller effective energies by studying events which contain a high-energetic photon emitted from the initial electron or positron. Using the technique of ISR, the energy range from threshold up to 4.5 GeV can be accessed at *BABAR*.

The cross section $e^+e^- \rightarrow \pi^+\pi^-$ contributes with approximately 70% to the hadronic part of the anomalous magnetic moment of the muon a_μ^{had} . This important channel has been measured with a precision of better than 1%. Therefore, the leading contribution to the uncertainty of a_μ^{had} at present stems from the invariant mass region between 1 GeV and 2 GeV. In this energy range, the channels $e^+e^- \rightarrow \pi^+\pi^-\pi^0\pi^0$ and $e^+e^- \rightarrow \pi^+\pi^-\pi^+\pi^-$ dominate the inclusive hadronic cross section. The measurement of the process $e^+e^- \rightarrow \pi^+\pi^-\pi^+\pi^-$ will be presented in this thesis. This channel has been previously measured by *BABAR* based on 25% of the total dataset. The new analysis includes a more detailed study of the background contamination from other ISR and non-radiative background reactions. In addition, sophisticated studies of the track reconstruction as well as the photon efficiency difference between the data and the simulation of the *BABAR* detector are performed. With these auxiliary studies, a reduction of the systematic uncertainty from 5.0% to 2.4% in the peak region was achieved.

The $\pi^+\pi^-\pi^+\pi^-$ final state has a rich internal structure. Hints are seen for the intermediate states $\rho(770)^0 f_2(1270)$, $\rho(770)^0 f_0(980)$, as well as $a_1(1260)^\pm\pi^\mp$. In addition, the branching ratios $\mathcal{B}_{J/\psi \rightarrow \pi^+\pi^-\pi^+\pi^-}$ and $\mathcal{B}_{\psi(2S) \rightarrow J/\psi\pi^+\pi^-}$ are extracted.

Contents

Preamble	1
1 Hadronic Cross Sections and their Impact on the Standard Model	5
1.1 The Running of the Fine Structure Constant α_{QED}	6
1.2 The Magnetic Moment of the Muon a_μ	11
1.3 Measurements of Hadronic Cross Sections	19
2 The <i>BABAR</i> Experiment	23
2.1 The Asymmetric Collider PEP-II	24
2.2 The <i>BABAR</i> Detector	26
3 ISR Physics at <i>BABAR</i>	37
3.1 ISR Analyses	38
3.2 Vacuum Polarization	40
3.3 Radiative Corrections	41
3.4 ISR vs. Energy Scan	45
4 Event Selection for $\pi^+\pi^-\pi^+\pi^-\gamma$	49
4.1 Dataset and Primary Event Selection	50
4.2 Constrained Kinematic Fit and Further Selection	51
4.3 Background Subtraction	54
4.3.1 Background in Peak Region ($1.2 \text{ GeV}/c^2 < M_{4\pi} < 2.2 \text{ GeV}/c^2$) . . .	55
4.3.2 Background at Large Invariant Masses ($M_{4\pi} > 2.2 \text{ GeV}/c^2$) . . .	60
4.3.3 Background at Small Invariant Masses ($M_{4\pi} < 1.2 \text{ GeV}/c^2$) . . .	64
4.3.4 Background Summary	67
4.4 Global Efficiency	70

5 Systematic Corrections and Uncertainties	73
5.1 Energy and Position Calibration of the EMC	74
5.1.1 Event Selection for $\mu^+\mu^-\gamma$	74
5.1.2 Consistency Check of Kinematic Fit with Simulation: Angles and Energy	76
5.1.3 EMC Energy Calibration and Alignment	80
5.1.4 Use of Photon Parameters in the Kinematic Fit	84
5.2 Photon Efficiency	87
5.2.1 Event Selection	87
5.2.2 Constrained Fit and Background	89
5.2.3 Matching Predicted and Reconstructed Photons	91
5.2.4 Results for Photon Inefficiency	92
5.2.5 Inefficiency Difference for ISR Studies	101
5.2.6 Systematic Uncertainties	103
5.2.7 MC Correction	108
5.2.8 Conclusion	108
5.3 Tracking Efficiency	109
5.3.1 Event Selection	109
5.3.2 Kinematic Distributions	117
5.3.3 Tracking Inefficiency	121
5.3.4 Track Overlap Corrections	122
5.3.5 Estimate of Uncertainties	125
5.3.6 Conclusion	130
6 Extraction of the Cross Section $\sigma(e^+e^- \rightarrow \pi^+\pi^-\pi^+\pi^-)$	131
6.1 Summary of Systematic Corrections and Uncertainties	132
6.2 The Cross Section $\sigma(e^+e^- \rightarrow \pi^+\pi^-\pi^+\pi^-)$	133
6.3 Comparison to Existing Data	135
6.4 Influence on prediction of a_μ and $\Delta\alpha_{QED}^{had(5)}$	139
7 Study of Internal Structures and Charmonium Branching Ratios	141
7.1 J/ψ and $\psi(2S)$	142
7.2 Scan For Additional Resonances	144
7.3 Substructures	144
Conclusion and Outlook	151

A Cross Section $\sigma(e^+e^- \rightarrow \pi^+\pi^-\pi^+\pi^-)$	152
B Estimating Systematic Uncertainties	154
C Relation between Width and Integrated Cross Section of J/ψ and $\psi(2S)$	155
D Comparison of PHOKHARA5 Simulation with Data	157

Preamble

Physics faces an arbitrarily large amount of complex problems. Solving these by subdividing them into smaller problems, classifying similar types of problems, as well as detecting common patterns and symmetries between problems is one of the paradigms of problem solving in physics. This procedure can be visualised as a pyramid ranging from the initial complex problem at the top to a large number of basic problems at the bottom, as illustrated in Fig. 1.

In order to understand and solve these basic problems, a theoretical description is needed. In Fig. 1, these theories are represented by the branches of a tree. A general motivation of physics has always been to create a common theoretical basis for the solvable problems at the bottom of the pyramid. This common foundation is represented as the trunk of the tree, comprising the specific theories and procedures to solve all basic problems in the different fields of natural sciences. Thus, the complex problem at the top of a problem pyramid can be solved based on one unified basic theory.

In the 16th century Newton realized that the same mechanism which forces planets to move on elliptical trajectories around the sun also forces an apple to fall from a tree to the ground. Since then, physicists have successfully continued to connect theory twigs to common branches. Maxwell's equations, formulated in the 19th century, unified the phenomena of electricity and magnetism.

In the beginning of the 20th century, Einstein formulated the theories of special and later general relativity. Almost at the same time, the theory of quantum mechanics was developed. These theories superseded existing ones. In addition to the well-established results they predicted new phenomena.

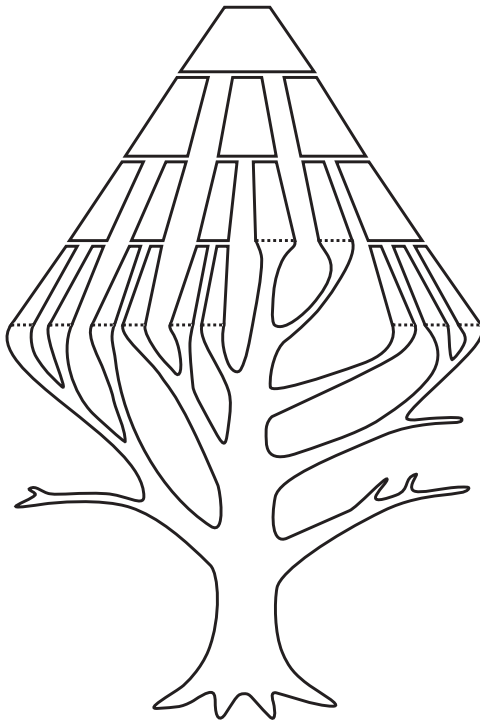


Figure 1: Illustration of the pyramidal problem structure as well as the tree-like theoretical basis describing these phenomena with a unified theory as the trunk.

The discovery of a structured periodic table of elements led to the assumption that the formerly thought to be fundamental particles called “atoms” have a substructure. The constituents are the protons, neutrons and electrons. Soon additional particles have been found in studies of cosmic rays as well as particle accelerator experiments. A combination of quantum mechanics and special relativity, the quantum field theory, was postulated in order to try to describe these phenomena. The first ingredients as well as the general recipe to formulate the standard model of particle physics were discovered.

According to the standard model, the fundamental point-like particles are the leptons and the quarks. They appear in nature in three families or generations, which differ in mass. For each of these fermions¹ the theory contains a corresponding anti-particle with opposite discrete quantum numbers. The standard model describes three out of the four known fundamental interactions: the weak, the electromagnetic and the strong interaction. The forces are transmitted via interaction particles, the so-called vector or gauge bosons. These standard model constituents are illustrated in Fig. 2.

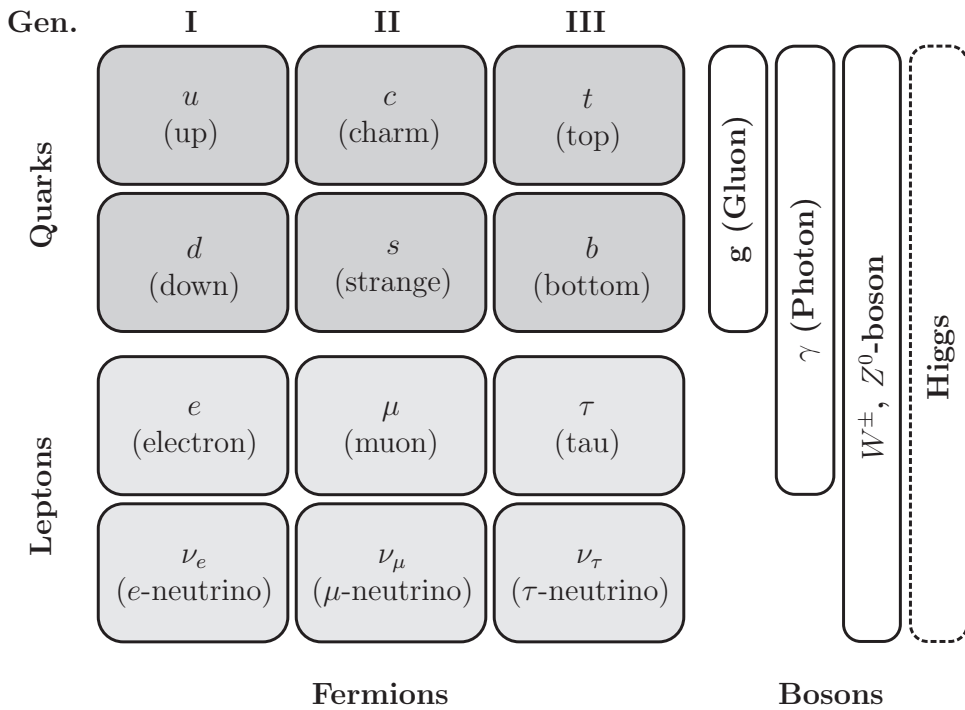


Figure 2: Elementary particles in the standard model: three generations of neutrinos (neutral leptons) coupling to the weak interaction (W^\pm , Z^0), charged leptons interacting in addition with photons, and finally quarks also coupling to the strong interaction transmitted via gluons. Through coupling to the Higgs particle, the fermions acquire their mass. The anti-particles are not listed.

The uncharged leptons - the very light neutrinos - only carry the weak charge and therefore are solely able to exchange the weak interaction particles (W^\pm and Z^0). The charged

¹In the standard model particles with half-integer spin are called fermions. Particles with integer spin are bosons.

leptons (electron e , muon μ , tau τ) carry electric charge and thus also couple to the photon. The quarks carry an additional charge called color, enabling them to couple to the strong interaction transmitted by gluons. They form strongly coupled composite objects like protons and neutrons. The Higgs particle is the only standard model constituent which has not been discovered, yet. The Higgs mechanism explains why in the electroweak interaction the photon is massless whereas the W^\pm - and Z^0 -bosons are massive. In addition, it generates the mass of the fermions.

The standard model, which describes all these fundamental interactions, has not been falsified until today. Many new particles and states had been predicted and found. However, there are fundamental reasons to believe that the standard model is only the low-energy limit of a more complete theory. Masses of the fundamental particles as well as additional parameters describing the interactions need to enter as input parameters and the distinct mass pattern is not understood. Furthermore, it is not understood why exactly three generations of leptons and quarks exist. In addition, the standard model provides neither an explanation for dark matter nor for dark energy. A complete theory should also incorporate the gravitational interaction described by the general relativity theory.

These and additional open questions lead to the common interest in tests of this theory in order to find its possible leaks and help theorists by finding the frontiers to look for phenomena of physics beyond the standard model. Experimental tests of the standard model fall into two distinct categories: The search for new structures at high energies on the one hand, and the performance of high precision measurements of parameters which can be calculated in the standard model to high accuracy at comparably low energies on the other hand.

One particular high precision test is provided by the anomaly of the magnetic moment of the muon, the so-called muon anomaly. The movement of a muon in an external magnetic field is sensitive to this quantity. This interaction and thus the muon anomaly has been measured with very high precision. The uncertainty of the theoretical prediction to the muon anomaly is limited by experimental input. This experimental input consists of hadronic cross sections which are measured with high precision as described within this thesis.

Chapter 1

Hadronic Cross Sections and their Impact on the Standard Model

This chapter introduces the electromagnetic coupling constant α_{QED} and the anomaly of the magnetic moment of the muon a_μ . Then the influence of hadronic cross section measurements at e^+e^- accelerators on the theoretical prediction of these physical quantities is discussed. Finally the present experimental situation of hadronic cross section measurements is presented.

In the standard model (SM), the strength of a fundamental interaction is parameterized by the corresponding coupling constant α . In a quantum field theory such as QED, virtual particle-antiparticle loops (“vacuum polarization”, VP) occur, to which a photon can couple. This leads to an energy (or scale) dependence of the effective coupling. This is briefly explained in the first part of this chapter.

Another example where the vacuum polarization plays a crucial role in a precision test of the standard model is the anomalous magnetic moment of the muon. Charged particles with spin carry a magnetic moment and therefore interact with magnetic fields. The strength of the interaction is proportional to the gyromagnetic factor g . According to the Dirac Theory for point-like particles with spin 1/2, g is equal to 2. A deviation of g from 2 is caused by virtual corrections. The size of this effect is usually given by the anomaly of the magnetic moment $a = (g - 2)/2$. The precision of the theoretical prediction within the standard model of particle physics of these corrections is limited by hadronic quark-antiquark loops, the hadronic vacuum polarization. Experimental determinations of the anomalous magnetic moment of the muon $a_\mu = (g - 2)_\mu/2$ are presented in this chapter as well as the theoretical predictions. It is moreover explained how experimental data on the cross section $\sigma(e^+e^- \rightarrow \text{hadrons})$ are related to these theoretical predictions via the fundamental assumptions of analyticity and causality. Finally, the current experimental situation concerning hadronic cross section data is presented.

1.1 The Running of the Fine Structure Constant α_{QED}

One fundamental input parameter for the electroweak SM is the fine structure constant α_{QED} . It is related to the electrical charge e via $\alpha = \frac{e^2}{4\pi\epsilon_0\hbar c}$ with the vacuum permittivity ϵ_0 , the reduced Planck Constant \hbar and the speed of light c . Vacuum polarization due to virtual particle-antiparticle pairs partially screens the electrical charge, modifying the value of the so-called bare charge e_0 . This effect is illustrated in Fig. 1.1.

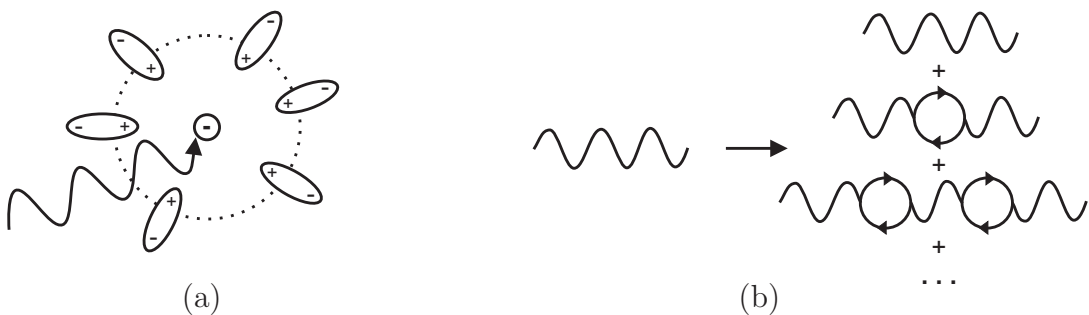


Figure 1.1: (a): Illustration of effective screening of the bare electrical charge through VP; (b): VP affects the coupling α_{QED} via higher order corrections in the SM.

Thus, e_0 needs to be replaced by a running charge depending on the momentum transfer q according to equation 1.1.

$$e^2 \rightarrow e^2(q^2) = \frac{e_0^2 \cdot Z_3}{1 + \Pi'_\gamma(q^2)} \quad (1.1)$$

The renormalization factor Z_3 ¹ is fixed by the boundary condition that in the limit $q^2 \rightarrow 0$ the running charge has to be equal to e_0 , $\Pi'_\gamma(q^2)$ is the so-called vacuum polarization amplitude. This leads to Formula 1.2 for the running of the fine structure constant,

$$\alpha_{QED}(q^2) = \frac{\alpha_{QED}(0)}{1 - \Delta\alpha_{QED}(q^2)}, \quad (1.2)$$

with $\alpha_{QED}^{-1}(0) = 137.035999084(51)$ as measured in [1]. The screening is more effective at low momentum transfers. Therefore the strength of interaction increases with growing q^2 . The value for the fine structure constant is approximately larger by 6% at $q^2 = M_Z^2$, the mass of the Z-boson squared, compared to $q^2 = 0$ [2]. It is convenient to subdivide this effect into three loop contributions:

$$\Delta\alpha_{QED}(q^2) = \Delta\alpha_{QED}^{\text{lep}}(q^2) + \Delta\alpha_{QED}^{\text{had}(5)}(q^2) + \Delta\alpha_{QED}^{\text{top}}(q^2). \quad (1.3)$$

The QED contribution from the leptonic sector $\Delta\alpha_{QED}^{\text{lep}}$ has been calculated in perturbation theory up to three loops. The following value has been determined at $q^2 = s = M_Z^2$ [3], where in the past most of the electroweak precision tests have been performed at LEP/CERN:

$$\Delta\alpha_{QED}^{\text{lep}}(M_Z^2) = 314.98 \times 10^{-4}. \quad (1.4)$$

In the hadronic sector, the contribution from the top-antitop quark loops is very small [4]:

$$\Delta\alpha_{QED}^{\text{top}}(M_Z^2) = -(0.728 \pm 0.014) \times 10^{-4}, \quad (1.5)$$

and has therefore been separated in equation 1.3. The hadronic contribution from the loops of the remaining five quarks ($u\bar{u}, d\bar{d}, c\bar{c}, s\bar{s}, b\bar{b}$) are grouped into $\Delta\alpha_{QED}^{\text{had}(5)}$. The optical theorem expresses the relation between the hadronic vacuum polarization amplitude and hadronic e^+e^- cross sections as illustrated in Fig. 1.2. Making use of the analytic-

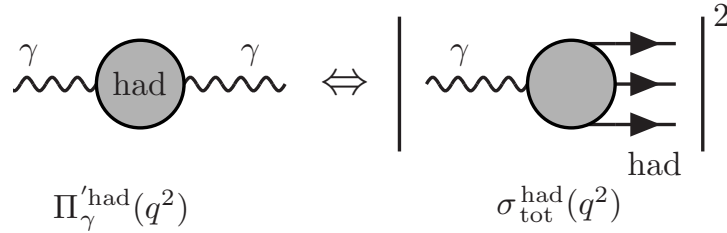


Figure 1.2: The optical theorem for the hadronic contribution to the photon propagator. [5].

ity of the vacuum polarization amplitude, in addition to the optical theorem allows to express the hadronic contribution to $\Delta\alpha_{QED}^{\text{had}(5)}$ via a dispersion relation:

$$\Delta\alpha_{QED}^{\text{had}(5)}(s) = \frac{-e^2 s}{12\pi^2} \text{Re} \int_{m_{\pi^0}^2}^{\infty} ds' \frac{R(s')}{s' - s - i\varepsilon}. \quad (1.6)$$

¹in a certain regularization scheme

$R(s)$ is given as the ratio of the hadronic to the muonic e^+e^- annihilation cross section:

$$R(s) = \frac{\sigma(e^+e^- \rightarrow \text{hadrons})}{\sigma(e^+e^- \rightarrow \mu^+\mu^-)}. \quad (1.7)$$

At high energies, perturbative quantum chromodynamics (pQCD) in an expansion of the strong coupling constant α_s can be applied in order to determine $R(s)$. Below a certain energy, E_{pQCD} , $R(s)$ has to be measured in e^+e^- experiments, because α_s is of $\mathcal{O}(1)$ at these energies. Therefore, the integral is subdivided into these two regions:

$$\Delta\alpha_{QED}^{\text{had}(5)}(s) = \frac{-e^2 s}{12\pi^2} \left[\text{Re} \int_{m_{\pi^0}^2}^{E_{pQCD}} ds' \frac{R(s')}{s' - s - i\varepsilon} + \text{Re} \int_{E_{pQCD}}^{\infty} ds' \frac{R(s')}{s' - s - i\varepsilon} \right] \quad (1.8)$$

Methods to determine this integral typically differ by the choice of E_{pQCD} and different approaches to combine the datasets for $R(s')$, e.g. the Adler function approach [6]. Concerning E_{pQCD} , some authors assume the validity of pQCD already above 1.8 or 2.5 GeV [7–10], while others prefer to use experimental data up to 12 GeV [10, 11]. Fig. 1.3 shows different evaluations of $\Delta\alpha_{QED}^{\text{had}}$ on the lower scale and the resulting $\alpha_{QED}^{-1}(M_Z^2)$ on the upper scale. It can be seen that the different assumptions are in reasonably good agreement with each other.

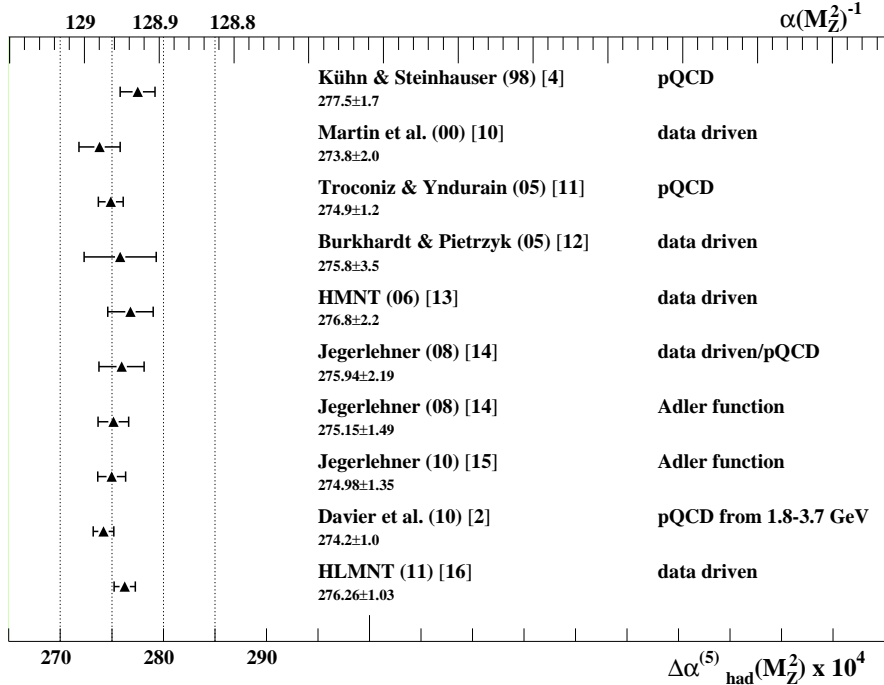


Figure 1.3: Evaluations of $\Delta\alpha_{QED}^{\text{had}}(M_Z^2)$ (lower scale) and the corresponding value of $\alpha_{QED}^{-1}(M_Z^2)$ (upper scale) at the Z boson mass M_Z . This information is presented in more detail in [16].

The most recent evaluation of $\Delta\alpha_{QED}^{\text{had}(5)}$ is given by [16]:

$$\Delta\alpha_{QED}^{\text{had}(5)}(M_Z^2) = (276.26 \pm 1.03) \times 10^{-4}, \quad (1.9)$$

leading via Equation (1.2) to the following prediction for the QED coupling constant at the Z boson mass:

$$\alpha_{QED}^{-1}(M_Z^2) = 128.944 \pm 0.014 \quad (1.10)$$

The uncertainty of $\alpha_{QED}^{-1}(M_Z^2)$ is completely dominated by the $\Delta\alpha_{QED}^{\text{had}(5)}(M_Z^2)$ contribution.

In Fig. 1.4 (left) it is shown how the data on $R(s)$ from different energy intervals \sqrt{s} contribute in Equation (1.6) to the absolute value of $\Delta\alpha_{QED}^{\text{had}(5)}(M_Z^2)$. Fig. 1.4 (right) shows the corresponding contributions to the uncertainty of $\Delta\alpha_{QED}^{\text{had}(5)}(M_Z^2)$ [5]. The leading contribution to the uncertainty stems from $R(s)$ data from the energy region between 1-2 GeV. Although the absolute contribution is small in this energy range (see Fig. 1.4 (left)), the contribution to the uncertainty is larger than 30%. The leading contribution to the inclusive hadronic cross section in this region stems from the hadronic reactions $e^+e^- \rightarrow \pi^+\pi^-\pi^+\pi^-$ and $e^+e^- \rightarrow \pi^+\pi^-\pi^0\pi^0$. Therefore, it is necessary to measure these contributions with the highest possible precision, since they dominate the uncertainty of the determination of α_{QED} .

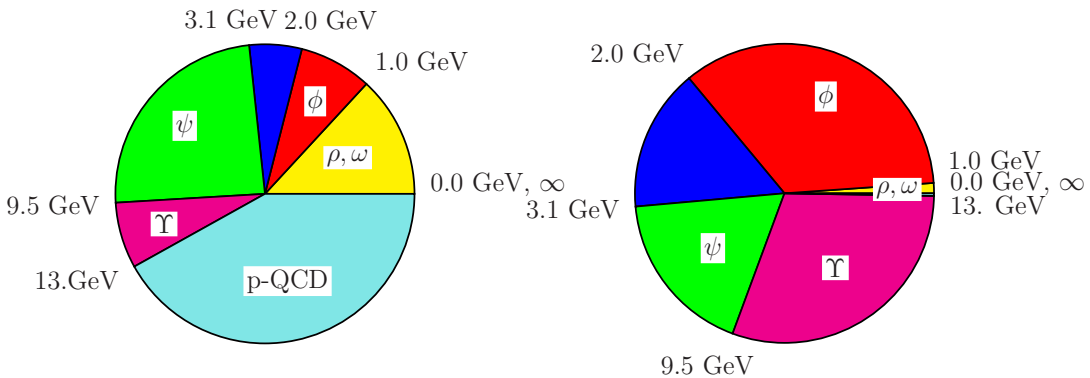


Figure 1.4: Fraction of total contributions (left) and uncertainty (right) to $\Delta\alpha_{QED}^{\text{had}(5)}(M_Z^2)$ from different energy intervals [5].

A precise knowledge of a set of SM parameters is needed to test its internal consistency and in order to make predictions for properties of so-far unknown particles as the mass of the Higgs-boson. These predictions are performed e.g. by the LEP (Large Electron-Positron Collider) ElectroWeak Working Group (EWWG) [17] or the Gfitter group [18]. They combine electroweak measurements from the LEP experiments with additional experimental results of NuTeV, CDF, D \emptyset and SLD in order to perform a SM fit. As an example, in Fig. 1.5 (left), experimental extractions of the sine-square of the Weinberg angle $\sin^2 \theta_{\text{eff}}^{\text{lept}}$ are shown [19]. This angle is obtained by asymmetry measurements at LEP-1 and SLC (Stanford Linear Collider) depending only on leptonic couplings (top three) as well as additional quark couplings (bottom three), which require small electroweak corrections. Also shown is the weighted average value as well as the SM prediction of the running of $\sin^2 \theta_{\text{eff}}^{\text{lept}}$ as a function of the Higgs-boson mass. The uncertainties due to the hadronic contribution of the fine structure constant $\Delta\alpha_{QED}^{\text{had}(5)}(M_Z^2)$ as well as due to the

uncertainty of the top-quark mass m_t are indicated. Using the average value of $\sin^2 \theta_{\text{eff}}^{\text{lept}}$ as well as other electroweak fits, the SM prediction of the Higgs-boson mass m_H is displayed in Fig. 1.5 (right). The regions excluded by direct measurements at LEP [20] and the Tevatron [21, 22] are also indicated. The Higgs-boson mass is predicted to be $m_H = 89^{+35}_{-26} \text{ GeV}/c^2$ at 68% confidence level as shown by the black curve ($\Delta\chi^2 = 1$). Most of this region is already excluded by direct LEP measurements. The fit result includes a theory based evaluation of $\alpha_{QED}^{\text{had}(5)}(M_Z^2)$ [23]. Including hadronic cross section measurements decreases the tension with the SM for the prediction of m_H . Thus, the prediction for the mass of the Higgs-boson strongly depends on the running of the fine structure constant and therefore on the hadronic cross section data.

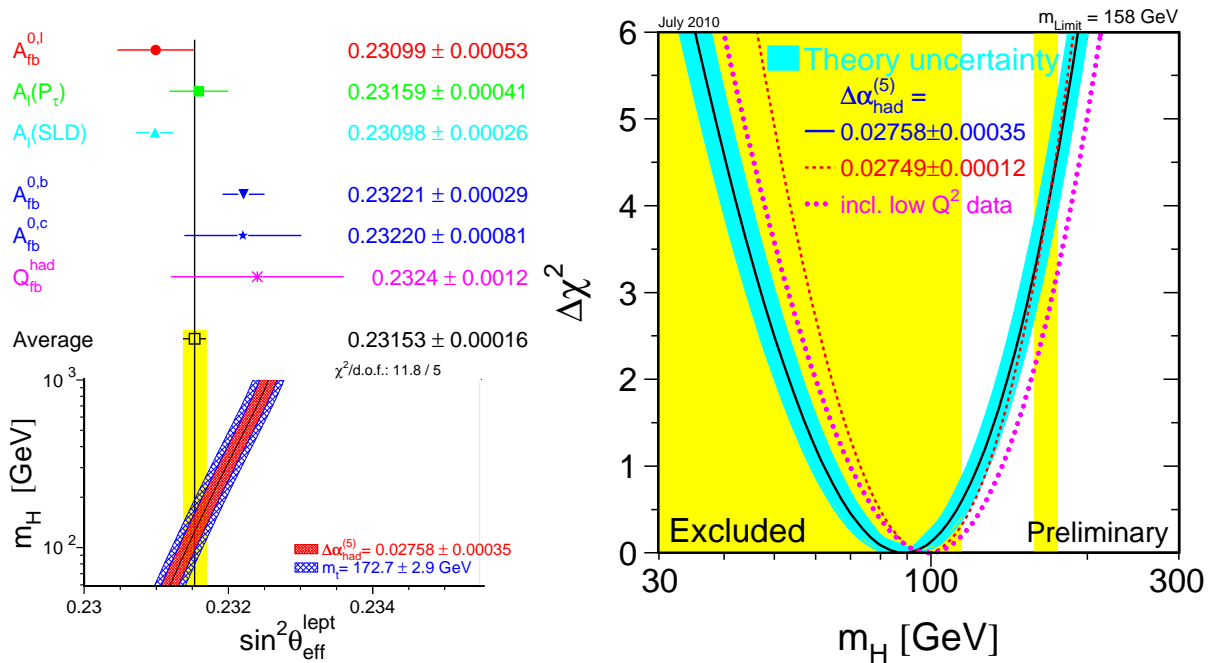


Figure 1.5: Left: Extractions of the Weinberg angle $\sin^2 \theta_{\text{eff}}^{\text{lept}}$ from LEP-1 and SLC measurements depending only on lepton couplings (top) and in addition on quark couplings (middle) as well as the weighted average; bottom: the running of the standard model prediction of $\sin^2 \theta_{\text{eff}}^{\text{lept}}$ as a function of the mass of the Higgs-boson m_H (black line); the uncertainties due to the hadronic contribution of the fine structure constant $\Delta\alpha_{QED}^{\text{had}(5)}(M_Z^2)$ (red band) as well as due to the uncertainty of the top-quark mass m_t (blue shaded band) are also indicated. Right: $\Delta\chi^2$ curve derived from the EWWG fit as a function of the Higgs-boson mass m_H , assuming the standard model to be valid. The vertical bands represent the excluded m_H regions with a confidence level of 95% derived by direct measurements at LEP [20] and the Tevatron [21, 22]. The dashed lines include a more recent evaluation of $\Delta\alpha_{QED}^{\text{had}(5)}(M_Z^2)$ based on hadronic cross section measurements [23] instead of a more theory based evaluation [24]. Also shown is the influence of additional low Q^2 data, e.g. from the NuTev measurement, [19]. Images are taken from [17, 19].

1.2 The Magnetic Moment of the Muon a_μ

A massive, charged particle with spin \vec{s} interacts with a magnetic field \vec{B} . The interaction causes an energy-splitting ΔE , which is proportional to \vec{B} and the magnetic moment $\vec{\mu}$ of the particle, $\Delta E = -\vec{\mu}\vec{B}$, where $\vec{\mu}$ is defined as:

$$\vec{\mu} = g \frac{e\hbar}{2m} \vec{s}. \quad (1.11)$$

In the Dirac theory of point-like particles with spin 1/2, the gyromagnetic factor g is equal to 2. In a relativistic quantum field theory, however, quantum corrections need to be considered, leading to a deviation of g from 2. This deviation is typically given in terms of the anomalous magnetic moment which is defined as $a_l = (g-2)_l/2$ ($l = e, \mu, \tau$).

Contributions to the anomalous magnetic moment of leptons δa_l by quantum fluctuations from higher energy scales or heavier particles are typically proportional to the square of the mass of the lepton:

$$\delta a_l \propto \frac{m_l^2}{M^2} (M \gg m_l) \quad (1.12)$$

Here M may be either the mass of a heavier SM particle or a heavy state beyond the SM, or an energy scale (ultraviolet cut-off) at which the SM is not valid anymore.

In order to test the SM predictions, free, point-like, massive, charged particles are needed. These requirements are fulfilled by the charged leptons (electron e , muon μ , tau τ). The electron anomaly is known with the highest precision, by a factor 2000 more precise than the muon anomaly a_μ . Due to the fact that in the case of the muon anomaly loop effects of heavy gauge bosons or hypothetical heavy particles beyond the SM are magnified by the factor $(m_\mu/m_e)^2 \approx 40000$, a_μ is 20 times more sensitive to physics beyond the SM (New Physics). For a_e the effects of the weak and the hadronic corrections cannot yet be resolved at the given level of experimental precision. Testing the electron anomaly is thus a unique test of QED and in addition allows an extremely precise determination of the fine structure constant α_{QED} at essentially zero momentum transfer [1]. a_τ is in principle even more sensitive to effects of New Physics in comparison to a_μ and a_e . However, by current experimental means a precision measurement is not feasible due to the short lifetime $t_{1/2}$ of the τ ($t_{1/2}(\tau) \approx 10^{-13}$ s). Thus a comparison of high precision measurements of a_μ with the SM prediction provides the best SM probe and is considered as a “monitor for New Physics”. At the same time, the physics of $(g-2)_\mu$ challenges also New Physics with a large parameter space already being ruled out with the given precision of theory and experiment. This section will cover the current experimental determination as well as the SM predictions of $(g-2)_\mu$.

Experiment: High precision measurements of $(g - 2)_\mu$

The concept of the $(g - 2)_\mu$ measurement is the following: Polarized muons are injected into a constant and well known homogeneous magnetic field \vec{B} . The muons perform a cyclotron motion with a characteristic angular frequency $\vec{\omega}_c$. Due to the motion of the muons' magnetic moment in \vec{B} , the spin axis is changed as described by the Larmor frequency $\vec{\omega}_l$. Because of the muon anomaly, $\vec{\omega}_l$ is slightly larger than $\vec{\omega}_c$. Therefore after each full circle the muon's momentum is unchanged, whereas the spin axis changes its relative angle as illustrated in Fig. 1.6 [25]. This results in a precessing muon spin according to the frequency difference $\vec{\omega}_a = \vec{\omega}_l - \vec{\omega}_c$.

$$\vec{\omega}_c = \frac{e\vec{B}}{m_\mu \gamma}, \quad \vec{\omega}_l = \frac{e\vec{B}}{m_\mu \gamma} + a_\mu \frac{e\vec{B}}{m_\mu}, \quad \vec{\omega}_a = a_\mu \frac{e\vec{B}}{m_\mu}, \quad (1.13)$$

with the relativistic Lorentz factor $\gamma = 1/\sqrt{1 - v^2/c^2}$ and the muon velocity v .

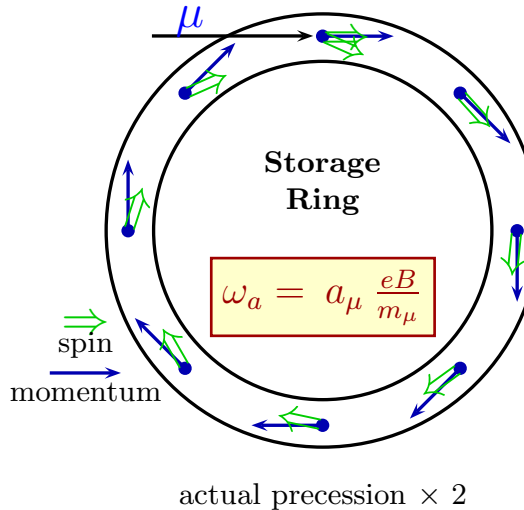


Figure 1.6: Spin precession due to a_μ in the $(g - 2)_\mu$ storage ring ($\sim 12^\circ/\text{circle}$) [25].

This basic principle of the a_μ measurement via the precession frequency $\vec{\omega}_a$ had already been used in the last CERN experiment [26]. It was re-adapted in the latest BNL experiment with major improvements including a high intensity primary proton beam provided from the proton storage ring AGS (Alternating Gradient Synchrotron) and a separate muon – instead of pion – storage ring with a super-ferric magnet [27]. The working principle of the muon $(g - 2)_\mu$ experiment at Brookhaven is illustrated in Fig. 1.7. Additional information is given in [28–30].

Pions are produced in the collision of the 24 GeV proton beam of the AGS with a fixed target. Eventually the pions decay into a muon and a neutrino. Thanks to the helicity structure of the weak decay the spin of the muons is directed along the direction of their momentum, i.e. the muons are longitudinally polarized. Next, they are injected into the

toroid-shaped ring with a 1.45 T magnetic field keeping them on a circular path with a diameter of 14 meters.

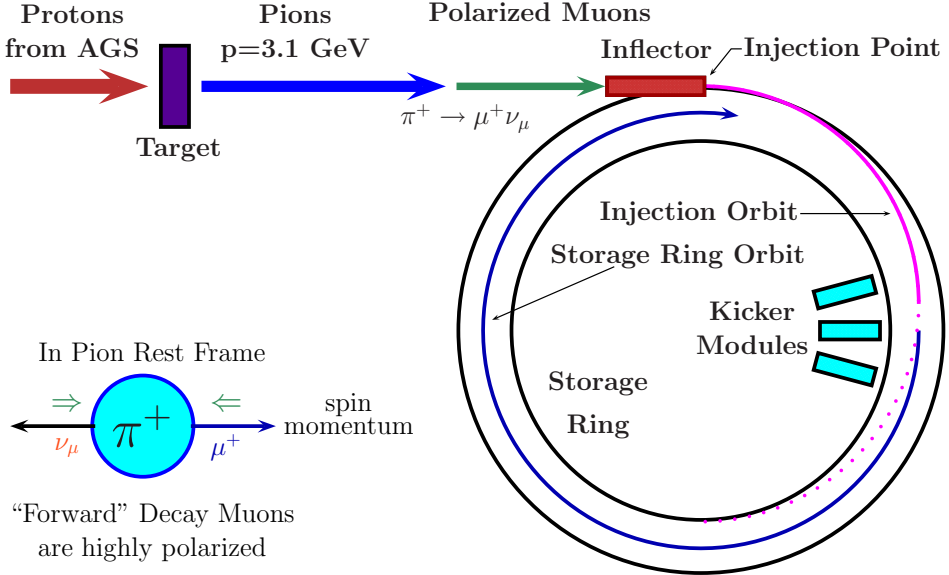


Figure 1.7: Illustration of muon production, injection and storage in the BNL $(g - 2)_\mu$ ring [25].

Retaining the muons on their trajectories requires an electrostatic focusing system. Therefore in addition to the magnetic field \vec{B} , an electric quadrupole field \vec{E} needs to be applied in the plane defined by the muon orbit. This transversal electric field has an impact on the precession frequency $\vec{\omega}_a$ as calculated by Bargmann, Michel and Telegdi in 1959 [31, 32]:

$$\vec{\omega}_a = \frac{e}{m_\mu} \left(a_\mu \vec{B} - \left[a_\mu - \frac{1}{\gamma^2 - 1} \right] \vec{v} \times \vec{E} \right). \quad (1.14)$$

It is remarkable that for a certain choice of γ ($\gamma = 29.3$), the term $(a_\mu - 1/(\gamma^2 - 1))$ approximately vanishes, such that the precession frequency $\vec{\omega}_a$ becomes almost independent of \vec{E} . This corresponds to a "magic" muon energy of $E_{\text{magic}} = \gamma m_\mu = 3.098 \text{ GeV}$. In addition to the suppression of the \vec{E} effect, this energy leads to a large time dilatation, increasing the lifetime of the muon in the laboratory frame from $2.20 \mu\text{s}$ to $64.4 \mu\text{s}$. Therefore the muons are circulating in the ring many times before decaying according to $\mu^+ \rightarrow e^+ + \nu_e + \bar{\nu}_\mu$. High-energetic positrons are emitted with high probability along the current spin axis of the muon. Again this relation is due to the structure of the weak decay. Finally, as illustrated in Fig. 1.8, the energy of the positrons is measured with 24 calorimeters distributed evenly inside the muon storage ring. This allows a selection of forward decaying positrons above a certain energy threshold E_T and thus to determine the direction of the muon's spin.

The number of detected decay positrons $N(t)$ with an energy above E_T emitted at time t after the muon injection is given by

$$N(t) = N_0(E_T) \exp\left(\frac{-t}{\gamma\tau_\mu}\right) [1 + A(E_T) \sin(\omega_a t + \phi(E_T))] \quad (1.15)$$

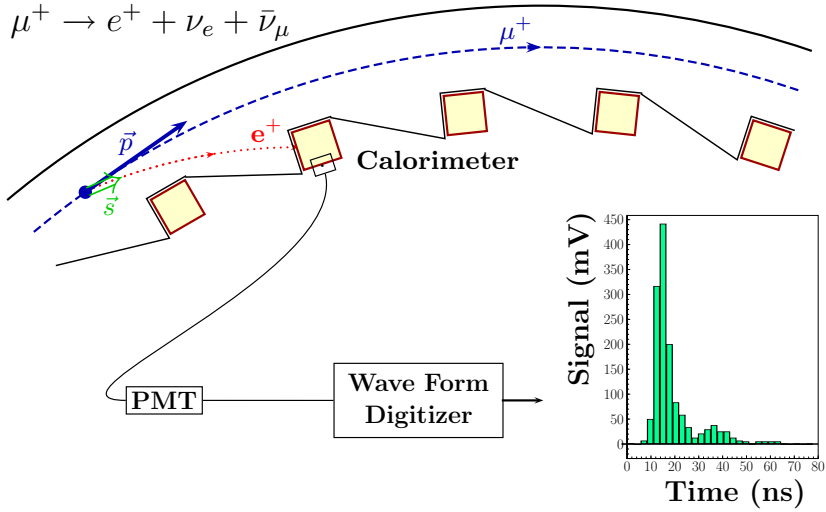


Figure 1.8: Decay of μ^+ and detection of the emitted e^+ [25]. High-energetic positrons are correlated with the current muon spin direction.

with a normalization factor $N_0(E_T)$, the muon life time τ_μ , the asymmetry factor $A(E_T)$, and a phase $\phi(E_T)$. This expected exponential decay law with a modulation due to the $(g - 2)_\mu$ precession is observed in Fig. 1.9 for approximately 3.6 billion recorded decays in the 2001 data-taking period.

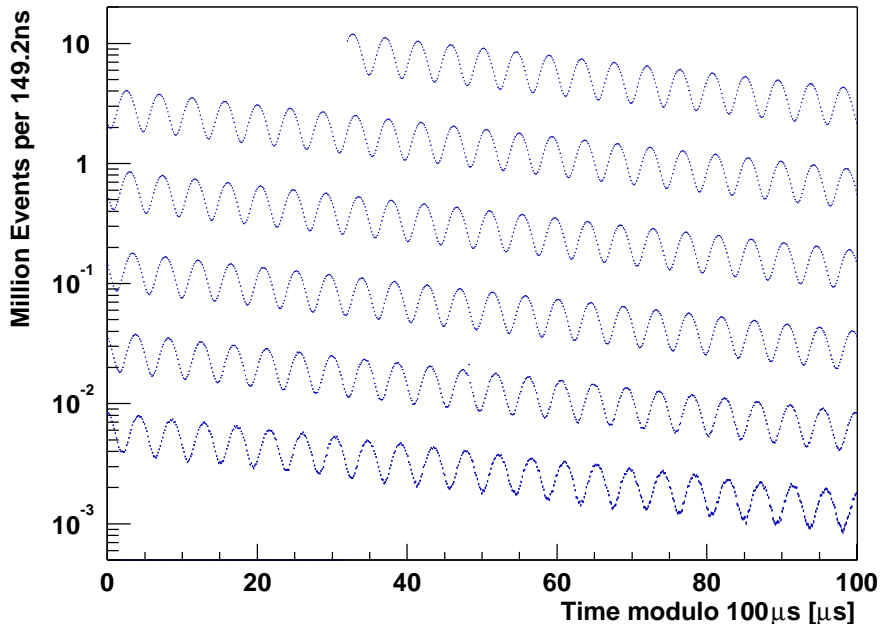


Figure 1.9: Counts of detected positrons versus time distribution for 3.6 billion decays in the 2001 μ^- data-taking period (E821 experiment, BNL) [27].

For a precision measurement of a_μ , in addition to \vec{B} (measurement described in [33]), also the mass of the muon m_μ must be known to very high precision. The experiments on the microwave spectrum of ground state muonium ($\mu^+ e^-$) [34] performed at LAMPF at Los Alamos in combination with the theoretical prediction of the muonium hyperfine splitting [35, 36] provides the needed result.

Experiment	Year	Polarity	$a_\mu \times 10^{11}$	$\Delta a_\mu/a_\mu$ [ppm]	Ref.
CERN I	1961	μ^+	114 500 000(2200000)	4300	[37]
CERN II	1962-1968	μ^+	116 616 000(31000)	270	[38]
CERN III	1974-1976	μ^+	116 591 000(1100)	10	[26]
CERN III	1975-1976	μ^-	116 593 600(1200)	10	[26]
BNL	1997	μ^+	116 592 510(1500)	13	[39]
BNL	1998	μ^+	116 591 910(590)	5	[40]
BNL	1999	μ^+	116 592 020(150)	1.3	[41]
BNL	2000	μ^+	116 592 040(90)	0.73	[42]
BNL	2001	μ^-	116 592 140(90)	0.72	[43]
Average			116 592 080(63)	0.54	[27]

Table 1.1: Summary of the CERN and BNL results. Information is taken from [27].

Table 1.1 summarizes all a_μ measurements from the CERN and BNL experiments. The average result for a_μ is published in [27]:

$$a_\mu = 116 592 080(54)(33) \times 10^{-11} \quad [0.54 \text{ ppm}]. \quad (1.16)$$

The uncertainties correspond to the statistical and systematic uncertainties, respectively.

Theory: Pre/Post-diction of a_μ

The radiative corrections giving rise to the muon anomaly are subdivided into QED, electroweak and hadronic contributions according to the nature of the interaction leading to the correction.

$$a_\mu^{SM} = a_\mu^{\text{QED}} + a_\mu^{\text{weak}} + a_\mu^{\text{had}} \quad (1.17)$$

The QED part includes all diagrams containing only photons and leptonic loops as radiative corrections and may in general be written as a power series in α/π . The Schwinger term containing the one-photon exchange correction, illustrated in Fig. 1.10 (a), accounts for more than 99% of the total correction. The corrections including two leptonic loops are illustrated in Fig. 1.10 (b)-(h). These two loop corrections [44, 45] as well as the three loop terms [46–48] are known analytically. The four loop corrections, containing already

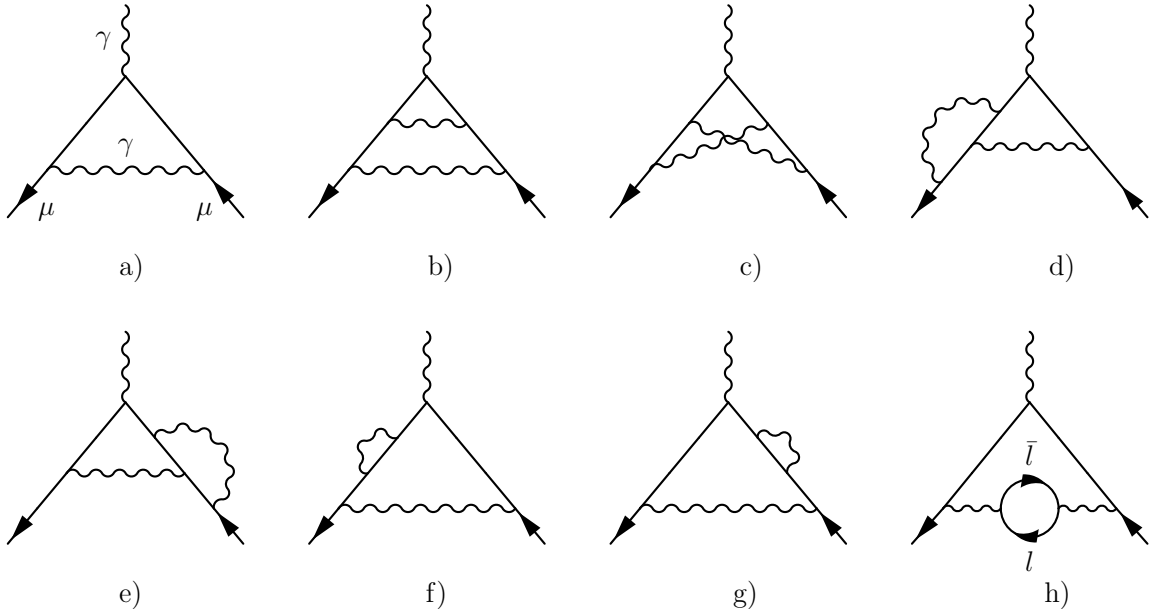


Figure 1.10: Leading order QED contribution (a) and NLO QED corrections (b-h) of $(g-2)_\mu$.

more than 1000 diagrams, as well as the most important five loop contributions are determined numerically. This leads to the following evaluation of the QED contribution to the muon anomaly [25]:

$$a_\mu^{QED} = (116\,584\,718.104 \pm 0.148) \times 10^{-11} \quad (1.18)$$

The uncertainty is dominated by the estimated uncertainty of the five loop contribution.

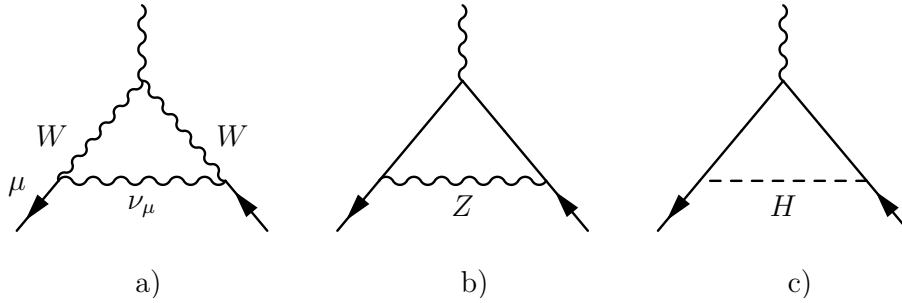


Figure 1.11: Leading order weak corrections of $(g-2)_\mu$.

The leading contributions of the electroweak correction are illustrated in Fig. 1.11. The most relevant graph at this order is the triple gauge boson vertex term shown in Fig. 1.11 (a). The graph including the virtual Z boson, Fig. 1.11 (b), has opposite sign and is half as large. The Higgs term Fig. 1.11 (c) is estimated to be smaller than 5×10^{-14} taking into account the current lower mass bound for the Higgs mass from the LEP experiments ($m_H > 114 \text{ GeV}/c^2$). Typical electroweak 2-loop corrections are a combination of the 1-loop diagrams with additional fermionic loop insertions. The electroweak contribution to a_μ is found to be [49, 50]:

$$a_\mu^{weak} = (153.2 \pm 1.0 \pm 1.5) \times 10^{-11}. \quad (1.19)$$

The first uncertainty is an estimate of hadronic loop effects, while the second uncertainty is due to estimates with different Higgs masses.

The hadronic contribution finally may be subdivided again into Leading Order (LO) and Higher Order (HO) terms as well as the hadronic Light-by-Light (LbL) scattering contribution.

$$a_\mu^{\text{had}} = a_{\mu,LO}^{\text{had}} + a_{\mu,HO}^{\text{had}} + a_{\mu,LbL}^{\text{had}} \quad (1.20)$$

The LO contribution is shown in Fig. 1.12 (a).

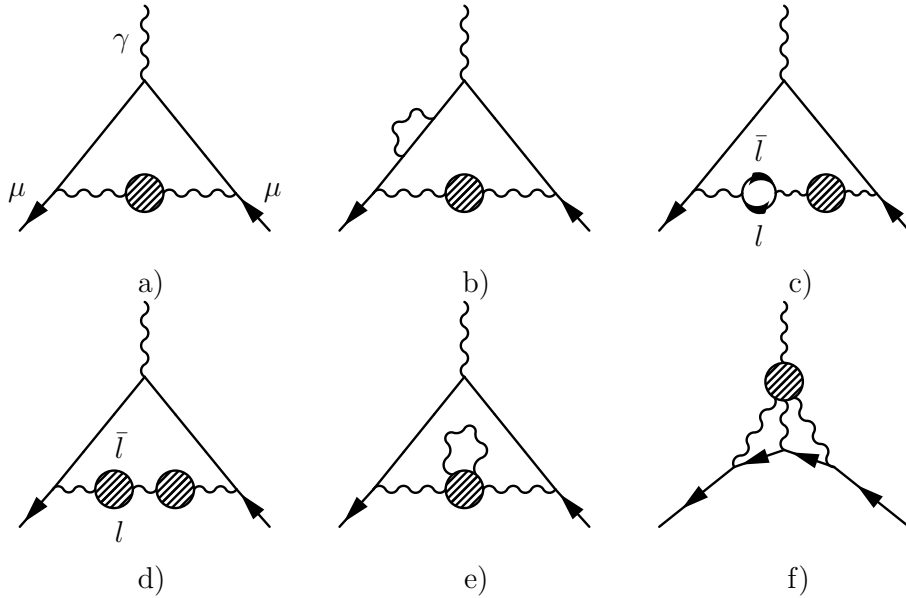


Figure 1.12: (a) Leading order hadronic contribution of $(g-2)_\mu$; (b)-(e) NLO corrections and (f) the hadronic LbL scattering contribution. The shaded circles represent the hadronic loop.

Fig. 1.12 (a)-(d) include LO vacuum polarization contributions, whereas Fig. 1.12 (e) in addition involves HO vacuum polarization corresponding to final state radiation (FSR) of hadrons. Fig. 1.12 (f) represents the leading order contribution of the hadronic LbL scattering contribution with three exchanged virtual photons. The LbL contribution to a_μ^{had} is theoretically estimated to be [51]

$$a_{\mu,LbL}^{\text{had}} = (105 \pm 26) \times 10^{-11}. \quad (1.21)$$

As described in Section 1.1, it is not possible to determine the vacuum polarization contribution theoretically. Experimental input is needed. Exploiting the analyticity and causality of the vacuum polarization amplitude enables us to relate the vacuum polarization to the inclusive hadronic cross section via a dispersion integral:

$$a_{\mu,LO}^{\text{had}} = \frac{1}{4\pi^3} \int_{m_{\pi^0}^2}^{\infty} ds \sigma_{\text{had}}(s) K(s) = \left(\frac{\alpha m_\mu}{3\pi} \right) \int_{m_{\pi^0}^2}^{\infty} ds \frac{R(s) \hat{K}(s)}{s^2} \quad (1.22)$$

where the Kernel functions $K(s)$ and $\hat{K}(s) = \left(\frac{3s}{m_\mu^2} \right) K(s)$ are known analytically². In this expression $\hat{K}(s)$ is a bound function between $\hat{K}(m_\pi^2) = 0.63$ and $\hat{K}(\infty) = 1$. This clarifies the $1/s^2$ dependence of the weighting of the $R(s)$ contributions in the dispersion integral. The dominant channel at low energies is $e^+e^- \rightarrow \pi^+\pi^-$, contributing with a relative fraction of 73% to the total hadronic correction of a_μ , as illustrated in Fig. 1.14 (left). The hadronic cross section measurements are presented in detail in Section 1.3. The following contribution to a_μ^{had} due to LO and HO hadronic corrections according to Ref. [2, 15] is found:

$$a_{\mu,LO}^{\text{had}} = (6923 \pm 42) \times 10^{-11}, \quad (1.23)$$

$$a_{\mu,HO}^{\text{had}} = (-97.9 \pm 0.9) \times 10^{-11}. \quad (1.24)$$

This leads to the SM prediction for a_μ according to [2]:

$$a_{\mu,SM}^{\text{had}} = (116\,595\,802 \pm 42 \pm 26 \pm 2) \times 10^{-11}, \quad (1.25)$$

where the uncertainties have been split into lowest and higher order hadronic, and other contributions, respectively.

In Fig. 1.13 the theoretical evaluations of a_μ using different experimental input are compared to the BNL measurement. Instead of electron-positron annihilation measurements, it is also possible to determine $a_{\mu,SM}^{\text{had}}$ from hadronic τ -decay measurements exploiting the conserved vector current. The $e^+e^- \rightarrow \pi^+\pi^-$ channel after isospin rotation corresponds to the $\tau^\pm \rightarrow \nu_\tau \pi^\pm \pi^0$ decay. After taking into account the QED and the isospin breaking effects, i.e. γ -radiation and the mass splitting ($m_u \neq m_d$), a difference to the electron-positron annihilation result remains. Recently a possible missing contribution to the correction due to the ρ - γ -mixing has been pointed out [52], shifting the τ -decay results into agreement with electron-positron annihilation measurements.

Including the newest *BABAR* data of the channel $e^+e^- \rightarrow \pi^+\pi^-$, the difference between the theoretical prediction and the measurement of a_μ has been determined to be [2]:

$$a_\mu^{\text{exp}} - a_\mu^{\text{theory}} = (287 \pm 80) \times 10^{-11}. \quad (1.26)$$

This corresponds to a difference with a statistical significance of 3.6 standard deviations. Whether this deviation is due to an underestimated uncertainty in the direct $(g-2)_\mu$

² $K(s) = \frac{x^2}{2} (2 - x^2) + \frac{(1+x^2)(1+x)^2}{x^2} \left(\ln(1+x) - x + \frac{x^2}{2} \right) + \frac{(1+x)}{(1-x)} x^2 \ln(x)$,
with $x = \frac{1-\beta_\mu}{1+\beta_\mu}$, $\beta_\mu = \sqrt{1 - 4m_\mu^2/s}$ according to [25].

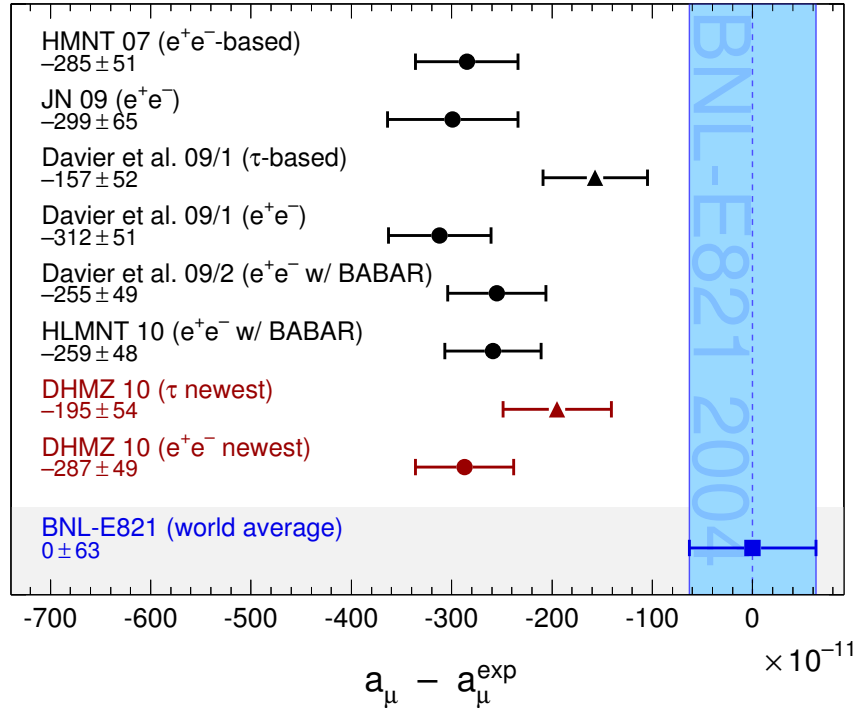


Figure 1.13: Compilation of recent results [2] for a_μ^{SM} (in units of 10^{-11}), subtracted by the central value of the experimental average [27,53]. The experimental BNL uncertainty is indicated with the blue-shaded vertical band. The SM predictions are determined in: DHMZ 10 [2], HLMNT (unpublished) [54] (e^+e^- -based, including BABAR and KLOE 2010 $\pi^+\pi^-$ data), Davier *et al.*, 09/1 [55] (τ -based), Davier *et al.*, 09/1 [55] (e^+e^- -based, not including BABAR $\pi^+\pi^-$ data), Davier *et al.*, 09/2 [56] (e^+e^- -based including BABAR $\pi^+\pi^-$ data), HMNT 07 [15] and JN 09 [25] (not including BABAR $\pi^+\pi^-$ data).

measurement or the SM prediction or whether New Physics leads to the difference is not known at present.

1.3 Measurements of Hadronic Cross Sections

The measurement of hadronic cross sections is essential for the determination of the hadronic vacuum polarization. As shown in 1.14 (left) the most important contribution from this vacuum polarization correction to a_μ comes from the low energy region. This region is dominated by the $e^+e^- \rightarrow \pi^+\pi^-$ cross section with a contribution of 73% to a_μ^{had} . The recent high precision cross section measurements of *BABAR* and *KLOE* of the exclusive channel $e^+e^- \rightarrow \pi^+\pi^-$ and various measurements of higher multiplicity channels are presented in the following.

The $e^+e^- \rightarrow \pi^+\pi^-$ Cross Section

The recent cross section measurement at *BABAR* [57] of this channel is shown in Fig. 1.15. The method of Initial State Radiation, which will be described in detail in Chapter 3, allows a cross section measurement from production threshold until 3 GeV. The dominant

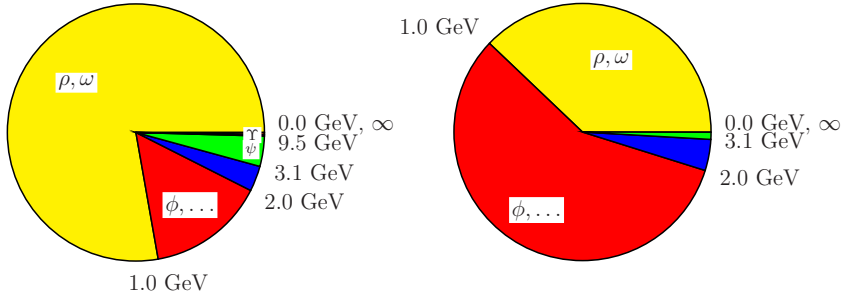


Figure 1.14: The distribution of contributions (left) and uncertainties (right) in % for a_μ^{had} from different energy regions. The uncertainty of a contribution i shown is $\sigma_{i\text{tot}}^2 / \sum_i \sigma_{i\text{tot}}^2$ in %. The total uncertainty combines statistical and systematic uncertainties in quadrature [25].

ρ peak is visible in Fig. 1.15 (a). The zoom in Fig. 1.15 (b) shows a striking drop on the high mass side of the peak which is due to $\rho - \omega$ interference. The systematic uncertainty in the ρ peak region is 0.5%. Between 1.5 and 1.6 GeV a dip due to interference of higher ρ resonances is seen as well as another structure at around 2.2 GeV.

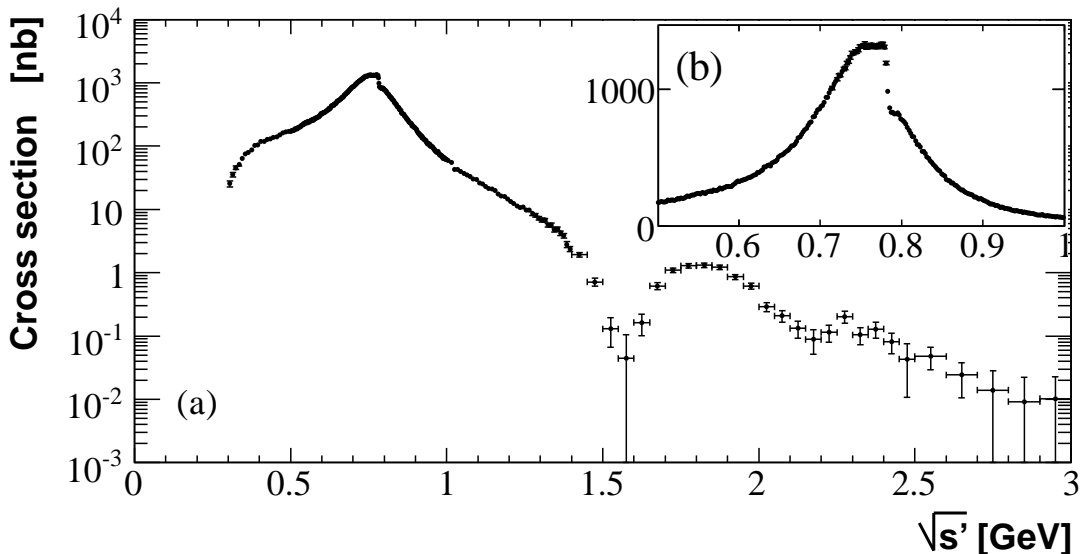


Figure 1.15: (a) The measured cross section for $e^+e^- \rightarrow \pi^+\pi^-(\gamma)$ from *BABAR* between 0.3 and 3 GeV; (b) Enlarged view of the ρ region in energy intervals of 2 MeV. The plotted uncertainties are from the sum of the diagonal elements of the statistical and systematic covariance matrices. This plot is published in [57].

The important cross section $\sigma(e^+e^- \rightarrow \pi^+\pi^-)$ has been measured by various experiments including TOF [58], OLYA [59, 60], CMD [59], CMD2 [61, 62], SND [63], DM1 [64], DM2 [65] and most recently KLOE [66–68]. All results are displayed together in Fig. 1.16 (top). Like *BABAR* the KLOE measurements also have a systematic uncertainty below 1%. Fig. 1.16 (bottom) compares the *BABAR* and KLOE data points using the HVPTools averaging tool [56]. Both experiments dominate the overall average. In the energy interval between 0.63 and 0.958 GeV, the discrepancy between the $a_\mu^{\text{had}, LO}[\pi\pi]$ evaluations from KLOE and *BABAR* amounts to 2.0σ [56].

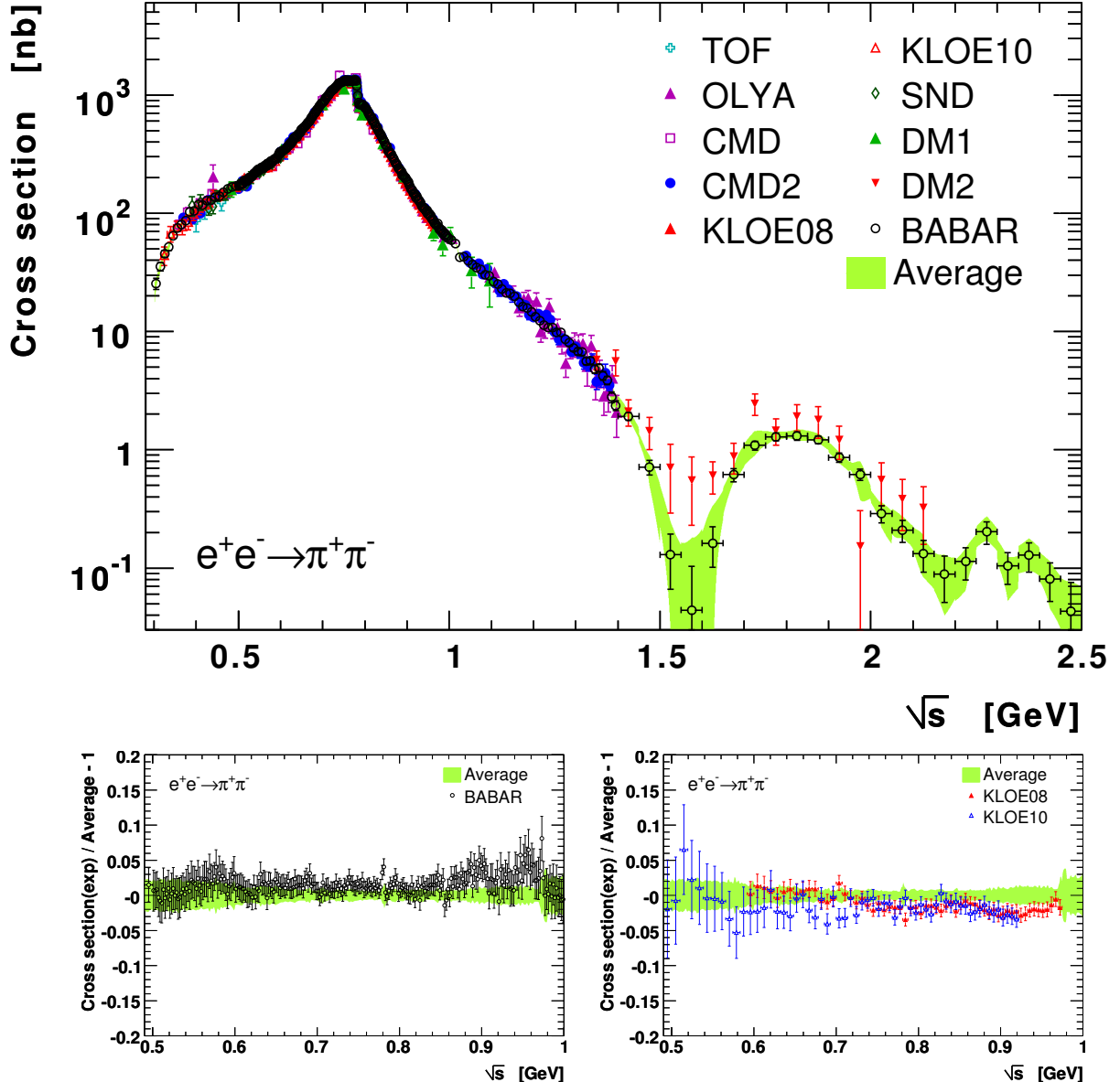


Figure 1.16: Top: $e^+e^- \rightarrow \pi^+\pi^-$ cross section as a function of center of mass energy. Shown are data from TOF [58], OLYA [59, 60], CMD [59], CMD2 [61, 62], SND [63], DM1 [64], DM2 [65], KLOE [66, 67] and BABAR [57]. The error bars show statistical and systematic uncertainties added in quadrature. The light shaded (green) band indicates the HVPTools average within 1σ uncertainties [2]. Bottom: Difference of BABAR (left) and KLOE (right) to the HVPTools average. These plots are published in [2].

The pie plot shown in Fig. 1.14 shows the relative fraction of contributions (left) and uncertainties (right) of different energy ranges to a_μ^{had} . Due to the very precise measurement of the largest contribution to a_μ^{had} from $\sigma(e^+e^- \rightarrow \pi^+\pi^-)$, the leading contribution to the uncertainty of a_μ^{had} stems now from the energy region between 1 GeV and 2 GeV, see Fig. 1.14 (right).

Higher Multiplicity Channels

A number of additional cross section measurements of channels with higher multiplicity have been performed at *BABAR* [69–76]. These results are displayed as a function of the center of mass energy $E = \sqrt{s}$ in Fig. 1.17. From this figure, it is clear that the

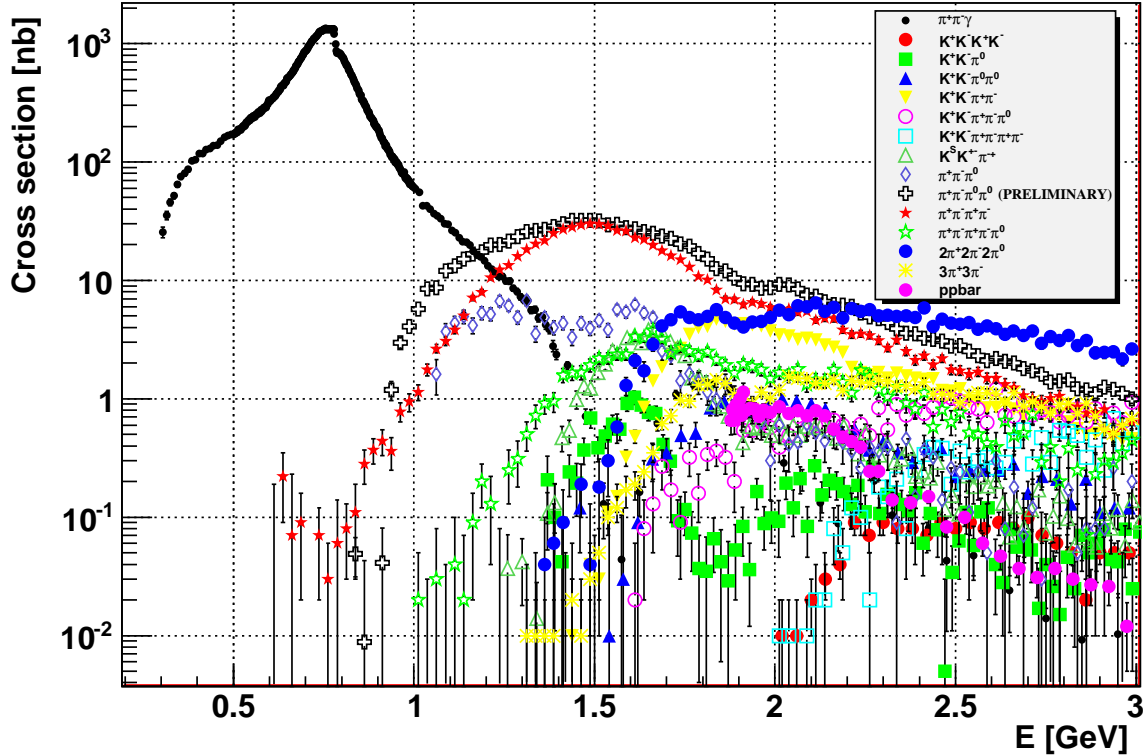


Figure 1.17: Cross section measurements performed at *BABAR*: $e^+e^- \rightarrow \pi^+\pi^-$ (black points), $e^+e^- \rightarrow \pi^+\pi^-\pi^0\pi^0$ (black crosses, preliminary results) and $e^+e^- \rightarrow \pi^+\pi^-\pi^+\pi^-$ (red stars). This image is published in [77].

channels $e^+e^- \rightarrow \pi^+\pi^-\pi^+\pi^-$ and $e^+e^- \rightarrow \pi^+\pi^-\pi^0\pi^0$ have the largest impact in the energy region $1 \text{ GeV} < \sqrt{s} < 2 \text{ GeV}$. The *BABAR* measurements provide the most precise available cross section evaluations for these channels. The preliminary $e^+e^- \rightarrow \pi^+\pi^-\pi^0\pi^0$ result will be finalized and published at the beginning of 2012 using the full data sample of $\mathcal{L} = 454.4 \text{ fb}^{-1}$. The $e^+e^- \rightarrow \pi^+\pi^-\pi^+\pi^-$ result shown in Fig. 1.17 is based on a luminosity of $\mathcal{L} = 89 \text{ fb}^{-1}$ with a systematic uncertainty of 5% in the peak region $1.2 \text{ GeV} < E < 2.2 \text{ GeV}$. It is the main goal of this work to improve the uncertainty of the $e^+e^- \rightarrow \pi^+\pi^-\pi^+\pi^-$ cross section measurement. In addition to the higher statistics due to the additional data, corresponding to a luminosity of $\mathcal{L} = 454.4 \text{ fb}^{-1}$, especially the systematic uncertainties should be improved. This is achieved by additional systematic studies and corrections as well as an alternative approach concerning background channel suppression. The systematic studies are also needed in order to finalize the preliminary $e^+e^- \rightarrow \pi^+\pi^-\pi^0\pi^0$ result. The results of this thesis will therefore reduce the uncertainty of a_μ^{had} and thus the theoretical uncertainty of a_μ .

Chapter 2

The *BABAR* Experiment

This chapter is dedicated to the BABAR experiment. In the beginning the accelerator and the experimental setup is discussed. Then a detailed description of the different sub-detection systems of the multi-purpose BABAR detector is given. The chapter closes with a brief overview of the data acquisition at BABAR.

The *BABAR* experiment was taking data in the years 1999-2008 at the *Stanford Linear Accelerator Center* (SLAC¹) in Menlo Park, California. The PEP-II collider operated at the Center-of-Mass (CM) energy of 10.58 GeV which corresponds to the mass of the $\Upsilon(4S)$ resonance, slightly above the $B\bar{B}$ production threshold. Due to the large cross section for the production of B meson pairs ($\sigma = 1.05$ nb [78]) at this CM energy and the high luminosity of PEP-II, the facility is called a *B* Factory. In this chapter, the PEP-II collider as well as the main features of the *BABAR* detector are presented. Ref. [79, 80] provide additional information.

2.1 The Asymmetric Collider PEP-II

The accelerator facility needed for the *BABAR* experiment is shown in Fig. 2.1. It is composed by an electron gun, a linear accelerator (linac), the positron source and the e^+e^- storage rings (PEP-II).

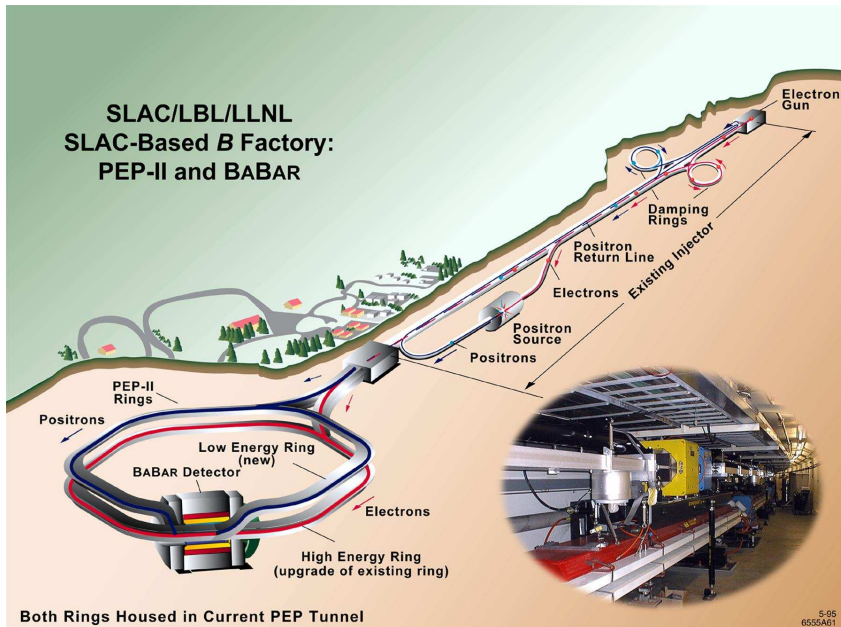


Figure 2.1: A schematic view of SLAC facility including the linear accelerator and the asymmetric PEP-II collider with the *BABAR* detector [81].

The electron gun produces the electron bunches and inserts them into the linac. Electromagnetic pulses with synchronized radio-frequency (RF) accelerate these bunches to an energy of approximately 1 GeV. Half of these bunches are inserted into and collected in a damping ring, where energy losses due to synchrotron radiation are compensated by RF cavities. This leads to a reduction of the spatial and momentum beam spread, the so-called cooling. The damped beam is redirected to the linac and accelerated to the final energy of 8.9 GeV. The other half of the generated electron bunches are further accelerated to 30 GeV and directed onto a tungsten target in order to generate the positron beam (positron source). The positron bunches are led back to the start of the linac.

¹since October 2010 renamed to SLAC National Accelerator Laboratory

Run	on-peak [fb^{-1}]	off-peak [fb^{-1}]
1	20.4	2.6
2	61.1	6.9
3	32.3	2.5
4	100.3	10.1
5	132.9	14.5
6	66.1	4.6

Table 2.1: Amount of accumulated data in various Run periods.

Similar to the electrons, they are pre-accelerated and damped in a separate damping ring for cooling and collection. Finally these positrons are further accelerated in the linac up to an energy of 3.1 GeV. After reaching their nominal energies, electron and positron bunches are injected from the linac into the PEP-II storage rings. They are continuously focused by a magnetic system, and again synchrotron-radiation losses are compensated by RF acceleration. The *BABAR* detector is located at the crossing point of the electron and the positron beam.

Data taking started in October 1999 and ended in April 2008. An integrated luminosity of 454.4 fb^{-1} in six Run periods at (on-peak) or in the vicinity (off-peak) of the $\Upsilon(4S)$ resonance has been recorded, see Table 2.1. Due to additional Runs on the $\Upsilon(3S)$ and $\Upsilon(2S)$ resonances, a total recorded integrated luminosity of 553.48 fb^{-1} was accumulated, see Fig. 2.2.

Due to the energy difference between the electron and positron beam, the e^+e^- center-of-mass system is boosted relative to the laboratory system. This boost is intended to allow separation of the decay vertices of B-mesons, which are produced almost at rest in the e^+e^- CM frame. This spatial difference translates into a time difference and therefore allows for the determination of decay time differences of B-decays, which is needed in many *BABAR* analyses [78]. PEP-II was designed for an instantaneous luminosity of $3 \times 10^{33} \text{ cm}^{-2}\text{s}^{-1}$. The peak luminosity has been improved in the course of the years to a luminosity value of $12 \times 10^{33} \text{ cm}^{-2}\text{s}^{-1}$.

One of the main goals of the *BABAR* physics programme was to over-constrain the CKM quark mixing matrix parameters. Some of these parameters can be extracted by measurements of CP asymmetries in B decays. The cleanest test of CP violation in the B meson system within the Standard Model consists of the study of time-dependent CP violation in the channel $B \rightarrow J/\psi K_S^0$. The B^0 and the \bar{B}^0 mesons decay with a different time behavior into the common final state. In studies of rare B decay channels, searches for physics beyond the SM are performed. The cross section for $e^+e^- \rightarrow c\bar{c}$ and $e^+e^- \rightarrow \tau^+\tau^-$ is similar as for the process $e^+e^- \rightarrow b\bar{b}$ at *BABAR*. In the open charm system, studies concerning mixing and CP violation in D decays are performed and one of the major discoveries of *BABAR* was indeed the evidence found for D^0 - \bar{D}^0 mixing. Concerning the τ sector, tests of lepton universality, searches for lepton flavor violation as well as a precision measurement of $|V_{us}|$ were performed. ISR studies are focused on cross section measurements of hadronic final states as well as spectroscopy. Various new resonances such as the $\Upsilon(4260)$ particle were discovered via ISR.

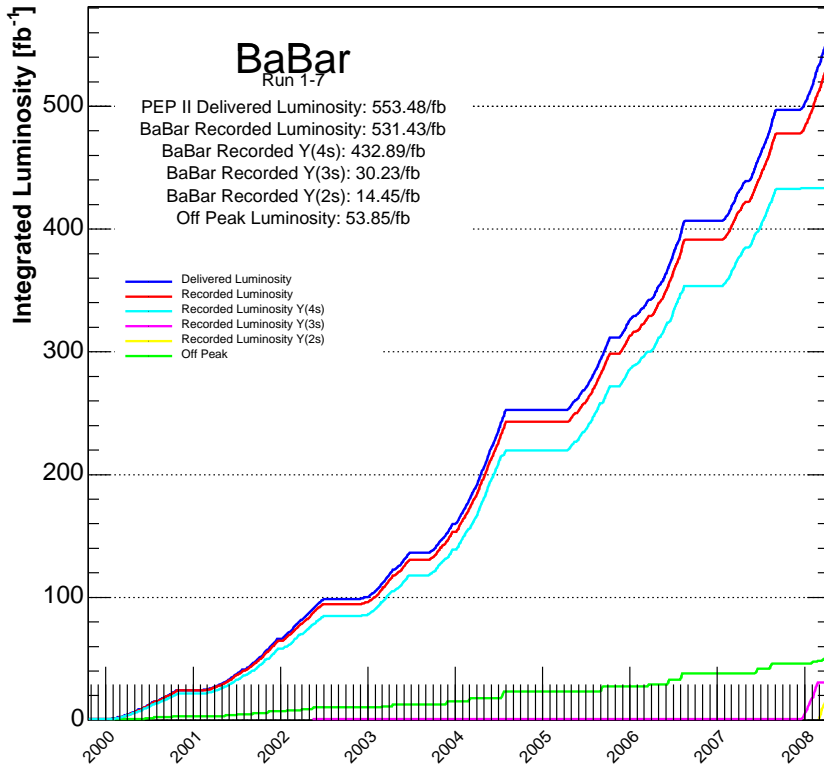


Figure 2.2: The PEP-II integrated luminosity recorded by the *BABAR* detector from the beginning of the data taking period in 1999 until 2008 [82].

2.2 The *BABAR* Detector

The asymmetric beam energies of PEP-II reflected also in the design of the *BABAR* detector. *BABAR* is a typical high energy physics detector, consisting of several detector elements, and being thus a multi-purpose detector.

Fig. 2.3 (a) shows a the longitudinal cross section of the *BABAR* detector. The high energy electrons enter the detector from the left, low energy positrons from the right hand side. The geometric center of the detector is offset in relation to the interaction point (IP) by 0.37 m in the direction of the high energy electron beam to maximize the geometric acceptance for the boosted B decays. The inner detection unit consists of a five-layer silicon vertex tracker (SVT) and a drift chamber (DCH) for vertex and track reconstruction, a Cherenkov detector (DIRC) for particle identification, and a CsI electromagnetic calorimeter (EMC) for the detection of photons. This inner detector is surrounded by a super-conducting solenoid creating a magnetic field of 1.5 T, which allows to measure the momenta of charged particle tracks. The instrumented steel flux return (IFR) enables muon and neutral hadron detection. Fig. 2.3 (b) shows a transverse cross section of the *BABAR* detector, where in addition the layers of the different detector components is visible.

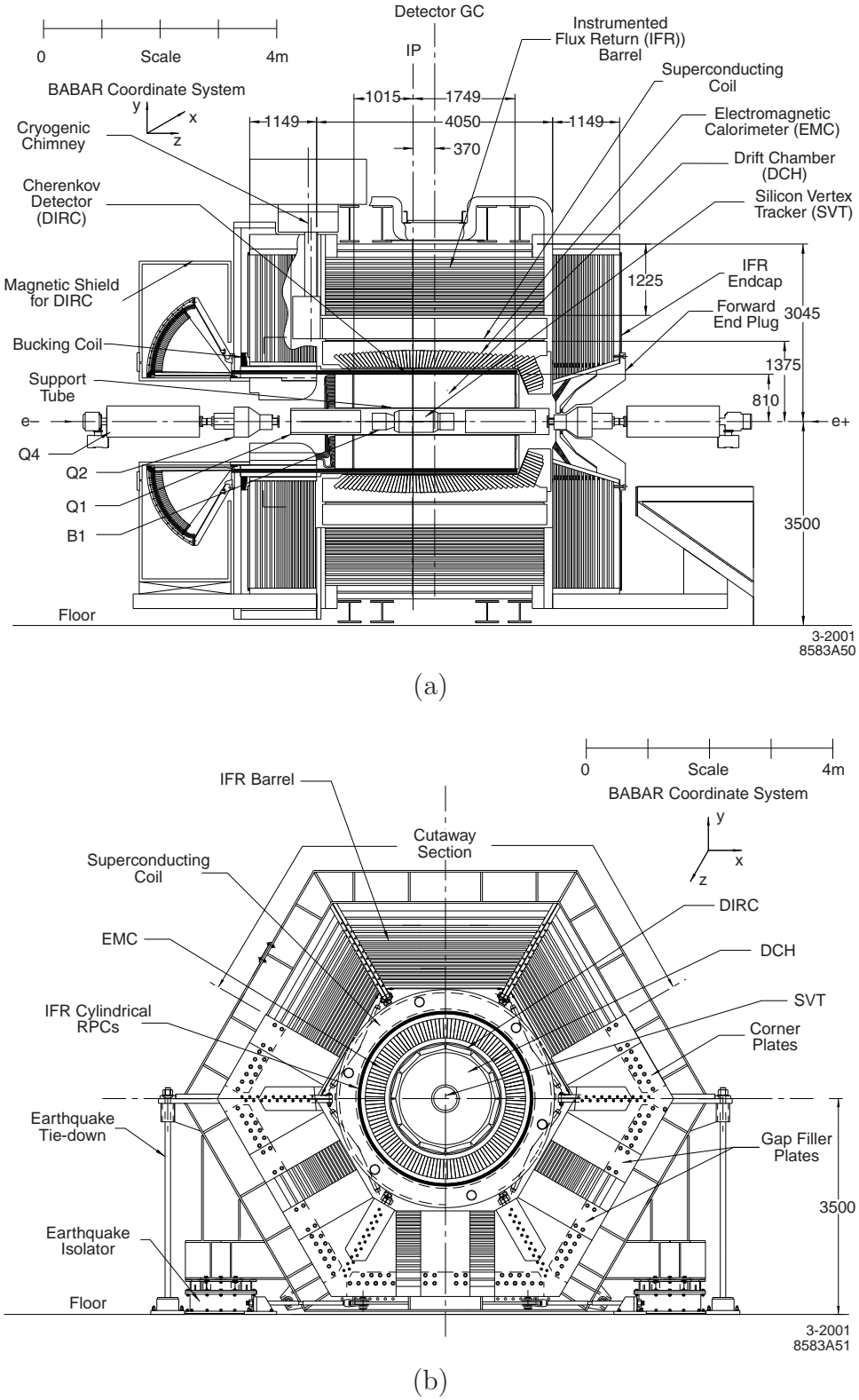


Figure 2.3: Cross section of the *BABAR* detector in longitudinal (a) and transverse (b) direction. The main components are the silicon vertex tracker, the drift chamber, the Cherenkov detector, the electromagnetic calorimeter and the instrumented flux return. The nominal interaction point (IP) as well as the geometric center (GC) are indicated. Also shown are the pairs of quadrupole and dipole magnets denoted with the symbols Q1/2/4 and B1 [80].

The material in the inner region of the detector is restricted to a minimum in order to minimize effects due to multiple scattering of tracks. Fig. 2.4 shows the material in units of radiation lengths before a high energy particle reaches the different detector sub-systems. The material budget is plotted as a function of the polar angle θ . In the following, the individual detector subsystems are described in more detail.

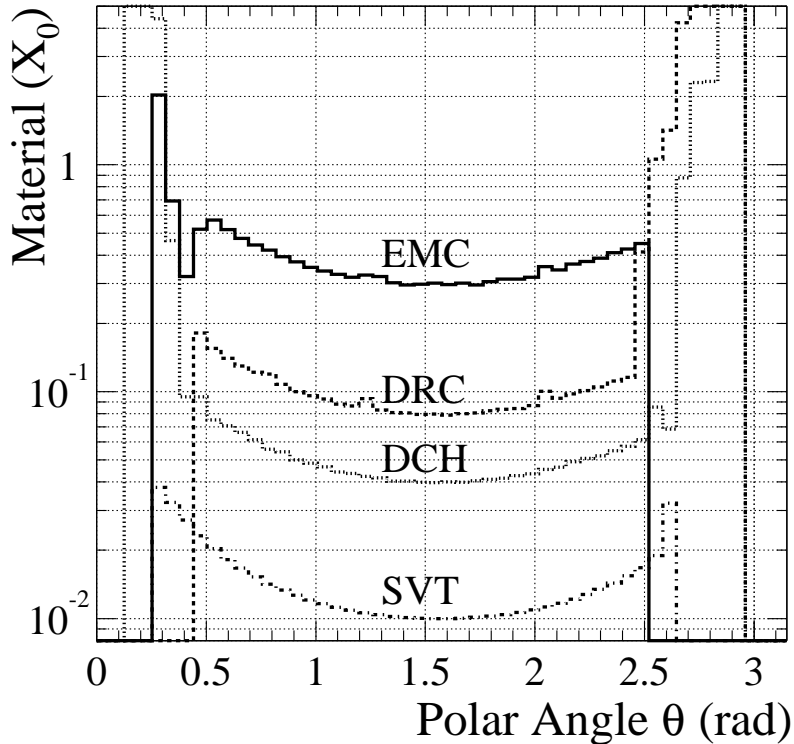


Figure 2.4: Material budget in units of radiation lengths for different detector systems for high energy particles before reaching the first active element of the named sub-detector system. Image is taken from [80].

Silicon Vertex Tracker

The *BABAR* tracking system, consisting of the SVT and the DCH, is designed to optimize the detection of charged tracks. With the information of the SVT, decay vertices can be reconstructed very precisely as well as momenta and energy loss dE/dx for charged particle identification (PID).

Fig. 2.5 displays a longitudinal (left) as well as a transverse (right) cross section of the SVT detector component. It consists of five cylindrically arranged layers of double-sided silicon micro strip sensors. The strips on the outer side of each layer are parallel to the z -direction allowing a precise ϕ measurement. The ones on the inner side are perpendicular and thus measure the z -coordinate. The polar angular range in the lab frame from 20° to 150° [80] is covered with active detection material leading to a coverage of approximately 90% of the solid angle in the CM system.

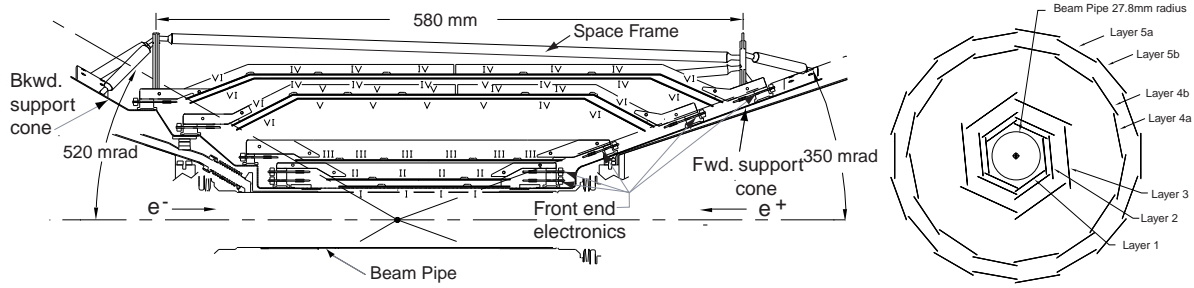


Figure 2.5: Cross section of the SVT in longitudinal (left) and transverse (right) direction [80].

The three inner detection layers ($r_1 \approx 32$ mm) are mounted directly outside the water-cooled beryllium beam pipe ($r \approx 27.8$ mm) in order to minimize the influence of multiple scattering on the tracks and vertex extrapolation. The purpose of the two outer layers ($r_5 \approx 144$ mm) is mainly to link the SVT hits to the DCH track information. The excellent vertex resolution of approximately $70 \mu\text{m}$ for fully reconstructed B meson decays is one of the main requirements in order to measure time-dependent CP asymmetries in B decays.

Drift Chamber

The main purpose of the multi-wire drift chamber is a precise measurement of the transverse momentum of the tracks using their curvature in the 1.5 T magnetic field. In addition, the energy loss measurement dE/dx is used for charged PID.

The cylindrical shaped detector component extends from a radius of 26.6 cm to 80.9 cm with a length of 280 cm as shown in Fig. 2.6 (left). Ten super-layers are subdivided in four layers each. The resulting 7104 hexagonal drift cells are formed by six gold-coated aluminum field wires with a diameter of $120 \mu\text{m}$ surrounding one gold-coated tungsten-rhenium sense wire with a diameter of $10 \mu\text{m}$. This allows up to 40 position and dE/dx measurements per trajectory. In order to enable a position measurement along the beam axis, only four *axial* super layers are parallel to the beam axis and six so-called *stereo* layers have alternating tilts of $\pm(45 - 76)$ mrad with respect to the beam axis. This design, as illustrated in Fig. 2.6 (b), guarantees an optimal mean spatial resolution of approximately $125 \mu\text{m}$ [80].

The transverse momentum resolution σ_{p_t} of the tracking system is [80]:

$$\frac{\sigma_{p_t}}{p_t} = (0.13 \pm 0.01)\% \cdot \frac{p_t}{\text{GeV}/c} \oplus (0.45 \pm 0.03)\%. \quad (2.1)$$

The resolution of the energy loss measurement is in the order of 7% [80] and allows to separate K from π for low momentum tracks, $p_{\text{Lab}} < 700 \text{ MeV}/c$, as can be seen in Fig. 2.7 (left). For tracks with higher momenta the DIRC complements the PID

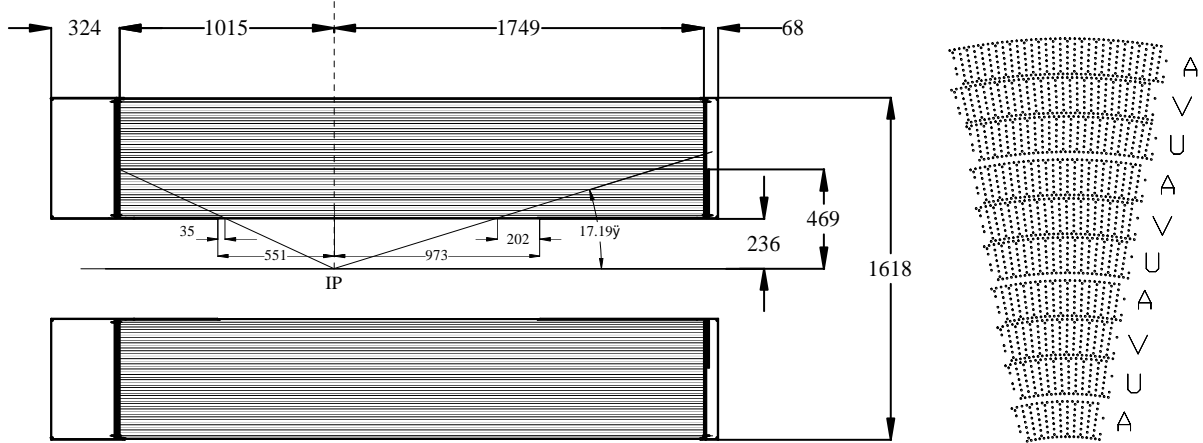


Figure 2.6: Longitudinal cross section of the DCH (left) and transverse cross section of one of its segments (right) indicating the pattern of axial (A) and stereo (U,V) layers. Dimensions are indicated in mm [81].

capability. The tracking efficiency for tracks traversing the good detection region of the DCH is approximately 97-98%. The track reconstruction efficiency and especially differences between data and MC are crucial for this analysis and are studied in detail as presented in Chapter 5.3.

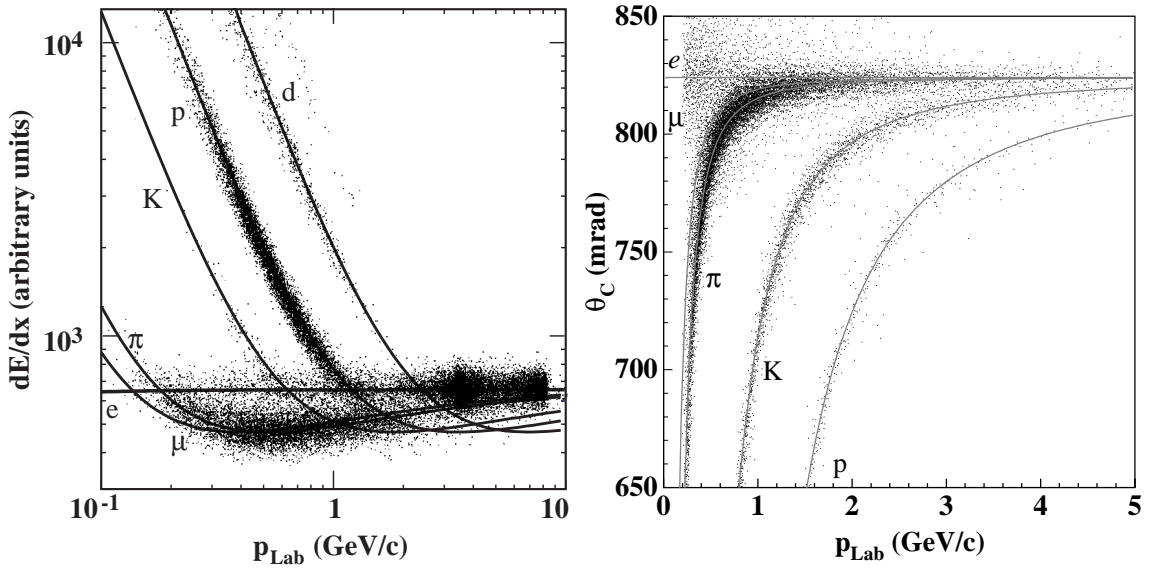


Figure 2.7: Left: specific energy loss, dE/dx , in the DCH as a function of the momentum for different types of charged particles, superimposed with predictions from the Bethe-Bloch formula. Image is taken from [81]. Right: measured Cherenkov angle θ_C as a function of the track momentum p_{Lab} for different types of particles. Image is taken from [83].

Detector of Internally Reflected Cherenkov Emission

The Cherenkov detector is used as a PID device. In particular, it has an excellent K/π separation for particles with a momentum of $p_{Lab} > 700$ MeV/c.

A novel design has been chosen in order to minimize the amount of material in front of the EMC. Fig. 2.8 (left) illustrates the concept of the detector. 144 bars of fused silica (quartz) with a refraction index of $n = 1.473$ are arranged in a 12-sided polygonal barrel with 12 bars per side (Fig. 2.8 (right)). Each bar has a width of 35 mm, a thickness of 17 mm and a length of 4.9 m. A charged particle traversing the quartz bars with $\beta = v/c \geq 1/n$ emits Cherenkov light in a cone at an opening angle θ_C :

$$\cos(\theta_C) = \frac{1}{n\beta} \quad (2.2)$$

with $\beta = v/c$, the velocity of the particle v , and the velocity of light in vacuum c . The emitted light is internally reflected to the rear end side outside the *BABAR* detector to the standoff box, which is filled with purified water (Fig. 2.8 (left)). About 1.2 m away from the end of the bars, 12 sectors of 896 photo multiplier tubes (PMTs) each are mounted on the wall of the standoff box in order to detect the light. After correcting for the different refraction indices of the quartz bars and the water, the Cherenkov angle can be obtained from the light cone opening angle in combination with the timing information measured by the PMTs.

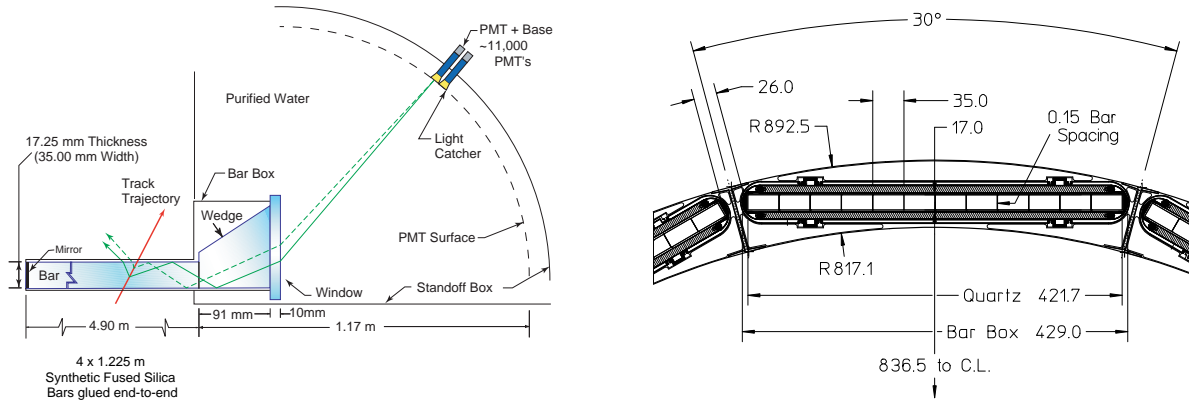


Figure 2.8: Left: Working principle of the DIRC illustrated for a single quartz bar. The traversing charged particle (red) emits Cherenkov light (green), which is internally reflected and finally detected by the PMT in the standoff box [83]. Right: Transverse cross section of one bar box containing 12 quartz bars [81].

Measuring the Cherenkov angle corresponds to a velocity measurement of the particle as shown in equation 2.2. In combination with the momentum measurement in the SVT and DCH, the mass of the particle can be identified:

$$m^2 c^2 = \frac{1 - \beta^2}{\beta^2} \cdot p^2 \quad (2.3)$$

Fig. 2.7 (right) shows the measured Cherenkov angle θ_C as a function of the measured track momenta for different types of particles. In combination with the DCH-information, an excellent π/K separation is achieved which is necessary in this study.

Electromagnetic Calorimeter

The EMC was constructed to measure the energy, shape and position of electromagnetic showers from 20 MeV to 9 GeV with high efficiency. In addition, it provides information for traversing muons and hadrons. The quantity E/p is the ratio of deposited energy E in the EMC to the momentum of a track p , determined in the tracking system. The value of E/p as well as the measured shower shape in the EMC are used for PID.

A schematic view of the EMC is shown in Fig. 2.9 and Fig. 2.10 (left) in longitudinal and transverse direction respectively. It is composed of a finely segmented array of 6580 thallium-doped cesium iodide (CsI(Tl)) crystals. The material has a short radiation length $X_0 \approx 1.85$ cm as well as a small Molière radius describing the scale of the transverse extension of the electromagnetic shower. This allows to fully contain the showers with high efficiency and achieves a good angular resolution in a compact EMC.

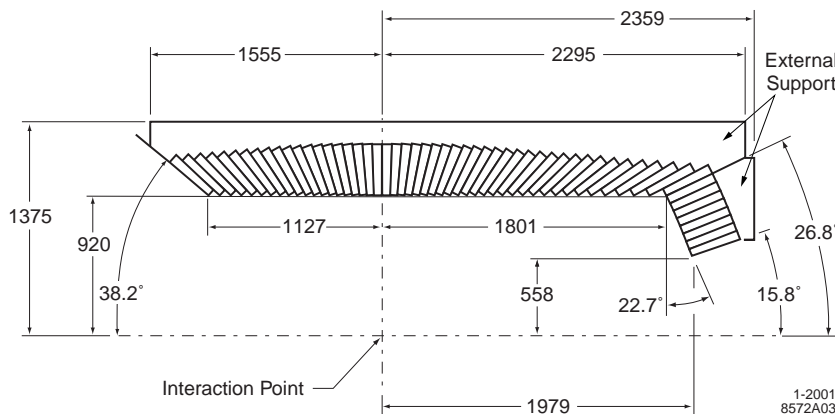


Figure 2.9: Schematic view on one crystal layer of the electromagnetic calorimeter. The crystals arrangement is subdivided in a barrel region and a forward region accounting for the asymmetry due to the boost. Each crystal represents one axially symmetric crystal ring. The indicated dimensions are given in mm [84]

The EMC consists of a central barrel ranging from a radius of 92 cm to 136 cm with a length of 3 m and a forward end-cap accounting for the asymmetry due to the boost in forward direction. The crystal length varies between 29.8 cm ($16.1X_0$) in the backward barrel and 32.6 cm ($17.6X_0$) in the end-cap. Two silicon photo-diodes at the rear end of each crystal read out the scintillation light emitted by the corresponding crystal.

The EMC provides excellent energy and angular resolutions, which can be empirically parameterized as [80, 85]:

$$\frac{\sigma_E}{E} = \frac{(2.32 \pm 0.30)\%}{\sqrt[4]{(E/\text{GeV})}} \oplus (1.85 \pm 0.12)\%, \quad (2.4)$$

$$\sigma_\theta = \sigma_\phi = \left(\frac{(4.16 \pm 0.04)}{\sqrt{(E/\text{GeV})}} \oplus (0.00 \pm 0.04) \right) \text{ mrad.} \quad (2.5)$$

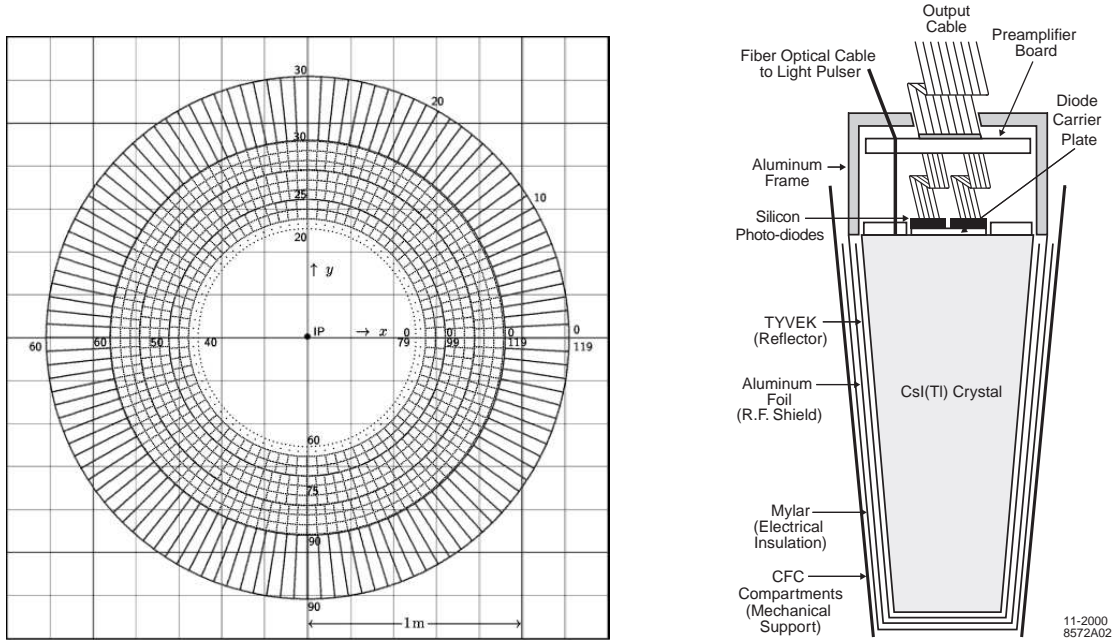


Figure 2.10: Left: Schematic transverse cross section of the EMC, showing the crystal arrangement of the barrel (outer ring) and the different end-cap layers (inner rings). Right: Composition of an EMC crystal including the readout photo-diodes [84].

Here, E represents the measured energy and θ and ϕ the polar and azimuthal angles respectively and \oplus is the quadratic sum. A detailed study for the EMC has been performed within this thesis concerning the energy and position measurement (Section 5.1) as well as the efficiency difference in photon detection between the data and the simulation (Section 5.2).

Instrumented Flux Return

The iron yoke of the solenoidal magnet has two main purposes. On the one hand, it returns the magnetic flux which is produced by the superconducting coil. The solenoidal magnetic field of 1.5 T is needed to get the curvature of the particle tracks in order to measure the momenta of the particles very precisely with the inner detector components. On the other hand, it is used for muon and neutral hadron detection.

It consists of a central barrel and two end-cap sections (Fig. 2.11). Between the iron plates, ionization detector layers are installed in order to measure the traversing particles. The original setup with resistive plate chambers (RPCs) has been partly replaced with limited streamer tubes (LSTs).

For this analysis the IFR detector is of special interest due to the fact that a $\mu^+\mu^-\gamma$ sample is used to fine-tune the EMC calibration and measure the photon efficiency (Chapter 5).

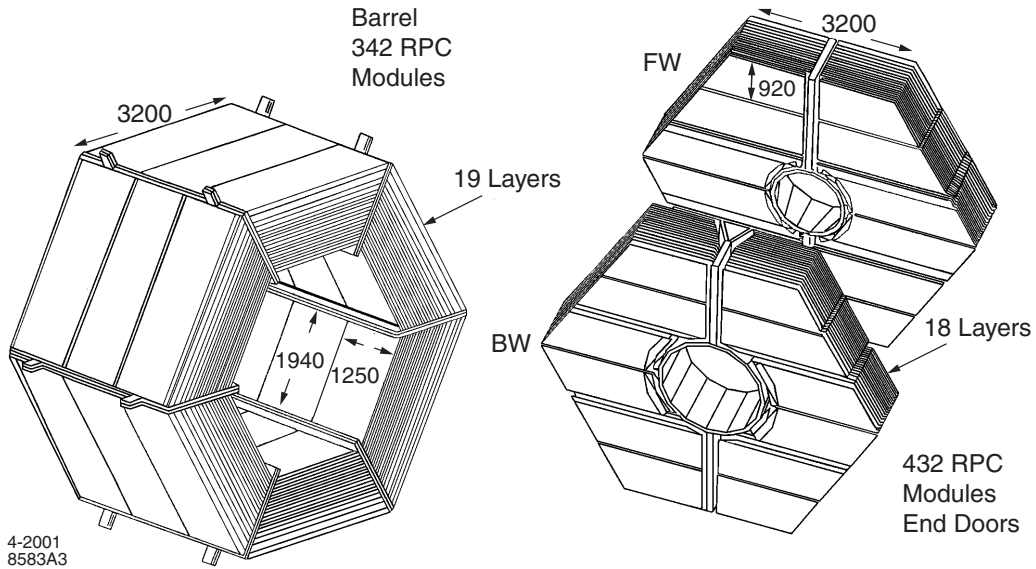


Figure 2.11: IFR overview: Barrel sectors (left) and forward and backward end doors (right) with 18 and 19 ionization detector layers respectively [80].

Trigger and Background Filter

The trigger and background filter are important tools of the data acquisition system of *BABAR*. They are incorporated in order to decide whether an event, observed by the *BABAR* detector, is interesting enough for further analysis. Recording exclusively these events significantly reduces the amount of recorded data.

The trigger consists of two levels: The Level 1 (L1) trigger operates on the hardware level, the Level 3 (L3) trigger on the software level. A Level 2 trigger is not present at *BABAR*.

The L1 trigger system contains four subsystems: the charged particle trigger (DCT), the neutral particle trigger (EMT), the cosmic trigger (IFT) and the Global Level Trigger (GLT). The DCT and EMT receive information from the DCH and the EMC detector sub-systems, respectively. This information is processed and forwarded as condensed data to the GLT. The GLT attempts to match the angular information of the EMC clusters and the tracks measured in the DCH. Hereby L1 triggers are generated and sent to the Fast Control and Timing System (FCTS), based on the results of the processing. The GLT also uses the IFT information to independently trigger on cosmic rays and $\mu^+\mu^-$ events. The Level 1 trigger rate for an instantaneous luminosity of $\mathcal{L} = 8 \cdot 10^{33} \text{ cm}^{-2}s^{-1}$ is typically 2.5 kHz.

Events fulfilling the L1 trigger criteria are forwarded to the L3 trigger. This trigger analyses data with more detailed information from the DCH and EMC sub-systems in combination with the L1 trigger content to further reduce background contributions. Background filters are applied in order to suppress various background contributions, such as Bhabha events. In addition, the L3 trigger selects various types of events for detector calibration and is used for online monitoring tasks. The L3 operates with fast

algorithms resulting in a processing time of ≈ 4 ms per event. Hereby, the L1 information is typically reduced by a factor of approximately 10, before the data is forwarded to the storage system.

Chapter 3

ISR Physics at *BABAR*

As described in Chapter 1.2, the particular interest in hadronic cross section measurements arises due to their impact on the theoretical prediction of $(g - 2)_\mu$ as well as $\alpha_{QED}(M_Z^2)$. In order to increase the precision of the hadronic contribution a_μ^{had} additional measurements of hadronic cross sections, especially at low Center-of-Mass energies, are essential.

Two experimental approaches to extract these hadronic cross sections are introduced: The energy scan and the ISR method. Then the influence of Vacuum Polarization (VP) on the hadronic cross sections is investigated. Radiative Corrections due to Next-to-Leading Order (NLO) ISR as well as due to Leading Order (LO) and NLO Final State Radiation (FSR) are discussed and quantified. Finally a comparison of the ISR and energy scan approaches is presented.

The cross section of hadron production in e^+e^- annihilation has been measured at e^+e^- colliders up to recently exclusively by energy scan experiments. These experiments run at different fixed CM energies as illustrated in Fig. 3.1 (a). The measurement of the $\pi^+\pi^-\pi^+\pi^-$ channel, using this method, has been performed at several experiments, most recently at VEPP-2M by SND [86] and CMD-2 [87, 88] up to 1.4 GeV. Older data has been obtained at DCI by DM2 [89] with a maximum CM energy of 2.0 GeV.

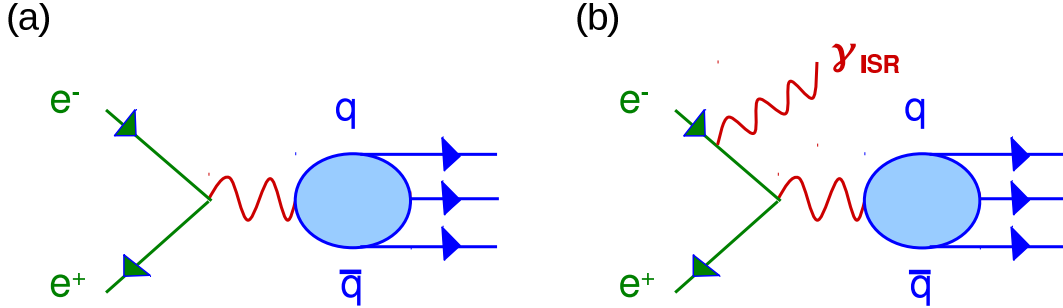


Figure 3.1: Principal concept of hadronic cross section measurement at energy scan experiments (a) in comparison to ISR experiments (b).

An alternative method, depicted in Fig. 3.1 (b), was developed during the last decade. The study using ISR events enables high statistics e^+e^- experiments running at a fixed CM energy to access hadronic processes at lower effective CM energies by studying events with a high energetic photon emitted from the initial state. The use of this technique at high luminosity ϕ - and B -factories has been discussed in detail in [90–92]. The *BABAR* Collaboration has an intensive program to investigate low multiplicity ISR processes [57, 69–76] at effective CM energies below 5 GeV as mentioned in Chapter 1.3. In addition to the cross section measurements, these studies include many additional physics topics, e.g. spectroscopy as well as nuclear form factor measurements.

3.1 ISR Analyses

The schematic analysis path using the ISR technique is illustrated in Fig. 3.2. The first step of an exclusive ISR analysis is a dedicated selection of the radiative hadronic channel of interest. This leads to the extraction of the number of events as a function of the invariant mass M_{had} , corresponding to the effective CM energy E_{CM} .

The same selection procedure is also applied to signal simulation (MC), which is needed to determine the selection efficiency for the corresponding specific final state. Additional simulation of other ISR and non-radiative background channels is used to estimate the contamination due to background. These background channels are then either subtracted according to simulation or removed via dedicated requirements, depending on the systematic uncertainty introduced by the applied procedure. Thus, simulation is needed for acceptance corrections on the one hand and background contribution estimation and/or subtraction on the other hand. All analysis items (e.g. background, efficiencies) need to

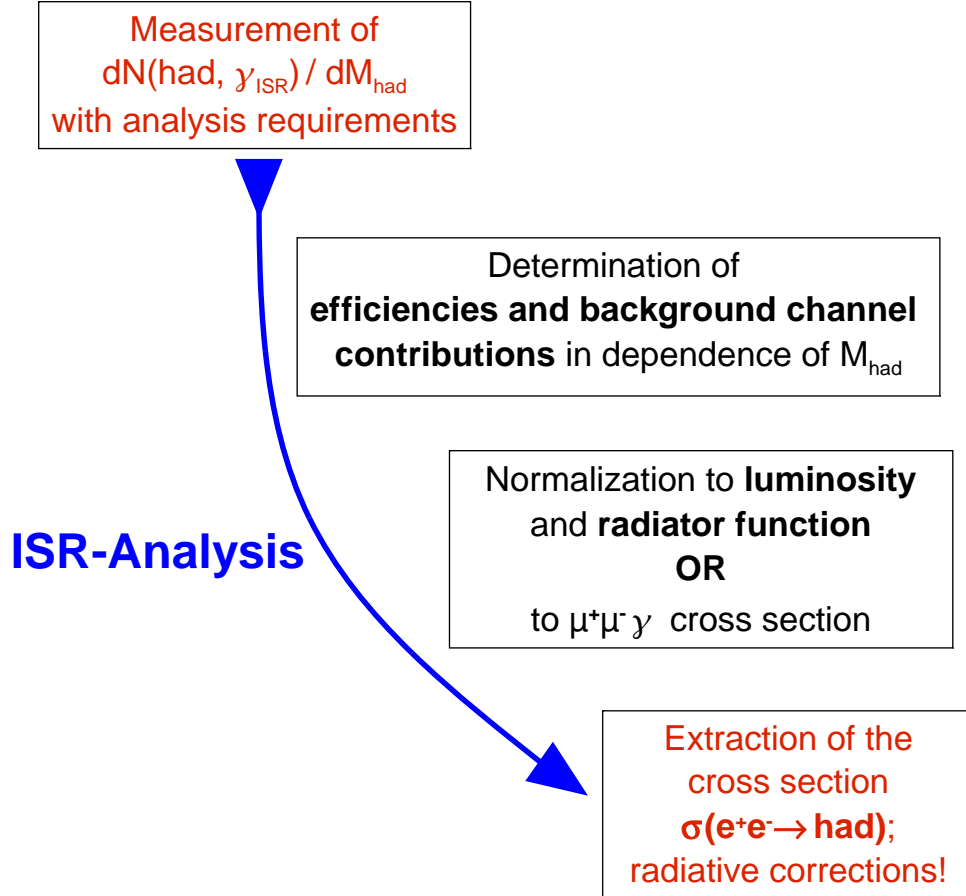


Figure 3.2: Typical ISR analysis path.

be studied as a function of the invariant mass of the hadronic system. In addition, both efficiency and efficiency corrections strongly depend on the investigated final state. This leads to complications in the determination of the inclusive hadronic cross section with high precision. So far, a much higher precision is achieved by studying hadronic channels exclusively.

Depending on the required precision, additional tests need to be performed, focusing on possible differences in the selection between data and simulation. The photon efficiency is of importance, since our ISR analyses require a detected high-energetic photon. A dedicated study of photon efficiency differences between data and simulation is presented in Section 5.2. In case of multi-hadronic events with charged tracks, a precise understanding of differences in the track reconstruction efficiency between data and MC is needed. This study is presented in Section 5.3. After these corrections, the invariant mass spectrum is weighted with the integrated luminosity in order to receive the so-called radiative or ISR cross section $\sigma_{\text{FS},\gamma}(m)$. This ISR cross section for a particular final state (FS) is related to the non-radiative cross section $\sigma_{\text{FS}}(m)$ through the following relation [92]:

$$\frac{d\sigma_{\text{FS},\gamma}(m)}{dm} = \frac{2m}{s} \cdot W(s, x, \theta_\gamma^*) \cdot \sigma_{\text{FS}}(m), \quad (3.1)$$

where $x = \frac{2 \cdot E_\gamma^*}{\sqrt{s}}$, \sqrt{s} is the nominal CM energy, θ_γ^* and E_γ^* are the polar angle and the energy of the ISR photon in the nominal CM frame, lowering the effective CM energy to $\sqrt{s'} = m$. The quantity $\sqrt{s'}$ is here the invariant mass of the virtual photon or - in absence of FSR effects - the invariant mass of the hadronic system. The radiator function W describes the photon emission probability in the angular range $|\cos(\theta_\gamma^*)| < C$ and can be derived analytically at leading order (LO) [92]:

$$W(s, x, \theta_\gamma^*) = \frac{\alpha}{\pi x} \cdot \left[(2 - 2x + x^2) \cdot \ln \frac{1+C}{1-C} - x^2 C \right]. \quad (3.2)$$

A considerably more precise determination of W is presented in Section 3.3. In principle, the radiative cross section is the product of the probability to emit a photon from initial state reducing the CM energy to the invariant mass of the hadronic system and the non-radiative cross section at this reduced CM energy. The assumption of factorisation between these two processes has been assumed in equation (3.1). As already mentioned, this formula does not take into account corrections due to final state radiation.

3.2 Vacuum Polarization

After resolving for the non-radiative cross section in equation (3.1), the so-called dressed cross section $\sigma_{dressed}(s)$ is obtained. This means the cross section contains vacuum polarization (VP) contributions of the intermediate photon and can be directly compared to e^+e^- energy scan measurements. However, the cross section to be put into the dispersion integral for a_μ^{had} has to be corrected for VP effects $\delta_{vac}(s)$ of the intermediate photon as well as for photons emitted from the final state (FSR). The extraction of the so-called undressed cross section $\sigma_{undressed}(s)$ requires the VP as a multiplicative factor [5]:

$$\sigma_{undressed}(s) = \sigma_{dressed}(s) \cdot \left(\frac{\alpha_{QED}(0)}{\alpha_{QED}(s)} \right)^2 = \frac{\sigma_{dressed}(s)}{\delta_{vac}(s)}. \quad (3.3)$$

This multiplicative correction factor $\delta_{vac}(s)$ due to the VP [93] is shown in Fig. 3.3 as a function of the CM energy $E_{CM} = \sqrt{s}$.

Since the cross section itself is used to derive the hadronic contribution $\Delta\alpha^{had}(s)$ to the running fine structure constant $\alpha(s)$, the correct procedure would be an iterative treatment of the VP correction. However, the size of the correction is at most of the order of a few percent and therefore the additional correction is negligible at the given level of precision.

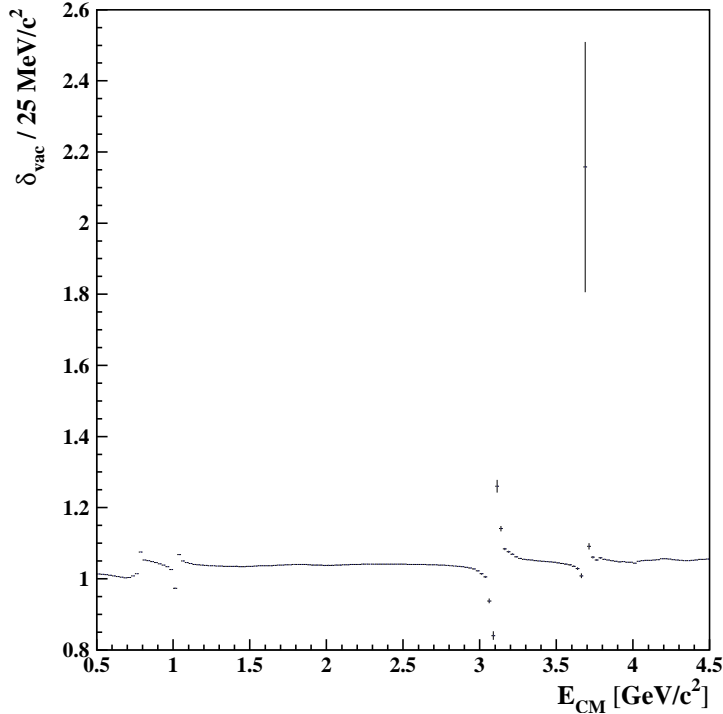


Figure 3.3: Multiplicative correction δ_{vac} factor due to VP [93] in dependence of the CM energy $E_{CM} = \sqrt{s}$.

3.3 Radiative Corrections

In equation (3.1), the relation of the radiative cross section to the non-radiative cross section via the radiator function W is introduced. This formula, shown in equation (3.2), is only correct for LO ISR photons. It is evident that additional NLO radiative corrections might influence the result significantly.

The event generator AFKQED [94] was used to produce the $\pi^+\pi^-\pi^+\pi^-\gamma$ signal MC. It is based on the EVA generator [95], which was then updated to PHOKHARA, the state-of-the-art event generator for the ISR channels of interest. The effects on the radiator function due to NLO ISR radiation are estimated with AFKQED and compared with version 5.0 of PHOKHARA [96]. While AFKQED contains a structure function approach for radiation beyond LO, the Phokhara code contains the full NLO correction. Differently from PHOKHARA, final state radiation is implemented in AFKQED via the PHOTOS package [97]. PHOTOS is not implemented in the PHOKHARA event generator for the $\pi^+\pi^-\pi^+\pi^-\gamma$ channel. The influence on the cross section due to LO as well as NLO FSR is investigated below.

Precision of NLO ISR Effects in AFKQED

The *BABAR* ISR simulation in AFKQED is performed with the requirement on the combined invariant mass of the four pions and the ISR photon to be:

$$Q^2 = (p_{4\pi} + p_{\gamma_{ISR}})^2 > (8 \text{ GeV}/c)^2, \quad (3.4)$$

where $p_{4\pi}$ and $p_{\gamma_{ISR}}$ correspond to the energy-momentum 4-vector of the hadronic system and the ISR photon, respectively. For events without NLO radiation the momentum transfer $Q^2 = (10.56 \text{ GeV}/c)^2$ is equal to the nominal *BABAR* CM energy. The requirement (3.4), therefore, suppresses the production of events with high-energetic NLO radiation (NLO-ISR or NLO-FSR). These events are filtered out in the event selection by the kinematic fit requirements (see Chapter 4). Adding these events to the simulation would simply decrease the global efficiency. This would be compensated by a shift of the radiator function.

Equation (3.2) allows us to relate the radiative cross section to the radiator function:

$$\frac{\sigma_{LO,4\pi\gamma}}{\sigma_{NLO,4\pi\gamma,Q^2>(8 \text{ GeV}/c)^2}} = \frac{W_{LO}}{W_{NLO,4\pi\gamma,Q^2>(8 \text{ GeV}/c)^2}} \quad (3.5)$$

Fig. 3.4 shows a comparison between two spectra obtained with AFKQED for (i) LO-ISR and (ii) NLO FSR with the requirement $Q^2 > (8 \text{ GeV}/c)^2$. Of course this comparison depends on the specific choice of the Q^2 requirement. Choosing the specific value $Q^2 > (8 \text{ GeV}/c)^2$ ensures that the radiator function is almost identical to the LO theoretical formula, equation (3.2).

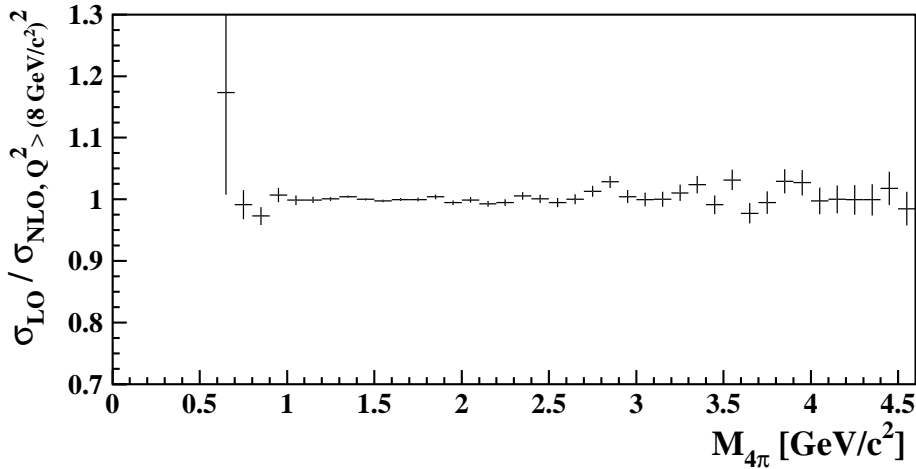


Figure 3.4: Ratio of the radiative cross section in LO $\sigma_{LO,4\pi\gamma}$ and the radiative cross section in NLO $\sigma_{NLO,4\pi\gamma,Q^2>(8 \text{ GeV}/c)^2}$ with the additional requirement $Q^2 > (8 \text{ GeV}/c)^2$. Event samples are produced with AFKQED [94].

As long as no final state radiation is investigated, the result in equation (3.5) is independent of the final state. The corresponding test in PHOKHARA has been performed

with the $\pi^+\pi^-\gamma$ final state. In Fig. 3.5 the corresponding distribution is shown for different requirements of Q^2 simulated with PHOKHARA. Fig. 3.5 (a) shows the difference between NLO and LO estimated with PHOKHARA for $Q^2 > 0 \text{ GeV}/c^2$. Differences in the order of 7% are observed. In Fig. 3.5 (b) it is seen that the radiator function with the $Q^2 > (8 \text{ GeV}/c)^2$ requirement for PHOKHARA is also almost identical to the radiator function in LO. It is important to mention that this agreement is rather accidental, because an even stronger requirement on the extra radiation would further increase the radiator function as shown in Fig 3.5 (c). Finally the test with PHOKHARA shows differences of $1.1\% \pm 0.2\%$ between AFKQED and PHOKHARA.

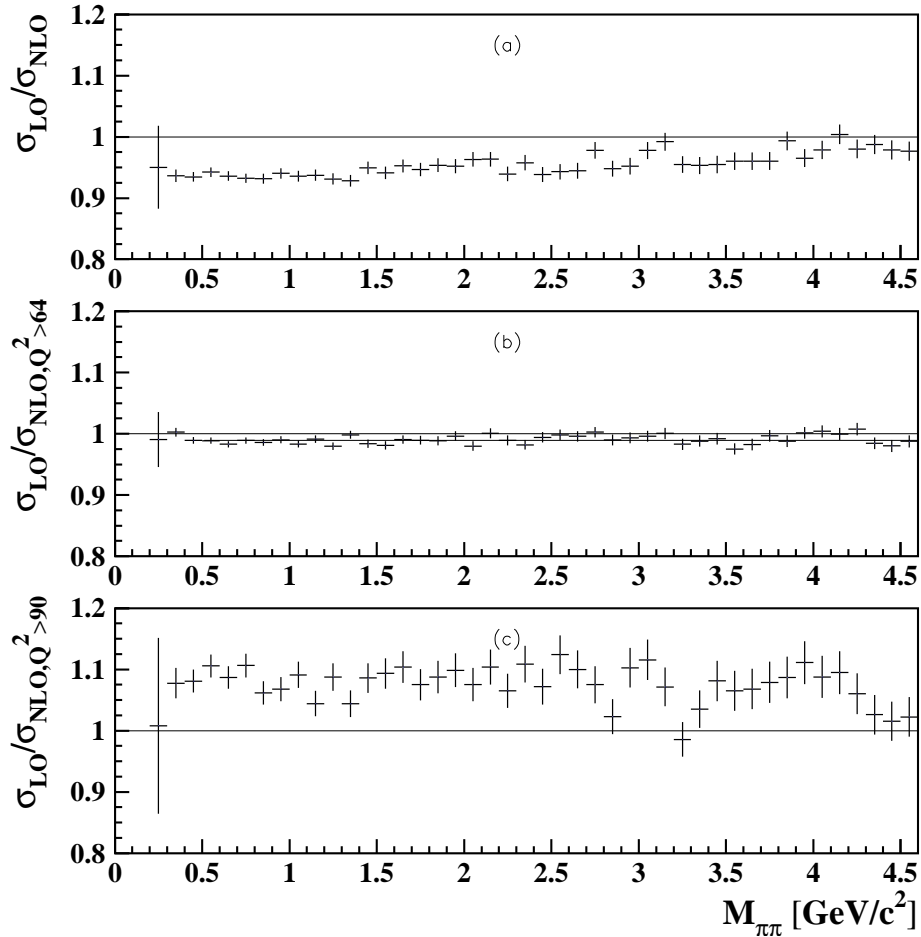


Figure 3.5: Ratio of $\sigma_{LO,\pi^+\pi^-\gamma}$ to $\sigma_{NLO,\pi^+\pi^-\gamma}$ with $Q^2 > 0(\text{ GeV}/c)^2$ (a), $Q^2 > 64(\text{ GeV}/c)^2$ (b) and $Q^2 > 90(\text{ GeV}/c)^2$ (c), event samples produced with PHOKHARA; in (b) a constant fit is performed: 0.989 ± 0.001 .

To summarize, according to AFKQED the radiator function in LO order is in perfect agreement with the radiator function in NLO with the additional requirement $Q^2 > (8 \text{ GeV}/c)^2$. The comparison with PHOKHARA shows, however, that a small correction of $1.1\% \pm 0.2\%$ needs to be applied, but allows us to use the LO radiator function to extract the non-radiative cross section from data. The difference observed between AFKQED and PHOKHARA can be understood due to the different approaches used in the calculation of the generators as discussed above.

Effect of LO and NLO FSR

In order to estimate the influence of LO FSR on the radiator function, a $\mu^+\mu^-\gamma$ and a $\pi^+\pi^-\gamma$ sample were simulated with PHOKHARA. In Fig. 3.6 (a), the radiative cross section for $\mu^+\mu^-\gamma$ is shown with and without LO FSR photons allowed. The ratio of these cross sections in Fig. 3.6 (b) shows that the correction of this effect is very important for the leptonic cross section. The corresponding distributions for the $\pi^+\pi^-\gamma$ sample are displayed in Fig. 3.6 (c) and (d). It can be observed that the LO FSR contributions are strongly suppressed and can be neglected. This is due to the fact, that the point-like $\mu^+\mu^-\gamma$ cross section is decreased by the additional electromagnetic form factor.

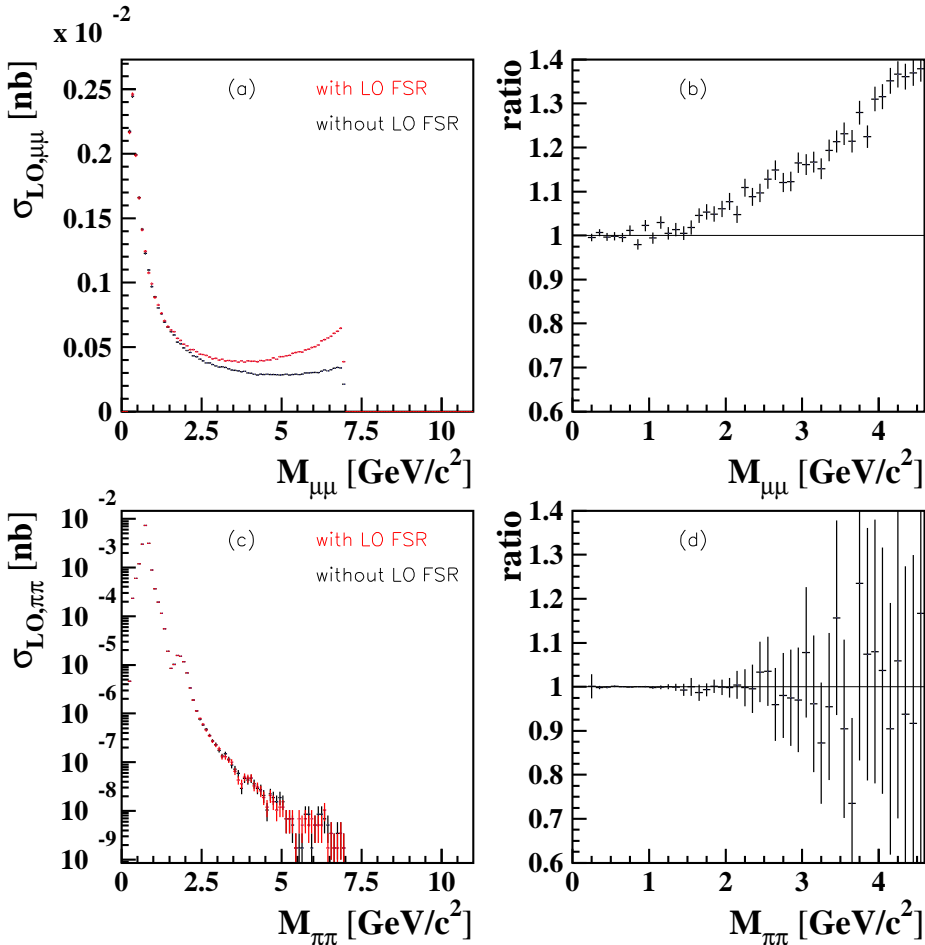


Figure 3.6: $\mu^+\mu^-\gamma$ cross section with and without LO FSR (a) and the corresponding ratio (b). The corresponding distributions for the $\pi^+\pi^-\gamma$ sample are shown in (c) and (d).

The study for NLO FSR photons was performed using AFKQED with PHOTOS for modelling the NLO FSR photons. In PHOKHARA, PHOTOS is not implemented for the $\pi^+\pi^-\pi^+\pi^-\gamma$ channel. Due to NLO FSR radiation, the invariant mass of the reconstructed hadronic system will be reduced compared to the virtual photon's invariant mass $\sqrt{s'}$. As a consequence, the measured cross section will be slightly shifted towards smaller masses. This effect is visualised in Fig. 3.7, where the ratio of $\sigma_{LO,4\pi\gamma}$ to $\sigma_{NLO,4\pi\gamma}$ with $Q^2 > (8 \text{ GeV}/c)^2$ and NLO FSR corrections included, is displayed. Differences of up to 3% are observed and are corrected for.

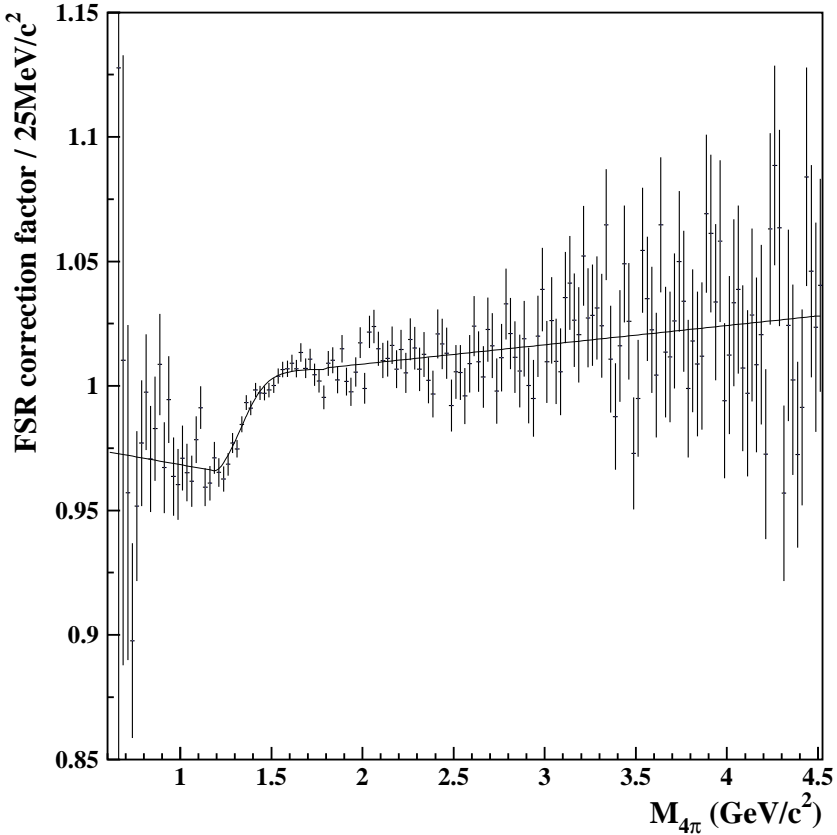


Figure 3.7: Ratio of $\sigma_{LO,4\pi\gamma}$ to $\sigma_{NLO,4\pi\gamma}$ with $Q^2 > (8 \text{ GeV}/c)^2$ and NLO FSR corrections included.

Summary of Radiative Corrections

AFKQED and PHOKHARA have been compared for the computation of the radiator function. A deviation of 1.1% is observed and used as correction on the final result for the non-radiative cross section $\sigma(\pi^+\pi^-\pi^+\pi^-)$. The influence of LO FSR is negligible. The effect of NLO FSR with deviations up to 3% is corrected according to the displayed fit function in Fig. 3.7.

3.4 ISR vs. Energy Scan

Thanks to the large data sample of *BABAR*, the *BABAR* statistics for ISR measurements is very high, even after taking into account that a high energetic photon has to be emitted from initial state. The effective ISR luminosity is plotted in Fig. 3.8. The luminosity achieved at *BABAR* is considerably higher than the one collected at a single E_{CM} with the existing energy scan experiments.

Due to the high statistics, the uncertainties of the low multiplicity cross section measurements are dominated by systematic effects. The measurements are limited by the precision of the modelling of the *BABAR* detector and reconstruction algorithms in the detector simulation. Thus a number of corrections have to be determined to extract

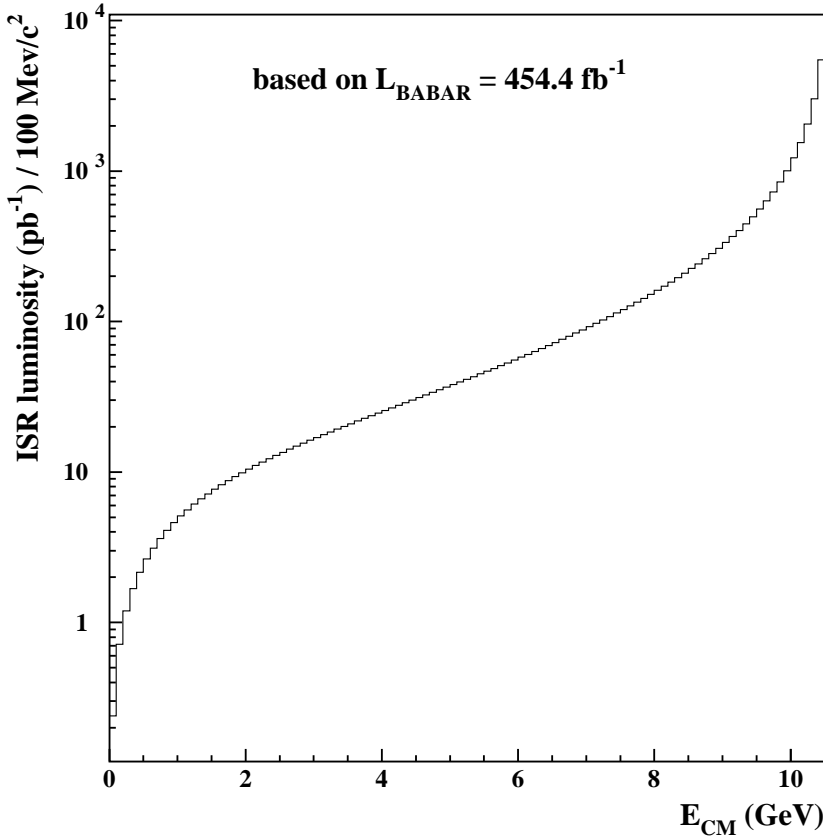


Figure 3.8: Effective *BABAR* luminosity at the CM energy $E_{CM} = \sqrt{s}$.

the final result. A drawback for ISR measurements is the requirement to rely on a theoretical radiator function W describing the emission of an initial state photon. This QED emission, however, is theoretically known at the few permil level and the radiator function implemented at NLO in the PHOKHARA event generator [96]. In principle this systematic uncertainty is avoidable, by normalizing the hadronic cross section to the $e^+e^- \rightarrow \mu^+\mu^-\gamma$ yield. This latter approach has been followed in the measurement of the pion form factor at *BABAR* [57]. Another disadvantage of the ISR method is the in general higher background level due to events (continuum background or ISR events) with different multiplicities, which have a similar event kinematics and are hence (almost) indistinguishable from signal events.

An important feature of ISR analyses at *BABAR* is the requirement of a high energetic photon. This photon requirement is known to have a 100% rejection power for $\Upsilon(4S)$ decays. On the other hand it leads to the typical ISR back-to-back topology between the high energetic ISR photon and a collimated hadronic system in the other hemisphere of the experiment. If the ISR photon is emitted at angles inside the active detection region, the hadronic system is with a high probability detected as well. This increases the geometrical acceptance in comparison to energy scan experiments. In addition, this event topology reduces systematic uncertainties which arise due to the limited knowledge of the hadronic form factor under study in the MC simulation. In classical energy scan experiments, all systematic uncertainties as well as the determination of the luminosity

have to be studied for each CM energy separately.

Another advantage of the ISR kinematics at *BABAR* is the fact that at the production threshold, when the sum of the invariant masses of the individual hadrons is almost as small as the invariant mass of the combined hadronic system, the momentum of these particles is very small. Typically the detection efficiency decreases for small momentum tracks. Due to the boost of the final state of the hadronic system in the laboratory frame, the momentum of these very slow particles increases and a measurement of the hadronic cross section is feasible almost from the production threshold of the hadronic system up to energies of 4-5 GeV. At higher masses, the cross section of most hadronic reactions with low multiplicities become very small and furthermore, background from B-decays cannot be neglected anymore.

The energy scan and the ISR method are complementary and therefore both are needed to learn more about the nature of the different systematic corrections. The highest precision in measurements with multiplicities of three hadrons or more at present is achieved in ISR measurements, but new results are expected soon from the SND2 and CMD3 experiments in Novosibirsk. For the measurement of the cross section $e^+e^- \rightarrow \pi^+\pi^-$ (time-like pion form factor), precision data with $\mathcal{O}(1\%)$ uncertainties exist also from the VEPP-2M experiments CMD-2 and SND. The ISR cross section measurement $\sigma(e^+e^- \rightarrow \pi^+\pi^-\pi^+\pi^-)$ at *BABAR* is explained in detail in Chapter 4.

Chapter 4

Event Selection for $\pi^+\pi^-\pi^+\pi^-\gamma$

This chapter is focused on the event selection for $\pi^+\pi^-\pi^+\pi^-\gamma$ events. Due to the typical ISR event topology, ISR events can be well separated from non-ISR background events. This signature in addition to a kinematic fit is the major selection criterion in order to separate signal from other ISR background channels as well as continuum events. The ratio of signal to background yield shows a strong dependence on the invariant mass of the hadronic system. Therefore different approaches are implemented to clean the experimental data from background depending on the invariant mass of the hadronic system. Finally the global acceptance is extracted with simulation.

4.1 Dataset and Primary Event Selection

The analysis of the $\pi^+\pi^-\pi^+\pi^-\gamma$ channel is based on the full *BABAR* dataset collected at (on-peak) or in the vicinity (off-peak) of the $\Upsilon(4S)$ resonance. This corresponds to an integrated luminosity of 454.3 fb^{-1} of data. The luminosity has been determined with the *BABAR* detector via large angle Bhabha ($e^+e^- \rightarrow e^+e^-$) and di-muon ($e^+e^- \rightarrow \mu^+\mu^-$) events, which may include radiated photons in the final state. The precision of the luminosity measurement is dominated by the theoretical precision of the event generators BHWIDE [98] and BKQED [99]. By implementing the Babayaga@NLO [100, 101] event generator and comparing the results of BHWIDE to Babayaga@NLO [101, 102], a reduction of the total uncertainty from 0.9% to 0.5% has been achieved.

The *BABAR* software continuously changed during the last decade due to further improvements, e.g. in terms of detector calibration and particle identification. In order to assure the usage of the correct conditions in an analysis, *BABAR* software is organized in releases with a fixed set of software conditions. The production release version used in the current analysis is 22.3.4 in combination with the R22d dataset. All systematic studies presented in this thesis are performed using these software conditions.

Concerning the event selection, the basic ingredients are tracks as pion candidates and neutral clusters as photon candidates. The selection criteria for charged tracks impose that the polar angle θ_{ch} points to the reconstruction region of the detector ($0.41 \text{ rad} < \theta_{ch} < 2.54 \text{ rad}$) and that they originate from the collision region. The latter is the case if the transverse distance of closest approach to the event vertex (docaXY) – or nominal interaction point if no primary event vertex is found – is smaller than 1.5 cm and the distance in beam direction (ΔZ) is smaller than 2.5 cm. Tracks with less than $100 \text{ MeV}/c$ transverse momentum are rejected. Photons are used if they have a minimum energy of $E_{\gamma,lab} > 50 \text{ MeV}$. The ISR-photon is restricted to the polar angle range inside the well-understood EMC detection region ($0.35 \text{ rad} < \theta_\gamma < 2.4 \text{ rad}$), and a minimum energy of $E_{\gamma,CM} > 3 \text{ GeV}$ is required.

Data was processed with some preliminary loose selection requirements, named ISRfilter and ISRselpass. The ISRfilter ensures the ISR photon energy requirement: $E_{\gamma,CM} > 3 \text{ GeV}$. In addition, the filter rejects $\gamma\gamma$ -events with another high energetic photon ($E_{\gamma,CM} > 4 \text{ GeV}$) in opposite direction to the first one. The ISRselpass requires at least one good track in the event and in addition demands the tracks to be in the opposite direction of the ISR photon. About 2% of all *BABAR* events satisfy the required criteria. For these events, all detected tracks and neutral clusters are stored in primary ntuples for further analysis.

In order to enable the determination of the event acceptance and detection efficiency, a simulation of the $\pi^+\pi^-\pi^+\pi^-\gamma$ process is needed. A special package of generators for radiative processes (AFKQED) based on the code of Ref. [94] has been developed and is available in the *BABAR* analysis framework as described in Section 3.3. This package

includes many exclusive ISR modes with the option to vary from 2-6 pions or kaons in the final states. For most of the modes, experimental e^+e^- data is used as input, partly including the description of intermediate states. For example, for the $e^+e^- \rightarrow \pi^+\pi^-\pi^0\gamma$ mode, the $\rho\pi$ dominance is implemented. In addition, experimental approximations of cross sections are included. The radiative corrections, multiple (real) photon emission by initial and final particles, have been added with the technique of the structure functions [103, 104] and the PHOTOS package [97]. Concerning the cross section measurement, the accuracy of radiative corrections is better or about 1% (Section 3.3). For the $\pi^+\pi^-\pi^+\pi^-\gamma$ final state, the simulation assumes a dominance of the $a_1(1260)\pi$ intermediate state as it was measured at CMD2 [105] and observed in the CLEOII and ALEPH data [106]. Due to the decay $a_1(1260) \rightarrow \rho^0\pi$ each event contains one pair of pions produced by the $\rho^0 \rightarrow \pi^+\pi^-$ decay. A comparison of the intermediate states between data and simulation is discussed in Chapter 7.

The sample of simulated MC events is reconstructed in the same way as experimental data. For the estimation of background contributions a relatively large sample of different ISR processes has been simulated. In addition, the non-ISR background resulting from $e^+e^- \rightarrow q\bar{q}$ ($q = u,d,s$) is available, simulated with the JETSET event generator [109] as well as $e^+e^- \rightarrow \tau^+\tau^-$ simulation based on the KORALB [110] software package. It is difficult to estimate the uncertainty on the given cross section of the continuum background, since internal branching ratios of the JETSET simulation do not reflect their actual physical values. Therefore a special procedure is applied in order to normalize continuum production (Section 4.3.2). The cross sections of the other processes and the branching fractions of the inclusive processes leading to final states similar to our signal are known with about 10% accuracy or better, which is sufficient for this measurement. The contributions from $\Upsilon(4S)$ decays and $c\bar{c}$ production are negligible. All simulated samples used in this study are listed in Tab. 4.1. Beside the total radiative cross section, the number of events within each sample $N_{produced}$ and the corresponding integrated luminosity \mathcal{L}_{MC} is listed as well as the scaling factor in order to scale the number of events to the luminosity of data.

4.2 Constrained Kinematic Fit and Further Selection

A relatively clean sample of $\pi^+\pi^-\pi^+\pi^-\gamma$ candidate events is already obtained by the preliminary selection of four charged tracks and one high energetic ISR photon. The selection leads to a relative amount of background of approximately 10% in respect to the $\pi^+\pi^-\pi^+\pi^-\gamma$ final state.

For signal events a minimum number of four tracks is required. In addition, events occasionally contain one or two extra tracks due to either beam losses, converted extra radiation, or other interaction. Therefore, events with 4, 5 or 6 tracks are considered as signal candidates. The four tracks closest to the event vertex are taken as input for the

final state	σ [pb]	$N_{produced}$	\mathcal{L}_{MC} [fb $^{-1}$]	scaling factor
$\pi^+\pi^-\gamma$	21.4	87.6M	4090	0.11
$\pi^+\pi^-\pi^0\gamma$	2.6	7.4M	2800	0.16
$\pi^+\pi^-\pi^0\pi^0\gamma$	3.7	3.5M	950	0.49
$\pi^+\pi^-\pi^+\pi^-\pi^0\gamma$	0.9	473k	530	0.87
$\pi^+\pi^-\pi^+\pi^-\pi^0\pi^0\gamma$	3.4	137k	40	10.9
$K_s^0 K^\pm \pi^\mp \gamma$	0.3	978k	3300	0.14
$K^+ K^- \pi^+ \pi^- \gamma$	0.6	100k	170	2.7
$\pi^+\pi^-\pi^+\pi^-\pi^+\pi^-\gamma$	0.7	357k	510	0.62
$\mu^+\mu^-$	42.9	49.25M	1150	0.40
continuum	2090	874.9M	420	0.23 (1.09)
$\tau\tau$	890	382.6M	430	1.06
$\pi^+\pi^-\pi^+\pi^-\gamma$	3.3	31.7M	9610	0.047

Table 4.1: Summary of background channel contributions to $\pi^+\pi^-\pi^+\pi^-\gamma$ from other ISR and non-ISR processes for Runs 1–6. The radiative cross section σ , the number of available simulated events $N_{produced}$ and the corresponding effective luminosities \mathcal{L}_{MC} as well as the resulting scaling factors are displayed for the different final states. Continuum background includes several non-ISR modes. The scaling factor strongly depends on the internal branching ratio for the individual background of interest. It is determined in a dedicated study, described in Section 4.3.2. The scaling factor in brackets corresponds to the given total cross section and therefore to an average scaling factor for different final states. It is not of interest for this study.

constrained kinematic fit procedure.

The fit uses the measured momenta and angles of the charged particles and the corresponding error matrices, as measured in the DCH and imposing the mass of the four pion candidates, and the measured photon energy and angles to solve the energy-momentum-equation. Therefore the four original constraints from the energy-momentum-equation lead to a fit with four constraints (4C).

Due to the fact that the parameters of the measured photon are used in the kinematic fit, they have to be known with very high precision. A micro-alignment and energy calibration of the EMC have been performed using a $\mu^+\mu^-\gamma$ sample (Section 5.1).

The kinematic fit is not only performed in the signal hypothesis of the $\pi^+\pi^-\pi^+\pi^-\gamma$ channel ($\chi^2_{4\pi}$), but also in the hypothesis $K^+K^-\pi^+\pi^-\gamma$ ($\chi^2_{2K2\pi}$) if two tracks are identified as kaons. This allows the application of dedicated $K^+K^-\pi^+\pi^-\gamma$ background suppression requirements. The selected events are recorded into a smaller set of $\pi^+\pi^-\pi^+\pi^-\gamma$ ntuples along with additional information, e.g. the goodness of fit χ^2 , recalculated (denoted *rec*) track and ISR photon momenta and angles. These values are used to apply tighter

$E_{\gamma_{ISR,lab}}^{rec} > 3.0 \text{ GeV}$
$0.35 \text{ rad} < \theta_{\gamma}^{rec} < 2.4 \text{ rad}$
$0.5 \text{ rad} < \theta_{ch}^{rec} < 2.4 \text{ rad}$
$Q_{tot} = 0$
$((E_{EMC}/p_{tot} - 1)/0.15)^2 + ((dE/dX_{DCH} - 690)/150)^2 > 1$
$\chi_{4\pi}^2 < 30$

Table 4.2: Signal selection criteria.

selection criteria (see Table 4.2). The high energetic ISR photon $E_{\gamma_{ISR,lab}}^{rec} > 3.0 \text{ GeV}$ is required to be directed into the well-understood polar angle of the EMC, $0.35 \text{ rad} < \theta_{\gamma}^{rec} < 2.4 \text{ rad}$. The polar angle requirement for the charged tracks is chosen to force these tracks in the DIRC acceptance, which significantly improves kaon from pion separation. In addition, the total charge of the four tracks has to satisfy $Q_{tot} = 0$. In order to suppress radiative Bhabha events, it is required that the deposited energy in the EMC E_{EMC} , the total measured momentum p_{tot} , and the specific energy loss in the DCH dE/dX_{DCH} of the two most energetic tracks satisfy the conditions, indicated in Table 4.2.

Fig. 4.1 shows the $\chi_{4\pi}^2$ distributions for data before background subtraction and the signal simulation in logarithmic (a) and linear scale (b). The distributions are normalized to the number of events in $\chi_{4\pi}^2 < 10$. The absolute difference between the data and MC $\chi_{4\pi}^2$ distributions is shown in Fig. 4.1 (d) for $\chi_{4\pi}^2 > 10$. For high $\chi_{4\pi}^2$ values the difference between the data and the simulation, which is due to the backgrounds shown in Fig. 4.1 (c), is nearly constant.

Towards small $\chi_{4\pi}^2$ values it is visible that the χ^2 resolution is slightly different for data and MC simulation. The data distribution is above MC simulation for $\chi_{4\pi}^2 < 3$ and below for $3 < \chi_{4\pi}^2 < 10$. Cutting into the χ^2 region, which is influenced by this resolution effect, might introduce an artificial efficiency difference between data and MC simulation. Therefore, it has to be ensured that the applied requirement is not too tight. This can be checked by varying the requirement to very high χ^2 values and comparing the relative change in data to simulation. Since the background description of MC simulation is not perfect, and the relative background contamination is higher for high χ^2 values, this might cause a difference between data and MC simulation. In order to get only the difference due to the χ^2 requirement, this variation has to be performed for a very clean sample. Therefore exactly four detected tracks and one photon are required. In addition, the four tracks have to be identified as pions. Fig. 4.1 (e) shows the χ^2 distributions for this clean sample for data and signal MC simulation normalized again to the number of events in $\chi_{4\pi}^2 < 10$ in data. The relative difference is shown in Fig. 4.1 (f). Varying the requirement of χ^2 from 30 to 200 increases the number of events in data by $12.7 \pm 0.3\%$ and in MC simulation by $12.5 \pm 0.1\%$. The difference between data and MC simulation is consistent with zero. Therefore no correction needs to be applied, but a systematic uncertainty of 0.3% on this χ^2 selection is assigned.

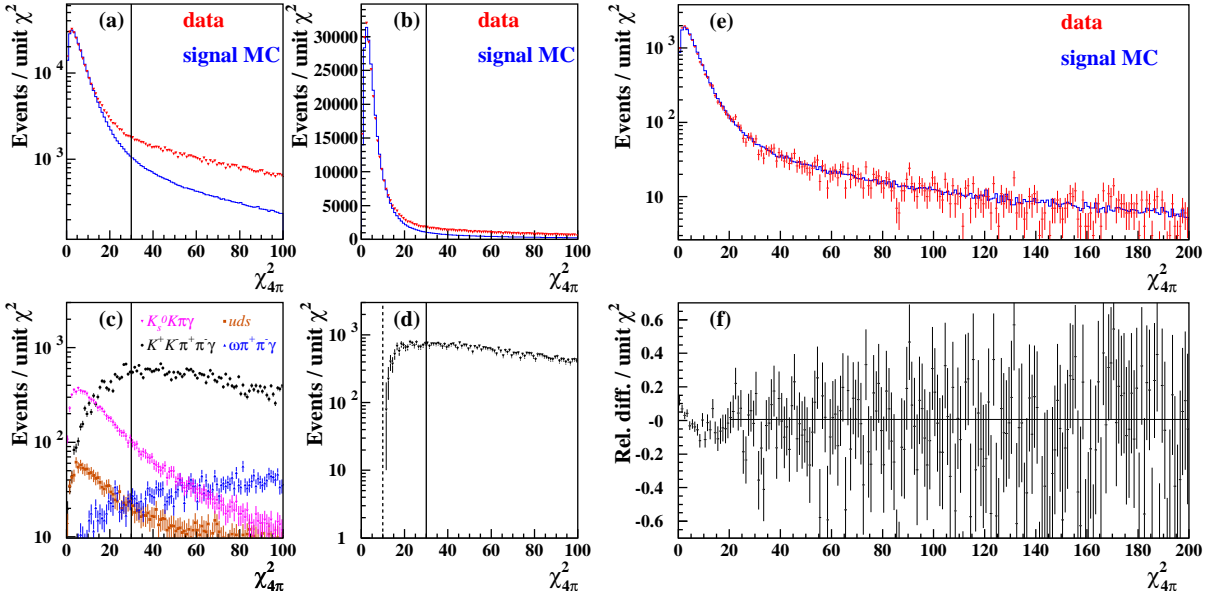


Figure 4.1: The $\chi^2_{4\pi}$ distributions in the $\pi^+\pi^-\pi^+\pi^-$ hypothesis for the data and signal MC in logarithmic (a) and linear scale (b). The simulated background MC samples are shown in (c) and the difference between the data and signal MC in (d). The dashed line indicates the the upper limit of the region of normalization for simulation according to the number of events in data ($0 < \chi^2_{4\pi} < 10$). (e): $\chi^2_{4\pi}$ distribution for events with exactly four detected pion tracks and one photon. The histogram shows the data (red) and signal MC simulation (blue) normalized to the number of events in $\chi^2_{4\pi} < 10$ in data. (f): Relative difference between data and simulation taken from (e).

4.3 Background Subtraction

A difference in the $\chi^2_{4\pi}$ distribution between the data and the MC simulation is observed in Fig. 4.1 (a). Essentially, this deviation is due to background contamination. The difference almost completely disappears in the clean sample with exactly four tracks and one photon detected, see Fig. 4.1 (e). This is an indicator of a non-negligible background contribution in our data.

Figure 4.2 (a) shows the invariant mass distribution $M_{4\pi}$ of the hadronic system for data after applying all selection requirements described above, together with the sum of all relevant simulated background channels. A large peak is visible in data most likely due to excited ρ resonances, e.g. the $\rho(1450)$. The background distribution also shows a peaking structure around the same mass. A signal from $J/\psi \rightarrow \pi^+\pi^-\pi^+\pi^-$ is clearly seen in data. There is also a J/ψ contribution present in the background simulation, visible as a broader structure at slightly lower invariant masses. The shift in the invariant mass $M_{4\pi}$ is due to a mis-identification of kaons as pions. In the data, an additional narrow peak at the $\psi(2S)$ invariant mass is visible. The background contamination is on the level of a few % in the $M_{4\pi}$ peak region, but contributes up to 20% at high invariant masses.

The individual background contributions are displayed in Fig. 4.2 (b). In the peak region ($1.2 \text{ GeV}/c^2 < M_{4\pi} < 2.2 \text{ GeV}/c^2$) the main contributions are coming from the ISR channels $K^+K^-\pi^+\pi^-\gamma$ and $K_S^0K^\pm\pi^\mp\gamma$, whereas above $2.2 \text{ GeV}/c^2$ the additional back-

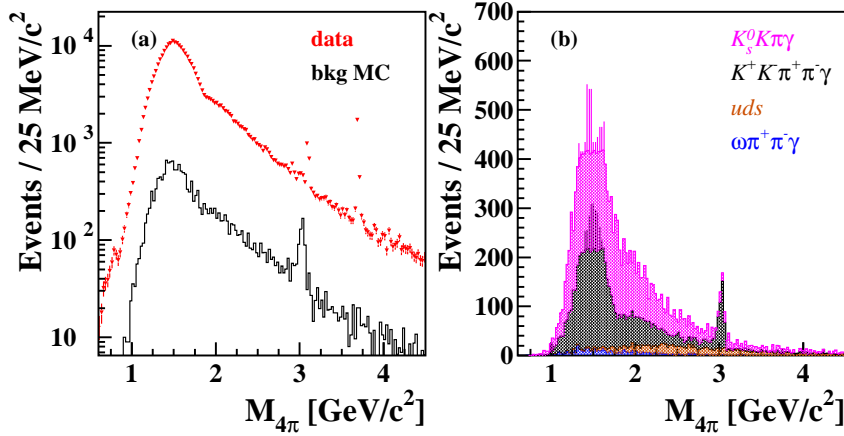


Figure 4.2: (a): The invariant $\pi^+\pi^-\pi^+\pi^-$ invariant mass distribution for data (red) and the sum of the simulated $K^+K^-\pi^+\pi^-\gamma$, $K_s^0 K^\pm \pi^\mp \gamma$ and continuum production background distributions (black). (b): The individual background contributions as a function of the $\pi^+\pi^-\pi^+\pi^-$ invariant mass.

ground of the non-ISR continuum events gains importance. At low invariant masses, $M_{4\pi} < 1.2 \text{ GeV}/c^2$, the $\pi^+\pi^-\gamma$ and $\pi^+\pi^-\pi^0\gamma$ are dominant and not included in Fig. 4.2. In the following, the different methods to clean data from the various background contributions are described.

4.3.1 Background in Peak Region ($1.2 \text{ GeV}/c^2 < M_{4\pi} < 2.2 \text{ GeV}/c^2$)

The background channels which dominate in the peak region of the invariant mass are the ISR final states $K^+K^-\pi^+\pi^-\gamma$ and $K_s^0 K^\pm \pi^\mp \gamma$. Two different approaches are used for the background subtraction, and the difference between the two methods serves as an estimate of the systematic uncertainty related to the background subtraction:

- Method 1: Subtract the simulated invariant 4-pion mass distributions of the background channels directly
- Method 2: Use specific selection criteria to suppress background channels

Method 1: Subtraction of Simulated Background Channels

The background channels simulated in AFKQED have not been updated yet according to the recent *BABAR* cross section measurements of these channels. The basic principle of this method is to scale the individual MC channels according to their cross section and to the luminosity of data. The same event selection for data, signal MC and the background MC channels is applied. Then the $M_{4\pi}$ spectrum of each background channel is subtracted from the $M_{4\pi}$ distribution of data. Figure 4.3 (a) and (b) display the invariant mass distributions of the simulation on generator level as well as the shape of the measured differential cross section as a function of the invariant mass for $K^+K^-\pi^+\pi^-\gamma$ [75] and $K_s^0 K^\pm \pi^\mp \gamma$ [76] respectively. Both distributions are normalized to the same integral.

Differences between the MC simulations and the measurements are clearly visible.

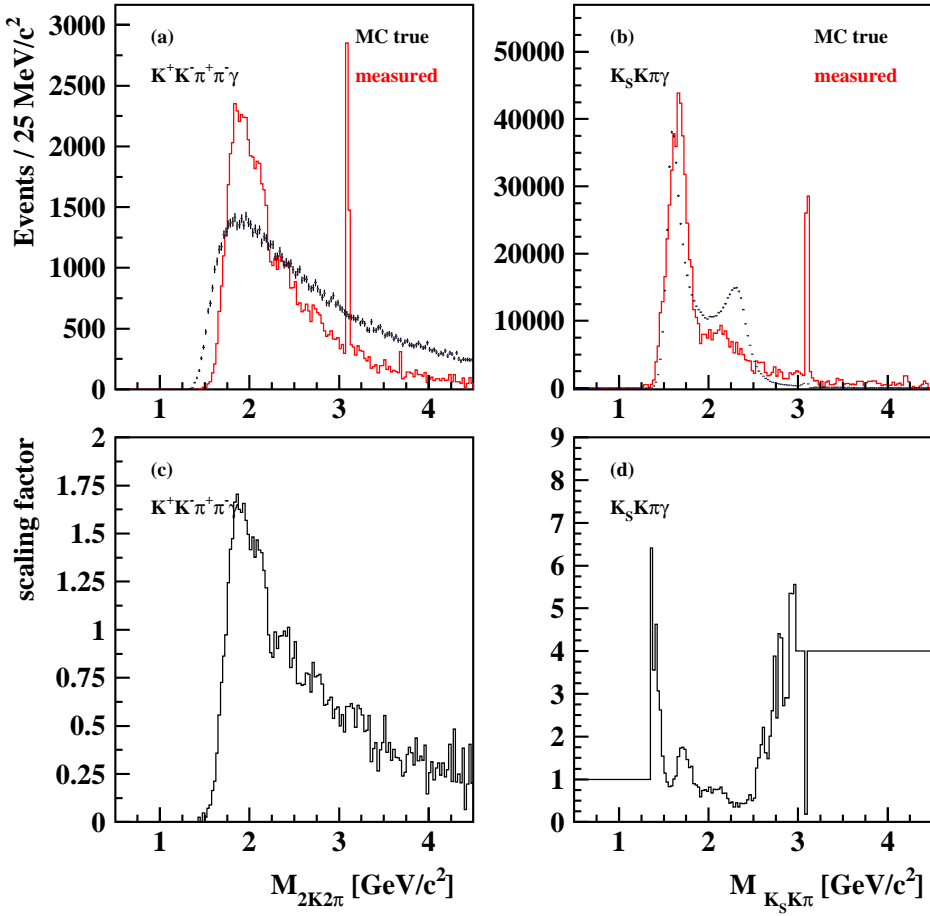


Figure 4.3: Invariant mass distribution of simulation on generator level (black) in comparison to the measurement (red) for (a) $K^+K^-\pi^+\pi^-\gamma$ [75] and (b) $K_s^0K^\pm\pi^\mp\gamma$ [76]. Scaling factor for $K^+K^-\pi^+\pi^-\gamma$ (c) and $K_s^0K^\pm\pi^\mp\gamma$ (d).

Consequently, each event in the invariant mass distribution needs to be weighted according to its true invariant mass information in order to assure that the MC invariant mass distribution matches the measured distributions. The corresponding scaling factors are displayed in Fig. 4.3 (c) and (d). After this re-weighting process, the background contributions of $K_s^0K^\pm\pi^\mp\gamma$ and $K^+K^-\pi^+\pi^-\gamma$ in the invariant $\pi^+\pi^-\pi^+\pi^-$ -mass spectrum are displayed in Fig. 4.4 (a) and (b). Only the J/ψ peak, which is not generated in $K^+K^-\pi^+\pi^-\gamma$, is not reproduced. This has to be taken into account when measuring the branching ratio $\mathcal{B}(J/\psi \rightarrow \pi^+\pi^-\pi^+\pi^-)$, see Chapter 7.1.

Method 2: Specific Background Requirements

The basic principle of this approach is to apply specific selection criteria in order to suppress the $K^+K^-\pi^+\pi^-\gamma$ and $K_s^0K^\pm\pi^\mp\gamma$ background contributions. This is achieved by

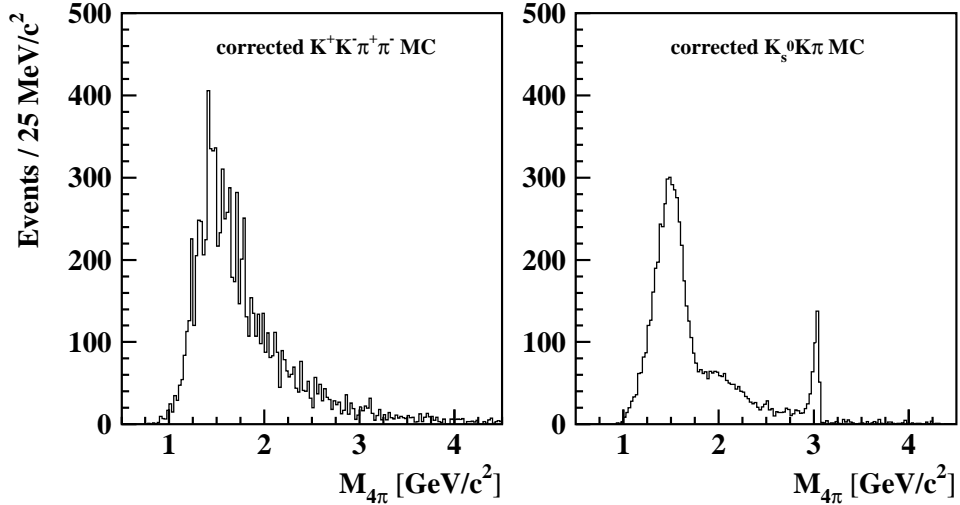


Figure 4.4: Re-weighted $\pi^+\pi^-\pi^+\pi^-$ invariant mass distribution $M_{4\pi}$ for $K_s^0 K^\pm \pi^\mp \gamma$ and $K^+ K^- \pi^+ \pi^- \gamma$ simulation, Run 5.

the following two requirements: the $K_s^0 K^\pm \pi^\mp \gamma$ veto and the $K^+ K^- \pi^+ \pi^- \gamma$ veto.

The $K_s^0 K^\pm \pi^\mp \gamma$ veto is performed if exactly one track is identified as charged kaon according to a tight PID requirement. According to simulation, the pion fake rate for this requirement is about 1.0% per event (0.25% per track). In addition, the invariant $\pi^+\pi^-$ -mass $M_{2\pi}$ of two of the three pions in the event is required to lie near the nominal invariant mass of the K_s^0 , $0.460 \text{ GeV}/c^2 < M_{2\pi} < 0.535 \text{ GeV}/c^2$. The $M_{2\pi}$ distributions for events with one detected K^\pm is shown in Fig. 4.5 for data, signal MC and $K_s^0 K^\pm \pi^\mp \gamma$ MC. The K_s^0 peak is clearly visible in data in addition to a flat background due to $\pi^+\pi^-\pi^+\pi^- \gamma$ events with one pion misidentified as kaon. A corresponding flat distribution is seen in Fig. 4.5 (b) for signal MC. As expected, a peaking structure at the K_s^0 mass is visible for $K_s^0 K^\pm \pi^\mp \gamma$ MC in Fig. 4.5 (c).

Due to this veto, when the K_s^0 and the K^\pm are identified, approximately 1% of signal MC is lost and 73% of $K_s^0 K^\pm \pi^\mp \gamma$ are removed as can be seen in Table 4.3. The total number of events in data is approximately 280000. The sum of predicted loss with MC (8774 events) matches the real loss in data (8072 events) reasonably well. The differences of 702 events are either due to the uncertainty in the scaling of the $K_s^0 K^\pm \pi^\mp \gamma$ MC or to data-MC differences of the kaon PID selector. In comparison to the total number of events in data the difference is very small (< 0.3%), which is a measure for the systematic uncertainty due to this veto.

The $K^+ K^- \pi^+ \pi^- \gamma$ veto is performed if the event contains two tracks which are identified as kaons according to a slightly looser kaon PID selector than the one used for the $K_s^0 K^\pm \pi^\mp \gamma$ veto. In addition the event needs to satisfy $\chi^2_{2K2\pi} < 10$ in order to be rejected. By this requirement, almost no signal is lost (< 0.1%), see Tab. 4.3. This is due to the fact that the pion as kaon mis-identification rate of the PID selector is quite low for two pions simultaneously. In combination with the $\chi^2_{2K2\pi} < 10$ requirement – the corresponding distributions are shown in Fig. 4.6 – almost no signal is rejected. However,

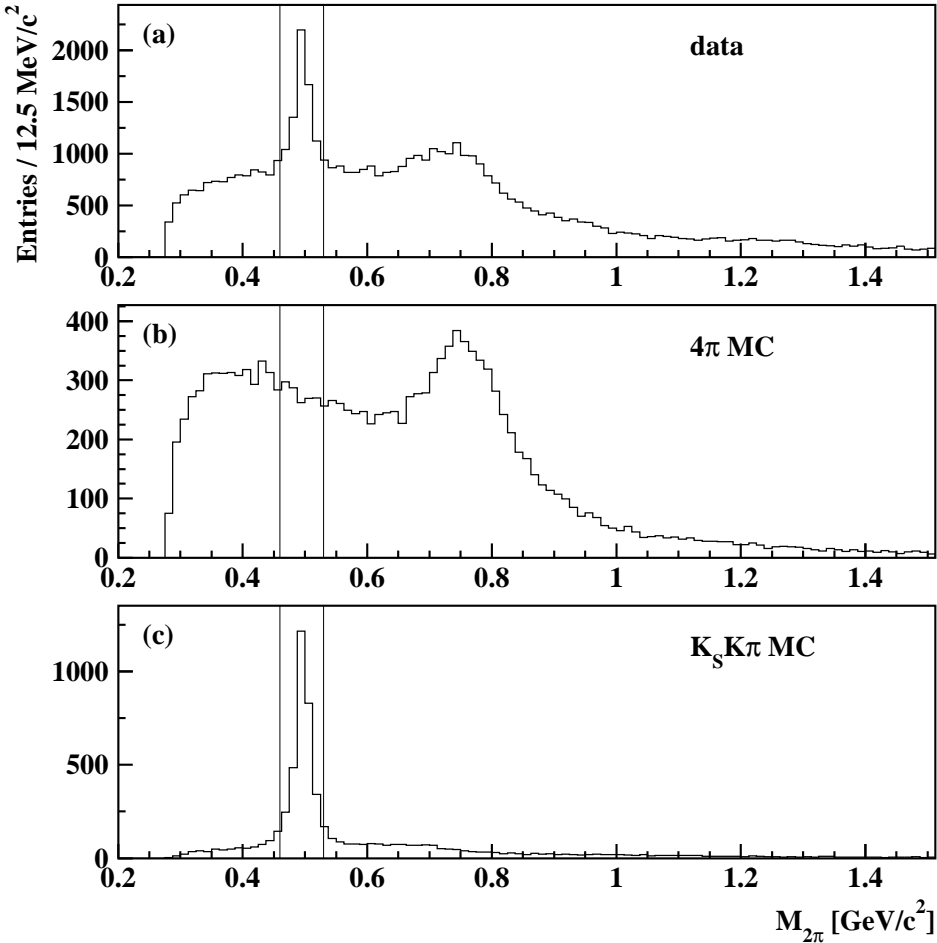


Figure 4.5: Invariant $\pi^+\pi^-$ -mass distribution $M_{2\pi}$ for events with one identified kaon for data (a), signal MC (b) and $K_s^0 K^\pm \pi^\mp \gamma$ MC (c); 2 entries per event, Run 5. Vertical lines represent the K_s^0 selection $0.460 \text{ GeV}/c^2 < M_{2\pi} < 0.535 \text{ GeV}/c^2$.

a reduction of 55% of $K^+K^-\pi^+\pi^-\gamma$ background events (5432 events) is achieved. 45% remain because the kaon selector has an average efficiency of approximately 90%. The difference between data and MC is on the level of 1%. Since 2 kaons are required, approximately 80% of the $K^+K^-\pi^+\pi^-\gamma$ are properly identified. Not all of them satisfy the $\chi^2_{2K2\pi}$ requirement, as can be seen in Fig. 4.6. The remaining 42% of $K^+K^-\pi^+\pi^-$ background can finally be subtracted according to method 1. The small difference between the number of lost events in data (5019) and MC (5432 events) is due to differences in the kaon PID selection and differences in the shape of the $\chi^2_{2K2\pi}$ distributions. This global difference in comparison to the number of signal events is a measure of the systematic uncertainty of this method which is approximately 0.2% ($\frac{413}{264000}$ see Table 4.3).

The number of events removed in data due to the vetoes (-4.9%) is very well reflected by the luminosity-weighted MC (-4.6%). The remaining background events are finally subtracted according to method 1.

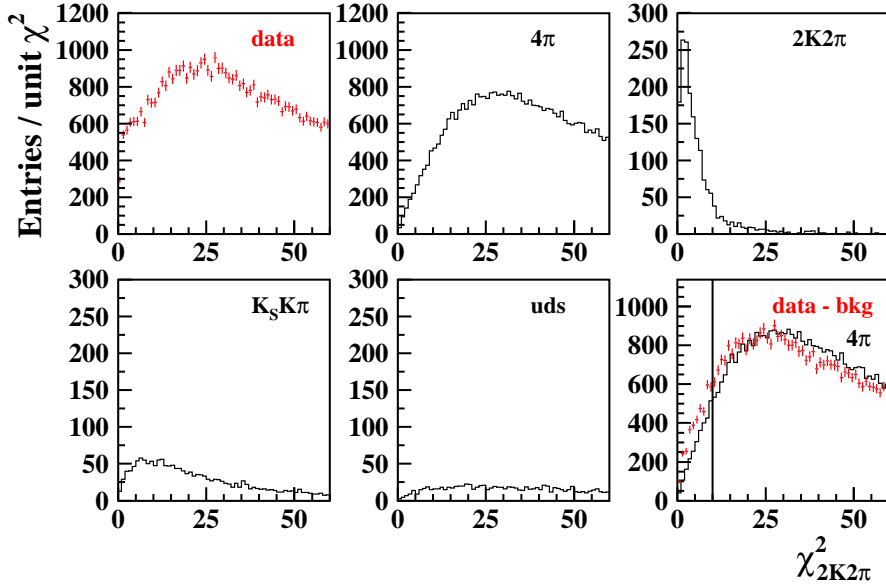


Figure 4.6: The $\chi^2_{2K2\pi}$ distributions for data (red) and various simulated final states (black), Run 5.

Comparison of Method 1 and Method 2

Performing the two methods leads to a good estimate of the systematic uncertainty due to $K^+K^-\pi^+\pi^-\gamma$ and $K_s^0K^\pm\pi^\mp\gamma$ background subtraction. This can be seen in Table 4.3. On the one hand, the total number of subtracted events with the two methods matches

final state	Method 1	Method 2				
		$K_s^0K^\pm\pi^\mp$ veto	$K^+K^-\pi^+\pi^-$ veto	combined veto		complete
$\pi^+\pi^-\pi^+\pi^-\gamma$	264000	261130	263960	261090	-1.1%	261090 -1.1%
$K_s^0K^\pm\pi^\mp\gamma$	6744	1798	6663	1742	-74.2%	0 -100%
$K^+K^-\pi^+\pi^-\gamma$	9598	8674	4305	3649	-62%	0 -100%
continuum	1110	1075	1093	1058	-4.7%	0 -100%
sum MC	281452	272677	276021	267539	-4.9%	261090 -7.8%
data	282250	274178	277231	269354	-4.6%	262905 -7.4%

Table 4.3: Number of events (second column), scaled to the data luminosity for different final states (first column). Third and fourth column display the remaining number of events after the $K_s^0K^\pm\pi^\mp\gamma$ and $K^+K^-\pi^+\pi^-\gamma$ veto, respectively. Since the $\pi^+\pi^-\pi^+\pi^-\gamma$ cross section is a result of this study, the $\pi^+\pi^-\pi^+\pi^-\gamma$ MC is preliminary scaled to the difference in number of events between data and the sum of all background contributions. The number of events with the combined veto is displayed in the fourth column and after subtracting the remaining background contribution according to simulation in the last column.

nicely as shown in Table 4.3. In addition, the background subtraction according to both methods agrees as a function of the invariant mass $M_{4\pi}$. Figure 4.7 shows the difference in the results of the invariant mass distributions using method 1 and 2. The plot on the

left hand side displays the differences in the two methods using the original MC invariant mass distribution. In the integral, hardly any differences is visible. However MC is not subtracted properly bin by bin. On the right hand side the corrected mass distribution of $K^+K^-\pi^+\pi^-\gamma$ and $K_s^0K^\pm\pi^\mp\gamma$ MC is used. The two methods agree much better, leading to the assumption of a systematic uncertainty of 1% due to the background subtraction. Finally, method 2, which is a hybrid of the vetos and the subtraction of the simulated background channels, is used in order to remove the background contributions, since it depends less on the absolute scaling of simulation.

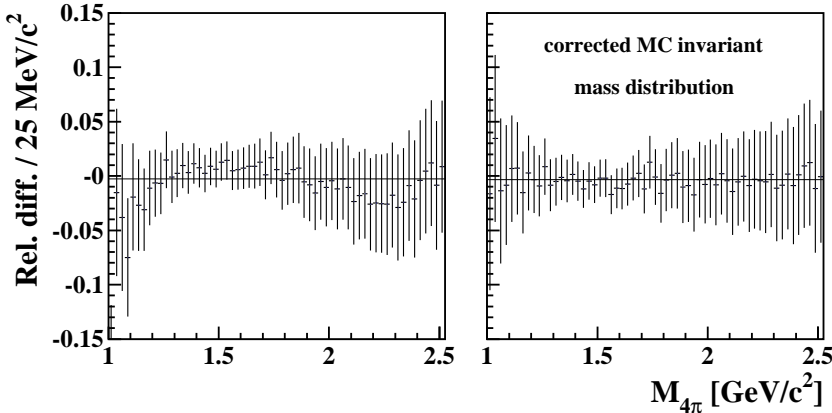


Figure 4.7: The relative difference of the invariant mass distributions of data between corrections according to method 1 or 2 without (left) and with (right) MC invariant mass corrections.

4.3.2 Background at Large Invariant Masses ($M_{4\pi} > 2.2 \text{ GeV}/c^2$)

The main background contribution at large invariant masses stems in addition to the $K^+K^-\pi^+\pi^-\gamma$ and $K_s^0K^\pm\pi^\mp\gamma$ contributions from non-ISR continuum background, increasing towards high invariant masses. The best choice to clean data from background at large invariant masses is to subtract continuum production MC from data. In the following, the method to determine the correct scaling factor for the continuum production is described. The largest contribution of the non-radiative continuum events that fake signal events is $\pi^+\pi^-\pi^+\pi^-\pi^0$, with $\pi^0 \rightarrow \gamma\gamma$. One of the two photons resulting from the π^0 decay can be misidentified as a fake ISR photon.

In previous similar studies, the invariant $\gamma\gamma$ -mass ($M_{\gamma\gamma_{ISR}}$) of the ISR photon with that photon which leads to the invariant mass closest to the π^0 -mass was compared between data and the sum of signal MC and continuum production MC. These distributions are shown in Fig. 4.8 for data (a), signal MC (c) and continuum production MC (e). Plotting only the combination with $M_{\gamma\gamma_{ISR}}$ closest to the π^0 -mass creates an artificial peak at the π^0 -mass. If the artificial peak in data and MC were very similar, the strategy would allow a proper determination of the scaling factor. However, this is not the case. Figure 4.8 shows all $M_{\gamma\gamma_{ISR}}$ combinations for data (b) and signal MC (d). It is visible that data and signal MC have a very different shape at low invariant masses. The peaking structure for signal MC close to threshold is much larger than in data. This peak clearly influences the

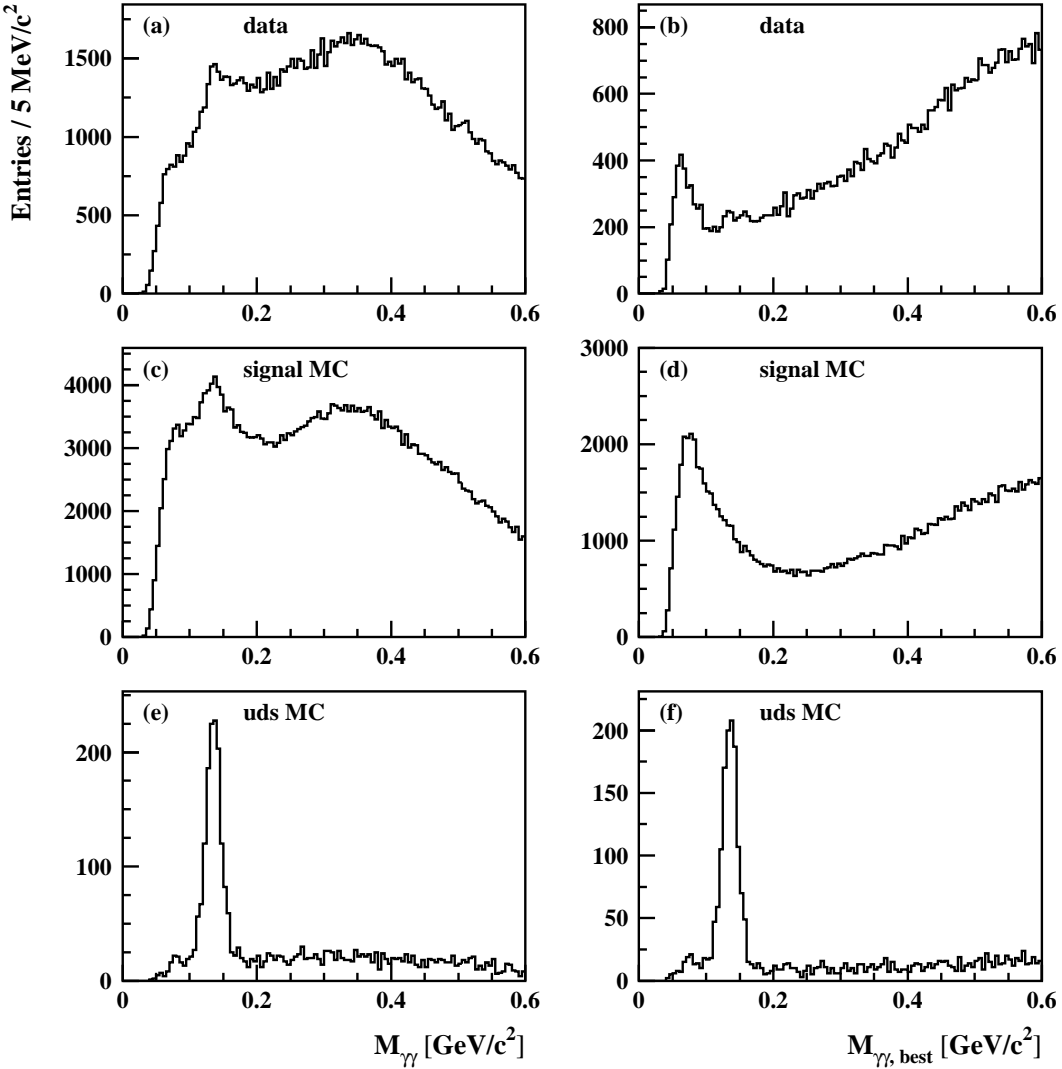


Figure 4.8: Invariant mass distribution for data (top), signal MC (middle) and continuum production MC (bottom). All combinations of ISR photon with other good photons ($E_\gamma > 50$ MeV) (right) and only the combination closest to the π^0 invariant mass (left) of all $\gamma\gamma_{ISR}$ combinations.

π^0 invariant mass region. Therefore the scaling of continuum production in this study is performed with the previously discussed event selection and the additional modification to subdivide the sample into two subsamples. The first sample is restricted to large invariant $\pi^+\pi^-\pi^+\pi^-$ masses ($2.2 \text{ GeV}/c^2 < M_{4\pi} < 4.5 \text{ GeV}/c^2$). In this invariant mass region continuum production is the largest source of background. All ISR background channels have a rather small contribution, and moreover their invariant $M_{\gamma\gamma_{ISR}}$ mass distribution should not be different from signal MC. The second sample with a very small continuum production content is at small invariant masses $M_{4\pi} < 2.2 \text{ GeV}/c^2$. For both samples, the $M_{\gamma\gamma_{ISR}}$ distribution of all possible pairings of the ISR photon with all other photons in an event are created. These distributions can be seen in Fig. 4.9 (a) for $M_{4\pi\gamma} < 2.2 \text{ GeV}/c^2$ and in (b) for $2.2 \text{ GeV}/c^2 < M_{4\pi\gamma} < 4.5 \text{ GeV}/c^2$. Only a small π^0 peak is visible in (a) as expected. This sample can be used to estimate the shape of the

non-continuum production distribution.

In order to describe the background properly, the sum of a Gaussian distribution, which describes the π^0 peak, and the function

$$f(x) = \frac{c_1}{c_2 \cdot x - c_3} + c_4 + c_5 \cdot x \quad (4.1)$$

is fitted to the $M_{\gamma\gamma ISR}$ distribution of data in (a).

Once the 5 parameters $c_1 - c_5$ are determined by the fit, the approximate shape of the background is known. As a next step, a second fit is performed for the histogram in (b) again with a Gaussian with three free parameters and $f(x)$ for the background distribution with the previously determined parameters $c_1 - c_5$ kept fixed in the fit. As a result of the fit, the parameters of the Gaussian are obtained and the number of events in the peak are determined.

Figure 4.9 (c) displays the corresponding distribution for continuum production MC. Using the sum of a flat and a Gaussian distribution gives a sufficient estimate for the number of events in the π^0 -mass peak region. This MC sample has to be rescaled in order to match the number of events in the peak in (b). The resulting scaling factor of 0.23 ± 0.05 will be used in the following to scale the continuum background.

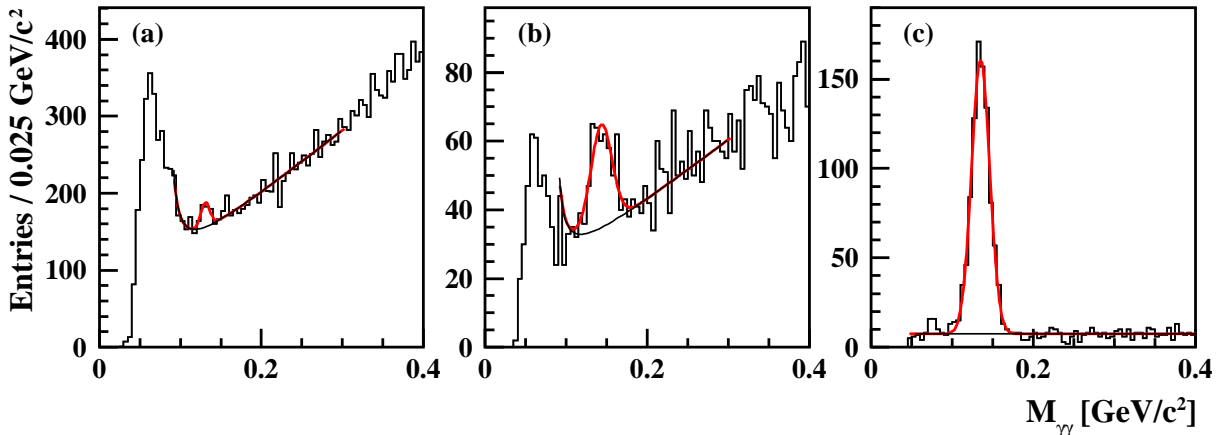


Figure 4.9: Invariant $\gamma\gamma_{ISR}$ mass distribution $M_{\gamma\gamma}$ for data at low invariant masses $M_{4\pi} < 2.2 \text{ GeV}/c^2$ (a). Corresponding distribution at large invariant masses $2.2 \text{ GeV}/c^2 < M_{4\pi} < 4.5 \text{ GeV}/c^2$ for data (b) and continuum production MC (c).

The main uncertainty of the resulting scaling factor is the uncertainty of the number of events in the Gaussian distribution describing the π^0 -mass peak. This scaling factor is the average scaling factor for all continuum events with $2.2 \text{ GeV}/c^2 < M_{4\pi} < 4.5 \text{ GeV}/c^2$. Figure 4.10 shows the relative variation of the final $\pi^+\pi^-$ cross section when varying the continuum scaling factor according to the fit result (0.23 ± 0.05) by one standard deviation to 0.18 and 0.28.

Determining the scaling factor with the same method using events with $M_{4\pi} < 2.2 \text{ GeV}/c^2$ gives a different result: 0.45 ± 0.2 . The relative uncertainty of 50% of this scaling factor in this region is due to the fact that the number of events in the π^0 -mass peak is difficult to determine due to the small contribution of continuum production in that region.

However, the impact of continuum production background at $M_{4\pi} < 2.2 \text{ GeV}/c^2$ is very small. Even the variation of the scaling factor from 0.23 to 0.45 influences the $\pi^+\pi^-\pi^+\pi^-$ cross section result by less than 0.5%, which is used as an estimate for the systematic uncertainty in this region.

The determination of the scaling factor separately for $3.0 \text{ GeV}/c^2 < M_{4\pi} < 4.5 \text{ GeV}/c^2$ gives a similar result (0.28 ± 0.06) as for the whole region $2.2 \text{ GeV}/c^2 < M_{4\pi} < 4.5 \text{ GeV}/c^2$. This supports the assumption that the variation of the scaling factor within our determined average value of 0.23 ± 0.05 leads to a reasonable estimate for the systematic uncertainty due to continuum background subtraction. The black lines in Fig. 4.10 are used as the systematic uncertainty for the indicated region of $M_{4\pi}$.

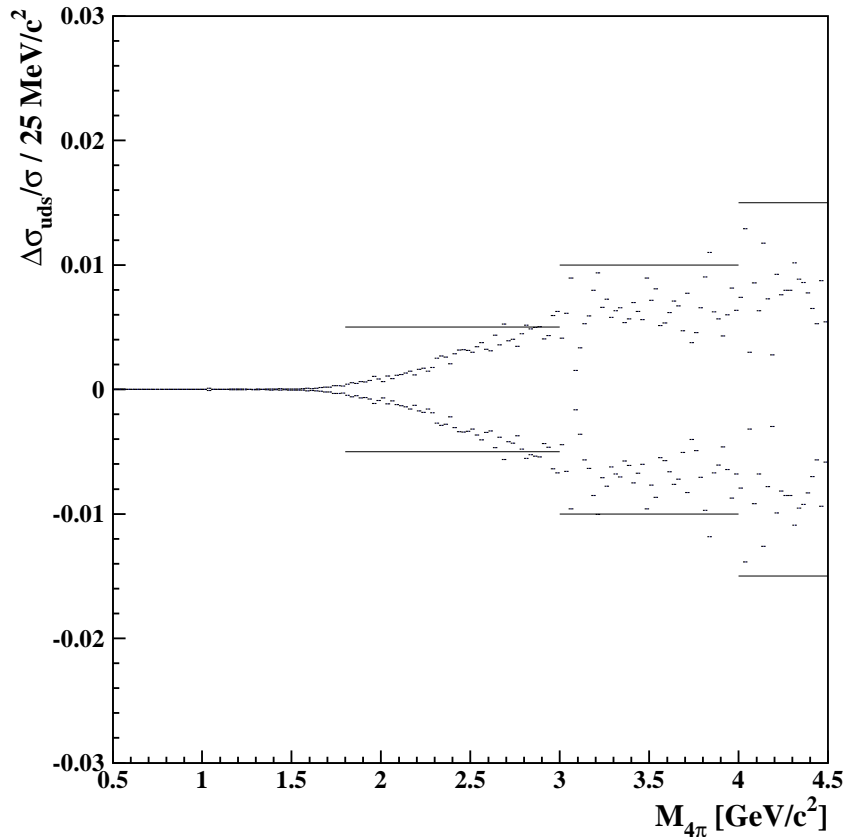


Figure 4.10: Systematic uncertainty due to continuum subtraction. Relative variation of the cross section $\sigma(e^+e^- \rightarrow \pi^+\pi^-\pi^+\pi^-)$ due to the variation of the continuum background scaling factor within its uncertainty to 0.18 and 0.28 (points); estimated systematic uncertainty due to this background subtraction (lines).

There is an additional background contribution in the charmonium region. Figure 4.11 (a) shows the $\pi^+\pi^-\pi^+\pi^-$ invariant mass distribution for data. Peaks around the J/ψ and $\psi(2S)$ masses are clearly visible. In Fig. 4.11 (b), the $\pi^+\pi^-$ invariant mass distribution $M_{2\pi}$ for events within the $\psi(2S)$ mass region $3.65 \text{ GeV}/c^2 < M_{4\pi} < 3.75 \text{ GeV}/c^2$, as indicated in Fig. 4.11 (a), are plotted. The distribution contains 4 entries per event. The J/ψ peak is clearly visible. The PDG value for the branching fraction of $J/\psi \rightarrow \pi^+\pi^-$ is two

orders of magnitude smaller than for $J/\psi \rightarrow \mu^+\mu^-$: $\frac{\mathcal{B}(J/\psi \rightarrow \mu^+\mu^-)}{\mathcal{B}(J/\psi \rightarrow \pi^+\pi^-)} \approx 400$. Due to the fact that no dedicated PID selector is used, events which contain muons are not suppressed. Also the kinematic fit does not suppress $\pi^+\pi^-\mu^+\mu^-$ events, because the mass difference between muons and pions is only $34 \text{ MeV}/c^2$. This mass difference is negligible, because both particles are highly relativistic, being produced by the J/ψ decay. Requiring that $M_{2\pi}$ is around the J/ψ -mass removes these background events as can be seen in Fig. 4.11 (c). The $\psi(2S)$ peak almost entirely consists of $\pi^+\pi^-\mu^+\mu^-$ events.

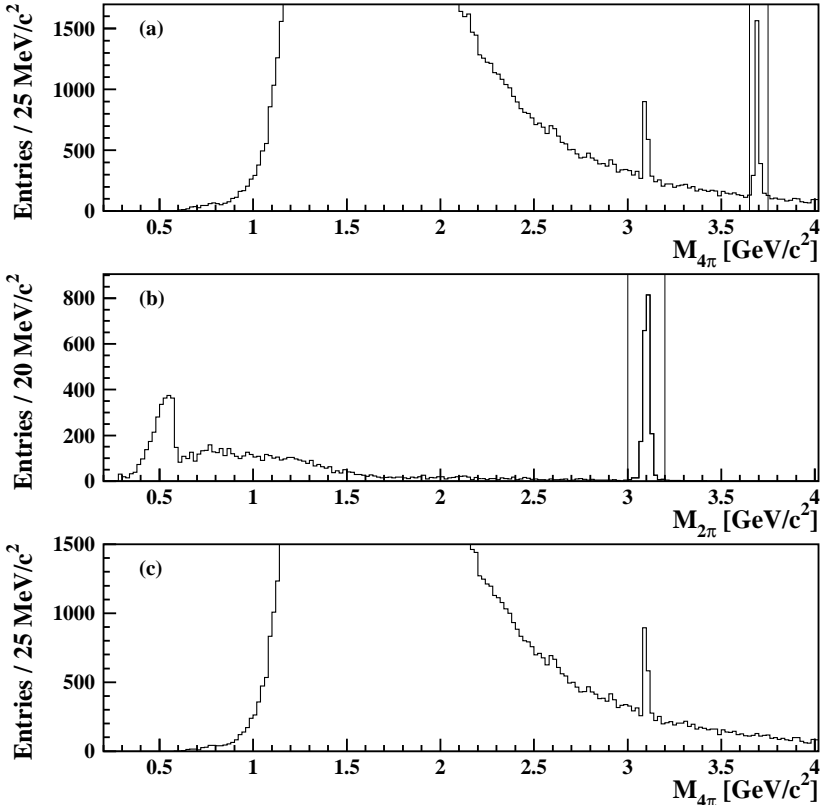


Figure 4.11: (a): $\pi^+\pi^-\pi^+\pi^-$ invariant mass distribution for data; (b): $\pi^+\pi^-$ invariant mass distribution for events within the $\psi(2S)$ invariant mass region $3.65 \text{ GeV}/c^2 < M_{4\pi} < 3.75 \text{ GeV}/c^2$ as indicated by the vertical lines in (a) (4 entries per event); (c): $\pi^+\pi^-\pi^+\pi^-$ invariant mass distribution for data without entries of the $\pi^+\pi^-$ invariant mass in the J/ψ mass region represented by the vertical lines in (b).

4.3.3 Background at Small Invariant Masses ($M_{4\pi} < 1.2 \text{ GeV}/c^2$)

At small invariant $\pi^+\pi^-\pi^+\pi^-$ -masses, there is a large signal pollution due to events coming from the ISR-channels $\pi^+\pi^-\pi^0\gamma$ and $\pi^+\pi^-\gamma$. These processes are illustrated in Fig. 4.12. In the case of the $\pi^+\pi^-\pi^0\gamma$ final state, the π^0 decays to two photons ($\pi^0 \rightarrow \gamma\gamma$) and one of the photons emitted from the π^0 converts in the detector. In the case of the $\pi^+\pi^-\gamma$ final state, NLO real radiation converts in the detector or NLO internal conversion takes place. These conversion electrons and positrons can get misidentified as pions.

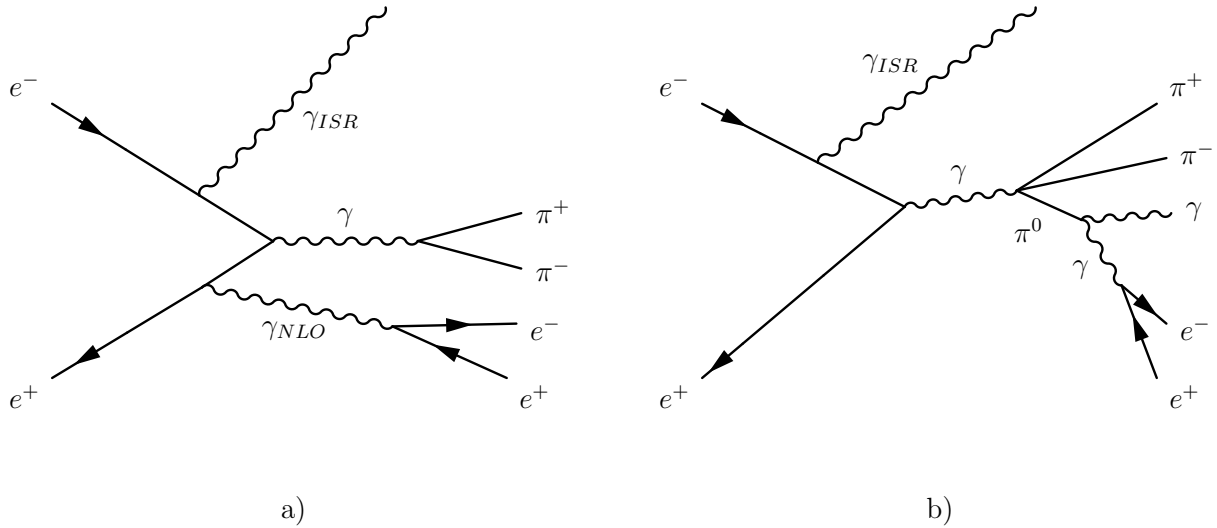


Figure 4.12: Illustration of background contributions due to the ISR-channels $\pi^+\pi^-\gamma$ (a) and $\pi^+\pi^-\pi^0\gamma$ (b).

As a result of the investigation of Chapter 5.2, an estimate of the ratio of real conversion to internal conversion of approximately 5:1 is obtained. Real conversion is dominant. The background contributions from this source are estimated with two different methods.

Method 1: Conversion Veto

A primary vertex routine computes a common vertex of all charged tracks of an event. It assigns a corresponding vertex probability P_{Vertex} , reflecting the probability that all tracks have been created at this vertex. Due to the fact that two real conversion tracks are not emitted from the interaction point, the primary vertex probability for this kind of events is small. Figure 4.13 (left) and (right) display the vertex probability distributions in logarithmic scale for data and MC respectively. Events which have a vertex probability of less than 0.01 are rejected. These events are clearly present in data and hardly present in MC. This requirement, however, will hardly reject very high energetic electrons, produced in the inner structure of the detector (beam-pipe, SVT). This is due to the fact that these conversion tracks are very straight and point back to the origin of the conversion photon. Furthermore, this method cannot reject events with internal conversion.

Therefore, this requirement needs to be combined with a veto which rejects events if two electrons are identified according to an electron PID selector. The selector used has a very high electron efficiency ($\approx 99\%$). However it has a non negligible pion mis-identification rate of approximately 5 – 10%, depending on momentum and polar angle.

Method 2: π -PID

Since the background contribution is high in this $M_{4\pi}$ mass region, a second approach is needed to confirm the result of method 1: Another way of estimating the signal distribution is to require actively a pion PID selector. This selector has a difference between

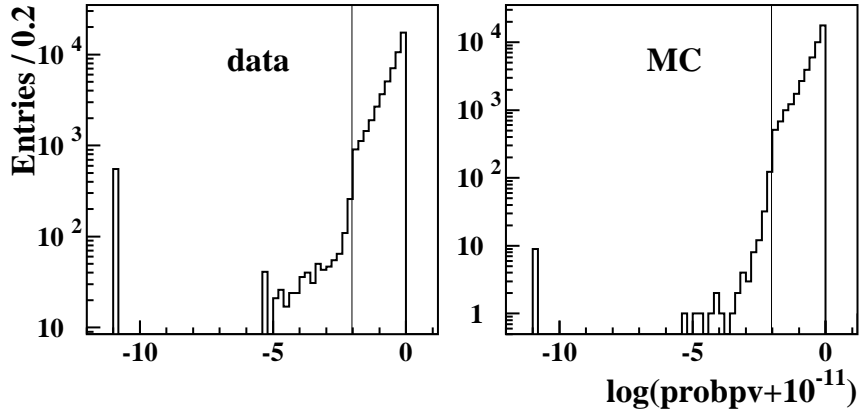


Figure 4.13: Vertex probability distribution for data (left) and MC (right). The large peak in data at -11 corresponds to a vertex probability of 0 and is hardly present in MC. It is due to real conversion events.

data and MC of up to approximately 1.5% per track, depending on its momentum. So finally, the requirement of all four tracks to be identified as a pion in the invariant mass region $M_{4\pi} < 1.1 \text{ GeV}/c^2$ is expected to introduce a systematic shift of approximately 2 – 5%. Therefore, it is not used in the peak region, $1.2 \text{ GeV}/c^2 < M_{4\pi} < 2.2 \text{ GeV}/c^2$, where the background contamination is very low and the previously described methods lead to a smaller systematic uncertainty. Since it is known that the relative background contamination is small in the peak region of $M_{4\pi}$, this region can be used to estimate the PID efficiency differences between the data and the MC simulation. In a first step, it is verified that the momentum distribution at $M_{4\pi} > 1.0 \text{ GeV}/c^2$ is similar to the momentum distribution at very low invariant masses, i.e. $M_{4\pi} < 0.8 \text{ GeV}/c^2$, since the PID efficiency differences depend on the momentum of the particle. Figure 4.14 (a) and (b) display the momentum distribution for tracks at small invariant masses ($M_{4\pi} < 0.8 \text{ GeV}/c^2$) for tracks identified as pions and not identified as pions. Both distributions at small invariant masses are very similar to the corresponding ones at higher invariant masses $M_{4\pi} > 1.0 \text{ GeV}/c^2$, which is shown in Fig. 4.14 (c) and (d). This allows us to measure the efficiency difference between data and MC due to the PID selector in the peak region and apply the corresponding correction at low invariant masses.

The shift in the peak region of the $M_{4\pi}$ distribution due to the π PID can be seen in Fig. 4.15 (a). In this clean region, a shift of slightly above 2% is observed and corrected, as shown in Fig. 4.15 (b).

The electron as pion mis-ID probability is approximately 5%. Therefore the probability to misidentify the two conversion electrons as pions is about $5\% \cdot 5\% = 0.25\%$. The number of events removed by the pion selection multiplied by 0.25% gives an estimate for the systematic uncertainty due to remaining conversion background.

The contributions to the uncertainty are shown in Fig. 4.16 for the π efficiency difference (black) and the remaining conversion background (blue). The sum of both contributions (red) gives an estimate for the total systematic uncertainty, which is approximately 3%.

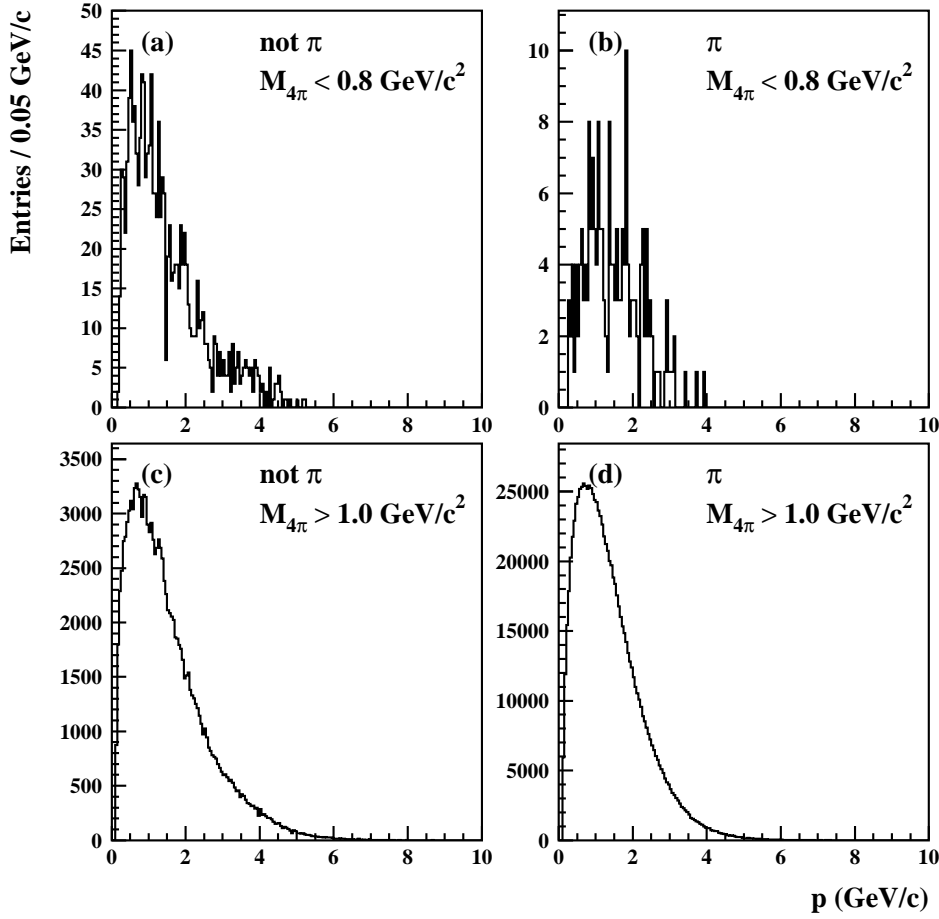


Figure 4.14: Momentum distribution of all four tracks of events with $M_{4\pi} < 0.8 \text{ GeV}/c^2$ (top) and $M_{4\pi} > 1.0 \text{ GeV}/c^2$ (bottom) for events with all 4 tracks identified as pions (right) and events with one track not identified as pion (left).

Comparison: Method 1 and Method 2

The cross section at low 4-pion masses with and without the two different background subtraction methods is displayed in Fig. 4.15 (c). Both methods remove the large fraction of conversion events and agree well. In the end the pion selector is used, and the distribution is corrected for the difference between data and MC as described before. It should also be noted that the peaking structure at approximately $700 \text{ MeV}/c^2$ strongly diminishes, and - if at all - only remains as a small shoulder after applying the vetos.

4.3.4 Background Summary

After applying standard selection requirements, the background contamination at low invariant masses is very low in comparison to the number of signal events in that region. Therefore it is suppressed by requiring all tracks to satisfy the pion PID selection. This allows a background subtraction with an uncertainty of 3%. In the peak region, the corresponding uncertainty due to the $K_S^0 K^\pm \pi^\mp \gamma$, $K^+ K^- \pi^+ \pi^- \gamma$ subtraction is 1%. This

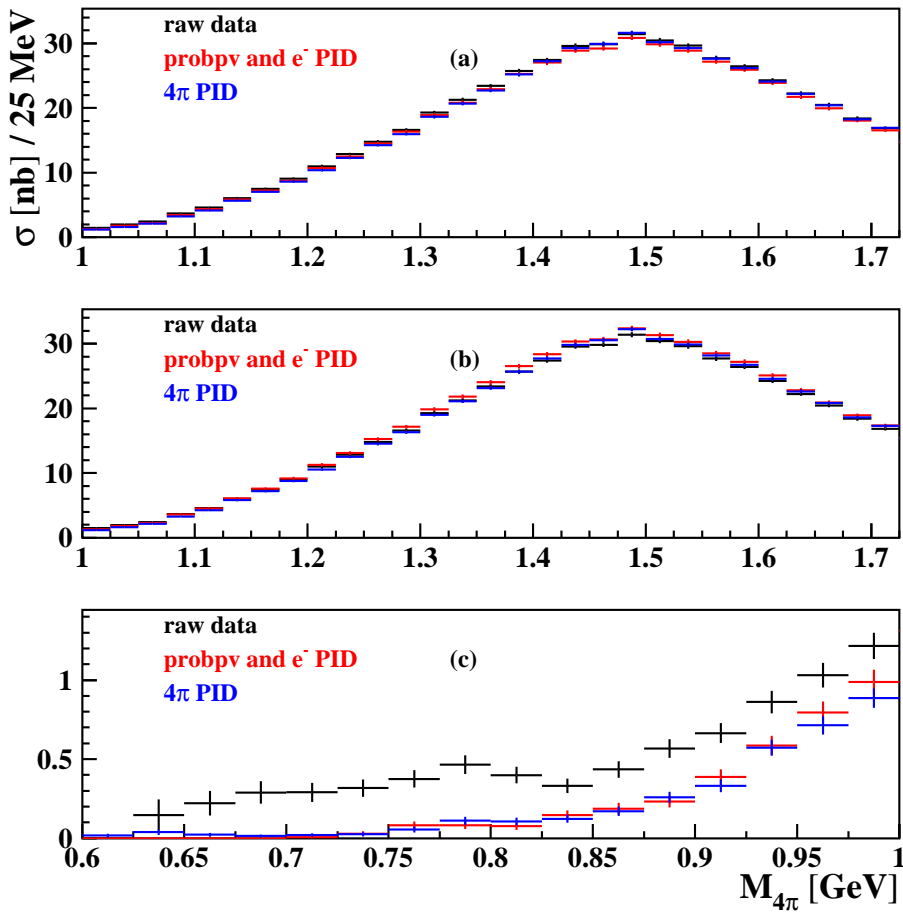


Figure 4.15: Cross section without and with two different electron vetoes in the $M_{4\pi}$ peak region (a). (b): Same distribution as (a) after correcting for MC-data difference of PID selector. (c): Result for cross section in the small invariant mass region after PID selector corrections.

uncertainty raises above $M_{4\pi} > 2.2 \text{ GeV}/c^2$ to up to 3% and 7% due to the increasing continuum contribution below $4 \text{ GeV}/c^2$ and $4.5 \text{ GeV}/c^2$ respectively.

In Fig. 4.17 (a) the χ^2 distribution for data and signal MC are shown after application of the described background vetoes and subtraction of the remaining background contributions. The difference of these distributions is displayed in Fig. 4.17 (b) and gives an estimate for the remaining background of approximately 55 events per bin. This difference can be explained due to uncertainties in the subtraction of the background channels $K^+K^-\pi^+\pi^-\gamma$ or $\omega\pi^+\pi^-\gamma$ as as previously described. In order to be conservative, it is assumed that the remaining tail is due to an additional uniform background contributions as a function of $\chi^2_{4\pi}$. In this case, the uncertainty on the cross section is below 0.4% for $M_{4\pi} < 2.8 \text{ GeV}/c^2$ and below 4.0% for $2.8 \text{ GeV}/c^2 < M_{4\pi} < 4.5 \text{ GeV}/c^2$.

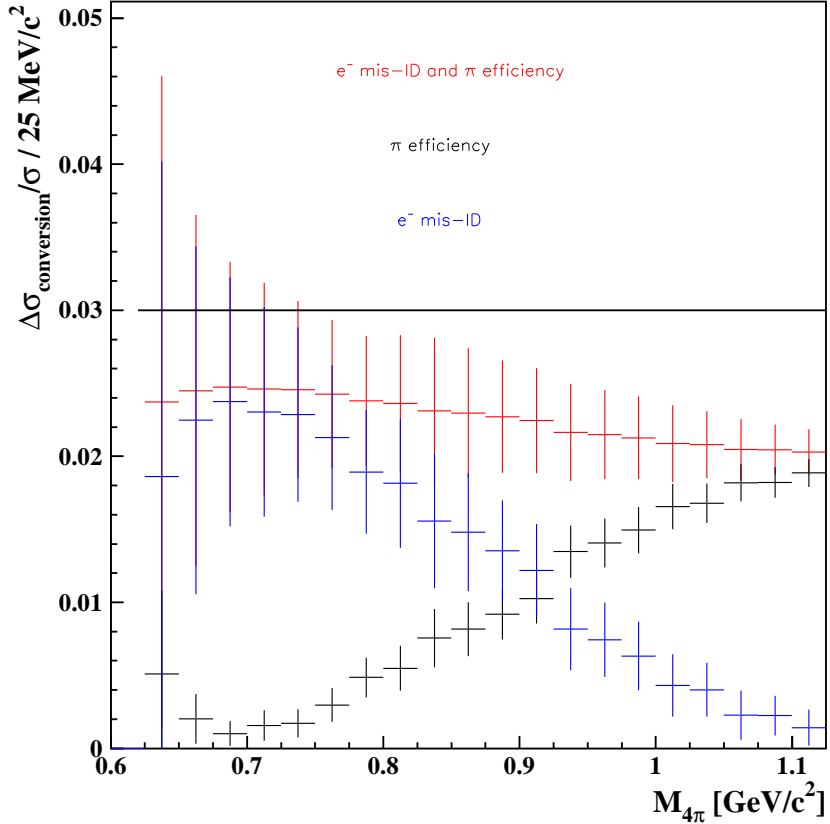


Figure 4.16: Systematic uncertainty in dependence of the invariant $M_{4\pi}$ mass due to the background suppression with the pion PID selector in the region $M_{4\pi} < 1.2 \text{ GeV}/c^2$. Variation of the cross section due to remaining conversion background (black) according to the electron as pion mis-ID rate and due to the efficiency difference in the pion selection (blue) and the sum of both effects (red).

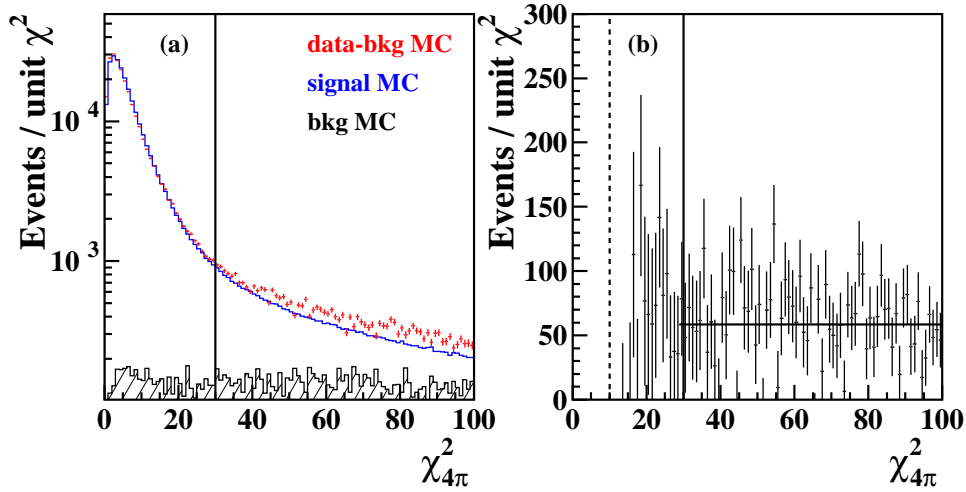


Figure 4.17: (a): The χ^2 distributions in the $\pi^+\pi^-\pi^+\pi^-$ hypothesis for data and signal MC simulation after background suppression. (b): Remaining difference between the distributions in (a).

4.4 Global Efficiency

The previously described selection and background suppression procedure is also applied to simulated signal MC. Fig. 4.18 (a) shows the invariant mass distributions from simulation for all generated signal events and the signal events that passed the event selection.

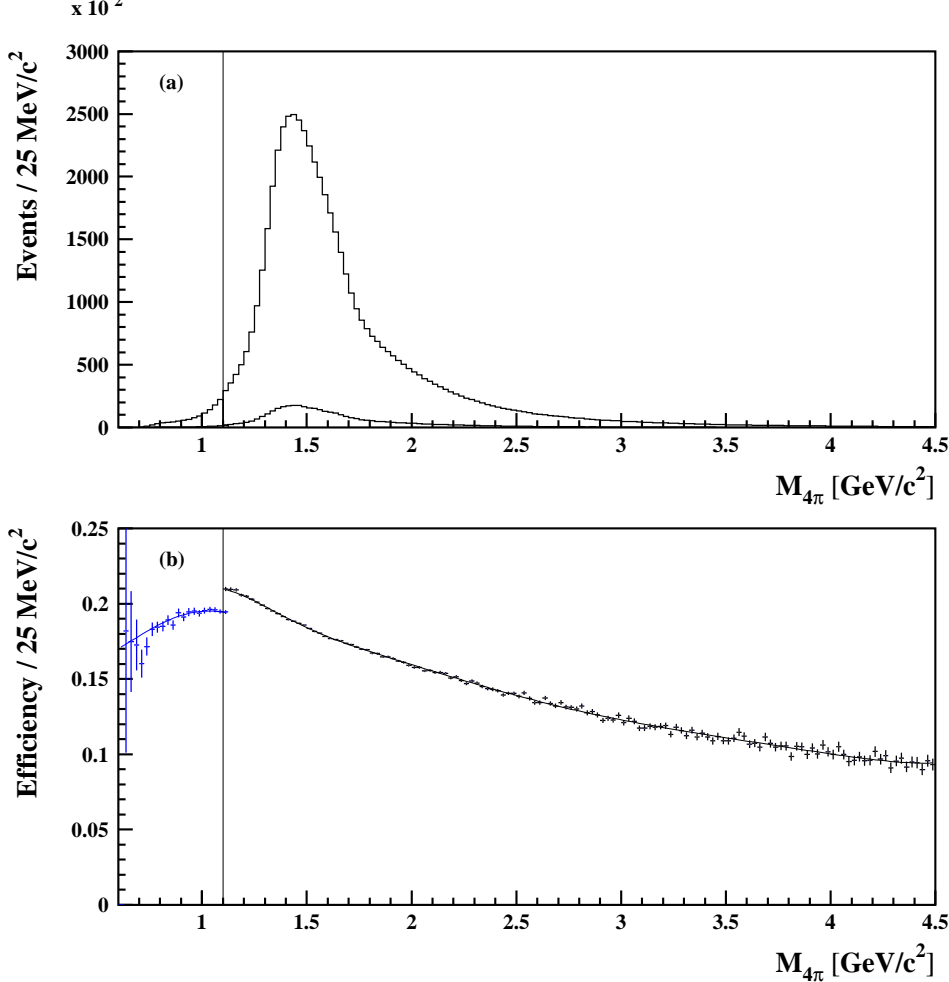


Figure 4.18: (a): The invariant mass $M_{4\pi}$ distribution from simulation for all generated signal events and events after final selection. (b): The resulting global efficiency vs. invariant mass $M_{4\pi}$ determined with simulation. Each line corresponds to a sum of a Gaussian and a polynomial fit. The vertical line at $M_{4\pi} = 1.1 \text{ GeV}/c^2$ separates the regions with and without π -PID requirement for the reconstructed tracks.

Fig. 4.18 (b) displays the distribution of the global detection and reconstruction efficiency, which is calculated as the ratio of selected $\pi^+\pi^-\pi^+\pi^-\gamma$ events to the number of generated events as a function of the invariant mass $M_{4\pi}$.

The influence of the individual requirements to the overall detection efficiency is shown in Table 6.1.

The usage of the ISRfilter and ISRselpass selectors removes almost 47% of the generated events. This is mainly due to the requirement on the photon with an energy of $E_{CMS} > 3 \text{ GeV}$: The simulation conditions are set for a wide ISR photon angular range $20^\circ < \theta_{\gamma,CMS} < 160^\circ$. An angle of 20° in the CM corresponds to approximately 11°

Requirement	N_{Events}	Fraction
All events	31706768	1
ISRfilter and Pass	17014876	0.537
$E_{lab} > 3 \text{ GeV}$	16806152	0.530
$N_{tracks} \geq 4$	10742561	0.339
Trigger & BGF	10727975	0.338
$Q_{tot} = 0$	10686431	0.337
Bhabha veto	10639690	0.336
$\chi_{4\pi}^2 < 30$	7001721	0.221
$0.35 \text{ rad} < \theta_\gamma < 2.4 \text{ rad}$	6747050	0.213
$0.5 \text{ rad} < \theta_\pi < 2.4 \text{ rad}$	5651529	0.178
$p_{t,\pi} > 0.1 \text{ GeV}/c$	5639186	0.178
$\Delta\psi > 1.0 \text{ rad}$	5580120	0.176
$N_{e^-} < 2$	5567618	0.1756
$K_s^0 K^\pm \pi^\mp$ veto	5507693	0.174
$K^+ K^- \pi^- \pi^-$ veto	5506874	0.174

Table 4.4: The number and fraction of events surviving various selection requirements in $\pi^+ \pi^- \pi^+ \pi^- \gamma$ simulation.

in the laboratory frame. Since most ISR photons are emitted at small polar angles, a large number of photons is therefore not detected because they have been emitted outside the detection region. The MC production is performed with $E_{CMS} > 3 \text{ GeV}$, however, the measured photon energy distribution has a tail due to the limited energy resolution towards low energies. Since also the true energy distribution increases towards low energies, many events are lost due to this energy requirement. The additional requirement $E_{lab} > 3 \text{ GeV}$ only has a small impact on the number of selected events.

Applying the requirement that the number of detected tracks is four or more is dominated by the angular requirement to keep all charged tracks in the well-understood region of the DCH and DIRC acceptance. As mentioned above, only events with $p_t > 0.1 \text{ GeV}/c$ for each track, close to the minimum DCH threshold, are accepted. Due to the very high efficiency of the *BABAR* trigger system (L1, L3, Bkgfilter) for signal events with four tracks and one high energetic photon, the resulting trigger and background filter inefficiency is in the sub-per mil level and thus negligible.

The $\chi_{4\pi}^2 < 30$ requirement decreases the number of events by approximately one third. All remaining requirements used to clean the data sample were discussed already above and result in a final overall efficiency of 17.4%. However, as can be seen in Fig. 4.18 the dependence on $M_{4\pi}$ has to be taken into account.

A MC model with the dominance of the $a_1(1260)^\pm \pi^\mp$ final state was used for simulation [95]. The $a_1(1260)^\pm$ mass and width were changed from $(M_{a_1} = 1.251 \text{ GeV}/c^2, \Gamma_{a_1} = 0.599 \text{ GeV})$ in the original code [95] to $(M_{a_1} = 1.33 \text{ GeV}/c^2, \Gamma_{a_1} = 0.57 \text{ GeV})$ as obtained

from a combined analysis of CLEO and CMD-2 data [106]. In the model used for the simulation, the $a_1(1260)$ is decaying to $\rho(770)^0\pi$. Due to theoretical expectations [95] (not yet confirmed by experiment) the model also includes the $f_0(1370)\rho$ final state.

The presence of other intermediate resonances with different spin structure in data is a possible source of systematic error for the cross section measurement. These resonances might lead to changes in the angular distributions of the charged tracks and therefore to a mis-calculated efficiency. A detailed study of these intermediate resonances is performed in Chapter 7. It is demonstrated that the influence on the efficiency is negligible.

Chapter 5

Systematic Corrections and Uncertainties

Thanks to the high luminosity delivered by PEP-II, the systematic uncertainties will dominate the precision of the $e^+e^- \rightarrow \pi^+\pi^-\pi^+\pi^-$ cross section measurement. It is therefore of utmost importance to understand the BABAR detector with high precision and fine tune the Monte Carlo simulation in order to minimize the systematic uncertainties.

The high integrated luminosity at *BABAR* allows the accumulation of approximately 280,000 measured $\pi^+\pi^-\pi^+\pi^-\gamma$ signal candidate events, which corresponds to the highest data sample of this channel ever collected. Therefore, especially in the peak region of the invariant mass, $1.2\text{ GeV}/c^2 < M_{4\pi} < 2.2\text{ GeV}/c^2$, the total uncertainty is dominated by systematic effects.

The energy and position of the ISR photon is measured with the EMC. In standard *BABAR* analyses, photons typically have energies smaller than 3 GeV, and the energy scale calibration focuses on these lower energetic photons. In the first part of this chapter, the fine tuning of the standard *BABAR* photon energy calibration and angular alignment for high energetic photons is presented. The second part focuses on the EMC photon reconstruction efficiency difference between data and simulation. In our particular final state, four charged particles are present. Thus, the track reconstruction efficiency of the tracking system and possible differences between data and simulation need to be determined. This measurement is described in the last part of this chapter.

5.1 Energy and Position Calibration of the EMC

Reconstructed quantities of the photons are an essential input for the kinematic fit of ISR analyses. Therefore a dedicated study to check the calibration of the photon energy and angles as well as the corresponding resolutions using the $\mu^+\mu^-\gamma$ final state has been performed. The two muon tracks are measured and used in a kinematic fit to predict the kinematic parameters of the ISR photon. Thus, the photon parameters are obtained using only tracking information from the SVT and DCH. To validate the kinematic fit, these predictions are compared in simulation to the true photon parameters. As a next step, the actually reconstructed position and energy values in the EMC are compared to the fit result for simulation and data. Hereby not only improved EMC-DCH alignment parameters, but in addition the energy and angular resolutions for data and simulation are obtained. This allows small corrections in data and a fine-tuning of MC.

5.1.1 Event Selection for $\mu^+\mu^-\gamma$

The primary ISR event selection as described in Section 4.1 is applied, with the modification that the minimum required measured ISR photon energy is reduced to 500 MeV. The following additional selection requirements have been chosen in order to filter out a clean $\mu^+\mu^-\gamma$ event sample:

- $N_{tracks} = 2$
- $\chi^2_{2\mu} < 5$
- $P_{V_{vertex}} > 0.01$
- $\text{PID}(\text{Track1}) = \text{PID}(\text{Track2}) = \mu$

- $|Z_{20}| > 0.82$
- $\theta_{\gamma,meas} > 0.31 \text{ rad}$
- $|\Delta\phi_\gamma| = |\phi_{\gamma,meas} - \phi_{\gamma,fit}| < 0.015 \text{ rad}$
- $|\Delta\theta_\gamma| = |\theta_{\gamma,meas} - \theta_{\gamma,fit}| < 0.015 \text{ rad}$

The vertex probability P_{vertex} requirement ensures that both tracks are emitted from a common vertex. The muon PID selector is a standard *BABAR* tool, combining information from several sub-detectors in a maximum likelihood fit. The Zernike moment Z_{20} is related to the shower shape of the neutral cluster which in addition needs to be located at polar angles $\theta_{\gamma,meas} > 0.31 \text{ rad}$, corresponding to the efficient detection region of the EMC. The $|\Delta\phi_\gamma|$ and $|\Delta\theta_\gamma|$ requirements lead to an additional reduction of background events as well as events with additional radiation.

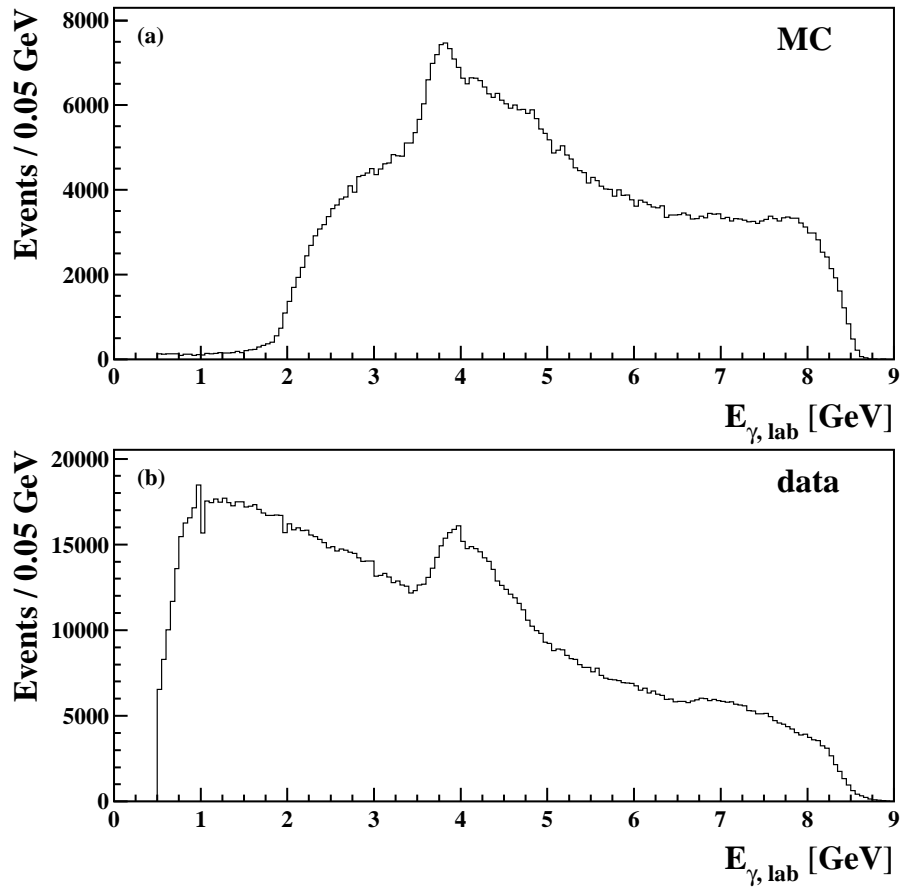


Figure 5.1: Measured ISR photon energy distribution in the laboratory system $E_{\gamma, \text{lab}}$ in the $\mu^+\mu^-\gamma$ event sample for simulation (a) and data (b).

Figure 5.1 compares the ISR photon energy distributions measured in the laboratory system for the data and the MC simulation. The $\mu^+\mu^-\gamma$ simulation is produced with a minimal energy for the ISR photons in the CM system of $E_{\gamma, \text{CM}} > 3 \text{ GeV}$ on generator

level. Thanks to the asymmetric beam energies of PEP-II this study is feasible in the energy region $2 \text{ GeV} < E_{\gamma,lab} < 8 \text{ GeV}$ with good statistics for the given simulation sample. In the energy range $1 \text{ GeV} < E_{\gamma,lab} < 2 \text{ GeV}$, a low statistics sample is still available, whereas for lower energies, the study is not feasible with the simulated sample of events.

The observed structure in the MC spectrum is due to this energy requirement, the PEP-II boost and the fact that ISR photons are preferably emitted in the direction of flight of the mother particle. In simulation, the positron emits photons in the energy range $3 \text{ GeV} < E_{\gamma,CM} < 5.3 \text{ GeV}$, preferentially in opposite direction of the boost vector ($\beta\gamma = 0.56$). Thus, the peaking structure at $3.5 \text{ GeV} < E_{\gamma,lab} < 4.0 \text{ GeV}$ is produced by the highest energetic photons emitted by the positrons which are boosted towards lower energies. The ones with low CM energy at small polar angles form the tail towards lower energies down to $E_{\gamma,lab} < 2.0 \text{ GeV}$. The very small tail at $E_{\gamma,lab} < 2.0 \text{ GeV}$ is due to not properly reconstructed photons. The photons emitted from the electrons, preferentially in the direction of the boost, end up with energies as high as $E_{\gamma,lab} = 8.5 \text{ GeV}$. The structure in data is similar with additional entries at low energies due to the fact that photons with $E_{\gamma,CM} < 3.0 \text{ GeV}$ are present.

5.1.2 Consistency Check of Kinematic Fit with Simulation: Angles and Energy

The accuracy of the prediction of the photon parameters obtained in the kinematic fit is studied by comparison with the generator-level (or true) information. In order to study energy dependent effects the sample is subdivided into eight 1 GeV wide energy regions between 1 GeV and 9 GeV.

Consistency of Photon Angles

Figure 5.2 (top) displays the average differences between the measured azimuthal photon angles $\phi_{\gamma,meas}$ on the one hand and the true angles $\phi_{\gamma,true}$ as well as the calculated ones in the kinematic fit $\phi_{\gamma,fit}$ on the other hand. The distributions $\phi_{\gamma,meas} - \phi_{\gamma,true}$ and $\phi_{\gamma,meas} - \phi_{\gamma,fit}$ are shown in Fig. 5.2 (a) for low energetic photons ($3.0 \text{ GeV} < E_{true,lab} < 4.0 \text{ GeV}$) and in (b) for high energetic photons ($7.0 \text{ GeV} < E_{true,lab} < 8.0 \text{ GeV}$). The corresponding distributions for the polar angles θ_{γ} are shown in Fig. 5.2 (c) and (d). In general, these angular distributions show shifts of about 0.001 rad or smaller. In Fig. 5.2 (a) a small shift of less than 0.0005 rad is observed. This corresponds to a slight rotation of the EMC with respect to the DCH. Figure 5.2 (b) shows that this shift slightly increases for high energetic photons. Due to the boost, these photons are emitted towards the very forward directions (EMC end-cap) at small polar angles. Therefore, the observed small increase in shift of more than 0.0005 rad seen for high energetic photons in Fig. 5.2 (b) corresponds to a slightly larger rotation of the EMC end-cap relative to the DCH. All observed shifts of less than 0.001 rad are, however, a very small effect in comparison to the angular resolutions as will be shown in the following. This self-consistent check shows the power of this method: The EMC-DCH alignment can be studied with a precision of

better than 0.001 rad. These plots also demonstrate that the EMC-DCH alignment in simulation is almost perfect, as expected.

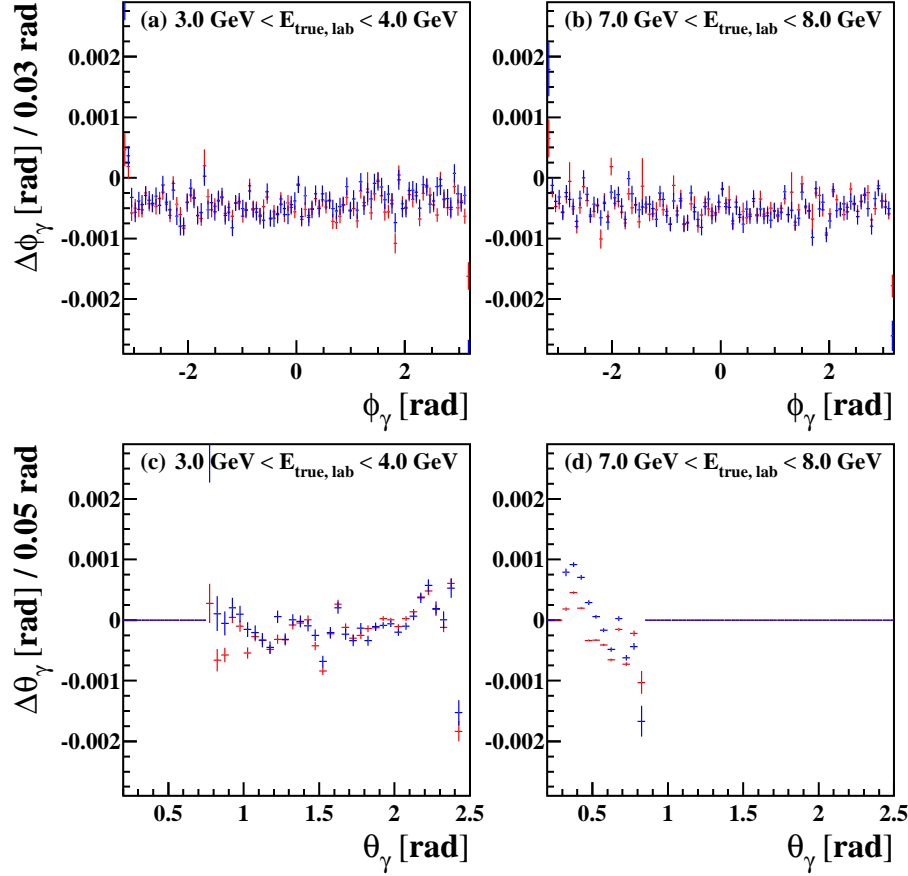


Figure 5.2: Top: Azimuthal misalignment shift vs. azimuthal angle in simulation: $\phi_{\gamma,meas} - \phi_{\gamma,true}$ (red) and $\phi_{\gamma,meas} - \phi_{\gamma,fit}$ (blue). These distributions are shown for $3.0 \text{ GeV} < E_{true,lab} < 4.0 \text{ GeV}$ (a) and $7.0 \text{ GeV} < E_{true,lab} < 8.0 \text{ GeV}$ (b) in the laboratory system. Bottom: Corresponding polar misalignment shift vs. polar angle.

For the same energy slices, the angular resolution of the ISR photon is investigated in Fig. 5.3. The red histograms are the resolutions calculated as the difference between reconstructed and true values of the angle of the photon; the blue histograms are resolutions relative to the calculated ones from the kinematic fit. The lines represent a single Gaussian fit. A double Gaussian fit would lead to a better fit result, with approximately 10% contribution from the wider Gaussian. In the kinematic fit, however, probability density functions (PDFs) corresponding to a single Gaussian resolution are used. Therefore, the parameters for the single Gaussian approximation are extracted.

As expected, the angular resolution obtained from the 1C fit is always worse than the true EMC resolution. The obtained resolutions (i.e. widths of the Gaussian distributions) are summarized in Figs. 5.3 (right). A better polar angle resolution for the high energy photons compared to lower energies is also observed. This is due to a geometrical effect, namely the increasing distance between the IP and the EMC.

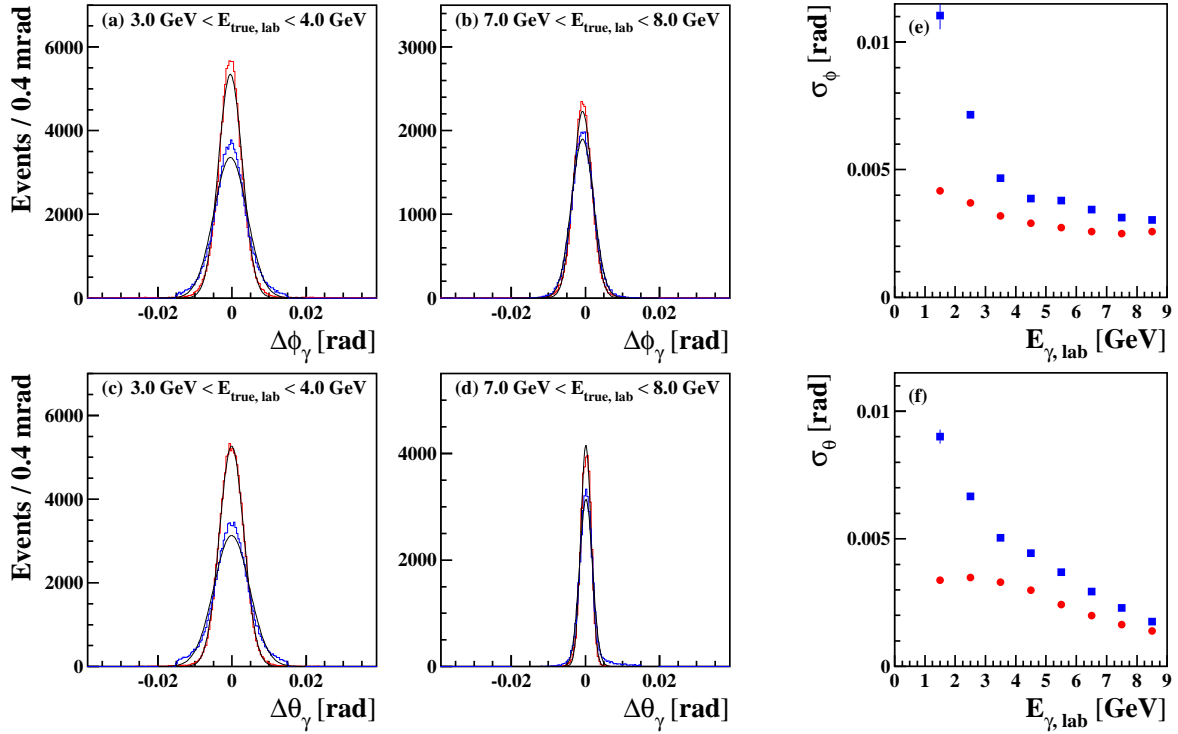


Figure 5.3: Left: Azimuthal angle resolution for 3-4 GeV (a) and 7-8 GeV (b) photons in MC. Corresponding distributions for the polar angle (c) and (d). Red: true resolution, blue: with the additional uncertainties from the kinematic fit. e: Azimuthal angular fit parameters (for single Gaussian fit) for the EMC response of MC events relative to the true (red) and the 1C fit values (blue); f: corresponding distribution for the polar angle.

Consistency of Photon Energy

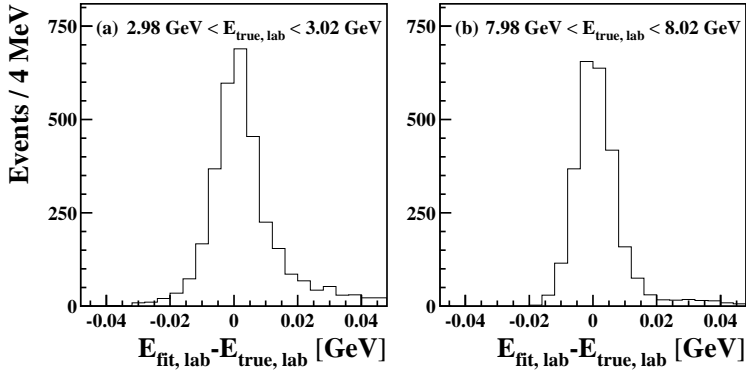


Figure 5.4: Difference of energies calculated in the kinematic 1C fit and true MC energies for 3 GeV and 8 GeV photons.

In order to study the energy resolution of the kinematic fit prediction of the ISR photon, small, ± 20 MeV wide energy slices around 3 GeV and 8 GeV are created to study the EMC-energy response.

For these events, Fig. 5.4 shows the difference between the fitted and the true energy of

the ISR photon. The kinematic fit prediction agrees with the true energies to an accuracy of approximately $10 - 15$ MeV. The small tails on the right hand side of the distributions are due to extra soft photon radiation, which is not included in the kinematic fit. The fit associates the extra energy to the ISR photon and predicts a higher energy. This small effect is not completely suppressed by the requirement $\chi^2_{2\mu} < 5$.

The ± 20 MeV slices are smaller than the EMC resolution. Similar to the angular study, the obtained energies after the full reconstruction procedure are considered as the EMC response. Figure 5.5 shows the EMC response for the different photon energy regions.

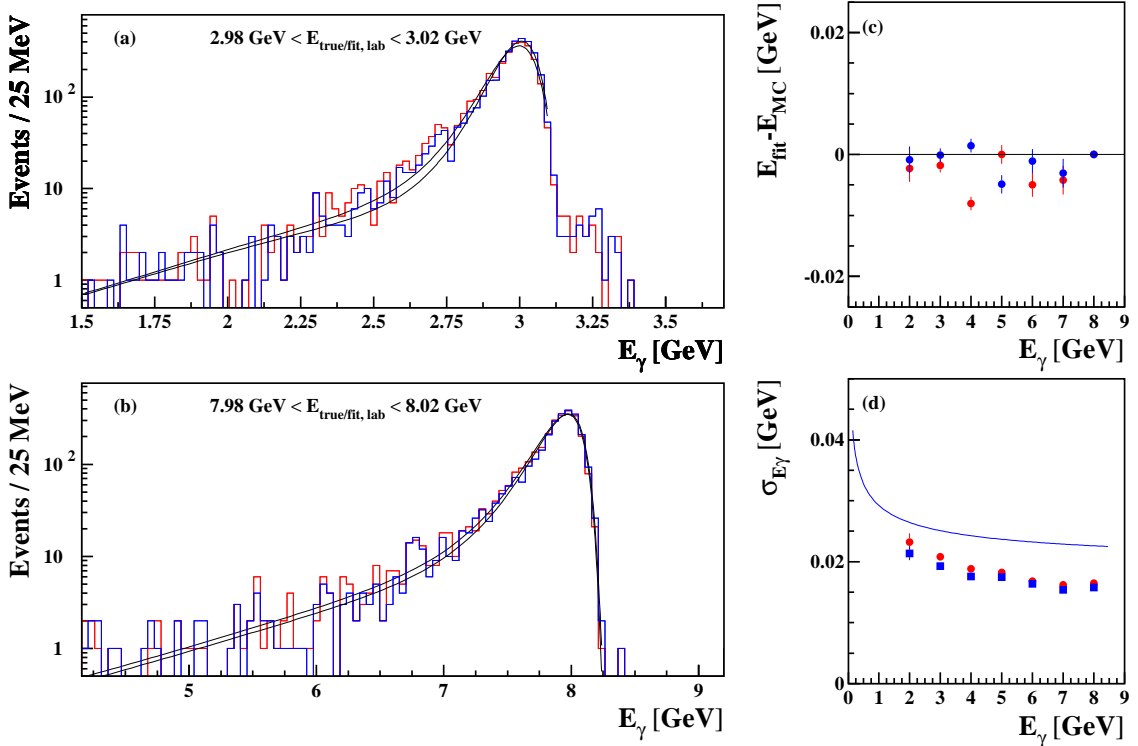


Figure 5.5: Left: Reconstructed energy in the EMC for 40 MeV wide energy slices according to MC true (blue) and fit prediction (red). Fit performed with the asymmetric “Novosibirsk” function. Right: Energy (c) and energy resolution (d) for the EMC response relative to true (blue) and kinematic fit values (red). The line is the “official” [80] *BABAR* resolution $\sigma_E/E_\gamma = \sqrt{(0.023/E_\gamma^{0.25})^2 + 0.018^2}$

An asymmetric tail at low energy is present due to shower leakage. This energy response shape is relatively well described by a PDF as suggested by the Novosibirsk group:

$$P(e_\gamma) = \frac{N_0}{\sqrt{2\pi}\sigma(e_0 - e_\gamma)} \cdot \exp\left(-\frac{Z^2}{2\sigma^2}\right), \quad (5.1)$$

where $e_\gamma = E_\gamma/E_0$, E_γ is the measured and E_0 the true photon energy, e_0 the asymmetry (or cut-off), Z and σ are determined as:

$$Z = \ln \frac{e_0 - e_\gamma}{e_0 - e_{\max}} - \sigma^2 \quad (5.2)$$

$$B_0 = \frac{2.35 \cdot (\sigma_{EMC}/E_\gamma)}{2(e_0 - e_{max})} \quad (5.3)$$

$$\sigma = \frac{1}{\sqrt{2 \ln 2} \cdot \ln(B_0 + \sqrt{1 + B_0^2})}, \quad (5.4)$$

and e_{max} corresponds to the peak value. By definition $\sigma_{EMC} = \text{FWHM}/2.35 \cdot E_0$ is correlated to e_0 . The parameter e_{max} is strongly correlated with E_0 and must be fixed during the fitting procedure at a value close to unity to provide the correct E_0 . The important feature of this function is that the PDF is a Gaussian relative to the parameter Z. Therefore, it can be used in the kinematic fitting programs which assume Gaussian distributions for the parameters. Small deviations between simulation and the “Novosibirsk” function are visible. It has an energy cut-off at $E = e_0 \cdot E_0$, whereas the experimental distributions have some statistical tails towards larger energies. In the limit of $e_0 \gg e_{max} \approx 1$, this PDF becomes symmetric and Gaussian.

This function is used to fit EMC responses for 3 GeV and 8 GeV photons selected by ± 20 MeV slices in the true energy or in the calculated from 1C fit. In both cases the distributions are practically identical. The results of the fits with five free parameters (e_{max} fixed at 0.9975) are shown in Fig. 5.5. For a better description of the tails, which correspond to true photon energies, not background, the PDF is modified by varying the asymmetry parameter as $e_0 = e_{00} + p_6 \cdot (e_\gamma^9 - 1)$. The power of 9 allows to keep e_0 constant at $e_\gamma \approx 1$ and $e_\gamma < 1$ but to increase rapidly at $e_\gamma \approx e_0$. This modification gives an excellent fit of the simulated distributions, including the long tails at low energies, as presented in Fig. 5.5 (a) and (b).

Fig. 5.5 (c) and (d) show the fit parameters as a function of the energy in case of the EMC true response and the EMC response obtained from the 1C fit. The energy prediction of the kinematic fit (E_0) agrees within 10 MeV with the true values in simulation as well as with the measured energy. In addition, the resolutions agree within approximately 1 MeV. Therefore, in the energy region above 2 GeV the kinematic fit method can be used to obtain the measured EMC energy and resolution. It is also seen that the present simulation has a better resolution in comparison to the “official” *BABAR* values as illustrated by the line in Fig. 5.5 (d). This is corrected by performing an additional Gaussian spread to simulation as will be shown in more detail in the following Fig. 5.7.

5.1.3 EMC Energy Calibration and Alignment

The DCH has small systematic uncertainties related to the momentum and angle calibration for charged tracks. As seen in Section 5.1.2, the predictive power of the kinematic fit, which relies on the DCH parameters, is very strong. Thus, the values calculated in the kinematic 1C fit for the ISR photon can be used to check the EMC energy calibration as well as the alignment of the EMC relative to the DCH. In Fig. 5.1 (b) the energy of the ISR photons is shown for $\mu^+ \mu^- \gamma$ events in data. The selection of $E_{\gamma,CM} > 0.5$ GeV is used and in principle photons in the range $1 \text{ GeV} < E_{\gamma,lab} < 9 \text{ GeV}$ can be studied. The statistics of the simulation sample for photons in the energy range $1 \text{ GeV} < E_{\gamma,lab} < 2 \text{ GeV}$ is, however, not sufficient for a detailed study (Fig. 5.1 (a)).

EMC Alignment

The EMC is composed of a barrel and an end-cap component (see Section 2.2). On the one hand, there is the possibility of a misalignment between these two EMC detector-units, on the other hand, time-dependent misalignment might occur most likely due to works on the detector between the Run periods. Thus, this alignment study is performed separately for both EMC components and the six Run periods. The method is based on comparing the prediction of the kinematic fit of the polar and azimuthal angles to the actual EMC photon cluster position. Not only possible misalignment between the EMC components relative to the DCH is investigated, but also the photon angular resolutions in the simulation and the data.

In general, a deviation between the prediction of the kinematic fit and the measurement in the azimuthal angle corresponds to a rotation of the EMC relative to the DCH. A sinusoidal behavior is related to a displacement in the x-y-plane. Displacements in the z-direction result to first order in a shift of the polar angles.

Figure 5.6 shows the differences in the cluster angles obtained from the EMC response and from the kinematic fit for Run 5 (a-f) and Run 6 (g-l) as a function of the corresponding angles. The azimuthal angular differences in the barrel are displayed in the top, the azimuthal differences in the end-cap in the middle, and the polar angular differences in the bottom.

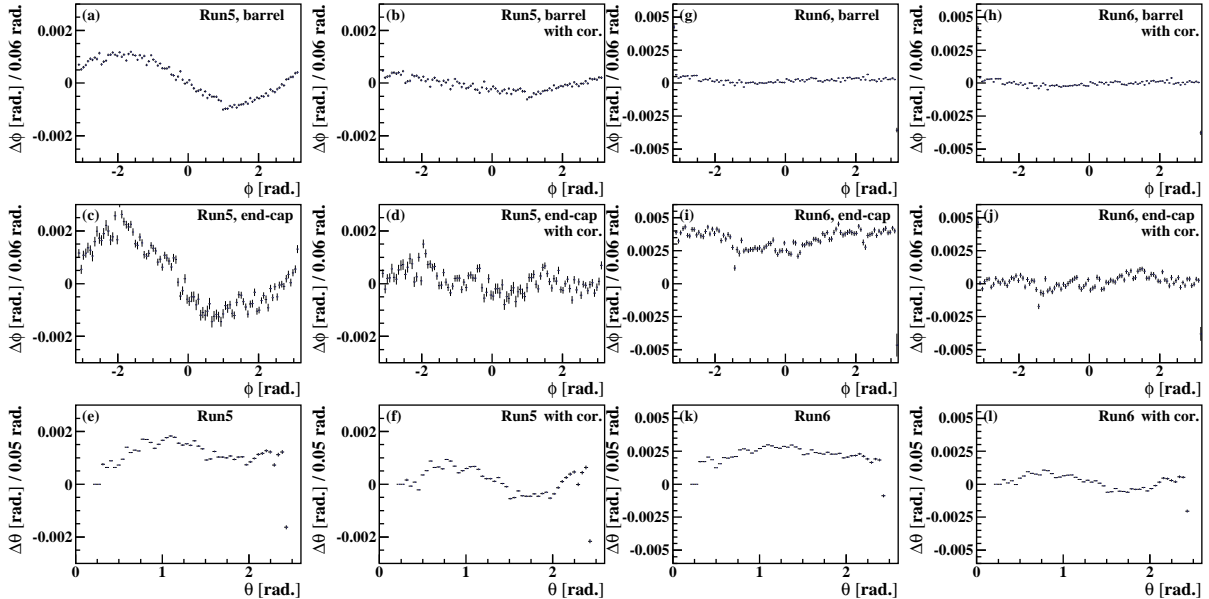


Figure 5.6: Left: Azimuthal and polar angle shifts vs. angles in Run 5 (a-f) and Run 6 (g-l). EMC barrel (top) and end-cap (middle) are studied separately. The results are shown with the standard *BABAR* misalignment parameters and with additional fine-tuning corrections.

A sinusoidal behavior in combination with a shift is visible in the azimuthal distributions (a) and (c) for Run 5. Therefore in the barrel (a) as well as in the end-cap (c) a small x-y

displacement in addition to a rotation is present. The shift in the polar angular distribution (e) reflects an additional shift in z-direction. Performing a fine-tuning of the EMC cluster position leads to the corresponding distributions (b), (d) and (f) with deviations of less than 1 mrad. In Run 6 a comparatively large deviation of 4 mrad is observed in the end-cap (i) and corrected (j). An additional small correction in z-direction is applied, transforming the small deviation of 2-3 mrad in the polar angle in (k) to an agreement within 1 mrad (l). The deviations for Runs 1-4 are in the same order of magnitude as or smaller than in Run 5 and also corrected for.

A fit with a single Gaussian distribution is used to describe the observed deviations of the measured angles and the ones obtained from the kinematic fit by the same way as shown in Fig. 5.3. The extracted fit parameters for the EMC response is shown in Fig. 5.7. The EMC response in simulation relative to the true information (red) and the kinematic fit prediction (blue) are displayed. Also indicated is the EMC response in data relative to the kinematic fit prediction for Runs 1-6 (other colors). The line shows the “official” EMC angular resolution [85]: $\sigma_{\phi,\theta} = \sqrt{(4.16)^2/E_\gamma(\text{GeV})}$ mrad. The true resolution of simulation agrees with the “official” resolution within 1 mrad. The resolution based on the kinematic fit prediction of simulation agrees nicely with the data. Thus, it can be summarized that the EMC angular resolutions are well described by the MC simulation.

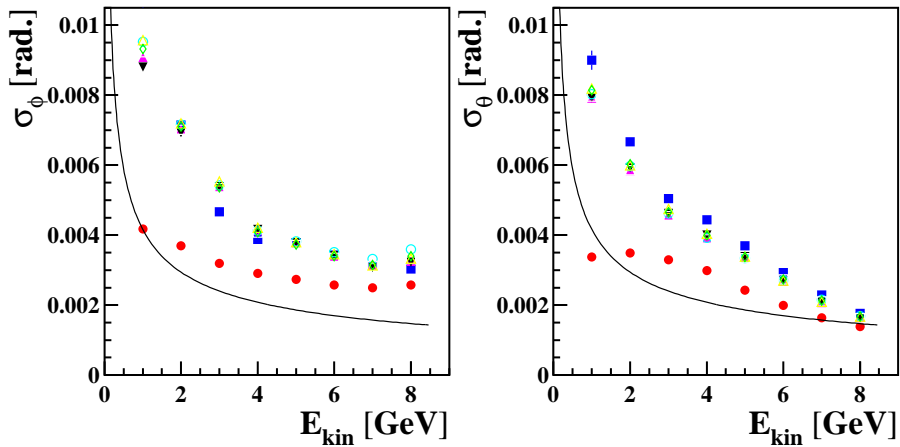


Figure 5.7: Azimuthal (left) and polar (right) angle fit parameters (single Gaussian fit) for the EMC response relative to true simulation information (red) and kinematic fit values of simulation (blue) and Runs 1-6 (all other colors). The line shows the “official” EMC angular resolution [85]: $\sigma_{\phi,\theta} = \sqrt{(4.16)^2/E_\gamma(\text{GeV})}$ mrad

The observed resolution is 3-4 times wider than the residual mis-alignment after all alignment corrections. It is seen, that after the standard *BABAR* alignment, a small level of misalignment remained especially for the Run 6 data taking period and is corrected. The alignment is improved.

Calibration of Photon Energy

In Section 5.1.2, the EMC energy response in simulation is investigated by selecting ± 20 MeV energy slices in the true MC energy. It was demonstrated that the fit prediction agrees within 10-15 MeV with the true information of simulation (Fig. 5.4). This enables us to perform the same check in data by selecting small energy slices around the kinematic fit predictions. The energy response is shown for ± 20 MeV energy slices around 3 GeV and 8 GeV for data and simulation in Fig. 5.8 and two different running periods, Run 1 and Run 5. The fit is performed to data according to function(5.1) and represented by the black line.

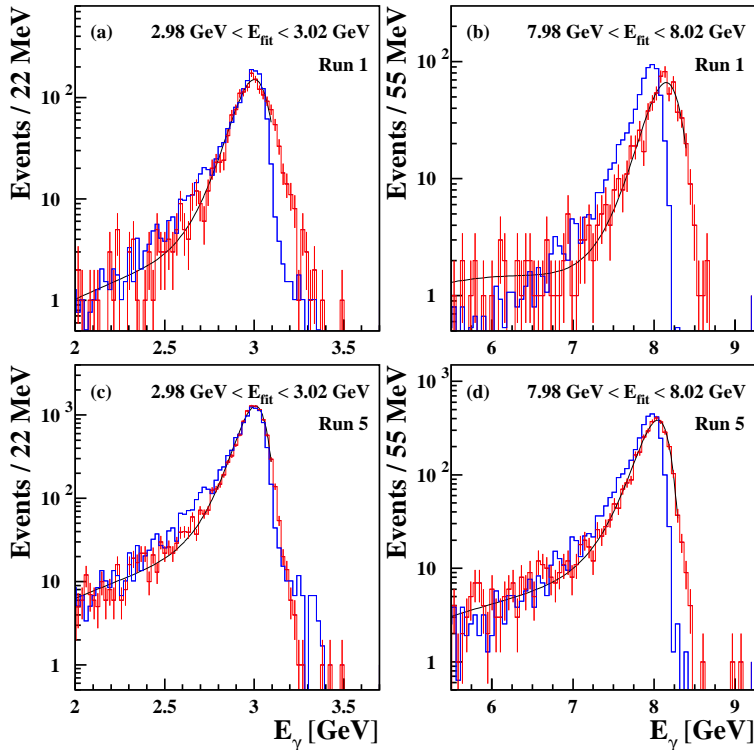


Figure 5.8: EMC energy response for 3 GeV (a) and 8 GeV (b) photons in the Run 1 data taking period. The corresponding distributions for Run 5 are displayed in (c) and (d). The fit is performed with a function according to equation 5.1.

It is seen in Fig. 5.8 (c) and (d) that for Run 5, the simulation is in good agreement with data, except for small shifts in the photon energy and differences in the resolution, which is small but visible. Run 1 data, however, demonstrates significantly different behavior. A clear discrepancy in shape and position is visible. These results are summarized in Fig. 5.9 for the difference of the energy prediction of the kinematic fit to the energy result of the fit to the EMC energy response according to equation 5.1. The results for simulation (blue), Run 1 data (red) and all other data (other colors) are shown. Runs 2-6 show a similar behavior with small shifts of up to 50 MeV for the energy response of the most energetic photons. A shift of almost 150 MeV is observed for the most energetic photons in Run 1. In Fig. 5.9 (b) the corresponding resolutions are displayed. Again a different behavior for Run 1 and Runs 2-6 is present. The “official” *BABAR* resolution

function [80]

$$\sigma_E/E_\gamma = \sqrt{(0.023/E_\gamma^{0.25})^2 + 0.018^2} \quad (5.5)$$

is also displayed. The present data is better described by the functions

$$\sigma_E/E_\gamma = \sqrt{(0.040/E_\gamma^{0.25})^2 + 0.012^2} \quad (\text{Run 1}) \quad (5.6)$$

and

$$\sigma_E/E_\gamma = \sqrt{(0.027/E_\gamma^{0.25})^2 + 0.010^2} \quad (\text{Runs 2 - 6}) \quad (5.7)$$

and the simulation by

$$\sigma_E/E_\gamma = \sqrt{(0.025/E_\gamma^{0.25})^2 + 0.009^2}. \quad (5.8)$$

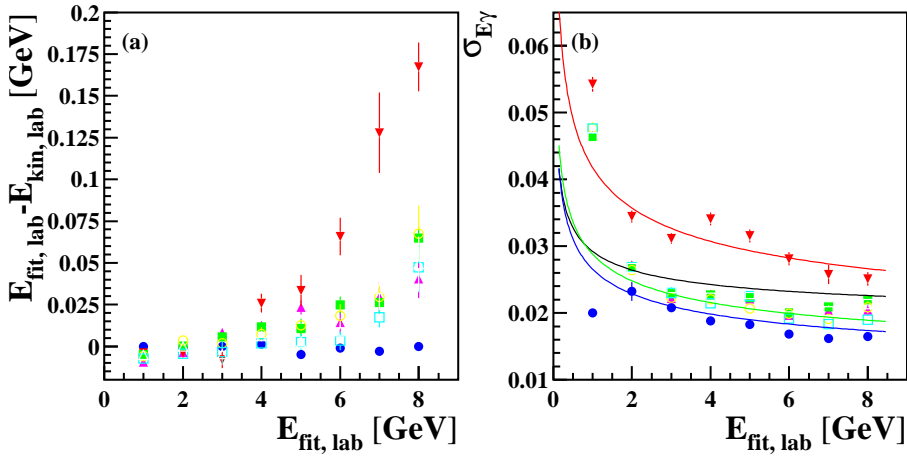


Figure 5.9: Deviation from the kinematic fit prediction for the energy and the EMC response fit (a). The corresponding resolution in (b). Simulation (blue), Run 1 (red points), Runs 2-6 (all other points). The Fit is performed with the asymmetric Novosibirsk function. The official *BABAR* resolution is represented by the black line. The additional lines are an estimate for the measured resolution in data for Run 1 (red) and Runs 2-6 (green) and in simulation (blue).

The obtained parameters allow to apply corrections for the photon energies in data according to the deviations observed in Fig. 5.9 (a). An additional Gaussian spread for the measured energy is applied to simulation in order to compensate for the small resolution difference seen in Fig. 5.9 (b). The results after these small additional calibration is shown in Fig. 5.10. It displays EMC response for data and simulation after the applied energy shifts to data and the extra Gaussian spread to MC. A relatively good agreement is seen.

5.1.4 Use of Photon Parameters in the Kinematic Fit

This study shows that the constrained kinematic based on energy-momentum conservation is a powerful tool for the event selection in ISR-events. However, small corrections to the standard *BABAR* EMC calibration and alignment should be applied. Including

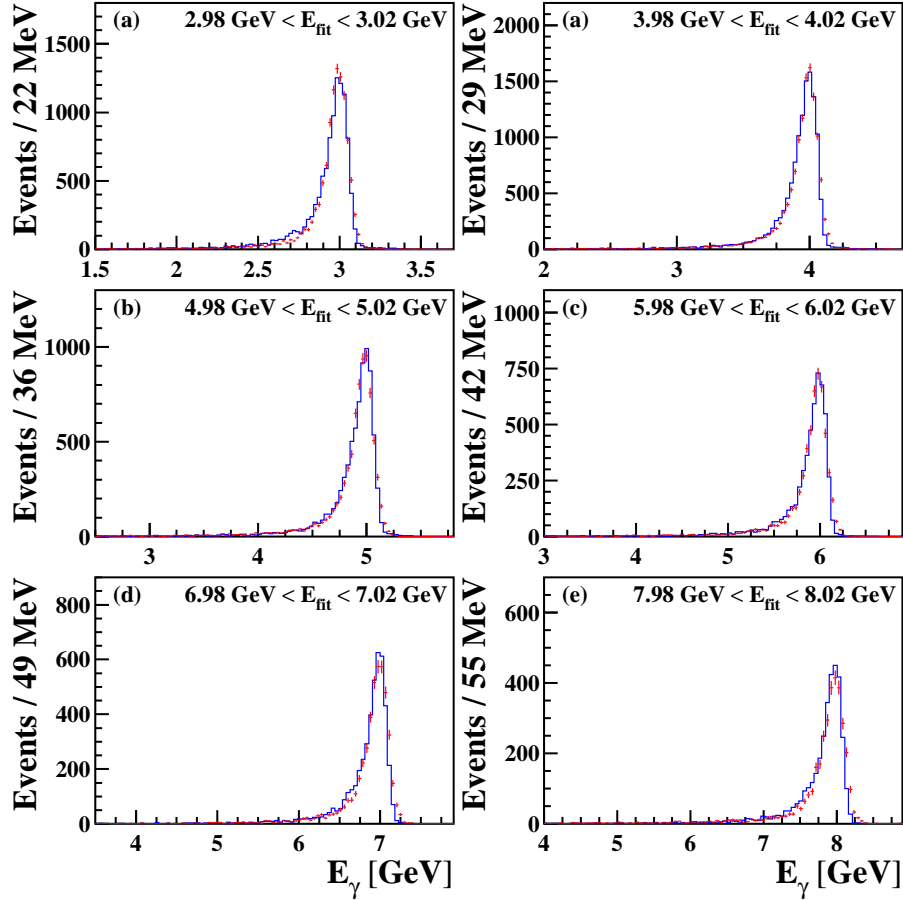


Figure 5.10: EMC energy response for 3 GeV, 5 GeV and 8 GeV photons in Run 5 for data (red) and simulation (blue) after all corrections. An energy shift is applied to data as well as an additional Gaussian spread to MC.

the photon parameters into the constrained fit becomes even more important for multi-photon events. It is demonstrated how the EMC response should be corrected for photons in data and simulation in order to obtain a better agreement. After the EMC-DCH misalignment correction for data the angular resolutions in data and simulation were found to be almost identical and the approximation $\sigma_{\phi,\theta} = \sqrt{(0.0045)^2/E_\gamma + (0.0015)^2}$ rad can be used in both cases.

There exist additional complications if the photon energies are used in the fit. The photon energy resolution is better in simulation compared to both Run 1 and Runs 2-6. An additional Gaussian smearing is applied to simulation with different widths for Run 1 and Runs 2-6 according to Fig. 5.9 (b). Fig. 5.9 (a) shows the necessary photon energy correction in Run 1 and Runs 2-6.

After the described corrections are applied the functions

$$\sigma_E/E_\gamma = \sqrt{(0.027/E^{0.25})^2 + 0.010^2} \quad (5.9)$$

for the energy resolution of Runs 2-6 and

$$\sigma_E/E_\gamma = \sqrt{(0.040/E^{0.25})^2 + 0.012^2} \quad (5.10)$$

for Run 1 provide a similar description of the photons in data and MC. However, some events would be rejected through the kinematic fit due to the very asymmetric response of the EMC.

Therefore the “Novosibirsk” function (equation 5.1) needs to be used in the kinematic fit, which has a normal Gaussian form relative to Z . Instead of the photon energy E_0 the fit parameter $e_{as} = \ln \frac{e_0 - e_\gamma}{e_0 - e_{max}}$ is used with the input value $e_{as} = 0$. In the equation for the energy-momentum conservation the true photon energy should be calculated as:

$$E_0 = \frac{E_\gamma}{e_{max} + (e_0 - e_{max}) \cdot \exp(e_{as} + \sigma^2)}. \quad (5.11)$$

In our case, after the correction, E_γ is the measured photon energy, $e_{max} = 1.0$ and e_0 is calculated via the obtained resolution parameters as described in the previous section.

The influence of the corrections on a typical ISR analysis has been checked with the $e^+e^- \rightarrow K^+K^-\pi^0\gamma \rightarrow K^+K^-3\gamma$ analysis. The corrections have been applied to all photons in the final state. Fig. 5.11 (left) shows the χ^2 distributions obtained in the 4C fit for the $4\pi\pi^0\gamma \rightarrow 4\pi 3\gamma$ MC events. All information from the three photons is included in the fit. The distributions with and without the described correction procedure are displayed. Using the requirement $\chi^2 < 50$, approximately 10% more events are selected with the asymmetric PDF and all corrections described above. This demonstrates that the correction procedure works as intended.

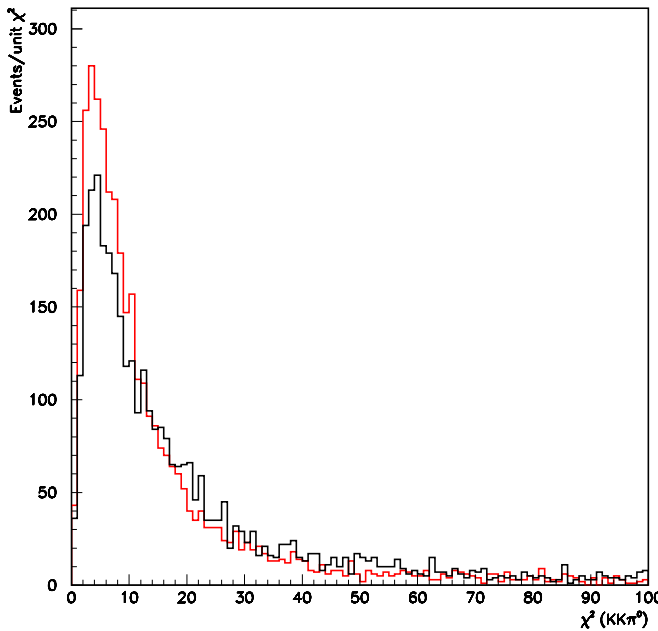


Figure 5.11: Comparison of χ^2 distributions obtained in the 5C kinematic fit for $K^+K^-\pi^0\gamma \rightarrow K^+K^-3\gamma$ data with the standard *BABAR* parameter error matrix used for the fit (black) in comparison to the result with corrected photon parameters and the asymmetric photon PDF (red).

5.2 Photon Efficiency

In Section 5.1, the EMC energy calibration and alignment were performed in order to optimize the agreement of the photon parameters between simulation and data. Differences in the photon reconstruction efficiency have a direct influence on the measured cross section and therefore need to be understood with high precision.

Initial State Radiation photons are produced at all angles relative to the collision axis. They are, however, emitted with a high probability close to the direction of flight of the emitting particle. This leads to an acceptance of approximately 10-15 % for ISR photons at *BABAR*. It is essential, not only for this analysis, but also for other *BABAR* analyses to know the reconstruction efficiency and in particular the difference in reconstruction efficiency between data and simulation for photons that have been emitted into the good detection region of the *BABAR* detector.

Similar to the EMC energy calibration and alignment studies, the photon inefficiency is measured with a $\mu^+\mu^-\gamma$ sample. The most important difference in the event selection in comparison to the cross section study is to not explicitly require the photon in the final state. The basic principle of the measurement is to predict the photon from the momenta and energies of the detected tracks of the two muons and the beam parameters, very similar to the method used for the EMC calibration in Section 5.1. This prediction is performed by a kinematic fit using energy and momentum conservation as four constraints. The energy and momentum of the ISR photon is not included in the kinematic fit. Imposing that the photon is massless leads to one remaining constraint (1C). The predictions of this 1C kinematic fit for the energy and momentum of the photon for each event can be compared to the actual measured photon. The photon inefficiency η in an arbitrary phase space volume element $\Delta\mathcal{V}$ is defined according to the following equation:

$$\eta = \frac{N_{ev, \text{no matched } \gamma}(\Delta\mathcal{V})}{N_{ev}(\Delta\mathcal{V})} \quad (5.12)$$

A sensible choice of variables to describe the phase space \mathcal{V} are the polar and azimuth angle of the photon θ_γ and ϕ_γ , and its energy E_γ . The study is performed separately for the barrel and end-cap components of the EMC. In the following the event selection with a focus on the difference to the selection in Section 5.1 is presented. The applied efficiency determination method is explained and the photon inefficiency and its difference between data and simulation are shown.

5.2.1 Event Selection

The study is performed with data collected “on” as well as “off” the $\Upsilon(4S)$ resonance, resulting in a total integrated luminosity of 454.4 fb^{-1} . Essentially, the same selection as described in Section 5.1 is applied, with the modification that no high energetic photon is required. The difference in momenta of the incoming beams and the sum of all tracks gives a first estimate of the missing momentum \vec{p}_{miss} . In order to decrease the amount of data to be processed, the following loose requirements have to be fulfilled:

- $|\vec{p}_{miss}| > 200 \text{ MeV}/c$
- $0.2 \text{ rad} < \theta_{miss} < 2.9 \text{ rad}$

Photon candidates are neutral clusters with a minimum measured energy of $E_{\gamma,lab} > 50 \text{ MeV}$. The photon calibration described in Section 5.1 is applied. It will be shown, however, in Section 5.2.6 that the effect of these corrections on the photon efficiency is negligible.

Additional selection criteria for the photon efficiency study are the trigger and the background filter (BGF). In order to avoid a bias introduced by the trigger, the events has to be triggered by the “L3OutDch” trigger line, which requires only at least two charged tracks in the DCH. Different choices of BGF allows the study of different effects: BGFRadT-twoProng is a special filter for the efficiency study with $\mu^+\mu^-\gamma$. It does not require a photon, but rejects events with more than two tracks. It is therefore perfectly suited for studies of detector inefficiencies due to dead crystals or gaps between detection elements (2-track sample). In addition, this BGF requires the missing momentum to point towards the polar angular region $0.25 \text{ rad} < \theta_{miss} < 2.1 \text{ rad}$, i.e. very backward photons cannot be studied. The study of the effect of lost photons due to pair production in the *BABAR* detector material (conversion) requires looser filter criteria. Accepting events if any of the BGFs accepts the event allows the study of these conversion events (conversion sample). However, it is important to demonstrate that the additional events are due to converted photons. This is achieved by the application of an additional electron veto (conversion sample with electron veto). A certain fraction of the extra tracks is due to internal conversion. In this case, no real photon entered the detector, but the e^+e^- pair is emitted from the event vertex. This creates an artificial inefficiency, which must not be included in the efficiency derived here. Therefore, an internal conversion veto is implemented, allowing to estimate the contribution to the inefficiency by internal conversion events (conversion sample with internal conversion veto). Therefore the following four data samples which are partially overlapping, are defined:

- **2-track sample:** Study of detector inefficiencies due to dead crystals or gaps between detection elements.
- **conversion sample:** Study of events with additional tracks allowing a dedicated study for conversion events.
- **conversion sample with electron veto:** Reject events with tracks from photon conversion to demonstrate that the inefficiency difference between the conversion and the 2-track sample is exclusively due to conversion events.
- **conversion sample with internal conversion veto:** Additional filter rejects internal conversion background events.

In order to compare the photon efficiency of data with simulation, the same $\mu^+\mu^-\gamma$ signal MC sample as in Section 5.1, produced with the AfkQed [94] event generator, was

used. In simulation, an ISR photon with $E_{\gamma,CM} > 3 \text{ GeV}$ is required in the CM system. In the laboratory system, however, a study of photon energies until $E_{\gamma,lab} \approx 2 \text{ GeV}$ is feasible, as shown in Fig. 5.1 (a). MC statistics becomes insufficient for energies below $E_{\gamma,lab} < 2 \text{ GeV}$. The contributions from background channels are estimated by simulating the main background processes $\pi^+\pi^-\gamma$ and $\pi^+\pi^-\pi^0\gamma$ and requiring the same selection criteria as for the data selection. These samples are scaled according to the data luminosity and their respective cross sections. The individual contributions are summarized in Table 5.1.

Final State	$\sigma, \text{ pb}$	454.4 fb^{-1}	MC sample size
$\pi^+\pi^-\gamma$	21.4	9.7M	87.6M
$\pi^+\pi^-\pi^0\gamma$	2.6	1.2M	7.4M
$\mu^+\mu^-(\gamma)$	42.9	19.5M	49.25M

Table 5.1: Summary of MC channels with cross section and corresponding expected number of events for the data luminosity of 454.4 fb^{-1} . Also shown is the used number of events before scaling simulation to data luminosity.

5.2.2 Constrained Fit and Background

The constrained kinematic fit uses the measured momenta and angles of charged particles and the corresponding error matrix as input. Only the beam information and the momentum of the charged tracks measured in the DCH are used in the fit. The photon energy and angles are the result from this kinematic fit with one constraint (1C).

The resulting χ^2_{1C} distributions for signal and background simulation are displayed in Fig. 5.12. The contribution of the $\pi^+\pi^-\gamma$ background channel is on the level of 4-5%. However, the kinematics of these events is almost identical to $\mu^+\mu^-\gamma$ events. Since the muon mass and the pion mass are very similar, even the fit predictions for the emitted ISR photon is sufficient. Using the π -tracks in the $\mu^+\mu^-\gamma$ -hypothesis will not introduce a sizable difference in the photon efficiency measurement. Therefore, this kind of background is not dangerous and can even be considered as signal. The $\pi^+\pi^-\pi^0\gamma$ channel is more dangerous if the π^0 is not reconstructed, since the energy of the undetected π^0 is assigned to the ISR photon by the kinematic fit. As a consequence, the fit prediction does not match the measured photon quantities, even if the photon is reconstructed perfectly. Therefore, these events are an unwanted source of artificial inefficiency. However, due to the suppression via the kinematic fit and the low cross section of this channel, this background is suppressed by more than 4 orders of magnitude and therefore can be neglected as well. The tight requirement $\chi^2_{1C} < 3$ has been chosen, in order to strongly suppress events with high energetic NLO radiation.

The energy distribution of the predicted photon is shown in Fig. 5.13 (left) and as a scatter plot versus the polar angle of the photon (right). As mentioned in Section 5.2.1, events with low ISR photon energies are not simulated. Therefore an additional requirement

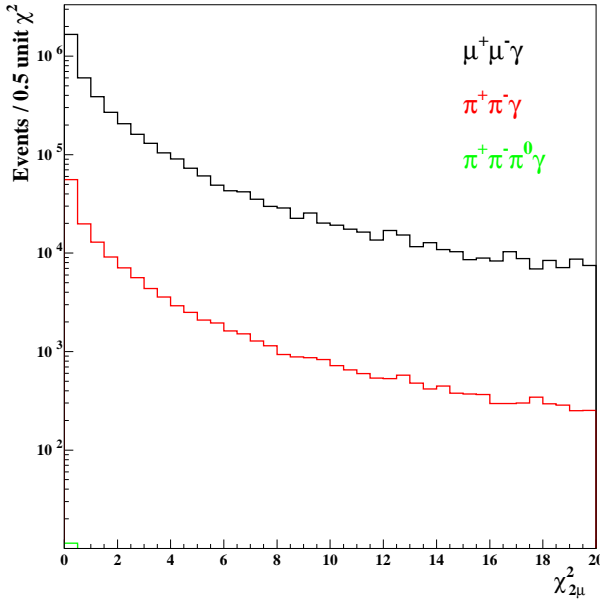


Figure 5.12: The $\chi^2_{2\mu}$ MC distributions for signal (black), $\pi^+\pi^-\gamma$ (red) and $\pi^+\pi^-\pi^0\gamma$ (green), scaled according to their cross sections and the luminosity in data.

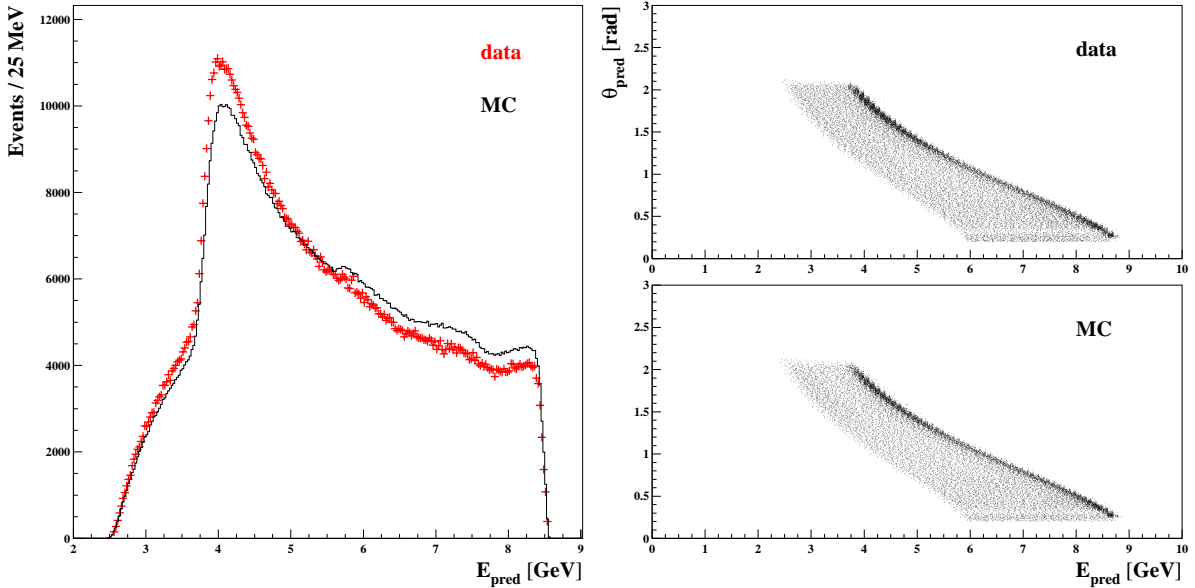


Figure 5.13: Left: Predicted energy distributions by the kinematic fit for data (red) and simulation (black); right: predicted energy vs. polar angle for data and MC.

on $M_{inv}(\mu^+\mu^-) < 6 \text{ GeV}/c^2$ ensures that the low energy tail of ISR photons in the data is removed and that the energy range is very similar in the data and the simulation. A remaining difference of up to 10% in the MC description of the energy distribution in data is visible. This effect, however, cancels in the inefficiency and is therefore negligible.

5.2.3 Matching Predicted and Reconstructed Photons

One essential element of the photon efficiency study is the matching requirement for reconstructed and predicted photons from the kinematic fit. This requirement is to a certain extent arbitrary and changes the numerical result for the inefficiency. It has to be the same (or very similar) in the efficiency study and the subsequent analysis. A very intuitive method declares the detected photon to be matched to the predicted photon if the following requirements are fulfilled:

- $0.5 < \frac{E_{\text{meas}}}{E_{\text{pred}}} < 1.2$
- $\Delta\psi = \Delta(\vec{p}_{\text{meas}}, \vec{p}_{\text{pred}}) < 0.1 \text{ rad}$

A photon candidate is matched, if it has more than half of the energy predicted by the kinematic fit. In addition, the 3-dimensional angle $\Delta\psi$ to the predicted photon direction has to be smaller than than 0.1 rad. The corresponding distributions are displayed in Fig. 5.14. The energy and angular resolutions for data and simulation are slightly different. This is partly due to differences in the detector resolution, but mostly due to imperfections in the description of extra radiation in MC. Since extra radiation photons are not used in the kinematic fit, a slight mis-prediction of the angle and energy of the ISR photon is expected. The requirement $\chi^2_{1C} < 3$ removes a significant fraction of events with extra radiation. The requirements on $\frac{E_{\text{meas}}}{E_{\text{pred}}}$ and $\Delta\psi$ have been chosen wide enough so that the inefficiency is not affected by these resolution effects.

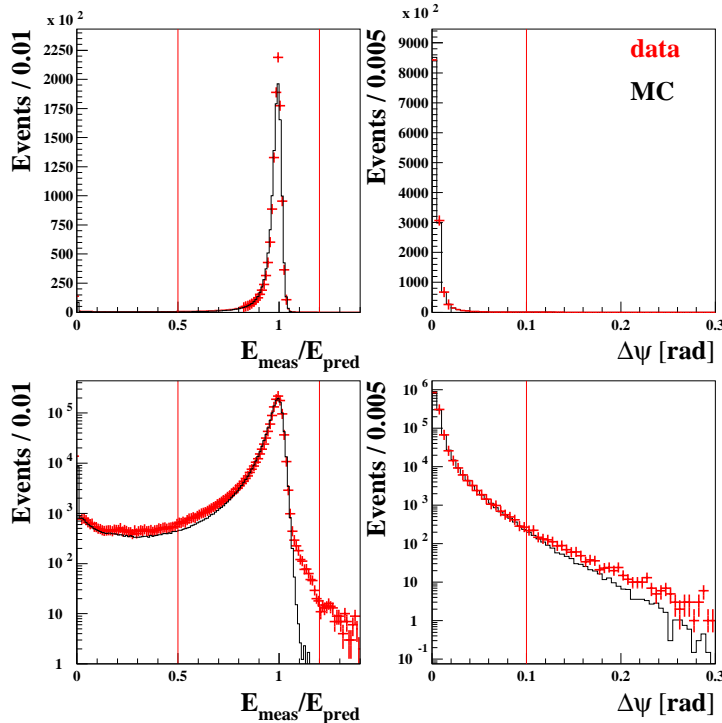


Figure 5.14: Left: Photon energy divided by predicted energy for data (red) and simulation (black) for the 2-track sample. Right: absolute value of 3-D angle between predicted and reconstructed photon for photons satisfying the energy condition. The distributions are shown in linear (top) as well as logarithmic scale (bottom).

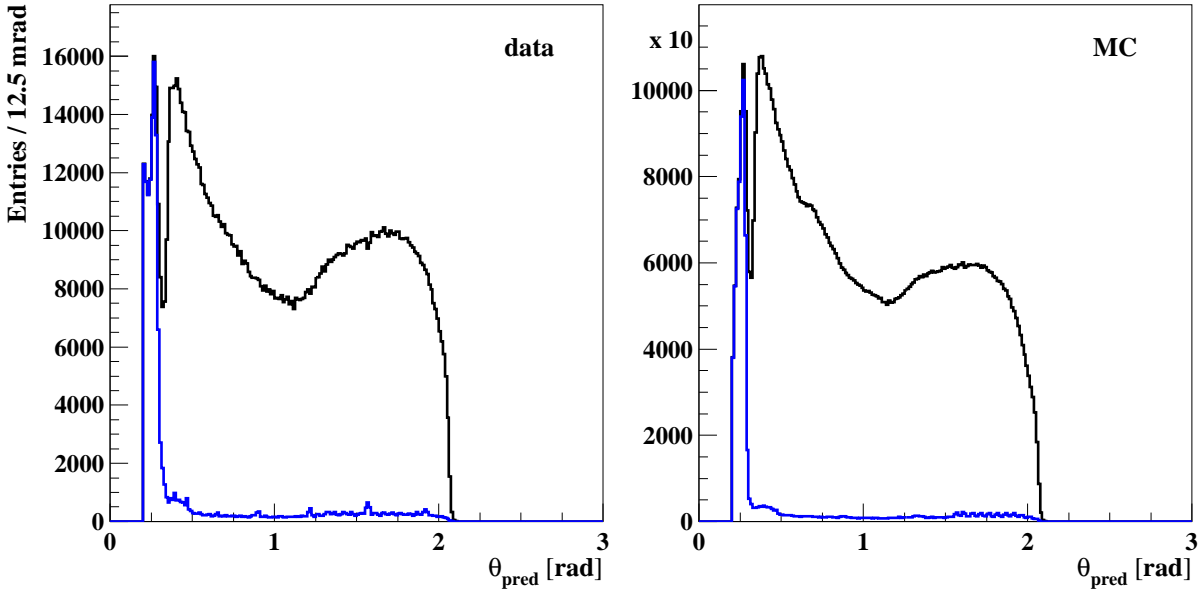


Figure 5.15: Polar angle distribution all photons (black) and for not matched photons (blue) in the 2-track sample for data (left) and simulation (right).

5.2.4 Results for Photon Inefficiency

The results of the inefficiency study are determined in four steps: First, detector inefficiencies due to dead crystals and detection gaps are investigated. This is performed with the 2-track sample. Since these events only contain two detected tracks, the effect of conversion needs to be studied separately. It is demonstrated that the difference between the conversion and the 2-track samples is exclusively due to conversion and that no additional artificial inefficiency is created by the different filter requirements of the samples. This is achieved by reproducing the result of the pure detector inefficiencies with the conversion sample and an additional electron veto. The conversion sample, however, does not only contain conversion events in which a real photon is emitted and converts in the detector material. In addition, it contains events with internal conversion, in which an electron-positron pair is produced at the vertex via a virtual photon. This process is not included in our simulation but is, of course, present in the data. Therefore, this effect creates a fake inefficiency only in data, finally leading to a data-MC photon efficiency difference. In order to remove this effect, a sample with the filter requirements of the conversion sample and an additional internal conversion veto is studied. It solely reflects the effects of detection inefficiencies as well as the inefficiency due to conversion in the detector material.

2-Track Sample

The 2-track sample contains approximately 1.3 million events. The angular distributions for all photons and predicted photons without match are shown in Fig. 5.15 for data (left) and simulation (right). The photon distribution shows an asymmetric shape with a double peak structure. The peaks result from the fact that photons are preferably emitted

in the direction of flight of the emitting particle. Due to the boost in forward direction, the polar angles of the forward photons gets smaller leading to an increasing peaking structure. In the backward region on the other hand, the same effect leads to a smearing of the peak towards smaller polar angles and broadens the peak. Below $\theta_\gamma = 0.35$ rad no active detection material of the EMC is present and therefore no reconstructed clusters match the predicted photons.

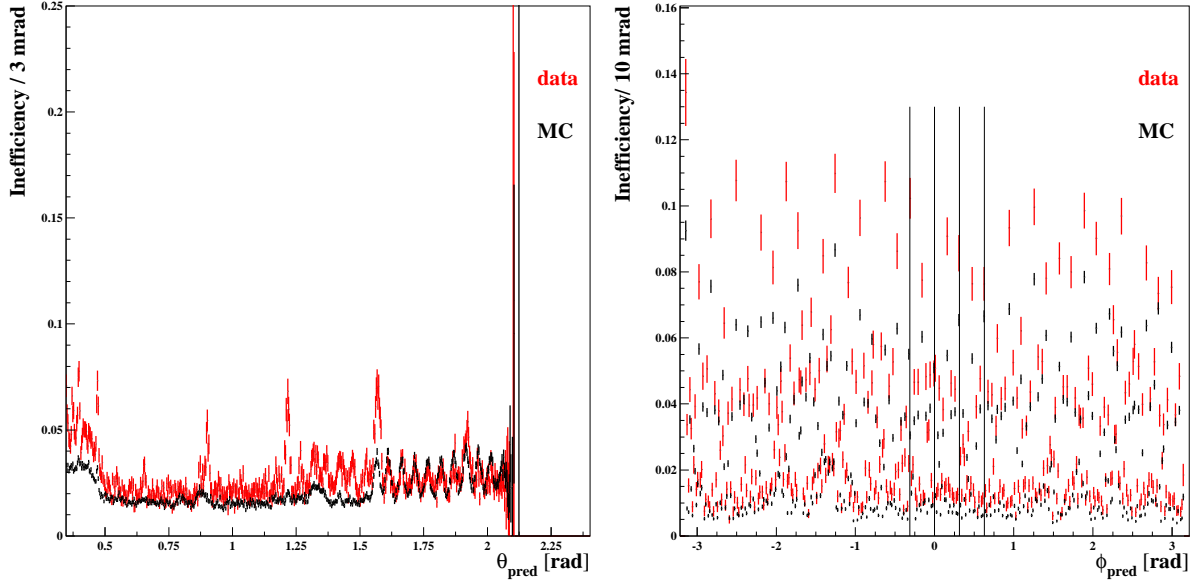


Figure 5.16: Photon inefficiency in dependence of θ (left) and ϕ (right) of the 2-track sample for data (red) and simulation (black).

The ratio of the distributions in Fig. 5.15 is the photon inefficiency as a function of the predicted polar angle θ_{pred} , displayed in Fig. 5.16 (left) for data and MC. The periodic structures result from the almost projective design of the EMC. The structure in modules, containing 7×3 ($\theta \times \phi$) crystals, leads to the major bumps, which are perfectly described by simulation in the backward region. In the forward region, however, the simulation description seems to be worse. Differences between data and simulation are visible. The constant inefficiency in θ which is approximately $1.7 \cdot 10^{-2}$ in the barrel is due to gaps between the crystals in the azimuthal angle ϕ . The inefficiency as a function of ϕ is shown in Fig. 5.16 (right). The large peaks in ϕ correspond to gaps between EMC crystals, which are schematically displayed in Fig. 2.10 (left). An overall difference in the inefficiency between the simulation and the data is visible.

The θ vs. ϕ distribution of the photon inefficiency for data and simulation is shown in Fig. 5.17. This plot nicely reflects the regions of low efficiency of the detector. The bumps in the θ and ϕ projections are now visible as bands. It is noticeable that the θ bands in the forward direction of barrel are not visible in MC. The small inefficient rectangular regions correspond to dead crystals, which, in principle, should also be present in the simulation. A few of them seem to be not properly described.

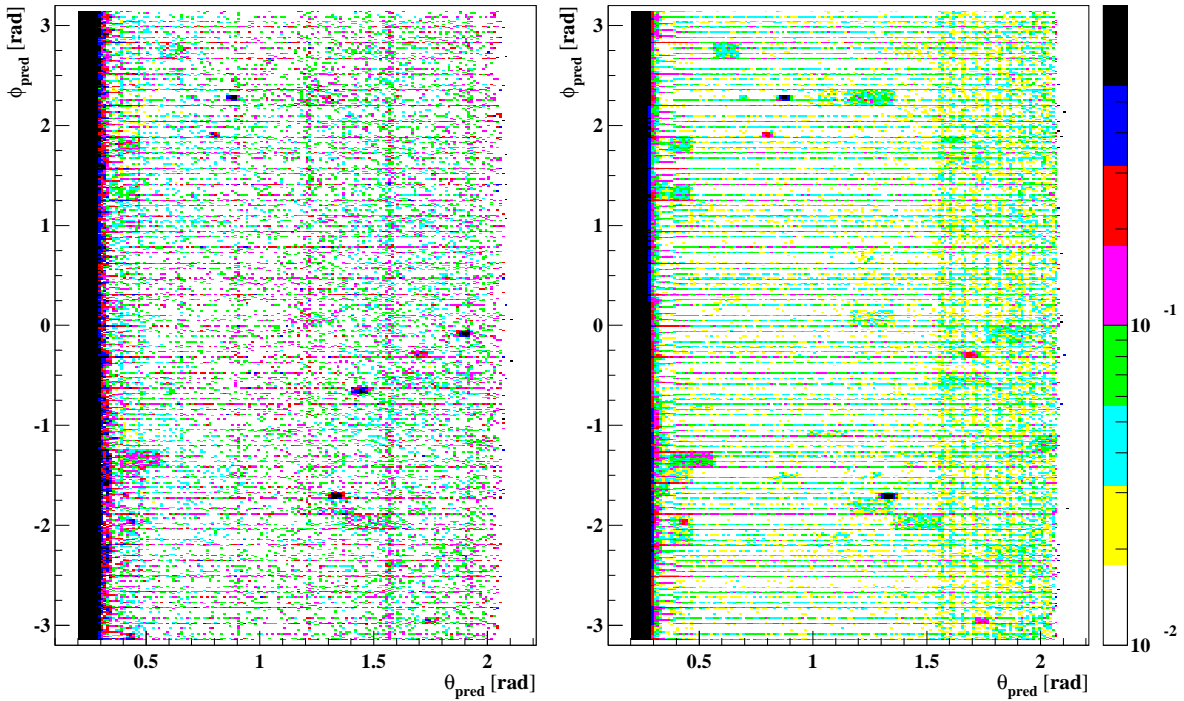


Figure 5.17: Photon inefficiency in dependence of the polar angle θ_{pred} and azimuthal angle ϕ_{pred} of the photon for the 2-track sample for data (left) and simulation (right).

Conversion Sample

The conversion sample contains additional events with more than two tracks and therefore includes events with converted photons. The sample size increases by approximately 20% to 1.55 million events. The corresponding inefficiency distributions in data and MC for this sample are presented in Fig. 5.18 (left). Again, the backward region of the barrel seems to be described well by simulation, with only a small shift towards higher inefficiencies for data. In the forward region, however, there is a larger difference between the data and the MC simulation in the order of $(1 - 2) \cdot 10^{-2}$. Especially in the endcap ($\theta_{pred} < 0.5$ rad), the difference rises to approximately $5 \cdot 10^{-2}$. The origin of this discrepancy is further studied in the following.

Conversion Sample with Electron Veto

As a next step an additional electron veto is implemented which rejects events with tracks identified as electrons according to a dedicated *BABAR* PID selector. This reduces the sample size by 5% to 1.48 million events. The corresponding inefficiency distributions for this sample are shown in Fig. 5.18 (right) and with zoom in Fig. 5.19 for data and MC.

The inefficiencies for data and simulation are almost exactly the same as for the 2-track sample in Fig. 5.16. The average inefficiency in the data increases by less than $0.1 \cdot 10^{-2}$ from $(2.89 \pm 0.02) \cdot 10^{-2}$ to $(2.96 \pm 0.01) \cdot 10^{-2}$ and in simulation from $(2.15 \pm 0.01) \cdot 10^{-2}$ to $(2.23 \pm 0.01) \cdot 10^{-2}$. The uncertainties correspond to statistical uncertainties only. This

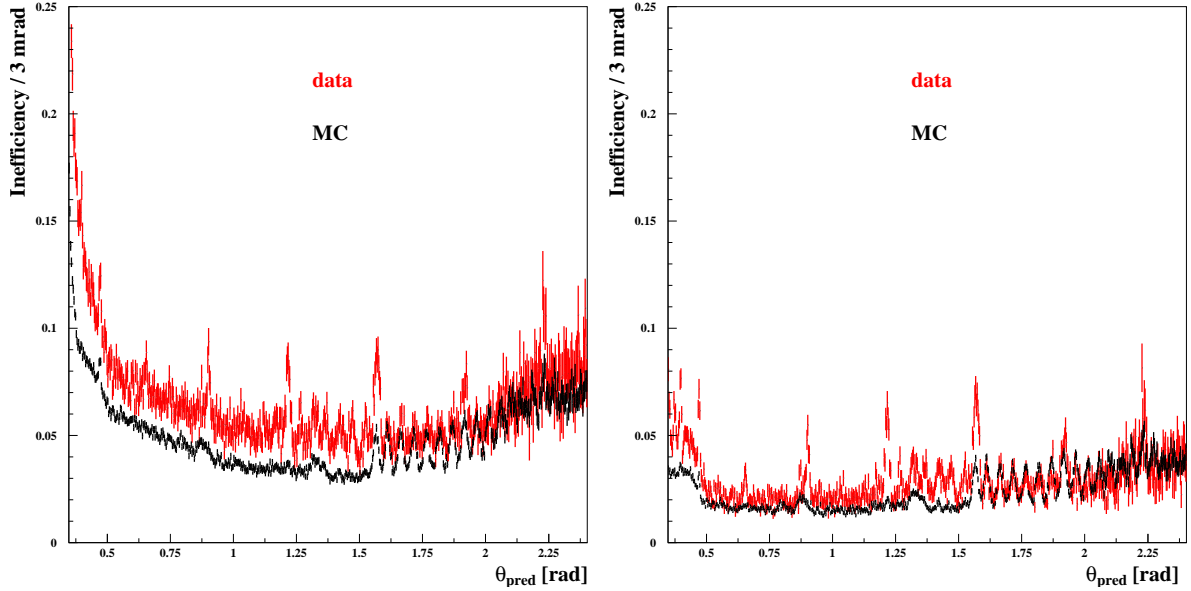


Figure 5.18: Left: photon inefficiency of the conversion sample including conversion (“real” and internal) for data (red) and simulation (black); right: corresponding distribution with additional electron veto in order to suppress events with conversion.

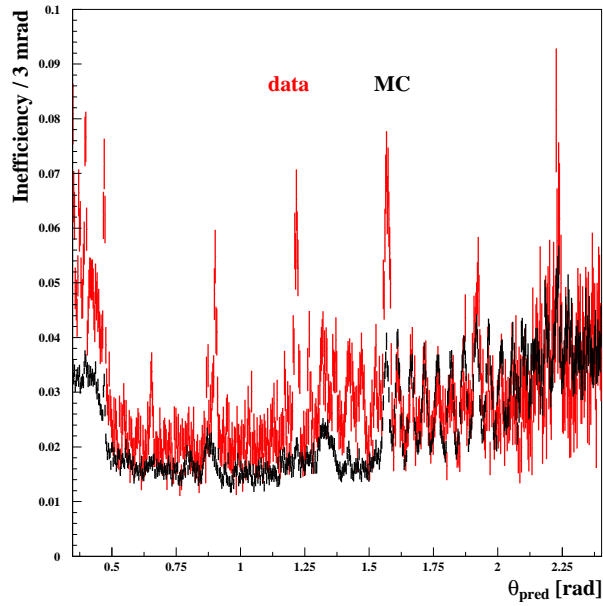


Figure 5.19: Zoom in on the photon inefficiency as a function of the predicted polar angle θ_{pred} of the conversion sample with an electron veto to suppress conversion events for data (red) and simulation (black).

confirms that the additional photon inefficiency in the conversion sample is solely due to events with conversion. It is due neither to background filter problems nor to any background not containing electrons. The only reasonable remaining background in data is internal conversion background, which is described and investigated in the following.

Conversion Sample with Internal Conversion Veto

As illustrated in Fig. 5.18 (left), there is quite a large difference between data and simulation in the sample containing events with conversion. This difference, however, is not only due to conversion events in which a real photon is emitted and converts in the detector material. A second source are internal conversion events in which an electron positron pair is directly produced via a virtual photon near the IP. Events of this type are present in data, but are not included in the simulation. They are therefore a source of an additional fake inefficiency. It is important to distinguish internal from real conversion events in order to study exclusively real photon inefficiencies.

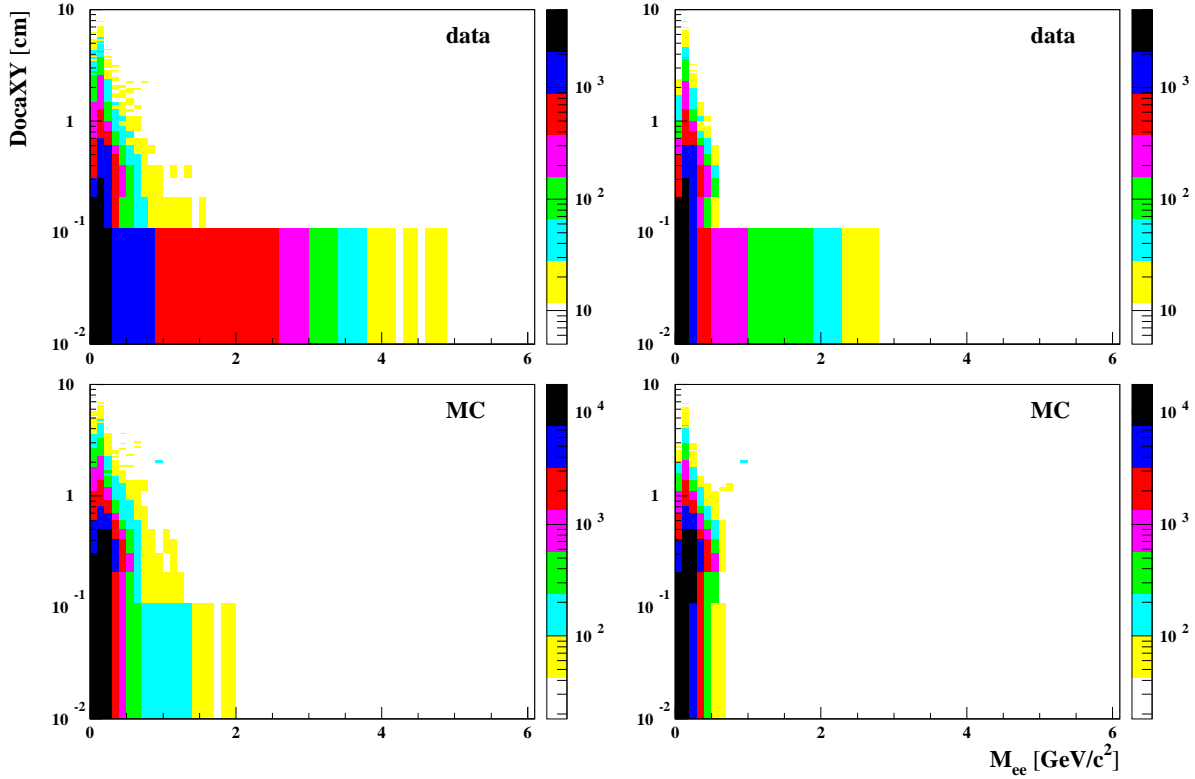


Figure 5.20: Left: DocaXY vs. M_{ee} for data (top) and simulation (bottom) for events with 4 tracks. Right: The corresponding plots with an additional veto in order to suppress events with internal conversion.

Internal conversion electrons are emitted from the IP and therefore have a very small transverse distance of closest approach to the event vertex (docaXY). They are produced by a virtual photon, so their invariant mass M_{ee} can be quite large. Events with real conversion, on the other hand, are produced in the detector material and therefore have a large tail in the docaXY distribution. Since they are produced by a real photon, M_{ee} is peaked near 0. The angle between the two conversion tracks is not reconstructed properly. Therefore, real conversion events also have a quite large tail towards larger invariant masses. However, Fig. 5.20 shows the docaXY vs. M_{ee} distribution for the two tracks which are not identified as muons in 4-track events. In data (top left) a band is visible at small docaXY and large M_{ee} , which is not present in simulation (bottom left).

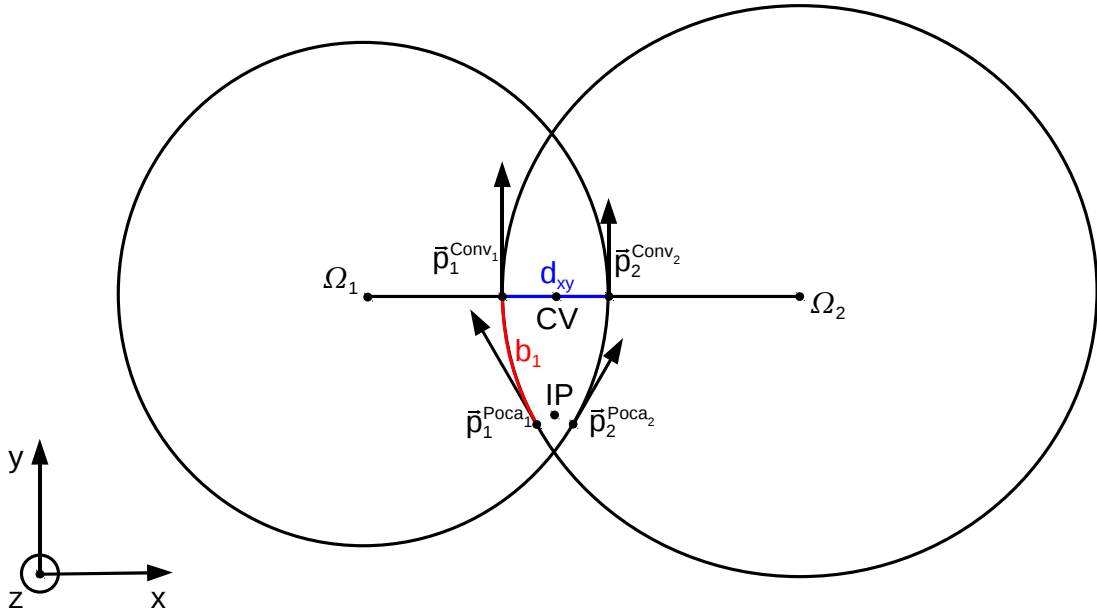


Figure 5.21: Illustration of the method to reconstruct the conversion vertex in the x-y-plane.

In order to properly separate events with internal conversion, the vertex of conversion needs to be reconstructed. The applied reconstruction method is illustrated in Fig. 5.21. The three-momenta $\vec{p}^{\text{Poca}1,2}$ are reported at the point of closest approach of the track to the z axis Poca_{1,2}. Since the conversion might, however, occur far from the IP, the momenta $\vec{p}^{\text{Poca}1,2}$ can differ significantly from the real three-momenta $\vec{p}^{\text{Conv}1,2}$ at the conversion point Conv_{1,2}. The absolute value of the momenta at the two different points is approximately the same, but the angle is not correctly reconstructed, as shown in Fig. 5.21.

The pair of tracks from a photon conversion has a very small opening angle at the conversion point. Knowing the magnetic field \vec{B} and the momenta $\vec{p}^{\text{Poca}1,2}$, the centers of curvature Ω_1 and Ω_2 can be reconstructed. The conversion points Conv_{1,2} are located at the intersection of the circles with the connection of the centers of curvatures as illustrated in Fig. 5.21. The actual conversion point is taken to be the midpoint of these two points. The z-coordinate of the vertex can be reconstructed via the ratio $\frac{p_z}{p_T}$ and the length b_1 of the virtual flight path of the electrons from Poca_{1,2} to Conv_{1,2}. The variable d_{xy} (d_z) is defined as the separation between the intersection points in the x-y plane (z-direction) and can be used as an estimate of the quality of the reconstruction.

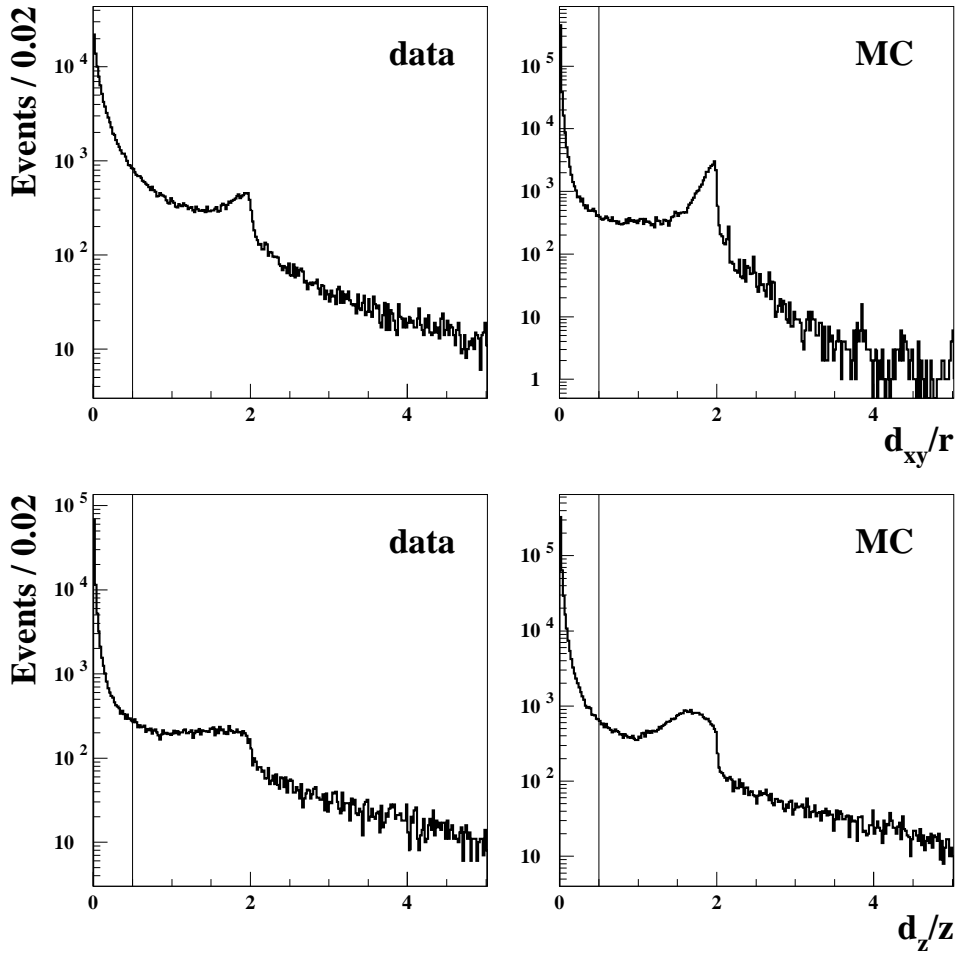


Figure 5.22: Top: Ratio of distance d_{xy} between reconstructed conversion points $\text{Conv}_{1,2}$ and the reconstructed radial distance of the conversion point to the IP r for the data and the MC simulation. Bottom: Ratio of distance d_z between reconstructed conversion points $\text{Conv}_{1,2}$ in z-direction d_z and the z-distance z of the conversion point to the IP. These distributions reflect the quality of the conversion vertex reconstruction.

The following quality requirements were chosen in order to study only well reconstructed conversion events with their conversion point well separated from the IP in order to filter out internal conversion:

- $N_{tracks} = 4$
- $r = \sqrt{(x + 0.05)^2 + (y + 0.3)^2} > 1.5 \text{ cm}$
- $d_{xy}/r < 0.5$
- $d_z/z < 0.5$ (for $z < 2\text{cm}$: $d_z < 1 \text{ cm}$)

Tracks that have been converted at a larger radius r (z -distance) are allowed to have a larger d_{xy} (d_z). This is reflected by the $\frac{d_{xy}}{r}$ ($\frac{d_z}{z}$) requirement. The corresponding distributions are shown in Fig. 5.22 for data and MC. Thus, the first three requirements ensure

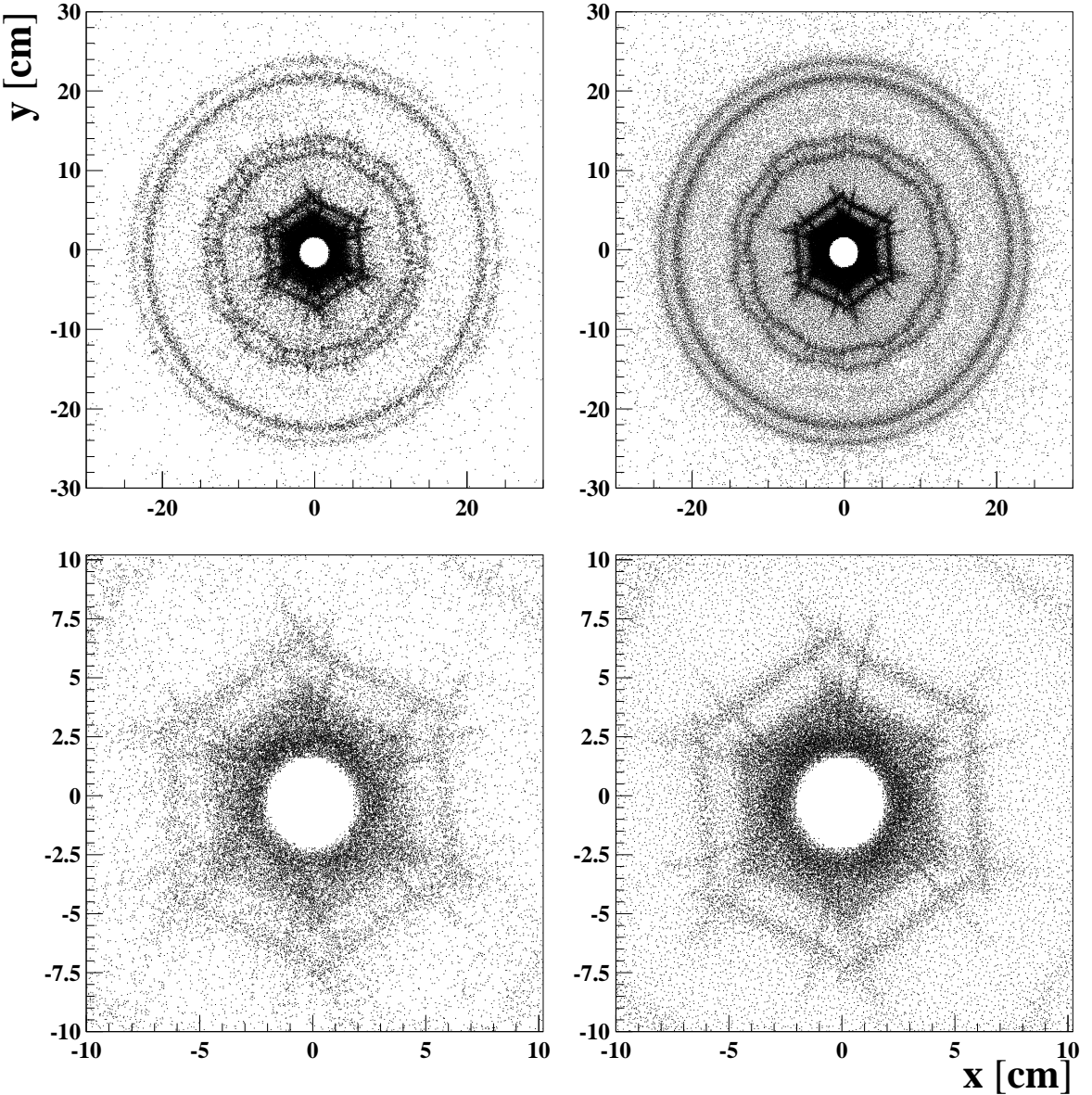


Figure 5.23: Top: conversion vertex distribution for data (left) and simulation (right); bottom: corresponding distributions with zoom.

a well reconstructed conversion event. The last one separates the real conversion from internal conversion events, which would be emitted from the IP inside the beam pipe. After the application of these requirements, the doca_{XY} vs. M_{ee} distribution is plotted on the right hand side of Fig. 5.20. The band at small doca_{XY} and large invariant masses which was present in data (top left) diminishes by more than one order of magnitude. This confirms the hypothesis that internal conversion events are removed in data by the above restrictions.

The x and y position of the reconstructed vertex for the two non-muon tracks in the events is displayed in Fig. 5.23 (top) for data (left) and simulation (right). In average,

the IP is approximately shifted 3 mm in y and 0.5 mm in x direction. This effect is well described by simulation. At a radius of approximately 10-12 cm, two circular structures corresponding to the two outer layers of the SVT can be observed. The beginning of the DCH is also visible at around 22 cm. The plots on the bottom are a zoom on the three inner layers of the SVT and the beam-pipe. The structures in radial direction reflect supporting material. In Fig. 5.24 the corresponding structures can be seen in the r-z plane.

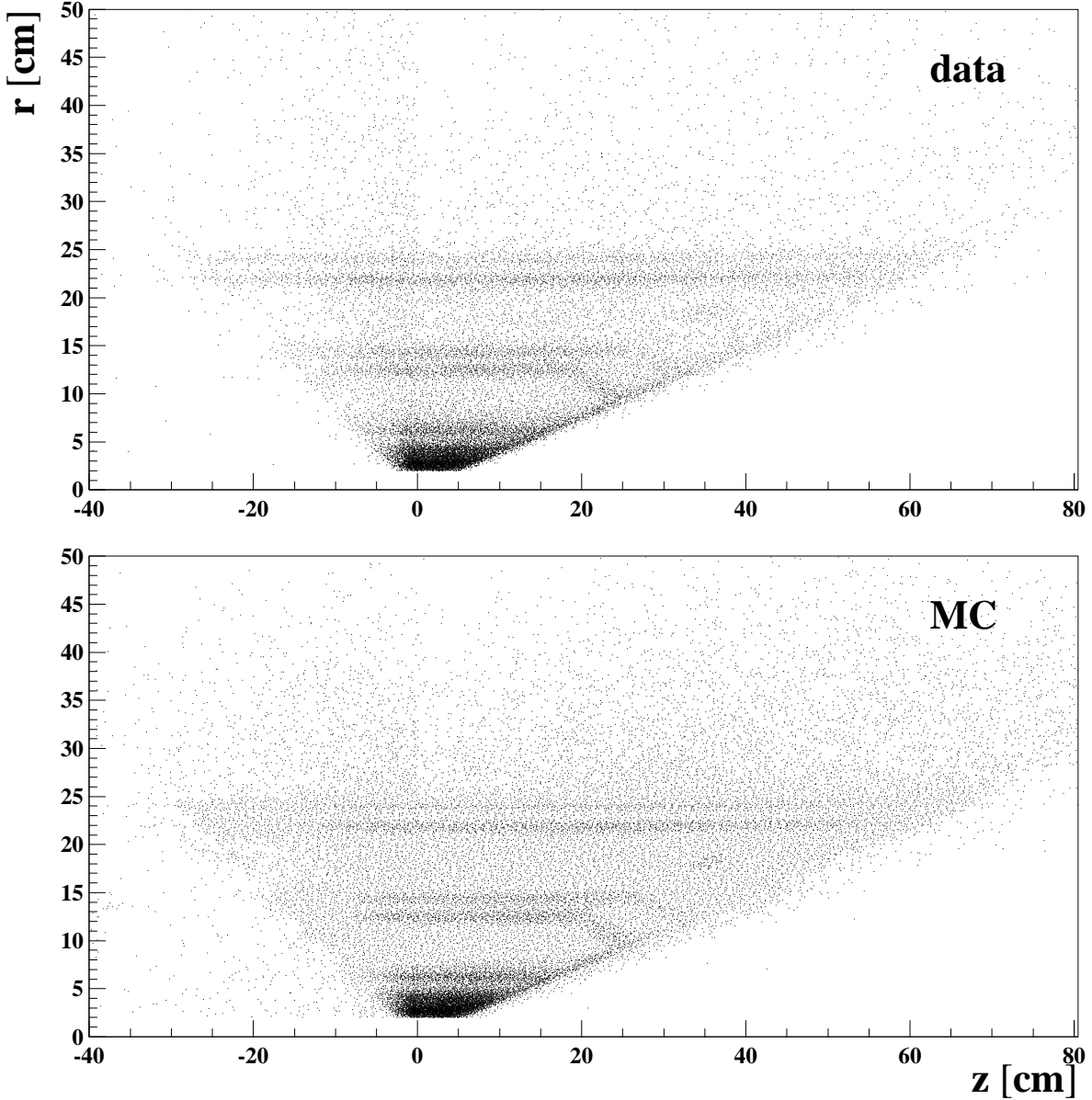


Figure 5.24: r vs. z of the conversion vertex for data (top) and simulation (bottom).

It should be noted that these requirements reduce a large fraction of internal conversion events, and in addition 87% of the 4 track-events in simulation have a well reconstructed vertex outside the IP region. Thus the reconstruction algorithm is very efficient. This method is therefore perfectly suited for the internal conversion study. In data 65% of

the events survive the requirements. Therefore, it can be assumed that approximately one-fourth of the conversion events correspond to internal conversion.

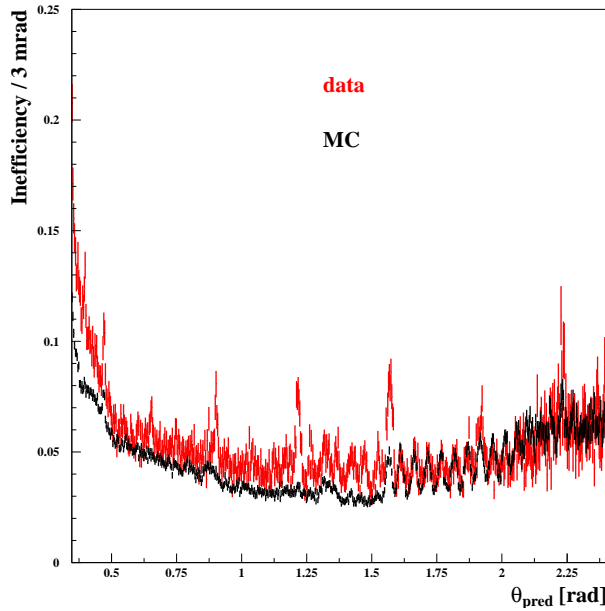


Figure 5.25: Photon inefficiency after all corrections in dependence of the predicted polar angle θ_{pred} of the photon for data (red) and simulation (black).

The final result for the inefficiency distribution as a function of θ_γ including all detector gaps as well as real photon conversion is shown in Fig. 5.25. The backward region of the barrel is described perfectly by simulation. The gaps in the forward direction are partially missing in MC, leading to a data-MC difference of $0.79 \cdot 10^{-2}$ in the barrel. The end-cap shows a large difference of $2.70 \cdot 10^{-2}$, mostly due to a lack of description of conversion events, which is probably due to imperfections in the dead material description at small polar angles, where most of the dead material is present. Table 5.2 displays the photon inefficiencies for data and simulation and the different event samples. It can be seen that internal conversion events have a quite large contribution of almost $1 \cdot 10^{-2}$ to the average photon efficiency difference between data and simulation and need to be removed.

5.2.5 Inefficiency Difference for ISR Studies

In ISR studies the definition of a photon candidate is different from the one described so far. The only requirement is the presence of a neutral cluster with more than 3 GeV energy within a cone with opening angle of 0.1 rad around the predicted direction of an ISR photon. This changes the inefficiency distribution according to Fig. 5.26 (left). Due to the small statistics of high energetic photons at large polar angles in the lab system, the binning is changed for $\theta > 2.1$ rad, which is displayed in Fig. 5.26 (right). The inefficiency distribution is similar to before at small polar angles. At large polar angles, in opposite direction to the boost, the average CM energy of the photons is relatively low. A large fraction has a true CM energy slightly above 3 GeV. As shown in Section 5.1, the

		barrel	end-cap	all
2-track sample	data	2.61 ± 0.02	4.80 ± 0.05	2.90 ± 0.02
	MC	2.01 ± 0.01	3.00 ± 0.01	2.15 ± 0.01
	data - MC	0.60 ± 0.02	1.80 ± 0.05	0.75 ± 0.02
conversion sample	data	5.98 ± 0.02	14.07 ± 0.09	7.02 ± 0.02
	MC	4.45 ± 0.01	8.97 ± 0.03	5.06 ± 0.01
	data - MC	1.53 ± 0.02	5.10 ± 0.09	1.96 ± 0.02
conversion sample & e^- -veto	data	2.70 ± 0.01	4.84 ± 0.05	2.96 ± 0.01
	MC	2.12 ± 0.01	2.99 ± 0.02	2.24 ± 0.01
	data - MC	0.58 ± 0.02	1.85 ± 0.06	0.72 ± 0.02
conversion sample & internal conversion veto	data	4.90 ± 0.02	10.42 ± 0.08	5.59 ± 0.02
	MC	4.11 ± 0.01	7.72 ± 0.03	4.59 ± 0.01
	data - MC	0.79 ± 0.02	2.70 ± 0.08	1.00 ± 0.02

Table 5.2: Photon inefficiency and inefficiency difference with statistical error in 10^{-2} for data and MC.

reconstructed energy distribution has a long tail towards smaller energies. Thus a large fraction of these events does not satisfy the 3 GeV selection criteria for the measured photon energy in ISR events. The principal behavior for the inefficiency difference between data and simulation is the same as for the previous photon requirements. The resulting differences in numbers are displayed in Table 5.3. The average inefficiency difference slightly increases from $1.0 \cdot 10^{-2}$ to $1.3 \cdot 10^{-2}$. This is partly due to small imperfections in the description of the strong rising inefficiency at large polar angles. However, it also reflects the fact that the backward region has a lower statistical weight than before.

		barrel	end-cap	all
standard	data	4.90 ± 0.02	10.42 ± 0.08	5.59 ± 0.02
	MC	4.11 ± 0.01	7.72 ± 0.03	4.59 ± 0.01
	data - MC	0.79 ± 0.02	2.70 ± 0.08	1.00 ± 0.02
ISR γ	data	7.38 ± 0.03	9.69 ± 0.08	7.69 ± 0.02
	MC	6.19 ± 0.01	7.31 ± 0.02	6.35 ± 0.01
	data - MC	1.19 ± 0.03	2.38 ± 0.08	1.34 ± 0.03

Table 5.3: Photon inefficiency and inefficiency difference in 10^{-2} for different photon definitions for the data and MC simulation. The uncertainty given is statistical only.

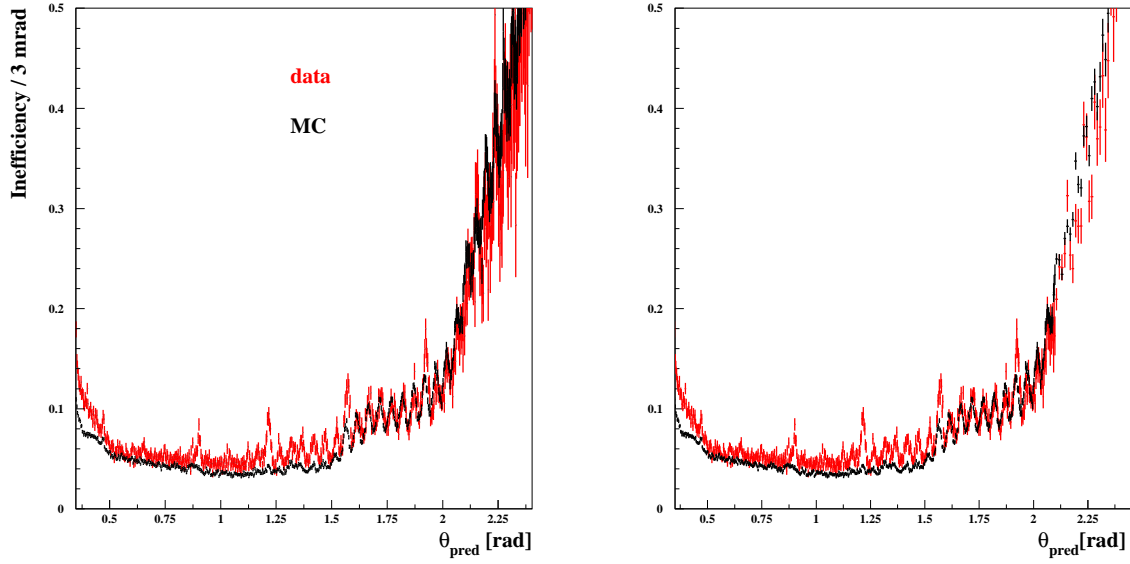


Figure 5.26: Photon inefficiency in dependence of the predicted polar angle of the photon θ_{pred} for data (red) and simulation (black). Conversion is included and the ISR photon definition is used.

5.2.6 Systematic Uncertainties

The photon inefficiency is an important correction for the $\pi^+\pi^-\pi^+\pi^-\gamma$ cross section measurement. Therefore, the systematic uncertainties due to the requirements for the event as well as the photon selection on the photon efficiency are studied in detail ($\chi^2, \frac{E_{meas}}{E_{pred}}, |\Delta\psi|$). The influence of the background filter is investigated as well as the possible impact of 3-track events. In addition, the influence of the additional photon calibration (see Section 5.1) on the photon inefficiency and the stability with time of the inefficiency correction are studied.

Variation of Requirements

Table 5.4 shows that a considerable variation of the requirement on $|\Delta\psi|$ changes the inefficiency difference between simulation and data on a sub-permil level. A larger effect on the inefficiencies results from the variation of the $0.5 < \frac{E_{meas}}{E_{pred}} < 1.2$ requirement because this distribution has a relatively large tail as can be seen in Fig. 5.12. As expected the inefficiency increases with a tighter requirement. The relative value for the inefficiency is almost exactly identical for the different requirements. However, the absolute value of the difference between data and simulation increases, leading to the largest contribution to the uncertainty. The inefficiency difference between the data and the simulation depends therefore on the definition of a good photon of the analysis and it can change $\Delta\eta$ by large amounts. The χ^2 requirement variation leads to a systematic uncertainty of less than $0.2 \cdot 10^{-2}$.

	standard cut	loose cut	tight cut
	$\chi^2 < 3$	$\chi^2 < 10$	$\chi^2 < 1$
data	5.59 ± 0.02	6.04 ± 0.02	5.37 ± 0.02
MC	4.59 ± 0.01	4.89 ± 0.01	4.44 ± 0.01
data - MC	1.00 ± 0.02	1.15 ± 0.02	0.96 ± 0.02
	$ \Delta\psi < 0.1 \text{ rad}$	$ \Delta\psi < 0.2 \text{ rad}$	$ \Delta\psi < 0.05 \text{ rad}$
data	5.59 ± 0.02	5.42 ± 0.02	6.28 ± 0.02
MC	4.59 ± 0.01	4.43 ± 0.01	5.26 ± 0.01
data - MC	1.00 ± 0.02	0.98 ± 0.02	1.02 ± 0.02
	$0.5 < \frac{E_{\text{meas}}}{E_{\text{pred}}} < 1.2$	$0.1 < \frac{E_{\text{meas}}}{E_{\text{pred}}} < 1.2$	$0.8 < \frac{E_{\text{meas}}}{E_{\text{pred}}} < 1.2$
data	5.59 ± 0.02	3.87 ± 0.02	8.93 ± 0.03
MC	4.59 ± 0.01	3.21 ± 0.01	7.16 ± 0.01
data - MC	1.00 ± 0.02	0.66 ± 0.02	1.76 ± 0.03
		$0.5 < \frac{E_{\text{meas}}}{E_{\text{pred}}} < 1.5$	$0.5 < \frac{E_{\text{meas}}}{E_{\text{pred}}} < 1.1$
data		5.58 ± 0.02	5.63 ± 0.02
MC		4.59 ± 0.01	4.59 ± 0.01
data - MC		0.99 ± 0.02	1.04 ± 0.02
	$E_{\text{meas}}, E_{\text{pred}} > 3 \text{ GeV}$	$E_{\text{meas}}, E_{\text{pred}} > 3.2 \text{ GeV}$	$E_{\text{meas}}, E_{\text{pred}} > 3.4 \text{ GeV}$
data	7.69 ± 0.02	8.09 ± 0.03	8.63 ± 0.03
MC	6.35 ± 0.01	6.66 ± 0.01	7.11 ± 0.01
data - MC	1.34 ± 0.02	1.44 ± 0.03	1.52 ± 0.03

Table 5.4: Photon inefficiency and inefficiency difference behavior due to systematic variations with statistical error in 10^{-2} for data and MC.

Background Filter

The effect of the background filter is estimated by comparing the 2-track and the conversion samples. The 2-track sample is produced with a dedicated filter for the $\mu^+\mu^-\gamma$ study. Requiring only an arbitrary filter might introduce an additional inefficiency, if the filter efficiency was different for events with and without a photon. However the fact that the inefficiencies of the two samples agree nicely after only applying the electron veto, indicates that no artificial inefficiency is introduced by the filter to the conversion sample. This hypothesis is strengthened by the following observation: The background filter for the 2-track sample restricts the sample to polar angles smaller than $\theta_\gamma < 2.1 \text{ rad}$. The conversion sample completes the distribution at larger angles continuously, which can be seen in Fig. 5.19. The contribution to the uncertainty of the filter requirement is smaller than $0.5 \cdot 10^{-2}$.

3-Track Events

A considerable number of three track events is present in our data sample when the filter requirements for the conversion sample are applied. These events are partly signal events with an additional random background track. A sample of these events should have the same inefficiency as the 2-track data sample. However, a non-negligible number of events are due to conversion events with only one reconstructed electron. This effect is estimated in Table 5.5. Including these events, the difference between data and simulation rises by approximately $0.3 \cdot 10^{-2}$. This increase is, however, partly due to internal conversion events with one missing electron. Therefore it is systematically too large. It can be used as a conservative estimate for the systematic error due to this effect.

	$ntr = 2, 4$	$ntr > 1$
data	5.59 ± 0.02	6.29 ± 0.02
MC	4.59 ± 0.01	5.95 ± 0.01
data - MC	1.00 ± 0.02	1.34 ± 0.02

Table 5.5: Photon inefficiency and inefficiency difference including and excluding 3-track events with statistical error in 10^{-2} for data and MC.

Photon Correction

In ISR analyses small additional photon corrections to the standard *BABAR* calibration is used as documented in Chapter 5.1. Table 5.6 clearly shows that these corrections have hardly any influence on the photon efficiency photon efficiency and can be neglected in comparison to other systematic uncertainties.

	including photon correction	no photon correction
data	7.02 ± 0.02	7.05 ± 0.02
MC	5.06 ± 0.01	5.07 ± 0.01
data - MC	1.96 ± 0.02	1.98 ± 0.02

Table 5.6: Photon inefficiency and inefficiency difference with and without photon energy corrections with statistical error in 10^{-2} for data and MC.

Run Dependence

Fig. 5.27 shows the Run dependence of the photon inefficiency in data and MC. There are slight differences between Run 1 and Runs 2-6, but neglecting a few dead crystals the difference is constant over time. If one chooses to correct the photon efficiency only for certain Runs this effect has to be estimated accordingly and needs to be taken into account as an additional systematic uncertainty. Since also for the $\pi^+\pi^-\pi^+\pi^-\gamma$ analysis the Run 1-6 data is used, no additional correction and systematic uncertainty needs to be included.

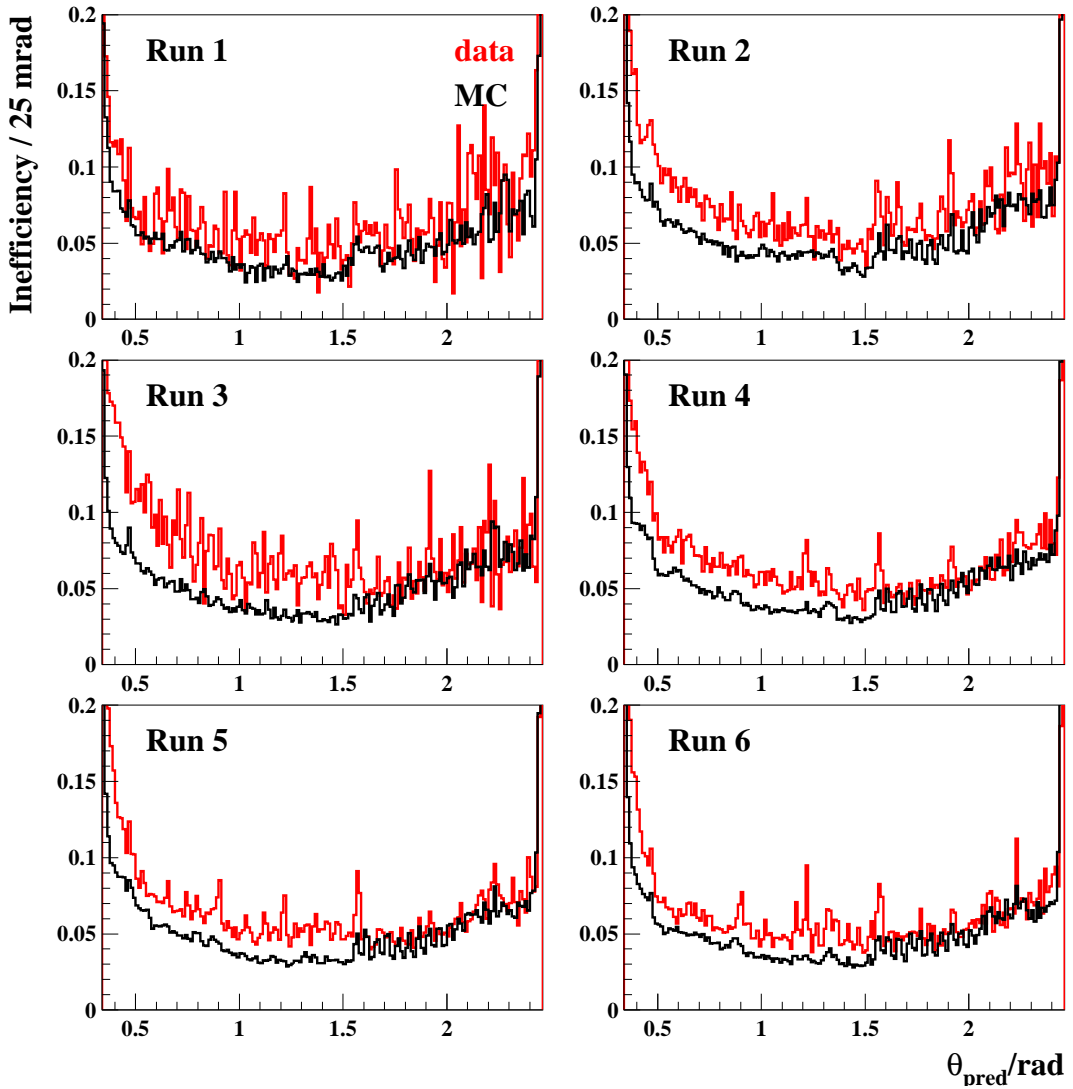


Figure 5.27: Photon inefficiency for data (red) and simulation (black) in different Run periods.

Summary of Systematic Uncertainties

Table 5.7 summarizes the systematic uncertainties for the difference in photon efficiency between the data and the MC simulation. For most of the uncertainties the maximum deviation has been chosen as systematic uncertainty. However, some requirement variations were very wide. The energy requirement on the photon in the analysis is chosen to be 50% of the predicted energy. This requirement was varied to 10% and 80%. It is hard to imagine that a real analysis filters this loosely or tightly on the photon. Basically these variations were chosen to see the maximum variation of the uncertainty. The estimate of the systematic uncertainty is taken to be $\frac{1}{\sqrt{3}}$ of this maximum deviation, as motivated in Appendix B. The photon energy requirement for the $\sigma(e^+e^- \rightarrow \pi^+\pi^-\pi^+\pi^-)$ analysis has been studied separately. Hereby a reduction of the systematic uncertainty from $0.44 \cdot 10^{-2}$ to $0.18 \cdot 10^{-2}$ is achieved. The same approach is chosen for the estimate of the systematic error for the 3-track sample, since most of the observed additional difference between data and simulation is due to the fact that it is impossible to filter out internal conversion in the 3-track events. An estimate for the number of remaining internal conversion events in the data can be obtained by comparing the difference between the data and the MC simulation in the conversion sample and in the conversion sample with internal conversion veto. 20% of this difference can be used as an estimate for the remaining internal conversion events. The reconstruction efficiency for real conversions is about 87%. Internal conversions are cut out, if they are reconstructed properly and therefore have a vertex near the IP (87%) or if the reconstruction failed and the d_{xy} (d_z) is large. The estimate of 13% of remaining internal conversion is based on MC simulation. Thus a more conservative estimation of 20% is used for the data.

	end-cap	barrel	end-cap & barrel
$ \Delta\psi $	0.10	0.01	0.02
$\frac{E_{meas}}{E_{pred}}$	1.10	0.35	0.44
χ^2	0.15	0.15	0.15
BGF	0.05	0.05	0.05
3-track events	0.75	0.11	0.20
ISR- γ -corr.	0.03	0.02	0.02
$E_{meas}, E_{pred} > 3 \text{ GeV}$	0.19	0.17	0.18
int. conversion correction	0.45	0.07	0.20
sum with $\frac{E_{meas}}{E_{pred}}$	1.42	0.41	0.55
sum with $E_{meas}, E_{pred} > 3 \text{ GeV}$	0.91	0.27	0.37

Table 5.7: Systematic uncertainties for the photon inefficiency difference between data and simulation in units of 10^{-2} .

5.2.7 MC Correction

In order to correct the observed MC-data difference, efficient as well as inefficient events have been re-weighted. The weight of an event is determined by the prediction of the polar angle of the photon. Fig. 5.28 (left) demonstrates that the re-weighting procedure works properly.

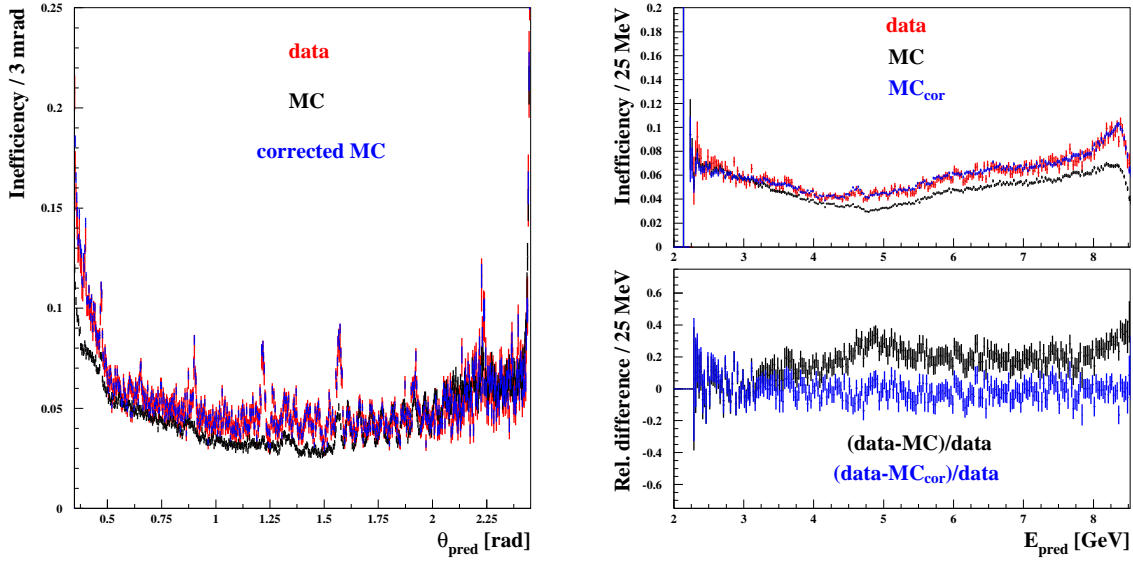


Figure 5.28: Left: photon inefficiency in dependence of θ for data (red), simulation (black) and re-weighted simulation (blue); Top right: photon inefficiency in dependence of the predicted photon energy for data (red), simulation (black) and re-weighted simulation (blue); Bottom right: relative difference of the photon inefficiency between data and simulation (black) and re-weighted simulation (blue).

A priori, a one-dimensional correction according to the photon's polar angle needs not be sufficient. It might be necessary to perform a two dimensional correction according to, e.g. the polar angle and the energy of the photon. Fig. 5.28 (right, top) shows the energy distribution before and after the correction according to the polar angle. After the correction the distributions agree to high precision. The chosen approach, to correct as a function of the photon's polar angle, is sufficient, as shown in Fig. 5.28 (right, bottom).

5.2.8 Conclusion

A photon inefficiency difference between data of $(0.79 \pm 0.02_{\text{stat}} \pm 0.41_{\text{syst}}) \cdot 10^{-2}$ in the barrel and $(2.70 \pm 0.08_{\text{stat}} \pm 1.42_{\text{syst}}) \cdot 10^{-2}$ in the end-cap is observed in this study. This leads to an average of $(1.00 \pm 0.02_{\text{stat}} \pm 0.55_{\text{syst}}) \cdot 10^{-2}$. Using the ISR photon requirement, the inefficiency difference is $(1.34 \pm 0.03_{\text{stat}} \pm 0.37_{\text{syst}}) \cdot 10^{-2}$. Since the difference is not distributed uniformly over the detector, it has to be corrected as a function of the polar angle of the photon as described in section 5.2.7.

5.3 Tracking Efficiency

In the previous sections, it is demonstrated that the reconstruction efficiency of the high energetic photon in ISR events is understood with an uncertainty of 0.4%. For the cross section measurement of $\sigma(e^+e^- \rightarrow \pi^+\pi^-\pi^+\pi^-\gamma)$, four charged tracks are present in a properly reconstructed signal event. A precise knowledge of the track reconstruction efficiency is therefore particularly important. Potential differences between data and MC of the tracking system (DCH and SVT) have to be understood and quantified. The tracking efficiency has previously been studied at *BABAR* with a sample of $e^+e^- \rightarrow \tau^\pm(\rightarrow \pi^\pm\nu_\tau)\tau^\mp(\rightarrow \pi^\mp\pi^+\pi^-\nu_\tau)$ events. The idea of this so-called τ_{31} study is to compare the number of reconstructed 3-track events to 4-track events in the final state in order to extract the tracking efficiency. It has been demonstrated that simulation and data agree within systematic uncertainties to the level of 0.3-0.4%. However, due to the specific ISR back-to-back topology of the high energetic photon and the hadronic system, the track overlap probability in ISR events is strongly enhanced in comparison to the $\tau\tau$ events. It needs to be tested whether this effect is sufficiently well simulated or demands additional corrections. These corrections are depending on the track-multiplicity and the momentum spectrum of the tracks.

Similar to the τ_{31} study, the essential point of this ISR study is the selection of two clean samples of $\pi^+\pi^-\pi^+\pi^-\gamma$ and $\pi^+\pi^-\pi^\pm\gamma$ events. In the three track sample, one track is lost due to either nuclear interaction or failed reconstruction of the track. Using energy and momentum conservation in a kinematic fit, the kinematic variables of the missing track are predicted.

By calculating the ratio of number of lost tracks $N_{lost\ tracks}$ to the total number of tracks N_{tracks} in the same phase-space volume element $\Delta\mathcal{V}$, the tracking inefficiency η , equation (5.13), and the tracking efficiency ϵ , equation (5.14), are obtained:

$$\eta = \frac{N_{lost\ tracks}(\Delta\mathcal{V})}{N_{tracks}(\Delta\mathcal{V})} \quad (5.13)$$

$$\epsilon = 1 - \eta \quad (5.14)$$

A sensible choice of variables to describe the phase space \mathcal{V} are the polar angle of the track θ_{ch} and the corresponding transversal momentum p_t . Additional variables, which are sensitive to the track overlap probability, will be introduced in Section 5.3.4.

5.3.1 Event Selection

The standard ISR pre-selection described in Chapter 4 is used to select event candidates. The most important feature for the track reconstruction efficiency is the definition of a track which is the same as for the $\sigma(e^+e^- \rightarrow \pi^+\pi^-\pi^+\pi^-\gamma)$ cross section analysis:

- $0.4 \text{ rad} < \theta_{ch} < 2.45 \text{ rad}$,

- $\text{DocaXY} < 1.5 \text{ cm}$,
- $\Delta Z < 2.5 \text{ cm}$,
- $p_t > 0.1 \text{ GeV}/c$.

The selection criteria for charged tracks require that the polar angle θ_{ch} is in the well-understood acceptance region of the detector ($0.4 \text{ rad} < \theta_{ch} < 2.45 \text{ rad}$) and that they originate from the collision region. The latter is the case if the transverse distance of closest approach to the event vertex (DocaXY) – or nominal interaction point if no primary event vertex is found – is smaller than 1.5 cm and the distance in beam direction (ΔZ) smaller than 2.5 cm. Tracks with transverse momentum less than $100 \text{ MeV}/c$ are rejected.

The pre-selected events are subdivided into a 3-track and 4-track sample according to the following criteria:

3-track sample: Events containing exactly three tracks and a total charge of $|Q_{tot}| = 1$.

4-track sample: Events containing four or more tracks. If more than four tracks are found, the four tracks with the smallest DocaXY and a total charge of $|Q_{tot}| = 0$ are chosen. Events with up to 7 tracks are considered.

The essential point in this efficiency study is to clean the $\pi^+\pi^-\pi^\pm(\pi^\mp)\gamma$ data sample from background channel contributions. In order to estimate the background contributions, a large number of background processes are studied with simulation. As for the cross section analysis, the background channels are divided into two types: ISR background and non-ISR background. For non-ISR background contributions, a JETSET [109] MC simulation was used in order to simulate $e^+e^- \rightarrow q\bar{q}$ events, the continuum background (*uds*). The $\tau\tau$ MC sample was produced with KORALB [110]. The ISR channels were simulated with the AFKQED generator package [94]. The number of available MC and the corresponding effective cross sections are listed in Table 5.8. These MC distributions are normalized according to the luminosity of data.

The best signal selection tool is a kinematic fit using the $\pi^+\pi^-\pi^+\pi^-\gamma$ hypothesis, which is performed for each event. The fit in case of the 4-track events sample contains the four tracks, the ISR photon and the kinematic information of the incoming electron and positron. Energy and momentum conservation lead to four constraints (4C). For 3-track events, the momentum and angle of the fourth, missing, particle are determined by means of the kinematic fit. The kinematic information of the fourth track is not available. The only remaining constraint is the imposed π -mass, leading to a one-constraint fit (1C).

Additional selection requirements are listed in Table 5.9. The requirements on the number of tracks N_{tracks} and total charge $|Q_{tot}|$ have already been discussed. The $\chi^2_{4\pi}$ requirements are discussed in the following. Fig. 5.29 displays the invariant mass distributions of data and the different MC channels in the $\pi^+\pi^-\pi^+\pi^-\gamma$ hypothesis. The selection on the invariant mass $1.2 \text{ GeV}/c^2 < M_{4\pi} < 2.4 \text{ GeV}/c^2$ suppresses mainly $\pi^+\pi^-\gamma$, $\pi^+\pi^-\pi^0\gamma$ at low masses and $\tau\tau$, $\omega\pi^+\pi^-\gamma$, $K_s^0 K^\pm \pi^\mp \gamma$ and *uds*-continuum background channels at

final state	σ , pb	events in 454.4 fb $^{-1}$	N_{MC}	3 - track events		4 - track events	
				signal	control	signal	control
$\pi^+\pi^-\gamma$	21.4	9.7M	69.8M	1240	242	45	21
$\pi^+\pi^-\pi^0\gamma$	2.6	1.2M	7.9M	682	95	78	55
$\pi^+\pi^-\pi^0\pi^0\gamma$	3.7	1.7M	3.5M	748	76	1	3
$\pi^+\pi^-\pi^+\pi^-\pi^0\gamma$	0.9	410k	473k	2588	473	233	451
$\pi^+\pi^-\pi^+\pi^-\pi^0\pi^0\gamma$	3.4	1.5M	137k	591	102	0	0
$K_s^0 K^\pm \pi^\mp \gamma$	0.3	140k	978k	463	35	790	200
$K^+ K^- \pi^+ \pi^- \gamma$	0.6	270k	100k	188	50	105	144
$\pi^+\pi^-\pi^+\pi^-\pi^+\pi^-\gamma$	0.7	220k	357k	15	7	0	5
SUM (ISR)				5915	1080	1252	876
uds	2090	950M	874.9M	926	566	830	235
$\tau\tau$	890	404M	382.6M	1071	2516	0	1
SUM (non-ISR)				1997	3082	830	236
$\pi^+\pi^-\pi^+\pi^-\gamma$	3.0	1.36M	3.5M	12700	1600	170906	12656
DATA	-	-		30079	9394	170986	13534

Table 5.8: Summary of the background contributions to $\pi^+\pi^-\pi^+\pi^-\gamma$ from other ISR and non-ISR processes for Runs 1-6. The individual final states and its cross cross section are shown as well as the resulting number of events corresponding to the data luminosity of 454.4 fb $^{-1}$. Column 4 displays the amount of available MC eventually scaled down to the corresponding expected number in column 3. The four columns on the right hand side reflect the number of background events in the signal and control region after all requirements for the 3-track and 4-track samples.

3-track sample	4-track sample
$N_{tracks} = 3$	$3 < N_{tracks} \leq 7$
$ Q_{tot} = 1$	$ Q_{tot} = 0$
$\chi^2_{4\pi,1C} < 3$	$\chi^2_{4\pi,4C} < 30$
$1.2 \text{ GeV}/c^2 < M_{4\pi} < 2.4 \text{ GeV}/c^2$	
$\Delta\psi > 1.0 \text{ rad}$	
$N_K < 1$	$N_K < 2$
$\chi^2_{2K2\pi} > 30$	

Table 5.9: Applied selection criteria for the 3- and 4-track sample.

high masses, while only removing a small fraction of signal events. The requirement on the smallest angle between the tracks and the ISR photon $\Delta\Psi > 1.0 \text{ rad}$ ensures the characteristic back-to-back topology of ISR events. After these selections, additional requirements are used in order to specifically remove the $K^+ K^- \pi^+ \pi^- \gamma$ contribution,

namely in form of an additional kinematic fit in the $2K2\pi$ -hypothesis and a veto on the output a dedicated K -PID algorithm.

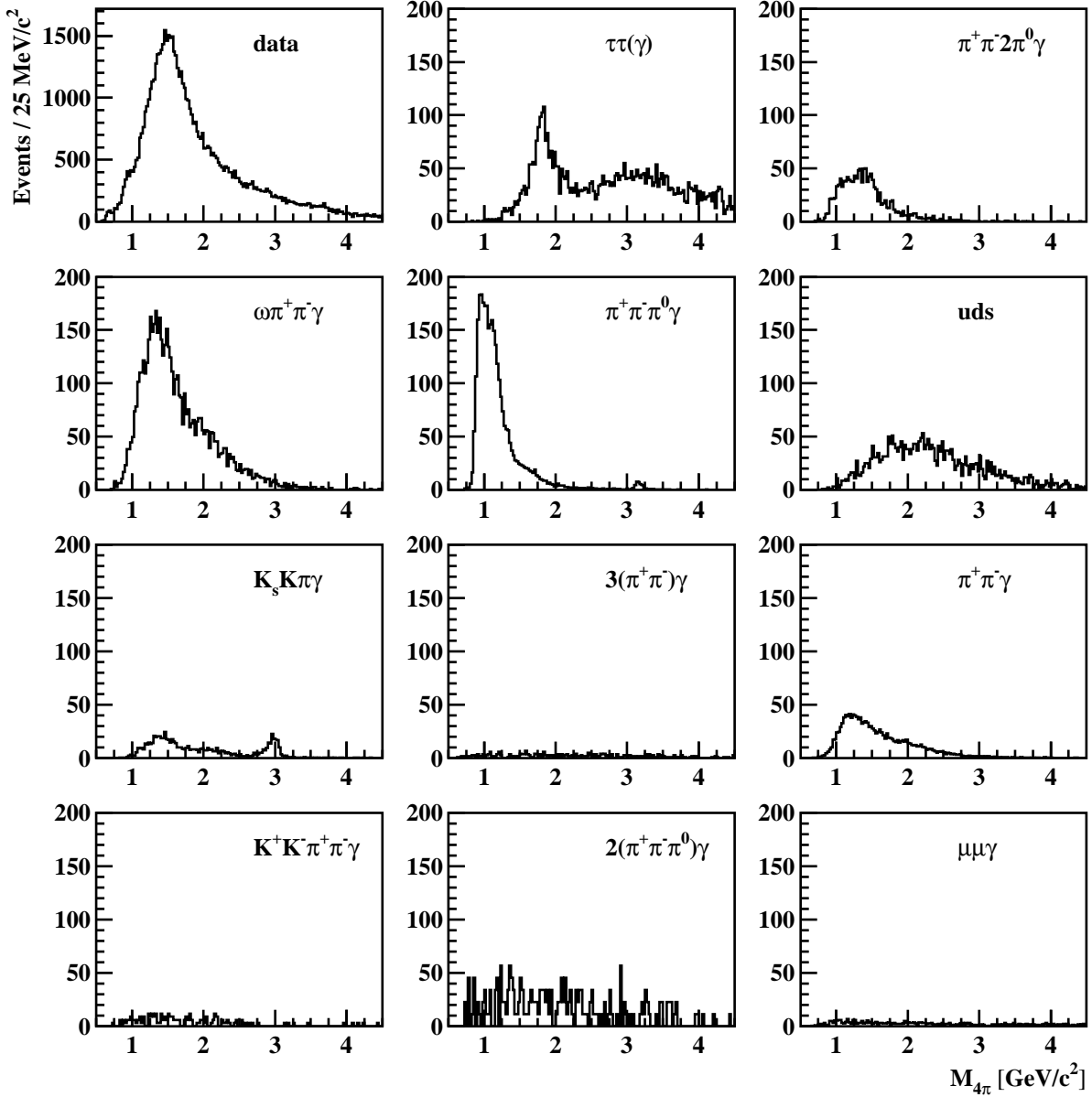


Figure 5.29: Invariant mass distributions in the $\pi^+\pi^-\pi^+\pi^-$ hypothesis $M_{4\pi}$ for the 3-track samples of MC. The fourth track is predicted by the kinematic fit. The individual MC distributions are scaled to the luminosity in data according to their cross section. Distributions are shown before the $1.2 \text{ GeV}/c^2 < M_{4\pi} < 2.4 \text{ GeV}/c^2$ requirement is applied.

After having applied the selection criteria except the $\chi^2_{4\pi,4C}$ requirement listed in Table 5.9, the resulting $\chi^2_{4\pi,4C}$ for the 4-track sample is shown in Fig. 5.30 for data, signal MC and the sum of background MC. The amount of background in comparison to data is negligible. The resulting $\chi^2_{4\pi,4C}$ distributions are wider than usual χ^2 distributions with four constraints. This reflects the fact that in addition to the detector resolution, NLO photons are not included in the kinematic fit, thus enlarging the χ^2 values. The contributions from the individual background channels are illustrated in Fig. 5.31. The

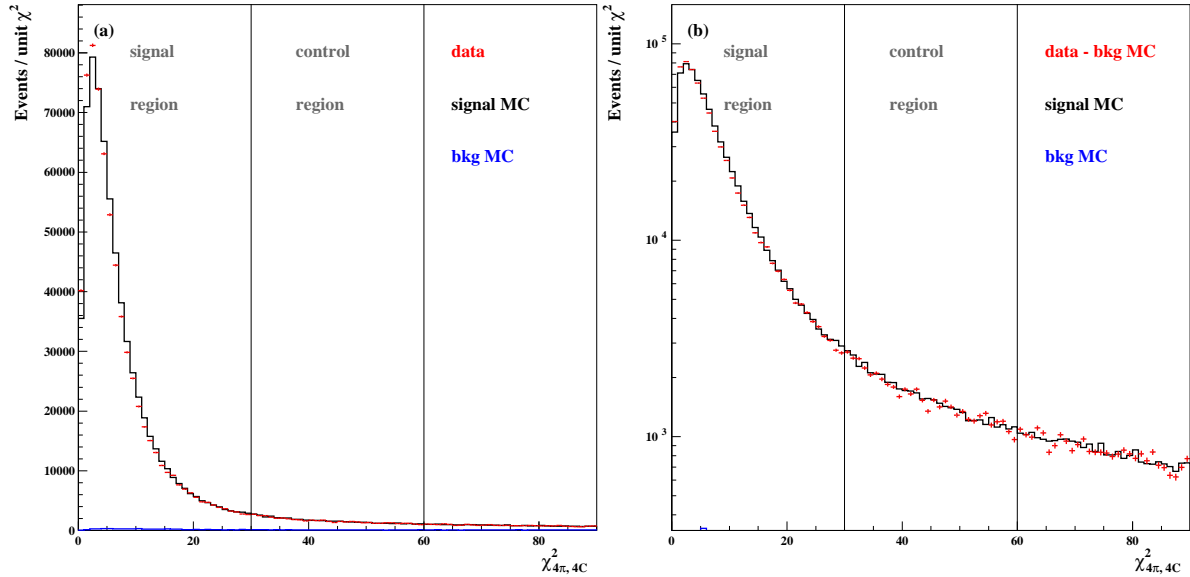


Figure 5.30: $\chi^2_{4\pi, 4C}$ distribution for the 4-track sample (4C fit). Data with subtracted background (red), signal MC (black) and the sum of background MC (blue) are shown.

major background contributions arise from the uds -continuum and $K_s^0 K^\pm \pi^\mp \gamma$ channels.

In Fig. 5.32 the corresponding $\chi^2_{4\pi, 1C}$ are shown for the 3-track sample with the additional constraint that the predicted missing track points to the well-understood acceptance region ($0.5 \text{ rad} < \theta_{\text{ch}} < 2.4 \text{ rad}$). The relative amount of background is much larger, since the kinematic closure of the 4-track sample that suppresses a lot of background is not present. The contributions from the individual background channels are illustrated in Fig. 5.33.

A difference in the integral of the $\chi^2_{4\pi, 1C}$ distributions between the data and MC distribution can be observed in Fig. 5.32 (a) and (b). This leads to the conclusion that more π tracks in data are lost than described by MC, reflecting a difference in tracking inefficiency between data and MC.

Figure 5.32 (c) displays the same $\chi^2_{4\pi, 1C}$ distribution as before for data and simulation. Here signal simulation data are normalized to the number of events in data with $\chi^2_{4\pi, 1C} < 1$ instead of the cross section. A difference in shape between the data and MC $\chi^2_{4\pi, 1C}$ distributions is observed. One reason for this disagreement might be a difference in the NLO photon production. The plateau at large χ^2 values, however, leads to the assumption that not all background is properly subtracted from data. In principle, there are two possible reasons for this plateau. On the one hand, the normalization of the background MC channels according to their cross section has a non-negligible uncertainty. The choice of a too small scaling factor, especially of $\tau\tau$ and uds -continuum, has a significant influence on the tail of the χ^2 distribution. The influence of the scaling factor on the track reconstruction efficiency is estimated in Section 5.3.5. The other possible source for the plateau is additional background with a linear χ^2 behavior. This kind of background is subtracted from the data sample with a sideband subtraction method in χ^2 :

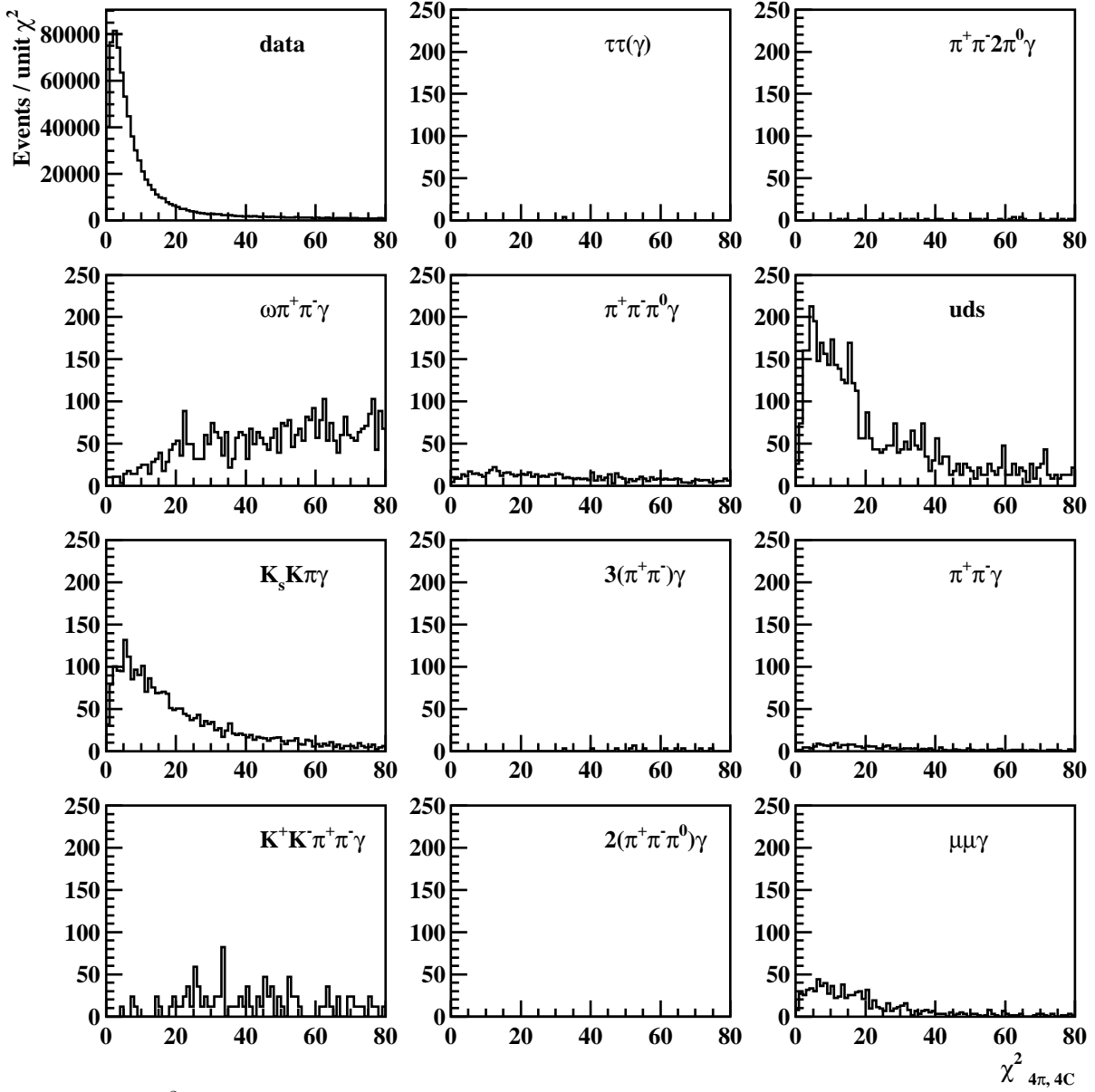


Figure 5.31: χ^2 distribution for data and the individual simulated background contribution in the 4-track sample (4C fit). Simulation data are normalized to the luminosity of data and the corresponding cross section.

The 3- and 4-track samples are sub-divided into two regions according to the χ^2 value, a signal and a control region. These regions were chosen for the 4-track sample as follows:

$$0 < \chi_{4C}^2 < 30 : \text{signal region},$$

$$30 < \chi_{4C}^2 < 60 : \text{sideband region}.$$

The signal region in the 3-track sample for the 1C fit was chosen with the requirement that the fraction of events in the signal region is the same as in the 4C fit signal region for the 4-track sample.

$$0 < \chi_{1C}^2 < 3 : \text{signal region}$$

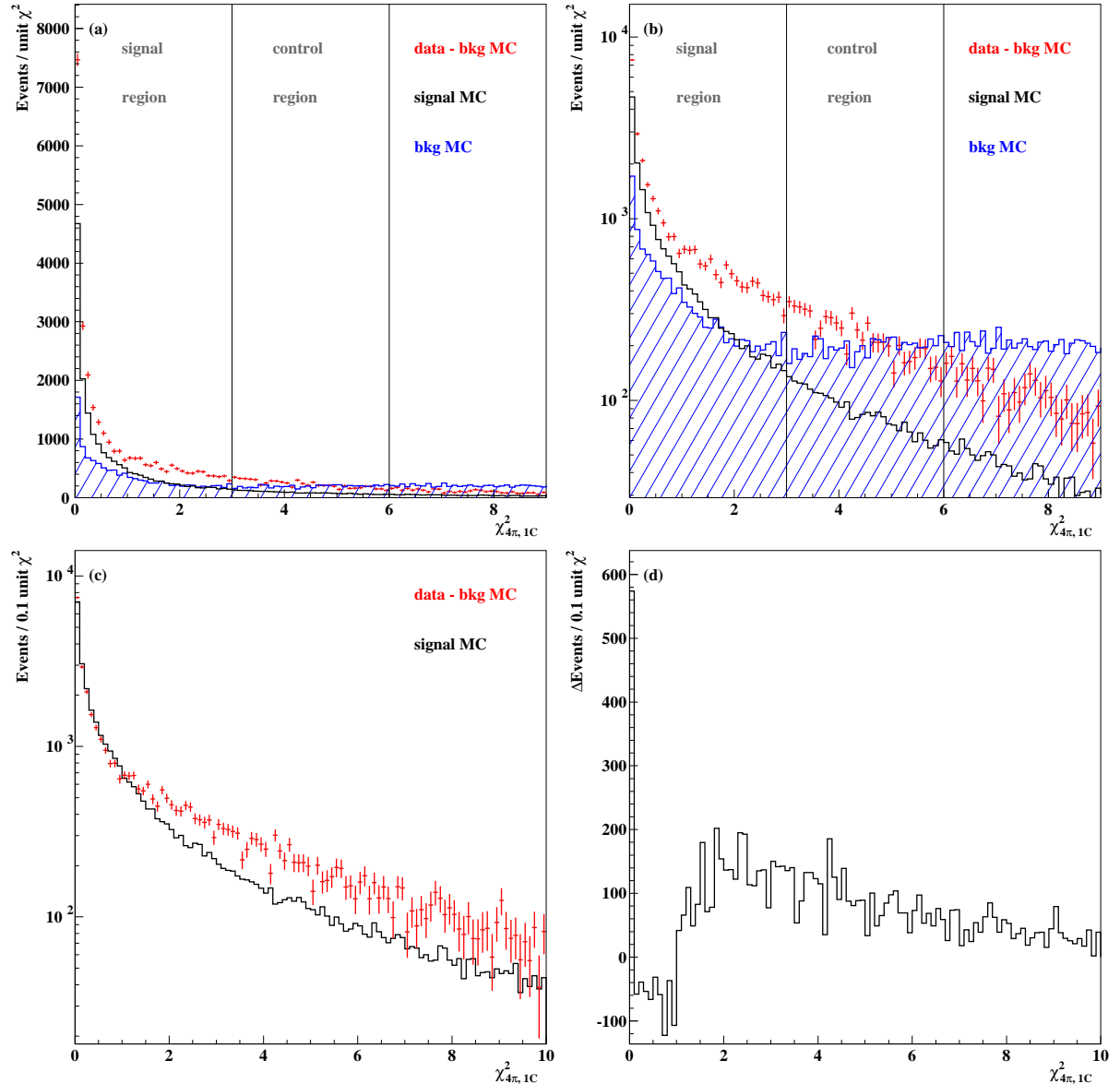


Figure 5.32: χ^2 distribution for events with one missing track in $0.5 \text{ rad} < \theta_{\text{ch}} < 2.4 \text{ rad}$ (1C fit). Data with subtracted background (red), signal MC (black) and the sum of background MC (blue). (c): χ^2 distribution for events with one missing track in $0.5 \text{ rad} < \theta_{\text{ch}} < 2.4 \text{ rad}$ (1C fit) for data after subtraction of background simulation (red) and signal MC (black). The distributions are normalized to the number of events in $\chi^2_{4\pi, 1C} < 1$. (d): difference between the χ^2 distribution between data and signal MC.

$$3 < \chi^2_{1C} < 6 : \text{sideband region}$$

The idea of the sideband subtraction is the following: As illustrated in Fig. 5.34 the sample is divided into the signal region containing N_1 events and the control region containing N_2 events. N_{1s} (N_{1b}) is the number of signal (background) events in the signal region. N_{2s} (N_{2b}) the corresponding number for the control region. Assuming one knows the ratios,

$$a = \frac{N_{2s}}{N_{1s}} \quad \text{and} \quad b = \frac{N_{2b}}{N_{1b}}, \quad (5.15)$$

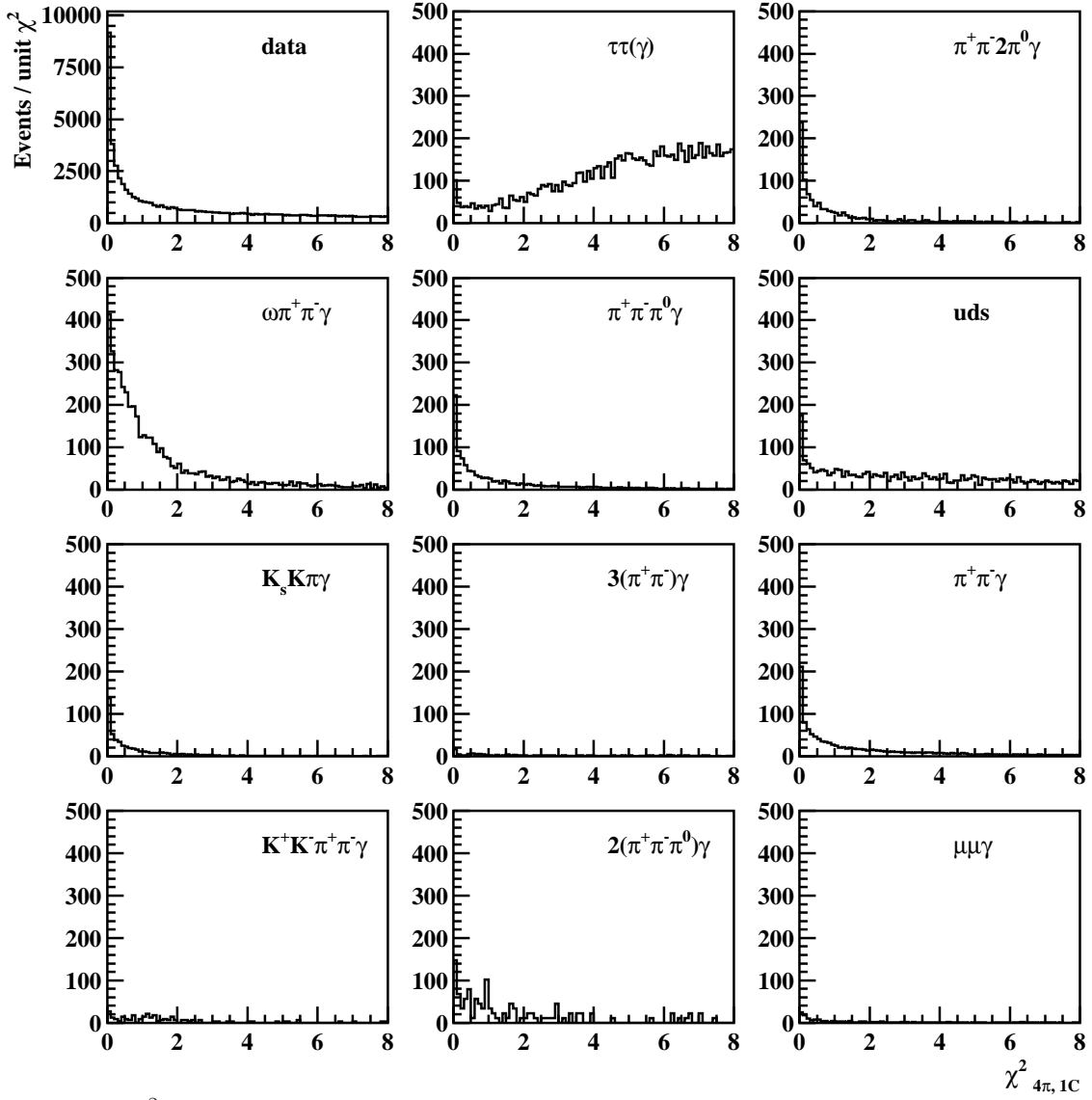


Figure 5.33: χ^2 distribution for data and the individual simulated background contribution in the 3-track sample (1C fit). Simulation data are normalized to the luminosity of data and the corresponding cross section.

the number of signal events can be calculated according to the following equation:

$$N_{1s} = \frac{b \cdot N_1 - N_2}{b - a}. \quad (5.16)$$

In this study, ratio a is determined with signal MC. Ratio b is found according to the following approach: It is assumed that a difference in tracking inefficiency between data and MC would result in a constant scaling factor between the χ^2 distributions in data and MC. Therefore a linear probability density function (PDF) is fitted to the difference between data and a free scaling factor times MC.

The result of the fit for Run 5 is shown in Fig. 5.35 (top) and with an additional zoom in Fig. 5.35 (bottom). In this example, the value for $b = 0.714 \pm 0.021$ with a χ^2 of 117.8 and 98 degrees of freedom is obtained. This corresponds to a χ^2 probability of

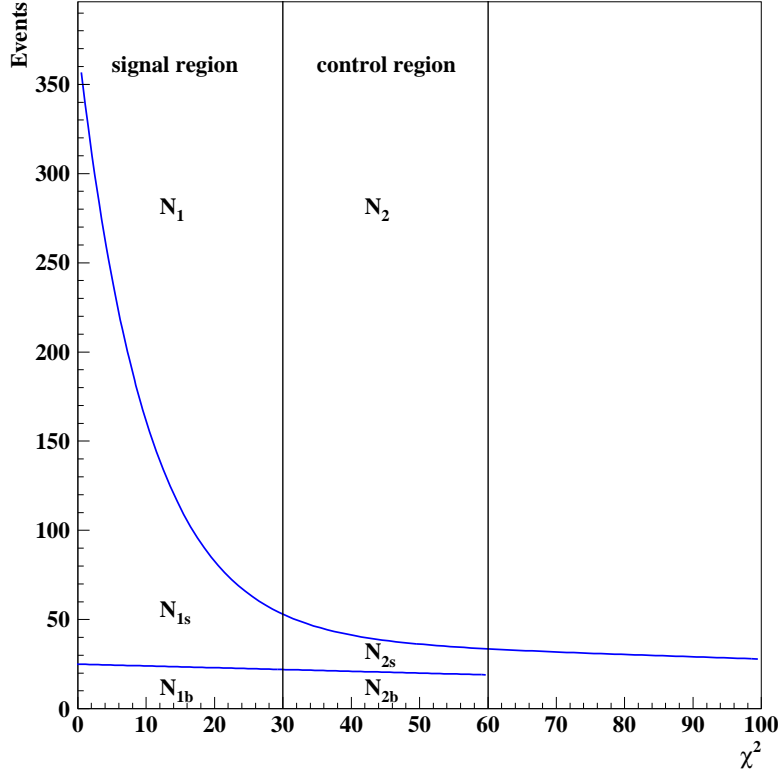


Figure 5.34: Illustration of the sideband subtraction method.

0.09. The small discrepancy of the reduced χ^2 from 1 indicates that there is still a small amount of peaking background in the data sample. This is very likely due to uncertainties in the knowledge of the cross section of the subtracted peaking MC background channels.

To summarize, the procedure is first to remove the largest background identified with the help of simulation. The scaling factor of the individual MC background channels is varied, corresponding to the uncertainty in knowledge of the cross section. The influence of the scaling factor variation on the track reconstruction efficiency is used as systematic uncertainty as described in Section 5.3.5. Additional linear background contributions in χ^2 are removed via the method of sideband subtraction.

5.3.2 Kinematic Distributions

The tracking inefficiency is investigated as a function of the polar angle θ_{ch} and the transverse momentum p_t of the tracks. Figure 5.36 (a) shows the polar angle distribution of tracks from the 4-track sample for data, signal MC, and the sum of all background contributions. The very small background contribution in this case is already subtracted from data. All four tracks have been properly reconstructed. The shape of the distribution reflects the ISR topology of the events. Towards the borders $\theta_{ch} = 2.4$ rad and $\theta_{ch} = 0.5$ rad the distribution decreases. The hadronic system in ISR events is back-to-back to the high energetic photon and confined into a rather small cone. If one track is close to the border, the probability that several other tracks are outside the selected

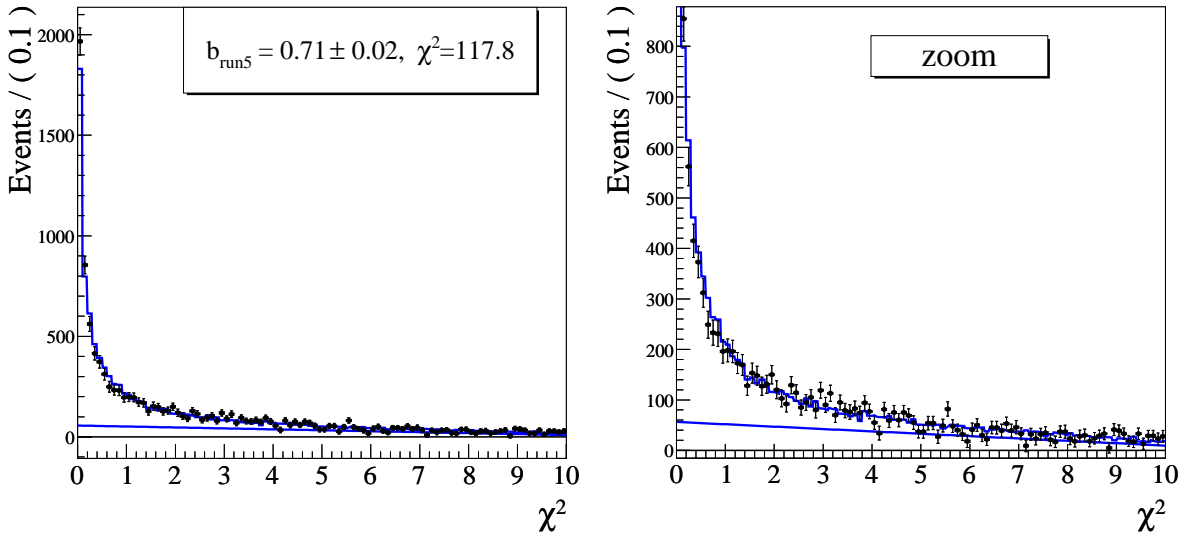


Figure 5.35: Upper plot: fitting signal MC (blue histogram) and a linear background (blue line) to data (black points); lower plot: the same distribution with zoom. The number of degrees of freedom for the fit is 100.

region or that the event is neither in the 4-track nor in the 3-track sample is strongly increased. In addition, it is visible that the data distribution drops below the MC value at large polar angles. This is most likely due to the difference in photon efficiency between data and MC. Due to the back-to-back topology of ISR events, photons in the forward region of the detector correspond to tracks in the backward region. In the forward region photon reconstruction in data is less efficient than in simulation due to imperfections in the material description. Therefore, in the backward region fewer tracks are expected in data than in simulation.

Figure 5.36 (b) shows the same distribution for the detected tracks in the 3-track sample, indicating the same features as in the 4-track sample. More events are present in data than in signal MC, indicating that the tracking inefficiency is different in data and MC. In Fig. 5.36 (c), the undetected tracks are displayed. Again, it is seen that more tracks are missing in data than in MC. A large fraction is not detected, because the track was simply located outside the acceptance region of the tracking system, causing the two bumps at very small and large polar angles. The tracking efficiency is studied in the following for all tracks inside the well-understood acceptance region ($0.5 \text{ rad} < \theta_{\text{ch}} < 2.4 \text{ rad}$).

For these tracks the transverse momentum p_t distributions are shown in Fig. 5.37 (a) for the 4-track sample, again for data, signal MC, and the sum of background contributions. The distribution is peaked at $p_t \approx 0.7 - 0.8 \text{ GeV}/c$. A good agreement between data and MC is visible. The detected tracks in the 3-track sample are shown in Fig. 5.37 (b). In Fig. 5.37 (c), it is visible that, as expected, the p_t distribution for the missing tracks is peaking at small transverse momenta.

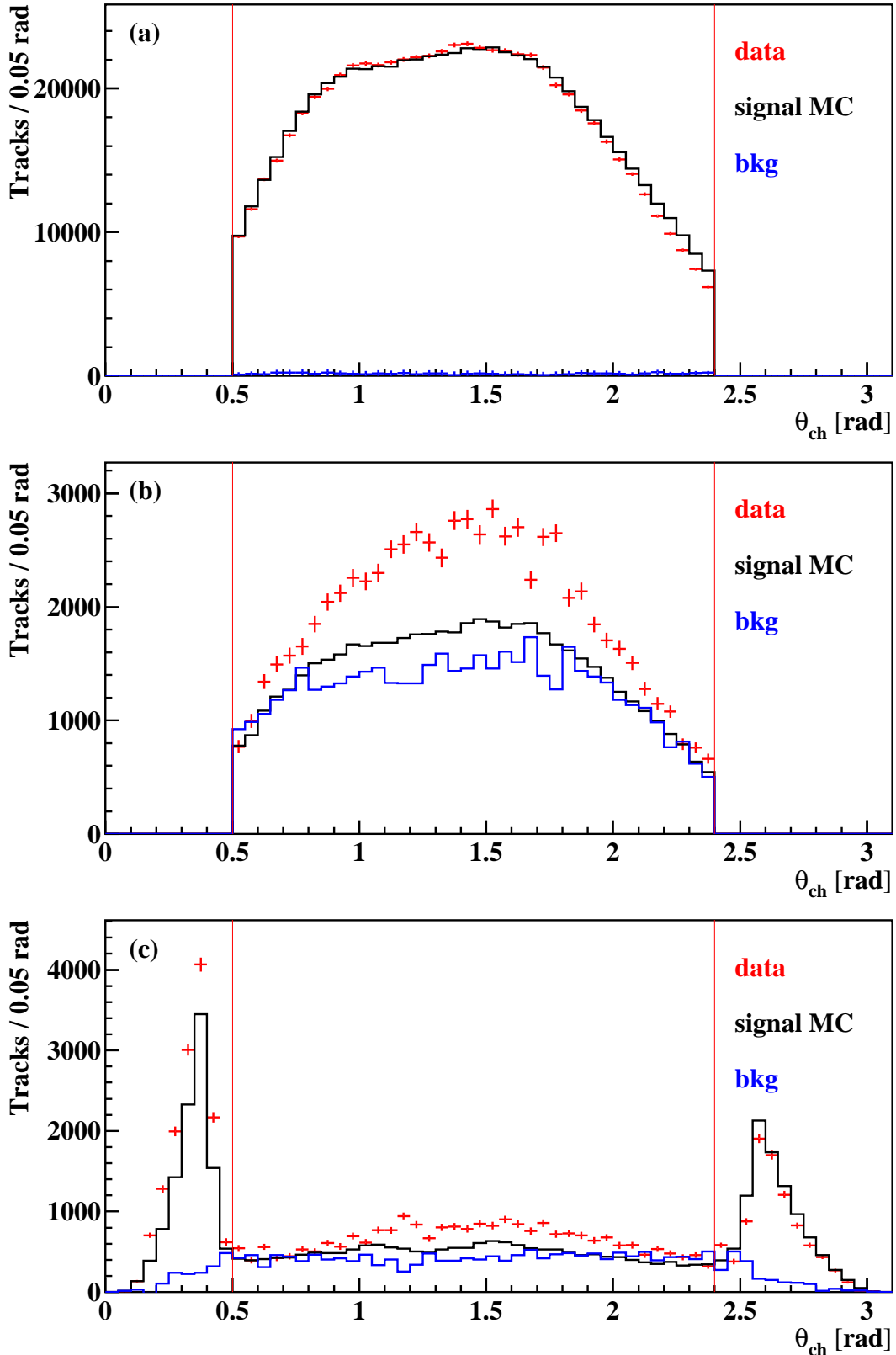


Figure 5.36: (a): polar angle distributions of background-subtracted data (red), signal MC (black) and the sum of background contributions including sideband subtraction (blue) in the 4-track sample; (b): corresponding distributions for the detected tracks in the 3-track sample. (c): prediction of the polar angle of the missing track in the 3-track sample.

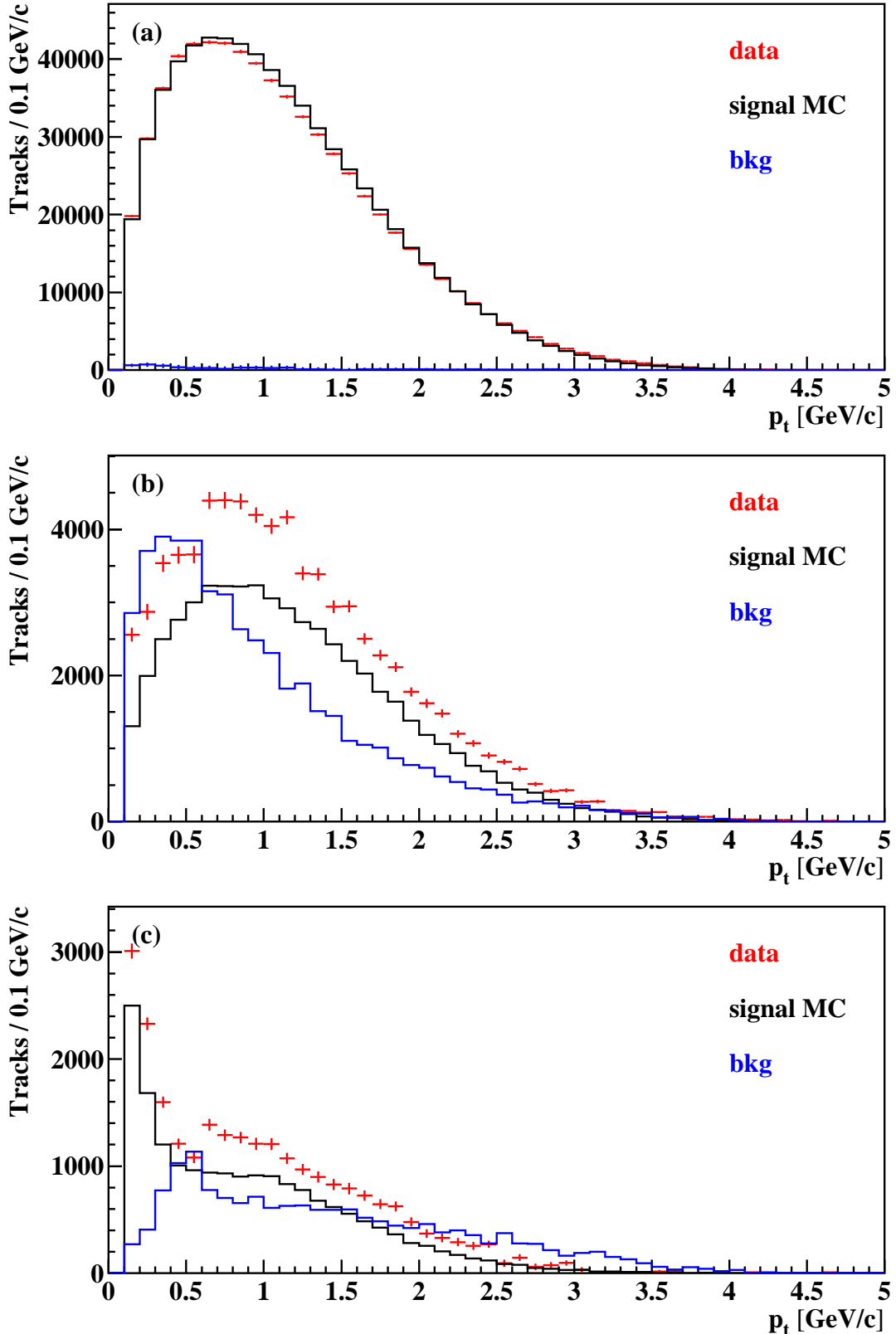


Figure 5.37: (a): transverse momentum distribution of background-subtracted data (red), signal MC (black) and the sum of background contributions including sideband subtraction (blue) in the 4-track sample for tracks within the well-understood acceptance region ($0.5 \text{ rad} < \theta_{\text{ch}} < 2.4 \text{ rad}$); (b): corresponding distributions for the detected tracks in the 3-track sample. (c): prediction of the transverse momentum of the missing track in the 3-track sample.

5.3.3 Tracking Inefficiency

The tracking inefficiency η is obtained according to equation 5.14. In case of the study as a function of the polar angle θ , it is the ratio of Fig. 5.36 (c) and the sum of histograms (a)-(c) for data and signal MC. The obtained inefficiency is shown in Fig. 5.38 (a) for events with all tracks pointed into the polar angular range $0.5 \text{ rad} < \theta < 2.4 \text{ rad}$. The same procedure is applied for the kinematic distributions in dependence of p_t with the corresponding inefficiency displayed in Fig. 5.38 (b) for the data and the MC simulation.

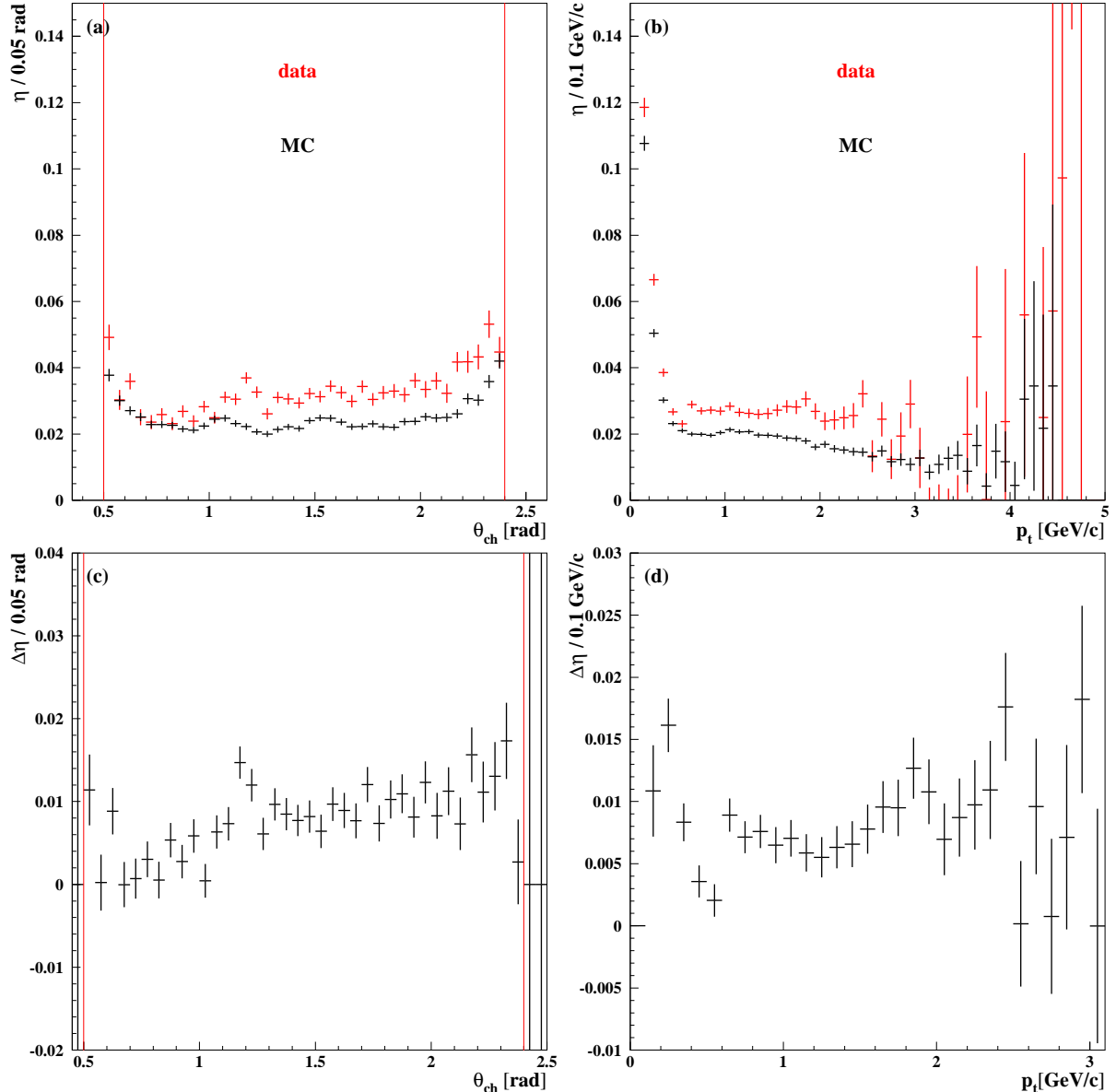


Figure 5.38: Tracking inefficiency in dependence of θ_{ch} (a) and p_t (b) for data (red) and signal MC (black), all runs. Absolute difference of the tracking inefficiency between data and MC in dependence of θ_{ch} (c) and p_t (d) between data and MC.

The difference in tracking inefficiency per track between data and MC for Runs 1-6 is determined as:

$$\Delta\eta_{Run1} = 0.0104 \pm 0.0013_{stat} \pm 0.0047_{syst}$$

$$\Delta\eta_{Run2} = 0.0059 \pm 0.0007_{stat} \pm 0.0047_{syst}$$

$$\Delta\eta_{Run3} = 0.0026 \pm 0.0010_{stat} \pm 0.0046_{syst}$$

$$\Delta\eta_{Run4} = 0.0066 \pm 0.0006_{stat} \pm 0.0040_{syst}$$

$$\Delta\eta_{Run5} = 0.0068 \pm 0.0005_{stat} \pm 0.0048_{syst}$$

$$\Delta\eta_{Run6} = 0.0099 \pm 0.0008_{stat} \pm 0.0054_{syst}$$

Analysing the total data sample (Runs 1-6) leads to the following inefficiency difference between data and MC:

$$\Delta\eta = (0.75 \pm 0.05_{stat} \pm 0.34_{syst}) \cdot 10^{-2}$$

Figure 5.38 (c) and (d) show the absolute tracking inefficiency difference between data and MC. The dependence on p_t (d) is flat within the uncertainties of 0.4%. A slight dependence on the polar angle in Fig. 5.38 (c) is visible with almost no difference between data and MC in the forward region at small polar angles and a difference of approximately 1% in the backward region. Due to the beam energy asymmetry at *BABAR*, high energy photons are preferably emitted in the forward direction. In ISR events the hadronic system is emitted back-to-back to the ISR photon. The energy of the photon is correlated to the opening angle of the cone of the hadronic system. This correlation leads to an increasing track overlap probability at large polar angles. The track loss due to track overlap seems to be not perfectly modeled in simulation. This will be further discussed in the following.

5.3.4 Track Overlap Corrections

The tracking efficiency, determined in Chapter 5.3.3, is perfectly suited for the $\pi^+\pi^-\pi^+\pi^-\gamma$ analysis. It is, however, of interest for other *BABAR* analyses and also for a better understanding of the tracking inefficiency differences between data and MC to further investigate this effect. In comparison to other *BABAR* analyses, ISR events have typically a rather large track overlap probability, because the final state hadrons are confined to a narrow cone opposite to the ISR photon. In the following, it is shown that the difference between data and MC is mostly due to track overlap. This track overlap strongly depends on the investigated physics channel. The single track loss effect is sub-divided in the effect of overlap of two tracks with opposite charge (**OC**) and overlap of two tracks with the same charge (**SC**). In this study, only events with at least three detected tracks are included. According to simulation, double or multiple losses are negligible.

Single Loss Due to Oppositely Charged Tracks

One important effect that has to be investigated is the single track loss due to overlapping tracks with opposite charges. A good variable to describe OC track overlap is $\Delta\phi_{OC} = \phi(\pi_{1,2}^+) - \phi(\pi_{1,2}^-)$. It is the signed difference azimuthal angle between the lost track and the reconstructed track with opposite charge: It is always taken to be the difference between the angle of the positively charged pion and the negatively charged pion. Since in this study there are always two pions with the opposite charge of the missing pion present, two combinations are obtained for each event. In Fig. 5.39 (a) the $\Delta\phi_{OC}$ distribution is plotted for all Runs.

Without the additional reconstruction inefficiency due to track overlap, a symmetric distribution around 0 is expected. The distributions, however, show a clear asymmetry. The distribution is a superposition of the distribution due detection inefficiency and a peaking distribution at small positive values for $\Delta\phi_{OC}$ due to track overlap losses. The number of tracks lost due to track overlap can be estimated by determining the difference of number of events on the right and left side. Reflecting the $\Delta\phi_{OC} < 0$ distribution through the axis $\Delta\phi_{OC} = 0$ demonstrates the asymmetry of the $\Delta\phi_{OC}$ distribution. This process is illustrated for simulation in Fig. 5.39 (b).

Single Loss Due to Same Charged Tracks

The next step is the investigation of single track loss due to overlapping tracks with the same charge (SC). A good variable to describe SC track overlap is $\Delta\phi_{SC} = |\phi(\pi_1^\pm) - \phi(\pi_2^\pm)|$. It is the azimuthal angle between the lost track and the reconstructed track with the same charge. In this case only one entry per event is expected. In Fig. 5.39 (c) and (d), the angle between lost track and reconstructed track with the same charge in the 3-track sample is plotted for data and MC, respectively. The corresponding distribution for the two detected tracks is also shown. Again the peak at small $\Delta\phi_{SC}$ is due to single loss induced by overlapping tracks. The distribution with one lost track is therefore the superposition of the distribution due to detection inefficiency and a peaking distribution at small $\Delta\phi_{SC}$ due to track overlap losses. The distribution due to usual detection inefficiency has the same $\Delta\phi_{SC}$ dependence as the distribution of the two measured tracks. The number of tracks lost due to track overlap is estimated by scaling down the distribution of the measured tracks until the tails of the distribution match with the distribution including one missing pion. The difference at small $\Delta\phi_{SC}$ is a good estimate for the number of tracks lost due to same-charge track overlap.

Overlap Corrections in Numbers

The number of tracks lost due to track overlap is determined as previously described. Concerning the tracking inefficiency only the numerator of equation 5.13 has to be corrected. The events with one lost track due to overlap are signal events. In principle, they need to be moved from the 3-track sample back to the 4-track sample. The overall number of tracks N_{tracks} therefore remains unchanged. Thus, the inefficiency is corrected

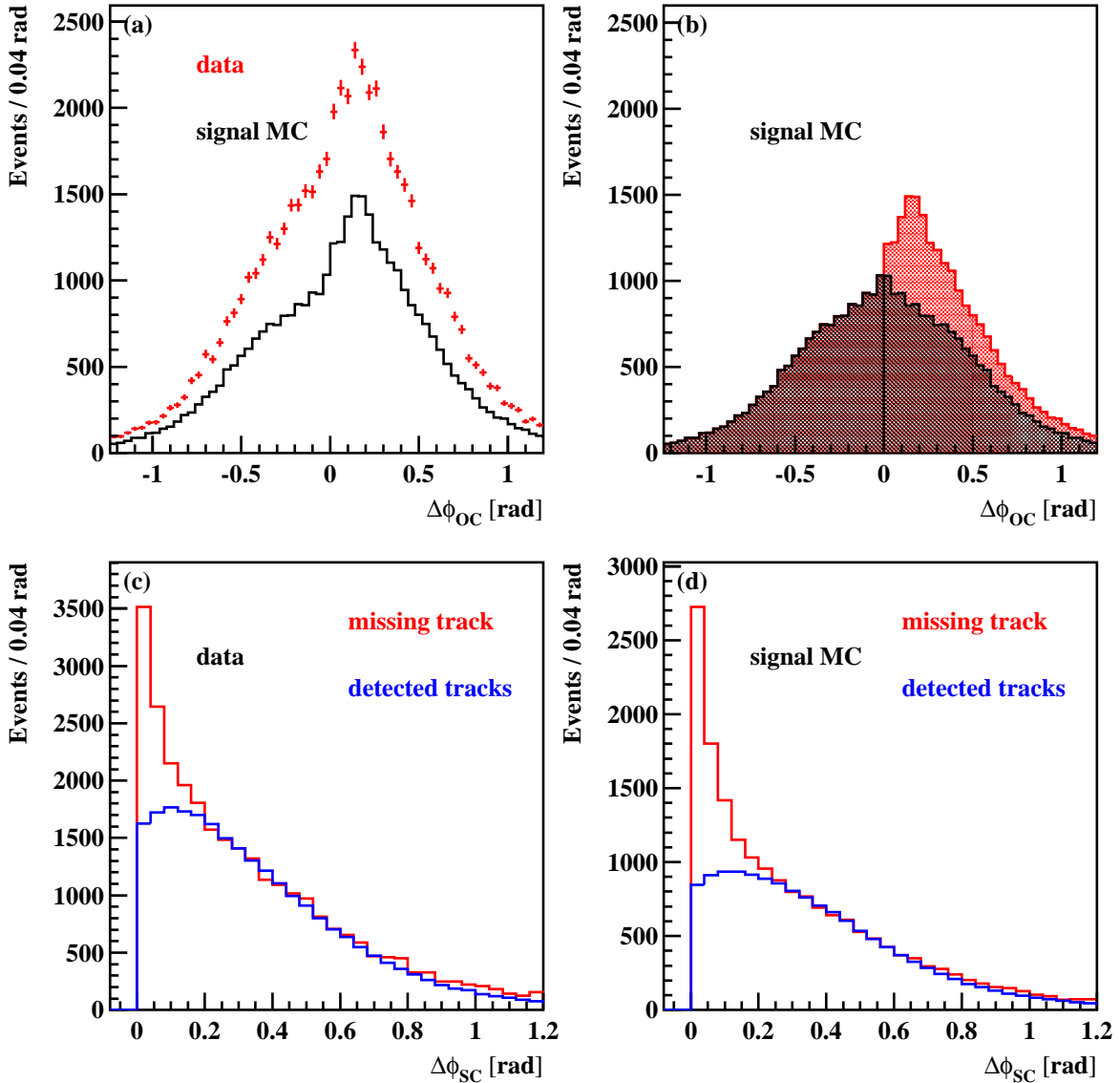


Figure 5.39: Angle between missing pion and detected pions with opposite charge (a) for data (red) and simulation (black); 2 entries per event; (b): illustration of extraction of asymmetry due to overlap of differently charged tracks. (c): angle between the lost track and the reconstructed track (red) with the same charge for data (c) and simulation (d). Corresponding angular difference distribution for detected tracks with the same charge (blue).

as indicated in equation 5.17:

$$\eta = \frac{N_{lost\ tracks}(\Delta\mathcal{V}) - N_{overlapping\ tracks}(\Delta\mathcal{V})}{N_{tracks}(\Delta\mathcal{V})} \quad (5.17)$$

The corrections on the tracking inefficiency for data and MC are applied Run by Run. These corrections for overlapping tracks with opposite charge OC and same charge SC are listed in Table 5.10.

Table 5.10: Corrections on tracking inefficiency for data and MC in percent, Runs 1-6.

Run	η_{data} in 10^{-2}			η_{MC} in 10^{-2}		
	no cor	OC	SC	no cor	OC	SC
1	3.05	-0.51	-0.44	1.97	-0.53	-0.44
2	2.80	-0.76	-0.55	2.16	-0.52	-0.47
3	2.69	-0.96	-0.27	1.92	-0.43	-0.38
4	2.93	-0.72	-0.62	2.17	-0.53	-0.45
5	3.51	-1.03	-0.72	2.68	-0.70	-0.58
6	3.65	-0.87	-0.66	2.67	-0.83	-0.60

Table 5.11: Corrections on tracking inefficiency difference between data and MC in percent, Runs 1-6.

Run	$\eta_{data} - \eta_{MC}$ in 10^{-2}			final value
	no cor	OC	SC	
1	1.07	+0.02	-0.01	1.08
2	0.64	-0.25	-0.08	0.31
3	0.77	-0.53	+0.12	0.36
4	0.77	-0.18	-0.16	0.42
5	0.82	-0.32	-0.14	0.37
6	0.98	-0.04	-0.07	0.87

5.3.5 Estimate of Uncertainties

Statistical Error

The tracking inefficiency η per track can be calculated with equation 5.18:

$$\eta = \frac{N_{lost\,trk}}{N_{lost\,trk} + N_{3trk} + N_{4trk}}, \quad (5.18)$$

with N_{4trk} the number of detected tracks in the 4-track sample, N_{3trk} the number of detected tracks in the 3-track sample, and the number of lost tracks in the 3-track sample $N_{lost\,trk}$. The corresponding numbers to determine the tracking inefficiency for Runs 1-6 are listed in Table 5.12.

The resulting statistical errors on the inefficiency η for data and MC as well as the inefficiency difference $\Delta\eta$ can be found in Table 5.13.

Systematic Uncertainty

As discussed previously, background subtraction is performed in two steps for either peaking or non-peaking background as a function of χ^2 . Peaking background is simulated with

Table 5.12: Numbers to determine tracking inefficiency, Runs 1-6.

Run	data after bkg-subtraction			signal MC			data before bkg-subtraction		
	$N_{losttrk}$	N_{3trk}	N_{4trk}	$N_{losttrk}$	N_{3trk}	N_{4trk}	$N_{losttrk}$	N_{3trk}	N_{4trk}
1	786	2357	34076	554	1663	35429	1447	4341	34848
2	2274	6821	99924	1791	5375	104441	4116	12348	101004
3	1088	3264	55014	807	2421	53980	2152	6456	55708
4	3733	11199	167059	2797	8393	168429	7032	21096	169784
5	6421	19264	214960	4718	14156	218014	10870	32610	218072
6	3122	9367	104038	2220	6662	103333	5280	15840	104528

Table 5.13: Statistical error on tracking inefficiency for data, MC and the difference between data and MC, Runs 1-6.

Run	$\Delta\eta_{data}$	$\Delta\eta_{MC}$	$\Delta(\eta_{data} - \eta_{MC})$
1	0.00117	0.00061	0.0013
2	0.00065	0.00036	0.0007
3	0.00087	0.00047	0.0010
4	0.00051	0.00028	0.0006
5	0.00046	0.00027	0.0005
6	0.00066	0.00039	0.0008

MC, normalized according to the luminosity and subtracted bin by bin in the kinematic distributions. The main uncertainty of this method is determined by the accuracy of the knowledge of the cross section of the individual background channels and the precision of the theoretical model of the MC generator to create the kinematic distributions of these channels. To check this, quantities unrelated to those used so far are compared. The $\tau\tau$ production is very precise: In Fig. 5.40 the minimum angle between the charged tracks and the ISR photon for each event is displayed. For signal events the ISR photon and the hadronic system are mostly back to back. The peak at small angles is dominated by $\tau\tau$ events.

The uncertainty of the cross section is estimated to be smaller than 15%. All other channels are normalized according to their radiative cross sections measured in other *BABAR* analyses. The resulting estimated systematic uncertainties on the knowledge of these cross sections are summarized in Table 5.14. The influence of the background normalization on the difference of the tracking inefficiency between data and MC is listed in Table 5.15 and visualized in Fig. 5.41 (left).

Background that has a linear behavior in χ^2 can be subtracted by means of the sideband subtraction method as described. The advantage of this method is that the cross sections

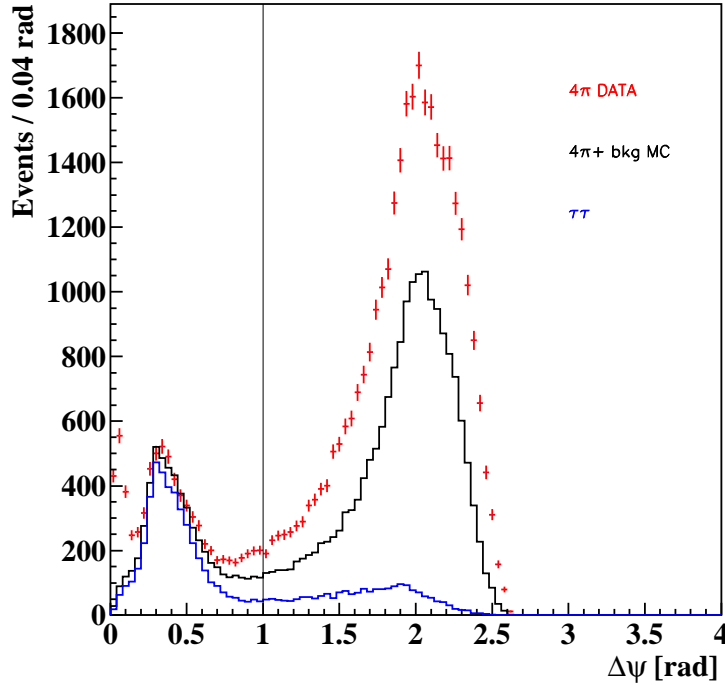


Figure 5.40: Minimum angle between γ_{ISR} and all charged tracks. Data (red), sum of signal and all background MC (black) and contribution of $\tau\tau$ MC (blue) for 3-track events. The vertical line indicates the event selection requirement $\Delta\psi > 1.0$ rad.

Table 5.14: Uncertainty of the cross section scaling factor in simulation.

final state	σ [pb]	estimated precision of σ
$\pi^+\pi^-\gamma$	21.4	5%
$\pi^+\pi^-\pi^0\gamma$	2.6	5%
$\pi^+\pi^-\pi^0\pi^0\gamma$	3.7	10%
$\pi^+\pi^-\pi^+\pi^-\pi^0\gamma$	0.9	40%
$\pi^+\pi^-\pi^+\pi^-\pi^0\pi^0\gamma$	3.4	10%
$K_S^0 K^\pm \pi^\mp \gamma$	0.3	10%
$K^+ K^- \pi^+ \pi^- \gamma$	0.6	10%
$\pi^+\pi^-\pi^+\pi^-\pi^+\pi^-\gamma$	0.7	10%
<i>uds</i> -continuum	2090	40%
$\tau\tau$	890	15%

of these background processes need not to be known. There is, however, an additional complication since the 4-track sample is fitted with a 4C fit, while the 3-track sample uses a 1C fit. Table 5.16 displays the 1C fit signal regions that are equivalent to the listed 4C fit signal regions concerning the fraction of events in the signal region. In Table 5.17 the influence of the choice of the χ^2 signal region on the tracking inefficiency difference between data and MC is listed. The corresponding tracking efficiency variation for the individual Runs is displayed in Fig. 5.41 (right) and summarized in Table 5.17.

Table 5.15: Dependence of tracking inefficiency difference in between data and MC on scaling of background MC.

Run	nominal scaling	high scaling	low scaling	$\sigma_{scaling bkg MC}$
1	0.0064	0.0051	0.0076	0.0013
2	0.0048	0.0035	0.0061	0.0013
3	0.0042	0.0029	0.0054	0.0013
4	0.0049	0.0036	0.0062	0.0013
5	0.0068	0.0055	0.0080	0.0013
6	0.0070	0.0056	0.0083	0.0014

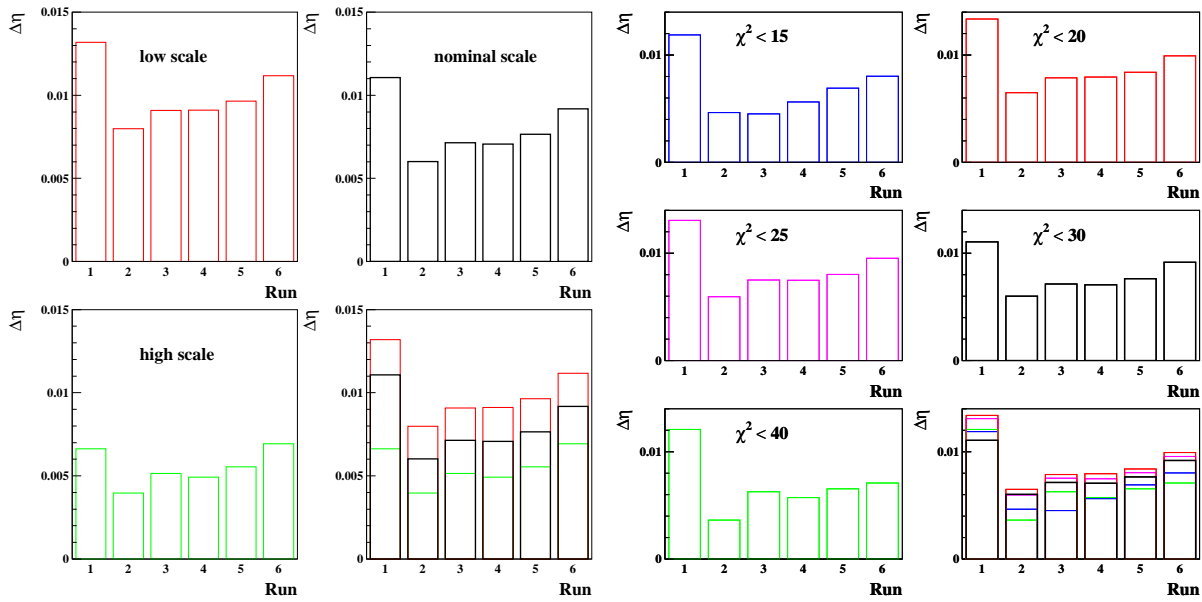


Figure 5.41: Left: dependence of tracking inefficiency difference on scaling of background MC for Runs 1-6. Right: dependence of tracking inefficiency difference on cut of signal region in χ^2 for Runs 1-6.

Fig. 5.42 (left) displays the dependency of the tracking inefficiency difference on the choice of the polar angular region for the detected and missing tracks. The region $0.4 \text{ rad} < \theta_{\text{ch}} < 2.45 \text{ rad}$ was required for the charged tracks. In order to suppress edge effects, the tracking inefficiency is determined in the polar angle region of $0.5 \text{ rad} < \theta_{\text{ch}} < 2.4 \text{ rad}$. In an additional study, effects of the requirements on the invariant mass were investigated. The results are shown in Fig. 5.42 (right). The resulting systematic uncertainty of the tracking inefficiency difference by these requirements is smaller than $0.05 \cdot 10^{-2}$, which is, conservatively taken as estimate for the uncertainty.

Table 5.16: Corresponding regions in 1C and 4C fit ensuring that the fraction of events in signal region is the same in both cases.

boarders of signal/sideband				fraction of events in signal region	
$\chi^2_{signal,4C}$	$\chi^2_{sideband,4C}$	$\chi^2_{signal,1C}$	$\chi^2_{sideband,1C}$	4C	1C
15	30	1.8	3.6	0.741	0.749
20	40	2.2	4.4	0.790	0.785
25	50	2.7	5.4	0.820	0.822
30	60	3.0	6.0	0.841	0.839
40	80	3.7	7.4	0.870	0.871

Table 5.17: Influence of variation of signal region on tracking inefficiency difference between data and MC.

Run	$\chi^2_{sig,4C} < 15$	$\chi^2_{sig,4C} < 20$	$\chi^2_{sig,4C} < 25$	$\chi^2_{sig,4C} < 30$	$\chi^2_{sig,4C} < 40$	$\sigma_{sig\ var}$
1	0.0066	0.0042	0.0061	0.0064	0.0061	0.0022
2	0.0029	0.0024	0.0038	0.0048	0.0052	0.0019
3	0.0025	0.0045	0.0043	0.0042	0.0041	0.0017
4	0.0042	0.0053	0.0047	0.0049	0.0054	0.0007
5	0.0061	0.0060	0.0069	0.0068	0.0072	0.0007
6	0.0061	0.0054	0.0068	0.0070	0.0081	0.0016

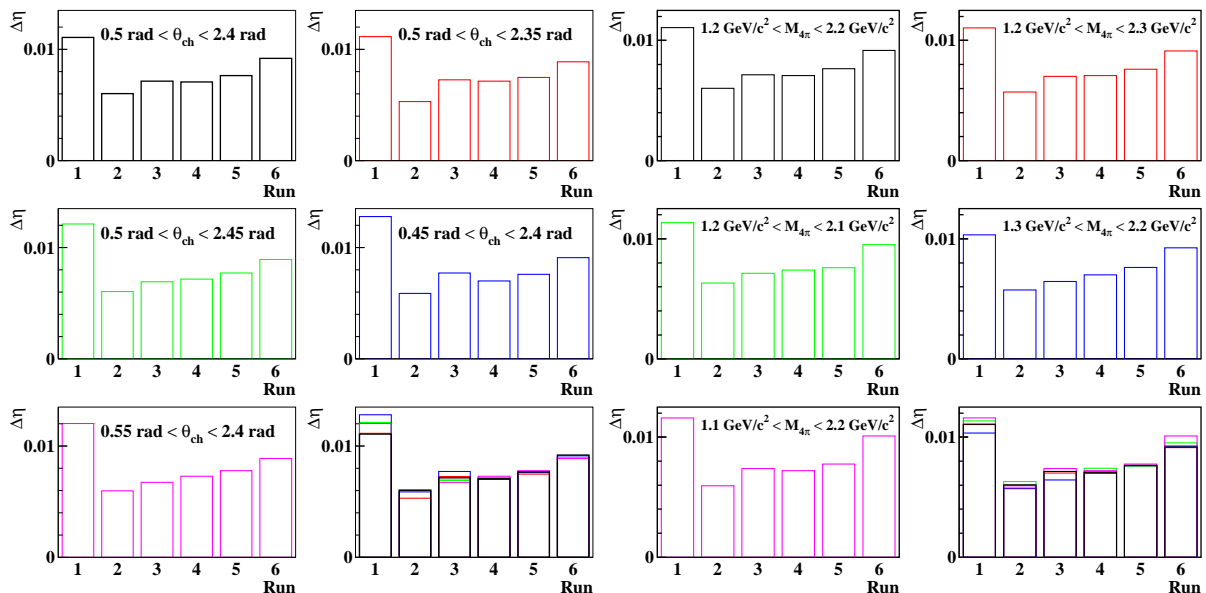


Figure 5.42: Left: dependence of tracking inefficiency difference on polar angular acceptance region for charged tracks for Runs 1-6. Right: dependence of tracking inefficiency difference on invariant mass acceptance region for charged tracks for Runs 1-6.

Finally, the differences in tracking inefficiency per track for Runs 1-6 are determined as:

$$\begin{aligned}\Delta\eta_{Run1} &= 0.0109 \pm 0.0017_{stat} \pm 0.0049_{syst}, \\ \Delta\eta_{Run2} &= 0.0035 \pm 0.0010_{stat} \pm 0.0042_{syst}, \\ \Delta\eta_{Run3} &= 0.0028 \pm 0.0014_{stat} \pm 0.0037_{syst}, \\ \Delta\eta_{Run4} &= 0.0060 \pm 0.0008_{stat} \pm 0.0039_{syst}, \\ \Delta\eta_{Run5} &= 0.0053 \pm 0.0008_{stat} \pm 0.0042_{syst}, \\ \Delta\eta_{Run6} &= 0.0099 \pm 0.0011_{stat} \pm 0.0043_{syst}.\end{aligned}$$

5.3.6 Conclusion

The difference in tracking inefficiency per track including track overlap, averaged over the whole *BABAR* data set, is determined as:

$$\Delta\eta = (0.75 \pm 0.05_{stat} \pm 0.34_{syst}) \cdot 10^{-2}.$$

This inefficiency correction will be used in the following for the cross section measurement of $\sigma(\pi^+\pi^-\pi^+\pi^-\gamma)$. A large fraction of this inefficiency difference is due to not properly described track loss caused by overlap in simulation.

Depending on multiplicity and kinematics, many *BABAR* analyses need the inefficiency without these track overlap effects. This leads to the following result, which is in agreement with the results of the τ_{31} study:

$$\Delta\eta = (0.38 \pm 0.05_{stat} \pm 0.39_{syst}) \cdot 10^{-2}.$$

Chapter 6

Extraction of the Cross Section $\sigma(e^+e^- \rightarrow \pi^+\pi^-\pi^+\pi^-)$

The measurement of the hadronic cross section $\sigma(e^+e^- \rightarrow \pi^+\pi^-\pi^+\pi^-)$ is the main result of this work.

The principal method to extract the hadronic cross section $\sigma(e^+e^- \rightarrow \pi^+\pi^-\pi^+\pi^-)$ is described in detail in Chapter 3. In the beginning of this chapter the systematic corrections and uncertainties are summarized. Then the result for the cross section measurement is presented and compared to previous measurements with a focus on the comparison to the previous *BABAR* publication.

6.1 Summary of Systematic Corrections and Uncertainties

The systematic corrections and uncertainties, e.g. background subtraction, photon and tracking efficiency, and global efficiency, have been discussed in detail. All individual contributions are summarized in Table 6.1, separately for different regions in the invariant $M_{4\pi}$ mass.

Table 6.1: Systematic corrections and uncertainties for the measurement of the $e^+e^- \rightarrow \pi^+\pi^-\pi^+\pi^-$ cross section for different invariant $M_{4\pi}$ mass regions in %.

$M_{4\pi} [\text{GeV}/c^2]$	< 1.1	1.1 – 2.8	2.8 – 4.0	4.0 – 4.5
$K^+K^-\pi^+\pi^-\gamma, K_s^0K^\pm\pi^\mp\gamma$	± 1.0	± 1.0	± 3.0	± 7.0
continuum background	-	± 0.5	± 1.0	± 1.5
$\pi^+\pi^-e^+e^-\gamma$	± 3.0	-	-	-
additional background	± 0.4	± 0.4	± 4.0	± 4.0
tracking efficiency	3.0 ± 1.4	3.0 ± 1.4	3.0 ± 1.4	3.0 ± 1.4
photon efficiency	1.3 ± 0.4	1.3 ± 0.4	1.3 ± 0.4	1.3 ± 0.4
rad. luminosity	± 1.0	± 1.0	± 1.0	± 1.0
AFKQED – PHOKHARA	-1.0 ± 0.2	-1.0 ± 0.2	-1.0 ± 0.2	-1.0 ± 0.2
FSR corrections	± 0.5	± 0.2	± 0.1	± 0.1
$\chi^2_{4\pi} < 30$	± 0.3	± 0.3	± 0.3	± 0.3
global efficiency	± 10.0	± 1.0	± 1.0	± 1.0
sum	± 10.7	± 2.4	± 5.5	± 8.5

The individual background contributions have been discussed in Chapter 4.3. At low invariant 4π -masses, $M_{4\pi} < 1.1 \text{ GeV}/c^2$, the leading background contributions stem from the low multiplicity hadronic background channels $e^+e^- \rightarrow \pi^+\pi^-\gamma$ and $e^+e^- \rightarrow \pi^+\pi^-\pi^0\gamma$. Misidentified tracks, e.g. from converted NLO photons lead to the $e^+e^- \rightarrow \pi^+\pi^-\pi^+\pi^-\gamma$ signal signature. These contributions are subtracted with an uncertainty of 3%. In the peak region, $1.1 \text{ GeV}/c^2 < M_{4\pi} < 2.8 \text{ GeV}/c^2$, the channels $e^+e^- \rightarrow K^+K^-\pi^+\pi^-\gamma$ and $e^+e^- \rightarrow K_s^0K^\pm\pi^\mp\gamma$ dominate the background contribution. Removing these events leads to an uncertainty of 1%. At higher invariant 4π -masses, $M_{4\pi} > 2.8 \text{ GeV}/c^2$ and $M_{4\pi} > 4.0 \text{ GeV}/c^2$, the subtraction of these ISR background channels leads to a systematic uncertainty of 3% and 7%, respectively. The additional background contribution

due to continuum events is removed with an uncertainty of 0.5% in the peak region, $1.1 \text{ GeV}/c^2 < M_{4\pi} < 2.8 \text{ GeV}/c^2$, increasing to 1.5% at $M_{4\pi} > 4.0 \text{ GeV}/c^2$. Remaining background can be estimated with an uncertainty on the cross section below 0.4% for $M_{4\pi} < 2.8 \text{ GeV}/c^2$ and below 4.0% for $2.8 \text{ GeV}/c^2 < M_{4\pi} < 4.5 \text{ GeV}/c^2$.

The observed tracking efficiency difference between data and MC simulation of 3% has been corrected with an uncertainty of 1.5% (Chapter 5.3). Concerning the photon efficiency effects (Chapter 5.2) an average shift of 1.3% with an uncertainty of 0.4% is applied. The radiative luminosity at *BABAR* is known with a precision of 1%. Comparing the radiator function modeled in the AFKQED simulation to the PHOKHARA simulation (Chapter 3.3) leads to a correction of 1% with a systematic uncertainty of 0.2%. The uncertainty on the correction of eventual differences concerning the FSR description by PHOTOS in simulation and data is estimated to be 0.5% for $M_{4\pi} < 1.1 \text{ GeV}/c^2$ and even smaller for larger invariant 4π -masses. The $\chi^2_{4\pi}$ distribution is properly described by simulation (Chapter 4.2) within a systematic uncertainty of 0.3%. Concerning the global efficiency, the uncertainty is estimated to be 1% for $M_{4\pi} > 1.1 \text{ GeV}/c^2$ (Chapter 4.4). Towards low invariant masses $M_{4\pi} < 1.1 \text{ GeV}/c^2$ a rather strong efficiency decrease of up to 10% is observed. A conservative estimate for the uncertainty of 10% has been chosen corresponding to the total efficiency decrease in this region.

All corrections listed in Table 6.1 have been applied to the measured hadronic cross section. Assuming no correlation, the individual uncertainties can be added in quadrature, resulting in the total systematic uncertainty for the $e^+e^- \rightarrow \pi^+\pi^-\pi^+\pi^-$ cross section measurement of 10.7% for $M_{4\pi} < 1.1 \text{ GeV}/c^2$, 2.4% for $1.1 \text{ GeV}/c^2 < M_{4\pi} < 2.8 \text{ GeV}/c^2$, 5.5% for $2.8 \text{ GeV}/c^2 < M_{4\pi} < 4.0 \text{ GeV}/c^2$ and 8.5% for higher invariant masses.

6.2 The Cross Section $\sigma(e^+e^- \rightarrow \pi^+\pi^-\pi^+\pi^-)$

The general extraction of the non-radiative hadronic cross section from the radiative cross section is performed by using equation (3.1), which translates in the case of $e^+e^- \rightarrow \pi^+\pi^-\pi^+\pi^-$ to

$$\sigma_{4\pi}(M_{4\pi}) = \frac{d\sigma_{4\pi,\gamma}(M_{4\pi})}{dM_{4\pi}} \cdot \frac{s}{2 \cdot M_{4\pi}} \cdot \frac{1}{W(s, x, \theta_\gamma^*)}. \quad (6.1)$$

The differential radiative cross section is obtained in dependence of the invariant $M_{4\pi}$ mass:

$$\frac{d\sigma_{4\pi,\gamma}(M_{4\pi})}{dM_{4\pi}} = \frac{dN_{4\pi,\gamma}(M_{4\pi})}{dM_{4\pi}} \cdot \frac{1}{\mathcal{L}_{tot} \cdot \epsilon_{eff} \cdot (1 + \delta_{rad,FSR})}, \quad (6.2)$$

where $dN_{4\pi,\gamma}$ corresponds to the number of selected signal events, \mathcal{L}_{tot} to the integrated luminosity, ϵ_{eff} to the global efficiency which has been corrected for tracking and photon efficiency differences between the data and MC, and $\delta_{rad,FSR}$ represents the radiative corrections including LO-FSR and NLO-FSR effects. This efficiency is corrected for the

effects of the tracking and photon efficiency difference between data and MC simulation as well as radiative effects.

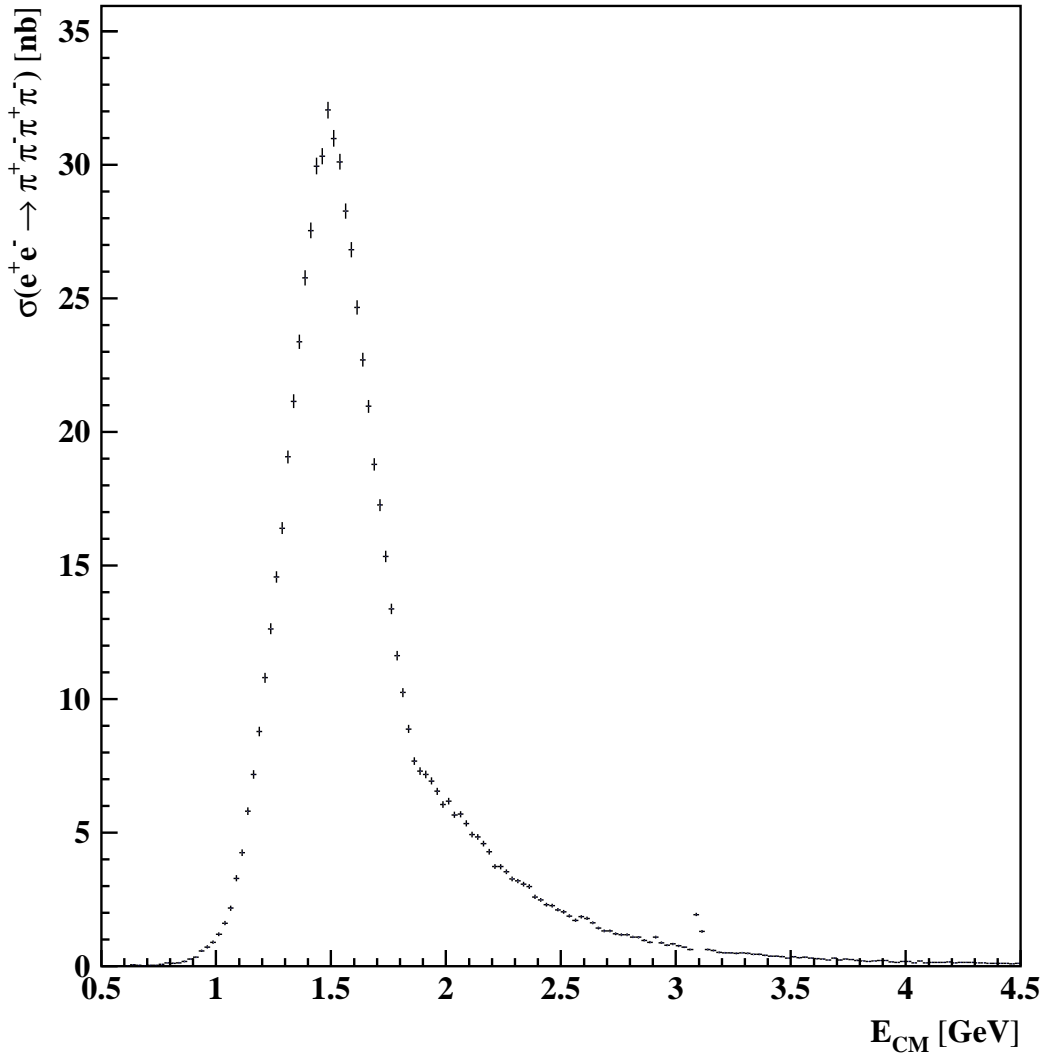


Figure 6.1: The cross section $\sigma(e^+e^- \rightarrow \pi^+\pi^-\pi^+\pi^-)$ as a function of the e^+e^- CM energy E_{CM} .

After having applied all radiative corrections and after having taken into account the relevant differences in efficiencies between the data and the simulation, equation 6.1 is applied and the non-radiative cross section $e^+e^- \rightarrow \pi^+\pi^-\pi^+\pi^-$ is extracted. It is displayed in Fig. 6.1 as a function of the center of mass energy of the hadronic system E_{CM} , which is equivalent to the invariant $M_{4\pi}$ mass of the hadronic system. A dominant structure from the $\rho(1450)$ is visible. In addition the J/ψ -peak can be clearly seen at $E_{\text{CM}} = 3.1 \text{ GeV}$.

6.3 Comparison to Existing Data

In Fig. 6.2 the extracted non-radiative cross section $\sigma(e^+e^- \rightarrow \pi^+\pi^-\pi^+\pi^-)$ of this work, together with the previous *BABAR* result [70] and all energy scan experiments running at fixed CM energies E_{CM} are shown. It agrees within the systematic uncertainty with the previous *BABAR* measurement and supersedes this measurement. The result is in good agreement and higher in precision with the data taken at VEPP-2M by SND [86] and CMD-2 [87, 88], as well as with data obtained at DCI by DM2 [89] in the 1.4-2.0 GeV range.

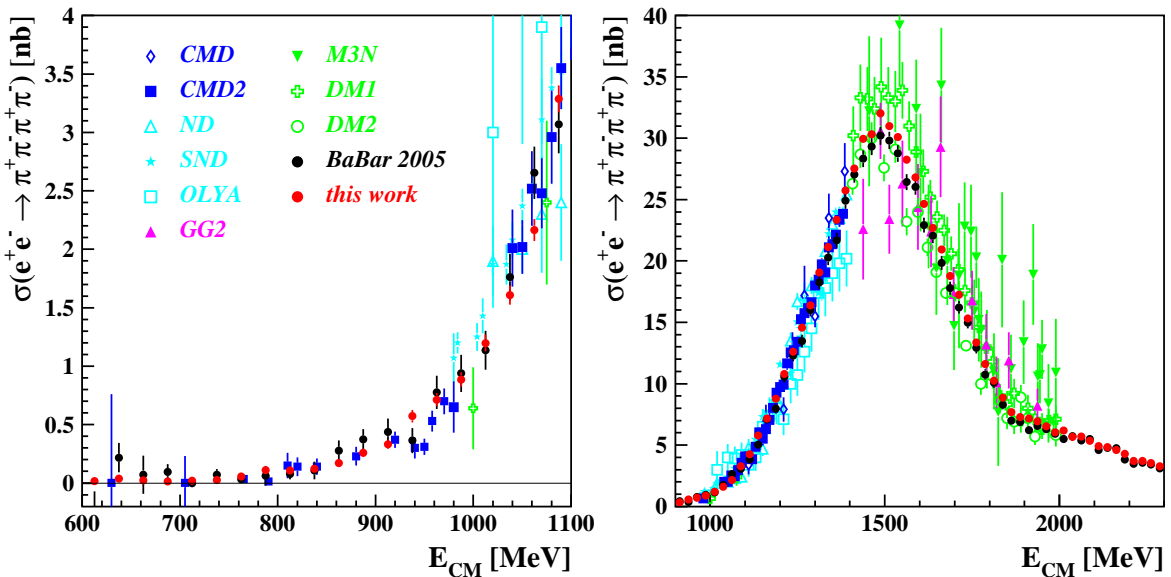


Figure 6.2: The cross section $\sigma(e^+e^- \rightarrow \pi^+\pi^-\pi^+\pi^-)$ in comparison to other experiments, error bars correspond to statistical errors only.

In the following, the differences between this analysis and the previously performed *BABAR* analysis are investigated. Fig. 6.3 shows the ratio of the cross sections in the peak region $1.2 \text{ GeV}/c^2 < M_{4\pi} < 2.2 \text{ GeV}/c^2$ and for invariant 4 π -masses $M_{4\pi} > 2.2 \text{ GeV}/c^2$. In the peak region, a constant deviation of 3.4% between the results of the two studies is observed, which is consistent within the systematic uncertainties. Besides the different statistics of the dataset, which corresponds to luminosities of 89 fb^{-1} in case of the 2005 *BABAR* analysis and 454 fb^{-1} in the new case, the systematic studies were significantly improved for the new result. This allows to understand the observed deviation.

The previous analysis included an upper limit on the amount of neutral energy per event $E_{neutral} < 3 \text{ GeV}$ in addition to the ISR photon. It is the sum of the energy of all additionally reconstructed photons. This requirement was used in order to reduce the amount of $\pi^+\pi^-\pi^0\gamma$ at small invariant masses and $\pi^+\pi^-\pi^+\pi^-\pi^0\gamma$ in the peak region. Simulation shows, however, that the amount of $\pi^+\pi^-\pi^+\pi^-\pi^0\gamma$ has only a small contribution in the $M_{4\pi}$ peak region and in addition in data no significant amount of π^0 was found. In addition (see Section 4.3.2), the amount of additional photons and especially the energy distribution of these photons is not perfectly modeled in simulation. This introduces an efficiency bias. Fig. 6.4 shows the ratio of the cross sections of the two analyses after

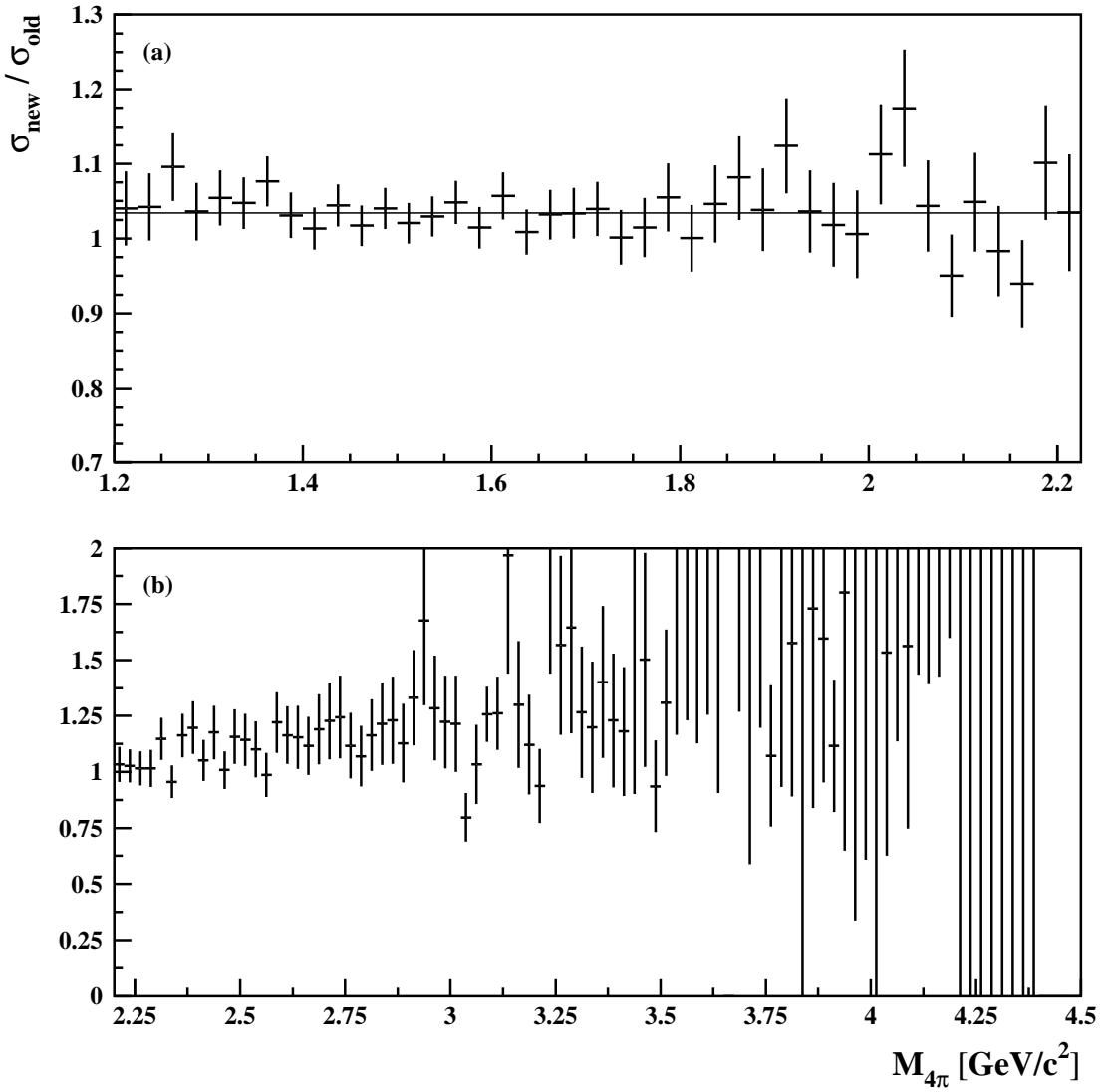


Figure 6.3: Ratio of cross section of this study to the previous study in the peak region (a) and at high invariant masses (b).

implementing this requirement on the neutral energy in this analysis. The distributions are displayed in the invariant 4π -mass regions $1.2 \text{ GeV}/c^2 < M_{4\pi} < 2.2 \text{ GeV}/c^2$ Fig. 6.4 (a) and $2.2 \text{ GeV}/c^2 < M_{4\pi} < 4.5 \text{ GeV}/c$ Fig. 6.4 (b). An agreement in the peak region within 1% is observed. At large invariant 4π -masses, the large difference between these two results is still present.

One additional difference between the analyses is the scaling of continuum background. This background is scaled according to the π^0 yield as explained in Chapter 4.3.2. There, it is also shown that the π^0 yield needs to be compared for all combinations of photons with the ISR photon. Choosing only one entry per event, which is closest to the π^0 -mass, introduces again a bias due to differences in the description of additional photons between data and simulation. Thus a different scaling parameter has been used in the previous analysis. Using the continuum background scaling factor from the previ-

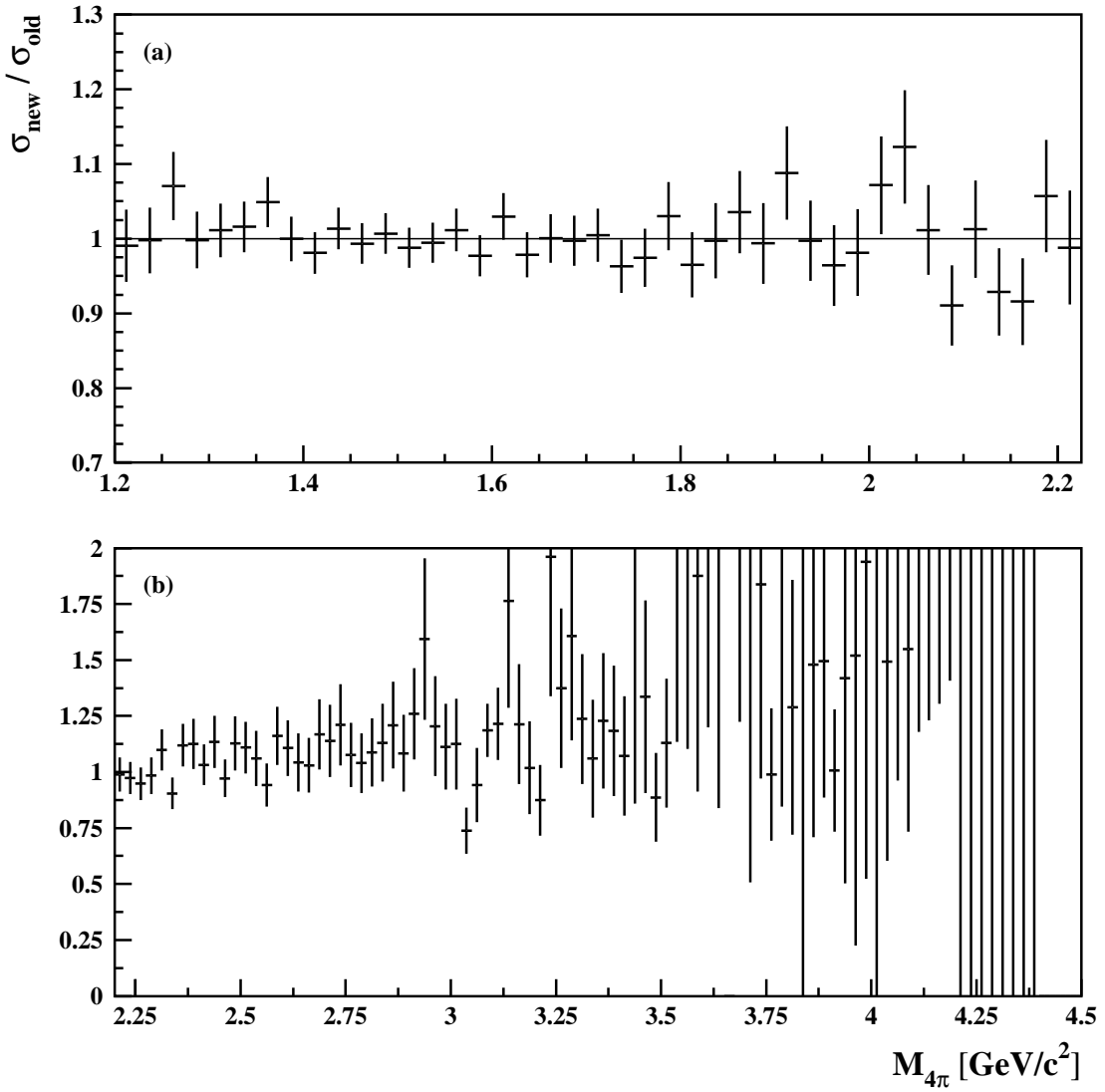


Figure 6.4: Ratio of cross sections of this study to the previous *BABAR* study in the peak region (a) and at large invariant masses (b) with a cut on the additional neutral energy $E_{\text{neutral}} < 3$ GeV.

ous *BABAR* study in this analysis allows to understand the observed differences in the cross section measurement at large invariant masses (Fig. 6.4 (b)). Fig. 6.5 (a) and (b) show the ratio of the cross section of this analysis and the previous *BABAR* study for $1.2 \text{ GeV}/c^2 < M_{4\pi} < 2.2 \text{ GeV}/c^2$ and $2.2 \text{ GeV}/c^2 < M_{4\pi} < 4.5 \text{ GeV}/c^2$ respectively, with the same continuum scaling factor. By comparing Fig. 6.4 (b) with Fig. 6.5 (b), it is visible that the difference of the results decreases significantly.

At small invariant masses, $M_{4\pi} < 1.2 \text{ GeV}/c^2$, more background is subtracted in this analysis than in the previous *BABAR* analysis. In the latter, no dedicated conversion veto (see Section 4.3.3) was applied. Simulation was used to subtract this background contribution. This is, however, not sufficient for low invariant 4 π -masses since an excellent description of NLO radiation of the $\pi^+\pi^-\gamma$ as well as the $\pi^+\pi^-\pi^0\gamma$ background channels

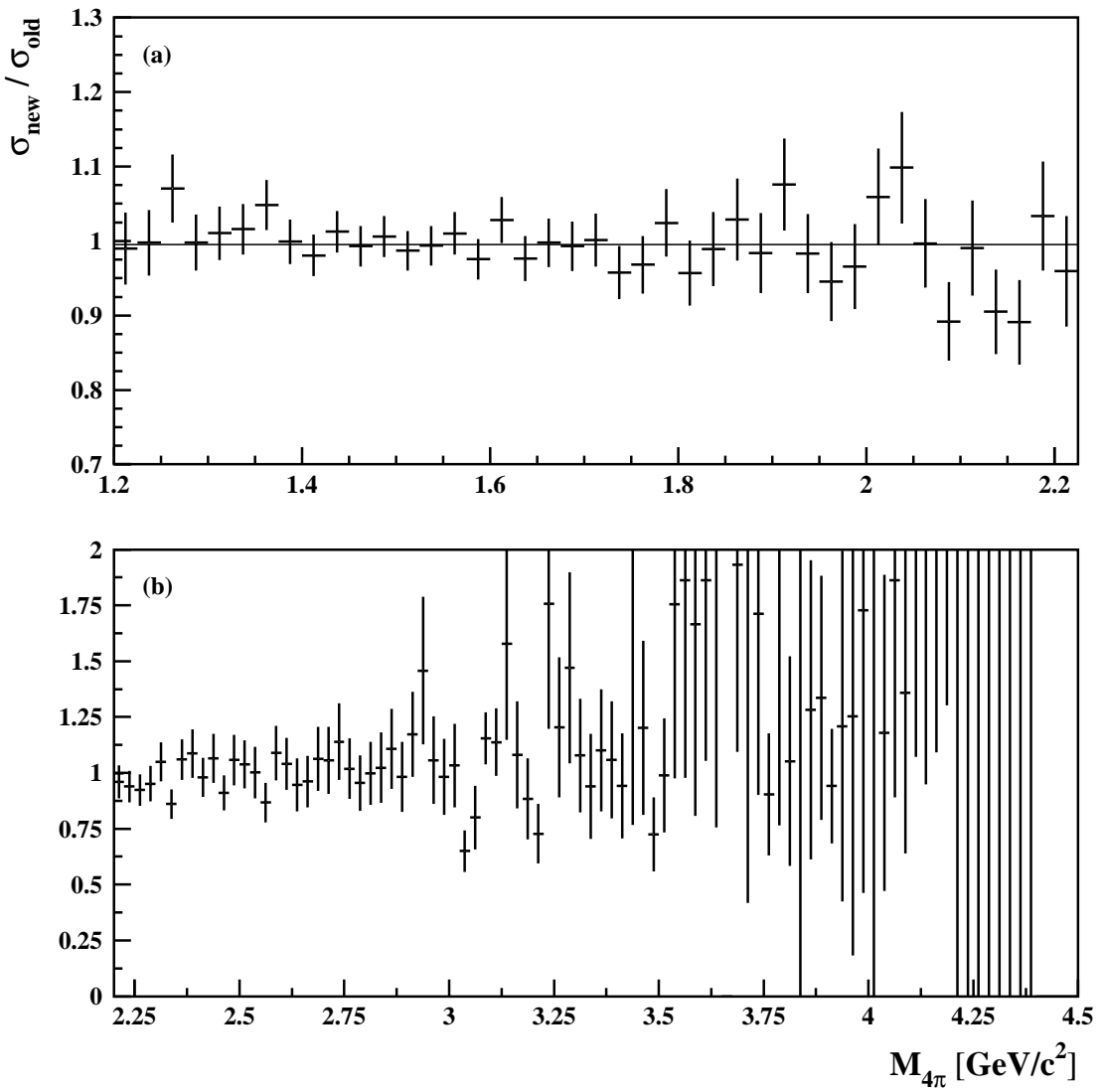


Figure 6.5: Ratio of cross section of this study to the previous study in the peak region (a) and at high invariant masses (b) with a cut on the neutral energy and the previously used continuum background scaling factor.

would be needed. The description of the conversion of these NLO photons is one source of uncertainty. Internal conversion is, however, also not included in the simulation. At very low invariant masses, the background contamination is so high that small variations in the simulation lead to significant changes in the signal distribution. This can be seen in Fig. 6.6, where the ratio of the cross sections at low invariant 4π -masses $M_{4\pi} < 1.2 \text{ GeV}/c^2$ is displayed. The agreement, which is sufficient around and above $M_{4\pi} = 1 \text{ GeV}/c^2$, becomes worse in the threshold region.

The additional systematic tests lead to a significant improvement in terms of understanding of the physical situation and therefore a reduction of the systematic uncertainties.

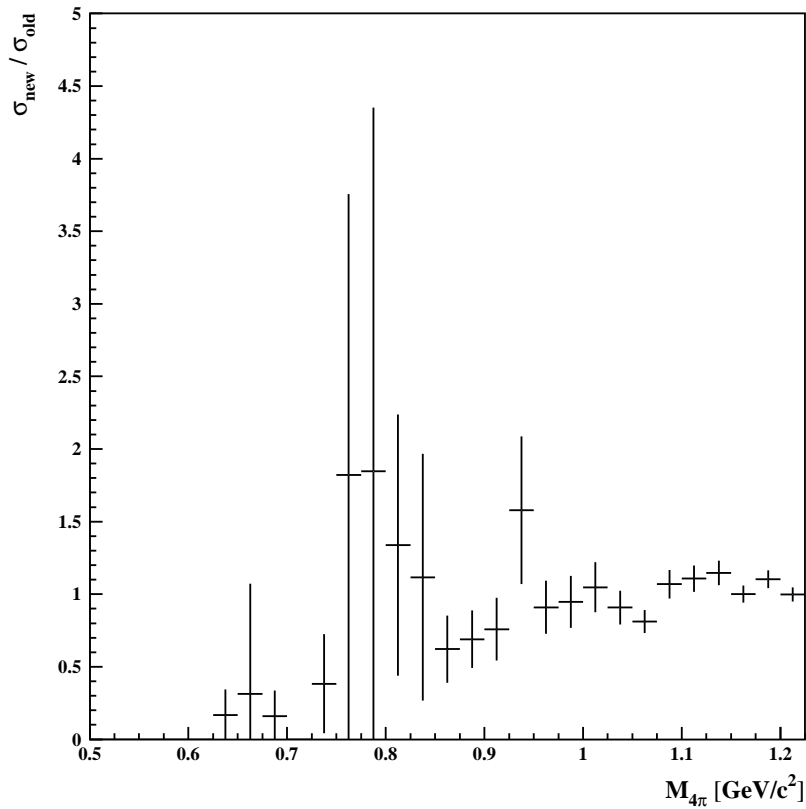


Figure 6.6: Ratio of cross sections of this study to the previous *BABAR* study at small invariant masses.

6.4 Influence on prediction of a_μ and $\Delta\alpha_{QED}^{had(5)}$

Using the new cross section measurement $\sigma(e^+e^- \rightarrow \pi^+\pi^-\pi^+\pi^-)$, the contributions of this channel to the anomalous magnetic moment of the muon a_μ and to the running of the fine structure constant $\Delta\alpha_{QED}^{had(5)}$ are computed via the dispersion relation described in Chapter 1.2 using the HVPTTool [56] in the energy region $0.6 \text{ GeV} < E_{CM} < 1.8 \text{ GeV}$:

$$\begin{aligned} a_\mu^{had}(e^+e^- \rightarrow \pi^+\pi^-\pi^+\pi^-) &= (136.4 \pm 0.3_{stat} \pm 3.6_{syst}) \cdot 10^{-11}, \\ \Delta\alpha_{QED}^{had(5)}(M_Z^2) &= (3.57 \pm 0.01_{stat} \pm 0.09_{syst}) \cdot 10^{-4}. \end{aligned}$$

The new evaluations are more precise than the current world average for these quantities:

$$\begin{aligned} a_\mu^{average}(\pi^+\pi^-\pi^+\pi^-) &= (133.5 \pm 1.0_{stat} \pm 4.3_{syst} \pm 2.9_{syst}) \cdot 10^{-11}, \\ \Delta\alpha_{QED}^{had(5)}(M_Z^2) &= (3.49 \pm 0.03_{stat} \pm 0.12_{syst} \pm 0.08_{syst}) \cdot 10^{-4}, \end{aligned}$$

where the first uncertainty is statistical, the second channel-specific systematic, and the third common systematic, which is correlated with at least one other channel [2].

Chapter 7

Study of Internal Structures and Charmonium Branching Ratios

This chapter is dedicated to the rich internal structure of the $\pi^+\pi^-\pi^+\pi^-$ final state

In addition to the important contribution of the hadronic cross section measurement $\sigma(e^+e^- \rightarrow \pi^+\pi^-\pi^+\pi^-)$ to the theoretical extraction of the anomalous magnetic moment of the muon a_μ as well as of the running fine structure constant at the Z-mass $\alpha_{QED}(M_Z^2)$, the final state $e^+e^- \rightarrow \pi^+\pi^-\pi^+\pi^-$ contains a rich internal structure.

A scan for additional resonances at high invariant masses follows. In addition, various invariant mass combinations have been studied for the data and the signal simulation in order to search for internal structures not included in the MC simulation model. Finally, the branching fractions $\mathcal{B}_{J/\psi \rightarrow \pi^+\pi^-\pi^+\pi^-}$ and $\mathcal{B}_{\psi(2S) \rightarrow J/\psi \pi^+\pi^-}$ are determined.

7.1 J/ψ and $\psi(2S)$

In the invariant $\pi^+\pi^-\pi^+\pi^-$ -mass spectrum in Fig. 4.2 (a) a clear J/ψ -peak at $M_{4\pi} = 3.095 \text{ GeV}/c^2$ is visible. Fig. 7.1 (a) shows an expanded view of the $\pi^+\pi^-\pi^+\pi^-$ cross section as a function of the invariant $\pi^+\pi^-\pi^+\pi^-$ -mass.

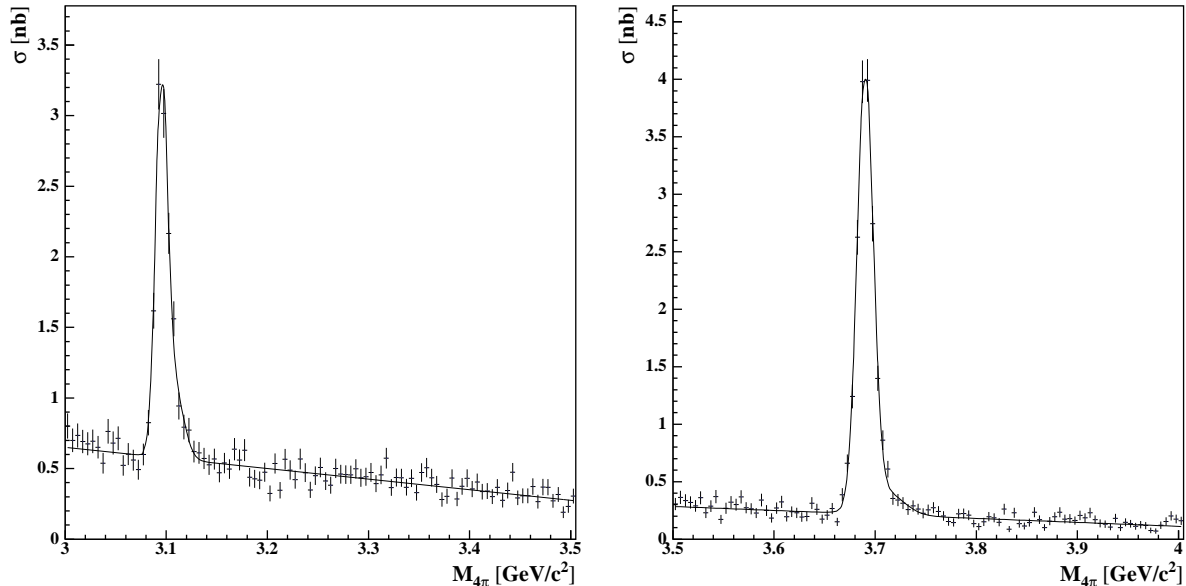


Figure 7.1: $\pi^+\pi^-\pi^+\pi^-$ cross section for data with an expanded view on the J/ψ -peak (a) and the $\psi(2S)$ -peak (b). In both cases, the fit consists of a sum of two Gaussian distributions, describing the sharp resonance, in addition to a linear fit, describing the non-resonant $\pi^+\pi^-\pi^+\pi^-$ contribution.

The measured width of the J/ψ , $\Gamma \approx 15 \text{ MeV}$, is due to the limited momentum resolution of the *BABAR* detector, since the nominal width of the J/ψ , $\Gamma_{J/\psi} = 93 \text{ keV}$ [111], is much smaller. The small tail towards higher masses is mostly produced by extra radiation, not included in the kinematic fit. In this case, the energy of the extra photon is assigned to the hadronic system by the kinematic fit. This smeared J/ψ -structure is described with the sum of two Gaussian distributions. In order to describe the non-resonant $\pi^+\pi^-\pi^+\pi^-$ production a linear approximation satisfies the needed precision. The integrated number of events of the J/ψ -peak $N(J/\psi \rightarrow \pi^+\pi^-\pi^+\pi^-)$ is used to measure the branching ratio

$\mathcal{B}_{J/\psi \rightarrow \pi^+ \pi^- \pi^+ \pi^-}$ according to Equations (7.1) and (7.2).

$$\mathcal{B}_{J/\psi \rightarrow \pi^+ \pi^- \pi^+ \pi^-} \cdot \sigma_{int}^{J/\psi} = \frac{N(J/\psi \rightarrow \pi^+ \pi^- \pi^+ \pi^-)}{d\mathcal{L}/dE \cdot \epsilon_{MC}} = (48.9 \pm 2.1_{stat} \pm 1.0_{syst}) \text{ MeV nb} \quad (7.1)$$

$$\mathcal{B}_{J/\psi \rightarrow \pi^+ \pi^- \pi^+ \pi^-} \cdot \Gamma_{ee}^{J/\psi} = \frac{N(J/\psi \rightarrow \pi^+ \pi^- \pi^+ \pi^-) \cdot M_{J/\psi}^2 c^4}{6\pi^2 \cdot d\mathcal{L}/dE \cdot \epsilon_{MC} \cdot C} = (20.4 \pm 0.9_{stat} \pm 0.4_{syst}) \text{ eV} \quad (7.2)$$

The relation between the partial electronic width $\Gamma_{ee}^{J/\psi}$ and the integrated cross section $\sigma_{int}^{J/\psi}$ is derived in Appendix C. The effective ISR luminosity $d\mathcal{L}/dE$ is visualized in Fig. 3.8. In addition to the efficiency ϵ_{MC} , determined with simulation (Section 4.4), and the conversion constant $C = (\hbar c)^2 = 3.8938 \cdot 10^{11} \text{ MeV}^2 \text{ nb}$, the J/ψ -mass, $M_{J/\psi} = 3096.92 \pm 0.01 \text{ MeV}/c^2$ [111], is needed as input. Using the electronic width $\Gamma_{ee}^{J/\psi} = 5.55 \pm 0.14 \text{ keV}$ [111] the branching fraction for $J/\psi \rightarrow \pi^+ \pi^- \pi^+ \pi^-$ can be calculated:

$$\mathcal{B}_{J/\psi \rightarrow \pi^+ \pi^- \pi^+ \pi^-} = (3.67 \pm 0.16_{stat} \pm 0.08_{syst} \pm 0.09_{external}) \cdot 10^{-3}. \quad (7.3)$$

The statistical uncertainty corresponds to the fit uncertainty on the area of the two Gaussian distributions, which is a fit parameter. The systematic uncertainty corresponds to 2.1% and covers the uncertainty of the luminosity and efficiencies as summarized in Table 6.1. Contributions from peaking background are negligible. The external uncertainty is due to the input values, dominated by the uncertainty of the electronic width $\Gamma_{ee}^{J/\psi}$. This measurement is higher in precision than the current PDG [111] value of $\mathcal{B}_{J/\psi \rightarrow \pi^+ \pi^- \pi^+ \pi^-} = (3.55 \pm 0.23) \cdot 10^{-3}$ and agrees within the uncertainties.

In Fig. 4.2 (a) a peaking structure due to the $\psi(2S) \rightarrow \pi^+ \pi^- \mu^+ \mu^-$ background channel is visible in data at $M_{4\pi} = 3.691 \text{ GeV}/c^2$. It was checked that the selection efficiency for this channel is the same as for the signal channel. This allows to obtain the $\psi(2S)$ branching ratio $\mathcal{B}_{\psi(2S) \rightarrow J/\psi \pi^+ \pi^-}$ for the reaction $\psi(2S) \rightarrow J/\psi \pi^+ \pi^-$ with $J/\psi \rightarrow \mu^+ \mu^-$. As in case of the J/ψ , the measured width of $\psi(2S)$, $\Gamma \approx 20 \text{ MeV}$, is due to the limited momentum resolution, since also the natural width of the $\psi(2S)$, $\Gamma = 317 \text{ keV}$ [111], is much smaller. This is slightly broader than in the J/ψ -case due to the additional smearing caused by the wrong mass hypothesis of the μ instead of the π -mass. Again, a fit with two Gaussian distributions was applied to describe the $\psi(2S)$ peak of the invariant mass spectrum in Fig. 7.1 (b). The non-resonant $\pi^+ \pi^- \pi^+ \pi^-$ production is estimated with a linear approximation.

The integrated number of events $N(\psi(2S) \rightarrow \pi^+ \pi^- \mu^+ \mu^-)$ is used to estimate the branching ratio $\mathcal{B}_{\psi(2S) \rightarrow J/\psi \pi^+ \pi^-}$:

$$\begin{aligned} \mathcal{B}_{\psi(2S) \rightarrow J/\psi \pi^+ \pi^-} \cdot \mathcal{B}_{J/\psi \rightarrow \mu^+ \mu^-} \cdot \sigma_{int}^{\psi(2S)} &= \frac{N(\psi(2S) \rightarrow \pi^+ \pi^- \mu^+ \mu^-)}{d\mathcal{L}/dE \cdot \epsilon_{MC}} \\ &= (84.7 \pm 2.2_{stat} \pm 1.8_{syst}) \text{ MeV nb} \end{aligned} \quad (7.4)$$

$$\begin{aligned} \mathcal{B}_{\psi(2S) \rightarrow J/\psi \pi^+ \pi^-} \cdot \mathcal{B}_{J/\psi \rightarrow \mu^+ \mu^-} \cdot \Gamma_{ee}^{\psi(2S)} &= \frac{N(\psi(2S) \rightarrow \pi^+ \pi^- \mu^+ \mu^-) \cdot M_{\psi(2S)}^2 c^4}{6\pi^2 \cdot d\mathcal{L}/dE \cdot \epsilon_{MC} \cdot C} \\ &= (49.9 \pm 1.3_{stat} \pm 1.0_{syst}) \text{ eV} \end{aligned} \quad (7.5)$$

$d\mathcal{L}/dE$, ϵ_{MC} , and C are defined as for the determination of the J/ψ branching ratio. In addition, for the result in Equation (7.5), the PDG value $M_{\psi(2S)} = 3686.09 \pm 0.04 \text{ MeV}/c^2$ is used [111]. The statistical uncertainty corresponds to the fit uncertainty on the area of the two Gaussian distributions and the systematic uncertainty of 2.1% covers the uncertainty of the luminosity and efficiencies. Contributions from other peaking background channels are negligible. Using the branching fraction $\mathcal{B}_{J/\psi \rightarrow \mu^+ \mu^-} = 0.0593 \pm 0.0006$ and the electronic width of the $\psi(2S)$ $\Gamma_{ee}^{\psi(2S)} = (2.38 \pm 0.04) \text{ keV}$ [111], the branching fraction for $\psi(2S) \rightarrow J/\psi \pi^+ \pi^-$ is determined:

$$\mathcal{B}_{\psi(2S) \rightarrow J/\psi \pi^+ \pi^-} = 0.354 \pm 0.009_{\text{stat}} \pm 0.007_{\text{syst}} \pm 0.007_{\text{external}}. \quad (7.6)$$

The external uncertainty is due to the input values dominated by the uncertainties of $\mathcal{B}_{J/\psi \rightarrow \mu^+ \mu^-}$ and $\Gamma_{ee}^{\psi(2S)}$. The result of this work agrees with the PDG world average $\mathcal{B}_{\psi(2S) \rightarrow J/\psi \pi^+ \pi^-} = 0.336 \pm 0.005$ [111] within the uncertainties. It is worthwhile to mention that it is comparable in precision to the individual contributions leading to the PDG average value and perfectly agrees with the most recent CLEO measurement $\mathcal{B}_{\psi(2S) \rightarrow J/\psi \pi^+ \pi^-}^{\text{CLEO}} = 0.3504 \pm 0.0007 \pm 0.0077$ [112].

7.2 Scan For Additional Resonances

Fig. 7.2 (a) displays the invariant $\pi^+ \pi^- \pi^+ \pi^-$ -mass distribution $M_{4\pi}$ for data at large invariant masses. This is the invariant mass region where many resonances, e.g. the $Y(4260)$, $Y(4350)$, were recently found [113, 114]. The data shown is not corrected for efficiency, but the efficiency in this $\pi^+ \pi^- \pi^+ \pi^-$ -mass is flat. No clear signal can be identified. However, there might be some interesting structure above 4 GeV. The inset, Fig. 7.2 (b), shows the same distribution with a zoom. A detailed study would be needed in order to prove the existence of resonant structures in this invariant $\pi^+ \pi^- \pi^+ \pi^-$ -mass region, but this is beyond the scope of this thesis.

7.3 Substructures

The scatter plots in Fig. 7.3 display the distributions of the invariant $\pi^+ \pi^- \pi^\pm$ - and $\pi^+ \pi^-$ -mass vs. the invariant $\pi^+ \pi^- \pi^+ \pi^-$ -mass for data and signal MC simulation. The $\rho(770)^0$ band is clearly visible in the invariant $\pi^+ \pi^-$ -mass of data and simulation. In general a good agreement is seen except in the narrow region of the J/ψ which is not included in the MC model.

In a more detailed study, Fig. 7.4, the invariant $\pi^+ \pi^- \pi^+ \pi^-$ -mass spectrum is divided into five intervals:

- **1.0-1.4 GeV/c^2** low mass region
- **1.4-1.8 GeV/c^2** peak region of the cross section

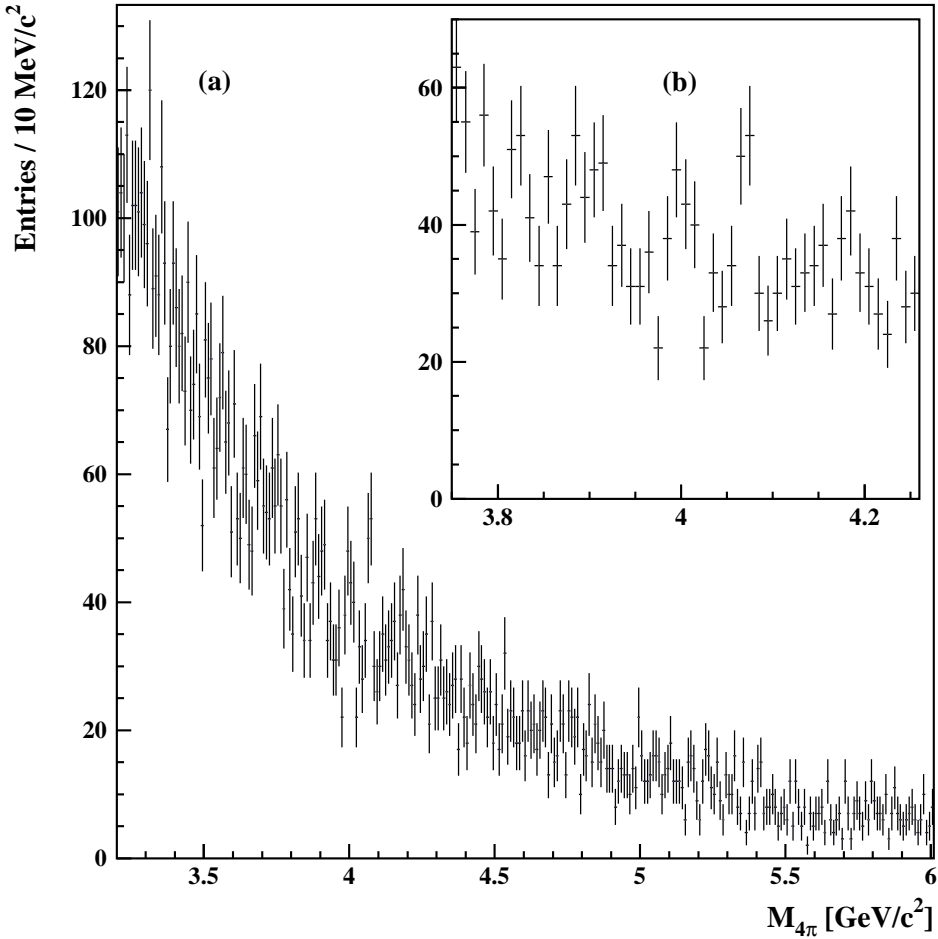


Figure 7.2: Invariant $\pi^+\pi^-\pi^+\pi^-$ mass distribution for the data in the invariant mass range $3.2 \text{ GeV}/c^2 < M_{4\pi} < 6.0 \text{ GeV}/c^2$ (a) and $3.75 \text{ GeV}/c^2 < M_{4\pi} < 4.25 \text{ GeV}/c^2$ (inset, b).

- 1.8-2.3 GeV/c^2 high mass “shoulder”
- 2.3-3.0 GeV/c^2
- 3.0-4.5 GeV/c^2 charmonium region without the narrow region around the J/ψ

Figs. 7.4 (left) show the distributions for the invariant $\pi^+\pi^-\pi^\pm$ -mass in these five invariant $\pi^+\pi^-\pi^+\pi^-$ -mass regions for the data in comparison with the MC simulation; 4 entries per event are plotted. In the region between $1.0-1.4 \text{ GeV}/c^2$, there is not enough phase space for direct $a_1(1260)^\pm$ production in the invariant $\pi^+\pi^-\pi^\pm$ -masses. For higher energies, $2.3 \text{ GeV}/c^2 < M_{4\pi} < 4.5 \text{ GeV}/c^2$, the contribution of $a_1(1260)^\pm$ is noticeable. It is visible as a peaking structure at a mass of $M_{3\pi} \approx 1300 \text{ MeV}/c^2$ and a width of $\Gamma \approx 200 \text{ MeV}$. In comparison, the averaged mass value given in the PDG [111] is $M_{a_1(1260)^\pm} = 1.230 \pm 0.040 \text{ GeV}/c^2$ with experiments varying from 1.04 to $1.33 \text{ GeV}/c^2$. The corresponding width varies between 250 and 600 MeV . In the simulation the parameters $M=1.33 \text{ GeV}/c^2$ and $\Gamma = 570 \text{ MeV}$ were used, which were obtained from combined analysis of CLEO and CMD-2 data [106]. The experimental distributions seem to be in

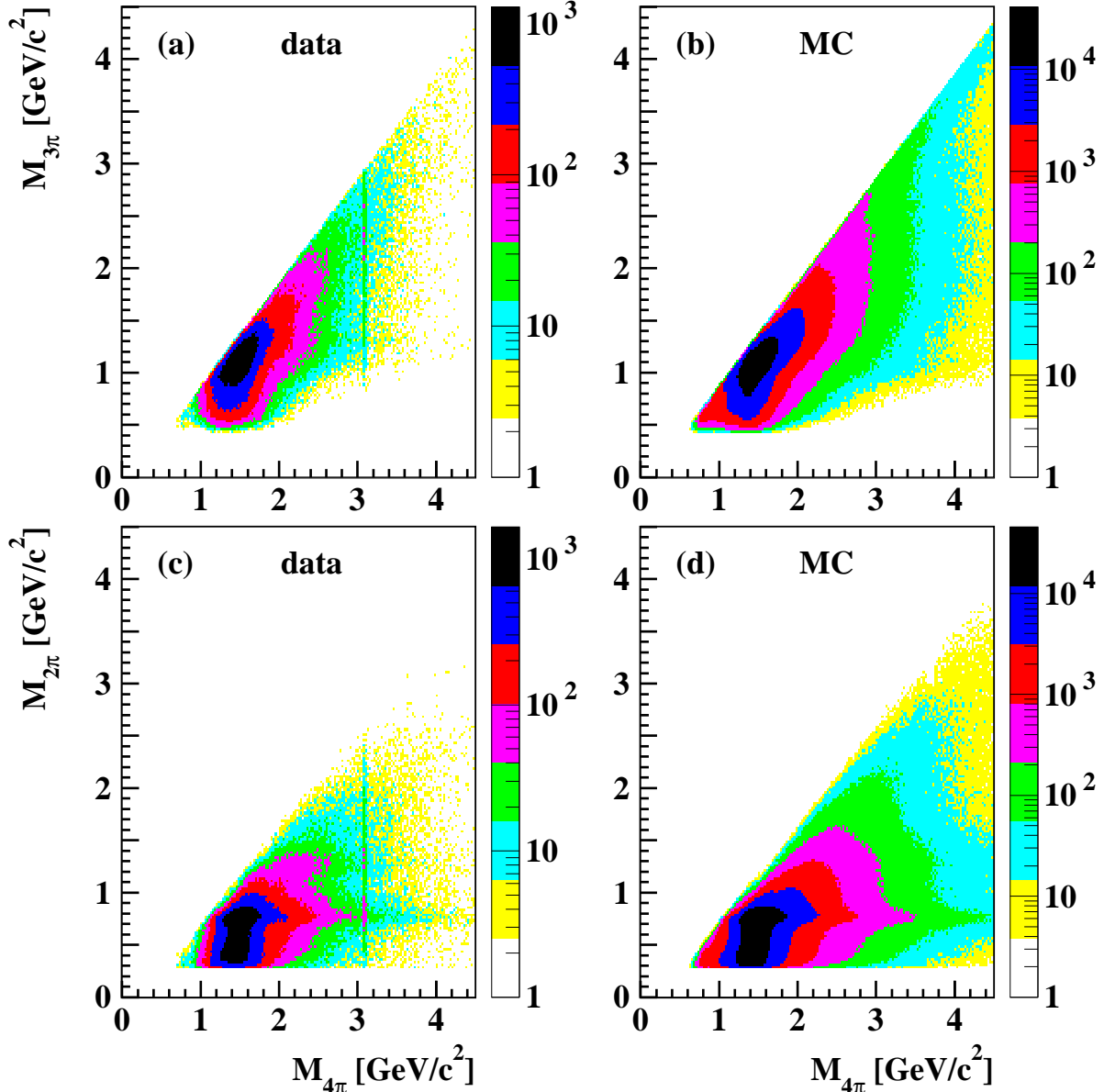


Figure 7.3: Invariant $\pi^+\pi^-\pi^{\pm}$ - and $\pi^+\pi^-$ -mass vs. invariant $\pi^+\pi^-\pi^+\pi^-$ -mass for the data (left) and the MC simulation (right) without background subtraction (number of events are in logarithmic scale).

favor of a slightly lower $a_1(1260)^{\pm}$ mass and a smaller width.

In the invariant $\pi^+\pi^-$ -mass distributions, Figs. 7.4 (middle), four entries per event are plotted. At low invariant $\pi^+\pi^-\pi^+\pi^-$ -masses and in the peak region, $M_{4\pi} < 1.8 \text{ GeV}/c^2$, solely the $\rho(770)^0$ resonance is seen. At larger invariant masses, a second peaking structure appears at a mass of $M_{2\pi} = 1270 \text{ MeV}/c^2$, which most likely corresponds to the $f_2(1270)$. This resonance is not present in the simulation. It is observed that in the entire invariant $\pi^+\pi^-\pi^+\pi^-$ -mass region, approximately 25% of the entries are in the $\rho(770)^0$ -mass peak. This leads to the conclusion, that in each event one $\rho(770)^0$ meson is present, since the $\rho(770)^0\rho(770)^0$ production is not allowed. In simulation, the $f_0(1300)$

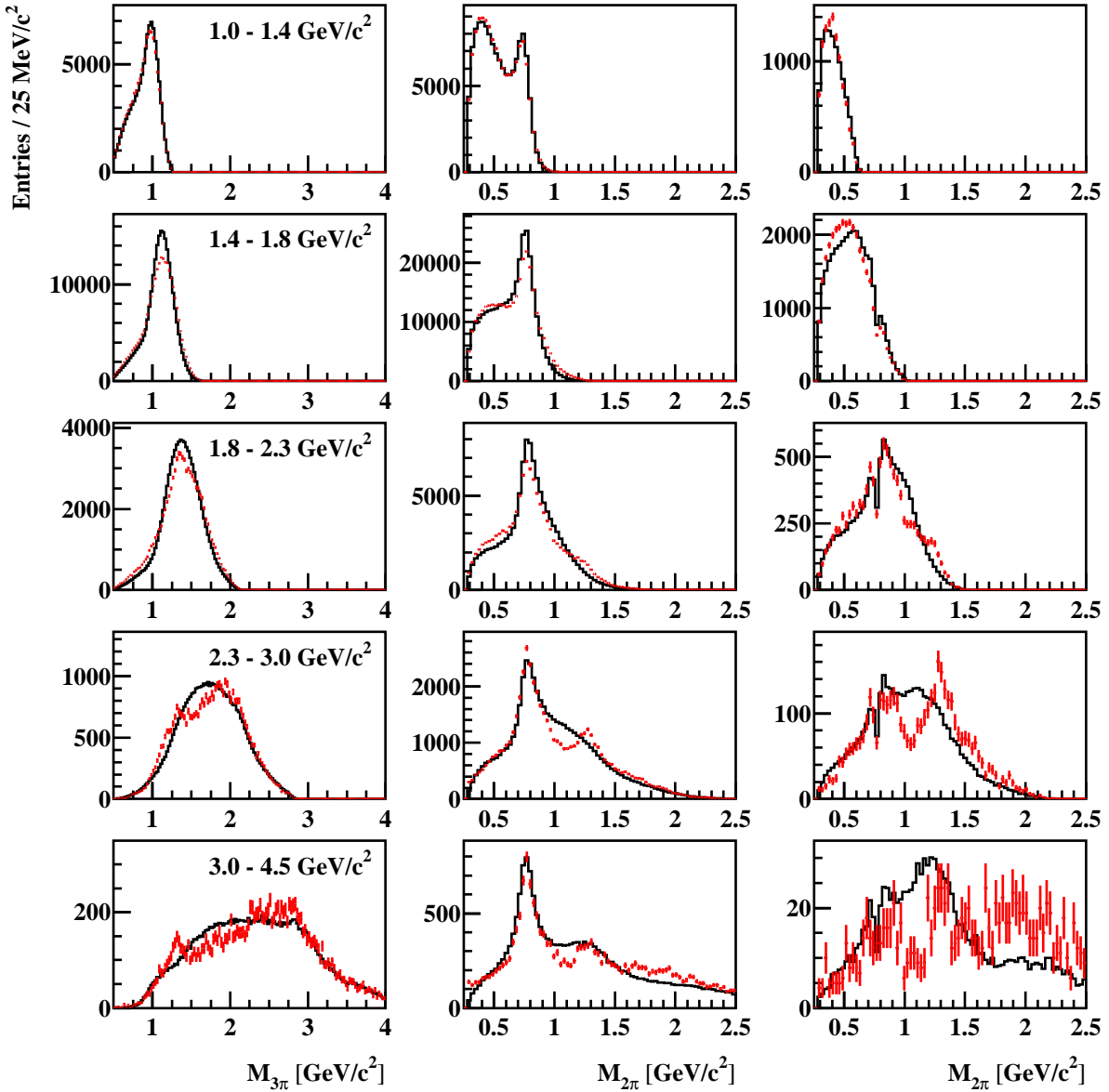


Figure 7.4: Invariant mass distributions for the data (red) and the AFKQED simulation (black); the data is not corrected for the efficiency. Left: Invariant $\pi^+\pi^-\pi^\pm$ -mass (4 entries per event) for different regions in $M_{4\pi}$. Middle: Invariant $\pi^+\pi^-$ -mass distributions (4 entries per event). Right: Invariant $\pi^+\pi^-$ -mass distributions with another $\pi^+\pi^-$ mass in the ρ -mass region.

is implemented. The mass and width are set to $1.3 \text{ GeV}/c^2$ and 0.6 GeV respectively. With the observed distributions it is not possible to confirm the parameters of this broad resonance.

In order to further investigate the presence of the $f_2(1270)\rho(770)^0$ final state the $\pi^+\pi^-$ combination is plotted with the additional requirement that the other invariant $\pi^+\pi^-$ -mass combination is located within $\pm 25 \text{ MeV}/c^2$ of the $\rho(770)^0$ mass $745 \text{ MeV}/c^2 < M_{2\pi} < 795 \text{ MeV}/c^2$. In these distributions, a dip at the $\rho(770)^0$ mass due to the $\rho(770)^0$ se-

lection is observed as expected. The $f_2(1270)$ resonance is already visible as a shoulder at $1270 \text{ MeV}/c^2$ in the $1.8 \text{ GeV}/c^2 < M_{4\pi} < 2.3 \text{ GeV}/c^2$ invariant mass region in Fig. 7.4 (right). It is even more prominent in the region $2.3 \text{ GeV}/c^2 < M_{4\pi} < 4.5 \text{ GeV}/c^2$, where enough phase space for the production of the $f_2(1270)\rho(770)^0$ final state is available. In addition an edge slightly below $M_{2\pi} = 1.0 \text{ GeV}/c^2$ seems to be present in the $M_{4\pi} > 1.8 \text{ GeV}/c^2$ invariant mass region in Fig. 7.4 (right). This might be the result of the interference with the $f_0(980)$ final state.

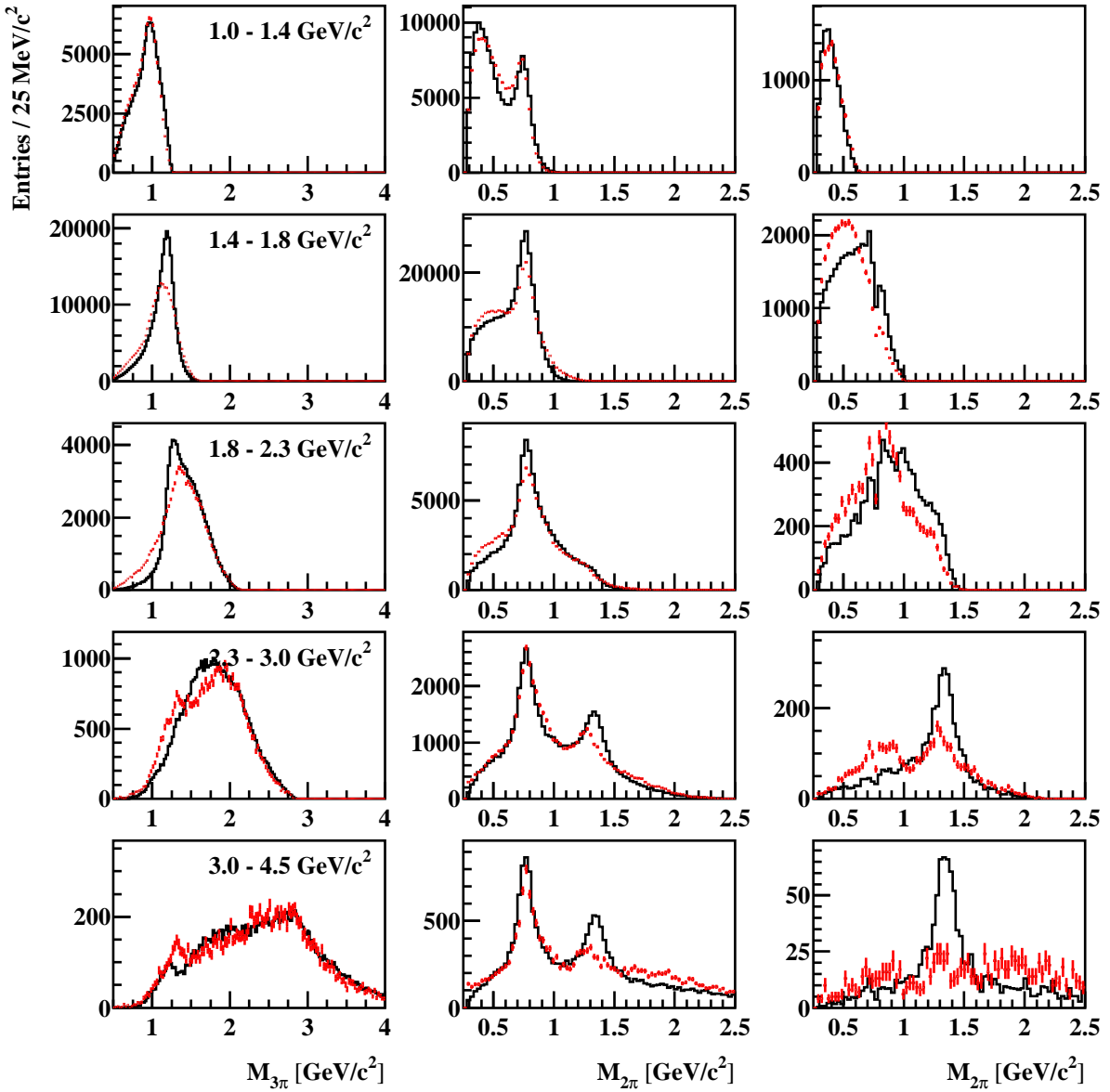


Figure 7.5: Invariant mass distributions for the data (red) and the PHOKHARA7 simulation (black); the data is not corrected for the efficiency. Left: Invariant $\pi^+\pi^-\pi^+\pi^-$ -mass (4 entries per event) for different regions in $M_{4\pi}$. Middle: Invariant $\pi^+\pi^-$ -mass distributions (4 entries per event). Right: Invariant $\pi^+\pi^-$ -mass distributions with another $\pi^+\pi^-$ mass in the ρ -mass region.

It is shown in Appendix D that a comparison between the stand-alone event generator

PHOKHARA5 (which is based on the same theoretical model concerning intermediate resonances as AFKQED) sample to the data leads to very similar results as observed in the comparison between AFKQED to data, shown in Fig. 7.4. This leads to the conclusion that it is justified to compare the data to the PHOKHARA simulation neglecting the effects of the *BABAR* detector. The efficiency is approximately uniform in dependence of $M_{2\pi}$ and $M_{3\pi}$ for the five given energy regions in $M_{4\pi}$.

An additional study is performed with the PHOKHARA7 (version 7) event generator, including a more recent update of the internal structures based on the results of the $\pi^+\pi^-\pi^0\pi^0$ final state as described in [96]. An event sample is created with similar acceptance requirements as in the presented $\pi^+\pi^-\pi^+\pi^-$ study. A detector simulation is not performed, since this event generator is not implemented in the *BABAR* software environment and as shown before, it is allowed to compare it directly to the data.

Figure 7.5 shows the corresponding $\pi^+\pi^-\pi^\pm$ - and $\pi^+\pi^-$ -mass distributions for the data and the events, simulated with PHOKHARA7. Concerning the $a_1(1260)^\pm$, the data prefers a larger mass and a larger contribution in comparison to the PHOKHARA7 simulation. On the other hand, the contribution of the $f_0(1370)\rho(770)^0$, which is included in the simulation, seems to be stronger than in the data. An interference with $f_0(980)$ is not included in the MC model. A partial wave analysis is needed to determine the parameters, e.g. mass, width, and the spin structure of these intermediate resonances.

Conclusion and Outlook

The ISR technique together with the large luminosity delivered by PEP-II and the excellent performance of the *BABAR* detector allows the extraction of the cross section $\sigma(e^+e^- \rightarrow \pi^+\pi^-\pi^+\pi^-)$ as a function of the invariant $\pi^+\pi^-\pi^+\pi^-$ -mass in the range from threshold up to $4.5 \text{ GeV}/c^2$ with unprecedented statistical and systematic precision. The luminosity and efficiencies are understood on the level of few percent, resulting in a systematic uncertainty of 2.4% in the peak region, 10.7% below $1.1 \text{ GeV}/c^2$, 5.5% above $2.8 \text{ GeV}/c^2$ and 8.5% above $4.0 \text{ GeV}/c^2$.

The resulting contribution of the cross section $\sigma(e^+e^- \rightarrow \pi^+\pi^-\pi^+\pi^-)$ to the anomalous magnetic moment of the muon $a_\mu^{had}(e^+e^- \rightarrow \pi^+\pi^-\pi^+\pi^-)$ and to the running of the fine structure constant $\Delta\alpha_{QED}^{had(5)}$ are evaluated according to the method described in [55] in the energy region $0.6 \text{ GeV} < E_{CM} < 1.8 \text{ GeV}$:

$$\begin{aligned} a_\mu^{had}(e^+e^- \rightarrow \pi^+\pi^-\pi^+\pi^-) &= (136.4 \pm 0.3_{stat} \pm 3.6_{syst}) \times 10^{-11}, \\ \Delta\alpha_{QED}^{had(5)}(M_Z^2) &= (3.57 \pm 0.01_{stat} \pm 0.09_{syst}) \times 10^{-4}. \end{aligned}$$

These evaluations are more precise than the current corresponding world average for these quantities [2]:

$$\begin{aligned} a_\mu^{average}(\pi^+\pi^-\pi^+\pi^-) &= (133.5 \pm 1.0_{stat} \pm 4.3_{syst} \pm 2.9_{syst}) \times 10^{-11}, \\ \Delta\alpha_{QED}^{had(5)}(M_Z^2) &= (3.49 \pm 0.03_{stat} \pm 0.12_{syst} \pm 0.08_{syst}) \times 10^{-4}, \end{aligned}$$

where the first uncertainty is statistical, the second channel-specific systematic, and the third common systematic, which is correlated with at least one other channel.

The invariant $\pi^+\pi^-$ and $\pi^+\pi^-\pi^\pm$ -mass distributions provide evidence of resonant substructure, with preferred quasi-three-body production of $\rho(770)^0\pi^+\pi^-$ and quasi-two-body production of $a_1(1260)\pi$. There are also indications for the intermediate states $f_0(980)\rho(770)^0$ and $f_2(1270)\rho(770)^0$. For a detailed understanding of the dynamics of the $\pi^+\pi^-\pi^+\pi^-$ final state, additional information from the $\pi^+\pi^-\pi^0\pi^0$ final state will help to disentangle the contributing intermediate states.

The extracted ISR dataset allows a study of the decays $J/\psi \rightarrow \pi^+\pi^-\pi^+\pi^-$ and $\psi(2S) \rightarrow \pi^+\pi^-\mu^+\mu^-$ production. The measurement of the product of decay branching fractions and e^+e^- width of the J/ψ is the most precise single measurement to date:

$$\begin{aligned} \mathcal{B}_{J/\psi \rightarrow \pi^+\pi^-\pi^+\pi^-} \cdot \Gamma_{ee}^{J/\psi} &= (20.4 \pm 0.9_{stat} \pm 0.4_{syst}) \text{ eV}, \\ \mathcal{B}_{\psi(2S) \rightarrow J/\psi\pi^+\pi^-} \cdot \mathcal{B}_{J/\psi \rightarrow \mu^+\mu^-} \cdot \Gamma_{ee}^{\psi(2S)} &= (49.9 \pm 1.3_{stat} \pm 1.0_{syst}) \text{ eV}. \end{aligned}$$

The anomalous magnetic moment of the muon a_μ provides one of the most precise tests of the electroweak SM. On the one hand the more than 3.5σ deviation [2] between theory and experiment constrains physics beyond the SM severely, but on the other hand can also be seen as a hint for physics beyond the SM:

$$\delta a_\mu^{NP} = a_\mu^{exp} - a_\mu^{theory} = (287 \pm 80) \times 10^{-11}.$$

There are various theoretical explanations for this deviation, assuming it to be an indication of something missing in the SM. These assumptions go into various directions, such as generic contributions from Physics beyond the SM, flavor changing processes, two-Higgs doublet models, supersymmetry, little Higgs models, extra dimensions, anomalous gauge couplings, or the Dark Photon. Also investigated are possible errors in the assumptions of the theory prediction, assuming the BNL direct measurement to be valid.

Clearly, the major source of the theoretical uncertainty enters via the hadronic contributions. The contribution and uncertainty on the Light-by-Light term in [51] has changed significantly through the last decade. However, if the discrepancy is exclusively due to a mis-evaluation of these contributions, they would need to be shifted by approximately 10 standard deviations. The other large hadronic contribution enters through the experimental measurements of the cross sections of hadronic final states. An increase of the hadronic cross sections at low energies could solve the muon anomaly discrepancy, even though it is unlikely due to the diverse independent measurements, confirming this deviation. However, increasing the hadronic cross section would directly lead to a decrease on the electroweak upper bound on the SM Higgs boson mass, as discussed in Chapter 1.1. This is evaluated in detail in [115]: The upper bound for the Higgs boson mass of currently $M_{Higgs}^{UB} < 160 \text{ GeV}/c^2$ at 95% confidence level – based on precision electroweak data and the preliminary top quark mass $M_t = 172.6(1.4) \text{ GeV}/c^2$ from a combined CDF-DØ fit – would be reduced to approximately $M_{Higgs}^{UB} < 130 \text{ GeV}/c^2$. Taking into account the lower bound of the $m_{Higgs}^{LB} = 114 \text{ GeV}/c^2$ at 95% confidence level obtained by direct searches at LEP [20], leaves only a narrow window for the mass of this fundamental particle.

There is an ongoing experimental effort to further reduce the systematic uncertainty on the hadronic contribution of the anomalous magnetic moment of the muon. The intensive program of ISR analyses at *BABAR* will continue with the publication of the final states K^+K^- and $\pi^+\pi^-\pi^0\pi^0$ in the beginning of 2012. At BES-III, the ISR measurement of the $\pi^+\pi^-$ cross section as well as final states with higher multiplicities is proposed. Also, the CMD3 Collaboration has already started a high precision measurement of the $\pi^+\pi^-$ and the 4π final states using the traditional energy scan method. Concerning the direct measurement of the muon anomaly, the proposal for a new $(g-2)_\mu$ experiment at Fermilab is approved, reducing the statistical uncertainty approximately by a factor 4. Thus not only the theoretical predictions, but also the experimental measurement will be improved in the near future in order to further investigate the present difference of 3.6 standard deviations.

Appendix A

Table 1: Summary of $e^+e^- \rightarrow \pi^+\pi^-\pi^+\pi^-$ cross section measurement. *Dressed* and *undressed* (without VP) cross sections are presented with statistical uncertainties only.

E_{CM} (MeV)	$\sigma_{4\pi}^{dr.}$ (nb)	$\sigma_{4\pi}^{undr.}$ (nb)	E_{CM} (MeV)	$\sigma_{4\pi}^{dr.}$ (nb)	$\sigma_{4\pi}^{undr.}$ (nb)	E_{CM} (MeV)	$\sigma_{4\pi}^{dr.}$ (nb)	$\sigma_{4\pi}^{undr.}$ (nb)
612.5	0.02 ± 0.01	0.02 ± 0.01	1912.5	7.17 ± 0.14	6.90 ± 0.13	3212.5	0.50 ± 0.03	0.47 ± 0.03
637.5	0.04 ± 0.02	0.04 ± 0.02	1937.5	6.93 ± 0.13	6.67 ± 0.13	3237.5	0.49 ± 0.03	0.46 ± 0.03
662.5	0.02 ± 0.01	0.02 ± 0.01	1962.5	6.54 ± 0.13	6.30 ± 0.13	3262.5	0.48 ± 0.03	0.45 ± 0.03
687.5	0.01 ± 0.01	0.01 ± 0.01	1987.5	6.04 ± 0.12	5.82 ± 0.12	3287.5	0.49 ± 0.03	0.47 ± 0.03
712.5	0.02 ± 0.01	0.02 ± 0.01	2012.5	6.18 ± 0.13	5.95 ± 0.12	3312.5	0.47 ± 0.03	0.45 ± 0.03
737.5	0.03 ± 0.01	0.03 ± 0.01	2037.5	5.66 ± 0.12	5.45 ± 0.12	3337.5	0.44 ± 0.03	0.42 ± 0.03
762.5	0.05 ± 0.02	0.05 ± 0.02	2062.5	5.68 ± 0.12	5.47 ± 0.12	3362.5	0.44 ± 0.03	0.42 ± 0.03
787.5	0.11 ± 0.03	0.10 ± 0.02	2087.5	5.34 ± 0.12	5.14 ± 0.11	3387.5	0.40 ± 0.03	0.38 ± 0.03
812.5	0.11 ± 0.02	0.10 ± 0.02	2112.5	4.92 ± 0.11	4.73 ± 0.11	3412.5	0.38 ± 0.03	0.36 ± 0.03
837.5	0.12 ± 0.03	0.12 ± 0.02	2137.5	4.83 ± 0.11	4.64 ± 0.11	3437.5	0.38 ± 0.03	0.36 ± 0.03
862.5	0.17 ± 0.03	0.16 ± 0.03	2162.5	4.59 ± 0.11	4.41 ± 0.10	3462.5	0.36 ± 0.03	0.34 ± 0.02
887.5	0.26 ± 0.04	0.25 ± 0.03	2187.5	4.28 ± 0.10	4.12 ± 0.10	3487.5	0.30 ± 0.02	0.28 ± 0.02
912.5	0.33 ± 0.04	0.32 ± 0.04	2212.5	3.72 ± 0.10	3.58 ± 0.09	3512.5	0.35 ± 0.03	0.33 ± 0.02
937.5	0.57 ± 0.05	0.55 ± 0.05	2237.5	3.72 ± 0.09	3.57 ± 0.09	3537.5	0.31 ± 0.02	0.29 ± 0.02
962.5	0.71 ± 0.06	0.69 ± 0.05	2262.5	3.53 ± 0.09	3.39 ± 0.09	3562.5	0.33 ± 0.02	0.31 ± 0.02
987.5	0.89 ± 0.06	0.86 ± 0.06	2287.5	3.26 ± 0.09	3.13 ± 0.08	3587.5	0.29 ± 0.02	0.28 ± 0.02
1012.5	1.20 ± 0.07	1.23 ± 0.07	2312.5	3.18 ± 0.09	3.06 ± 0.08	3612.5	0.27 ± 0.02	0.26 ± 0.02
1037.5	1.61 ± 0.08	1.51 ± 0.08	2337.5	3.06 ± 0.08	2.94 ± 0.08	3637.5	0.26 ± 0.02	0.25 ± 0.02
1062.5	2.17 ± 0.09	2.06 ± 0.09	2362.5	2.97 ± 0.08	2.86 ± 0.08	3662.5	0.22 ± 0.02	0.22 ± 0.02
1087.5	3.29 ± 0.11	3.14 ± 0.11	2387.5	2.59 ± 0.08	2.48 ± 0.07	3687.5	0.29 ± 0.02	0.13 ± 0.02
1112.5	4.49 ± 0.13	4.31 ± 0.12	2412.5	2.47 ± 0.08	2.38 ± 0.07	3712.5	0.23 ± 0.02	0.21 ± 0.02
1137.5	5.95 ± 0.14	5.72 ± 0.14	2437.5	2.30 ± 0.07	2.21 ± 0.07	3737.5	0.26 ± 0.02	0.24 ± 0.02
1162.5	7.37 ± 0.16	7.09 ± 0.15	2462.5	2.25 ± 0.07	2.16 ± 0.07	3762.5	0.25 ± 0.02	0.23 ± 0.02
1187.5	8.84 ± 0.17	8.51 ± 0.17	2487.5	2.11 ± 0.07	2.02 ± 0.07	3787.5	0.21 ± 0.02	0.20 ± 0.02
1212.5	10.79 ± 0.19	10.40 ± 0.18	2512.5	2.03 ± 0.07	1.95 ± 0.07	3812.5	0.19 ± 0.02	0.18 ± 0.02
1237.5	12.62 ± 0.20	12.17 ± 0.20	2537.5	1.87 ± 0.07	1.80 ± 0.06	3837.5	0.18 ± 0.02	0.17 ± 0.02
1262.5	14.56 ± 0.22	14.05 ± 0.21	2562.5	1.71 ± 0.06	1.65 ± 0.06	3862.5	0.18 ± 0.02	0.17 ± 0.02
1287.5	16.39 ± 0.23	15.83 ± 0.22	2587.5	1.85 ± 0.06	1.77 ± 0.06	3887.5	0.21 ± 0.02	0.20 ± 0.02
1312.5	19.06 ± 0.25	18.41 ± 0.24	2612.5	1.79 ± 0.06	1.72 ± 0.06	3912.5	0.20 ± 0.02	0.19 ± 0.02
1337.5	21.14 ± 0.26	20.42 ± 0.25	2637.5	1.62 ± 0.06	1.56 ± 0.06	3937.5	0.15 ± 0.02	0.14 ± 0.02
1362.5	23.37 ± 0.27	22.59 ± 0.26	2662.5	1.43 ± 0.06	1.37 ± 0.05	3962.5	0.14 ± 0.02	0.14 ± 0.01
1387.5	25.76 ± 0.28	24.90 ± 0.28	2687.5	1.31 ± 0.05	1.26 ± 0.05	3987.5	0.16 ± 0.02	0.16 ± 0.02
1412.5	27.53 ± 0.29	26.61 ± 0.29	2712.5	1.30 ± 0.05	1.26 ± 0.05	4012.5	0.17 ± 0.02	0.16 ± 0.02
1437.5	29.95 ± 0.30	28.96 ± 0.30	2737.5	1.21 ± 0.05	1.16 ± 0.05	4037.5	0.12 ± 0.01	0.11 ± 0.01
1462.5	30.32 ± 0.31	29.32 ± 0.30	2762.5	1.17 ± 0.05	1.13 ± 0.05	4062.5	0.20 ± 0.02	0.19 ± 0.02
1487.5	32.04 ± 0.31	30.97 ± 0.30	2787.5	1.17 ± 0.05	1.12 ± 0.05	4087.5	0.13 ± 0.01	0.12 ± 0.01
1512.5	30.98 ± 0.31	29.93 ± 0.30	2812.5	1.09 ± 0.05	1.05 ± 0.05	4112.5	0.14 ± 0.02	0.13 ± 0.01
1537.5	30.11 ± 0.30	29.06 ± 0.29	2837.5	1.07 ± 0.05	1.04 ± 0.05	4137.5	0.14 ± 0.02	0.13 ± 0.01
1562.5	28.26 ± 0.29	27.26 ± 0.28	2862.5	0.96 ± 0.05	0.93 ± 0.04	4162.5	0.14 ± 0.01	0.13 ± 0.01
1587.5	26.81 ± 0.28	25.86 ± 0.27	2887.5	0.89 ± 0.04	0.86 ± 0.04	4187.5	0.15 ± 0.02	0.14 ± 0.01
1612.5	24.66 ± 0.27	23.78 ± 0.26	2912.5	1.08 ± 0.05	1.05 ± 0.05	4212.5	0.11 ± 0.01	0.10 ± 0.01
1637.5	22.69 ± 0.26	21.89 ± 0.25	2937.5	0.88 ± 0.04	0.85 ± 0.04	4237.5	0.13 ± 0.01	0.12 ± 0.01
1662.5	20.95 ± 0.25	20.19 ± 0.24	2962.5	0.77 ± 0.04	0.75 ± 0.04	4262.5	0.13 ± 0.01	0.12 ± 0.01
1687.5	18.78 ± 0.23	18.09 ± 0.22	2987.5	0.82 ± 0.04	0.81 ± 0.04	4287.5	0.13 ± 0.01	0.12 ± 0.01
1712.5	17.25 ± 0.22	16.61 ± 0.21	3012.5	0.75 ± 0.04	0.74 ± 0.04	4312.5	0.11 ± 0.01	0.11 ± 0.01
1737.5	15.33 ± 0.21	14.75 ± 0.20	3037.5	0.71 ± 0.04	0.71 ± 0.04	4337.5	0.11 ± 0.01	0.11 ± 0.01
1762.5	13.37 ± 0.19	12.86 ± 0.19	3062.5	0.62 ± 0.04	0.66 ± 0.04	4362.5	0.09 ± 0.01	0.09 ± 0.01
1787.5	11.61 ± 0.18	11.17 ± 0.17	3087.5	1.93 ± 0.06	2.30 ± 0.08	4387.5	0.10 ± 0.01	0.10 ± 0.01
1812.5	10.23 ± 0.17	9.84 ± 0.16	3112.5	1.30 ± 0.05	1.03 ± 0.04	4412.5	0.11 ± 0.01	0.10 ± 0.01
1837.5	8.87 ± 0.15	8.53 ± 0.15	3137.5	0.62 ± 0.04	0.55 ± 0.03	4437.5	0.09 ± 0.01	0.09 ± 0.01
1862.5	7.67 ± 0.14	7.37 ± 0.14	3162.5	0.59 ± 0.03	0.54 ± 0.03	4462.5	0.09 ± 0.01	0.08 ± 0.01
1887.5	7.29 ± 0.14	7.02 ± 0.13	3187.5	0.51 ± 0.03	0.47 ± 0.03	4487.5	0.10 ± 0.01	0.09 ± 0.01

Appendix B

Estimating Systematic Uncertainties

This section is focused on the influence of certain selection criteria on a measured value \hat{x} . It is assumed that by varying the requirements in different analyses, \hat{x} stays within the borders x_{min} and x_{max} . The aim is to estimate the systematic uncertainty of \hat{x} assuming that the influence on the diverse selection criteria on \hat{x} can be described by a uniform probability density function $f(x)$:

$$f(x) = \begin{cases} \frac{1}{x_{max} - x_{min}} & , \quad \text{for} \quad x_{min} < x < x_{max}, \\ 0 & , \quad \text{for} \quad x < x_{min} \quad \text{or} \quad x > x_{max}. \end{cases}$$

Then according to $\sigma_{\hat{x}} = \sqrt{\langle x^2 \rangle - \langle x \rangle^2}$ after a short calculation, the variance is found to be $\sigma_{\hat{x}} = (x_{max} - x_{min}) \cdot \frac{1}{2\sqrt{3}}$. The assumption of a flat distribution of x is rather conservative, since most analyses require similar selection criteria, which are rather peaked near x . Furthermore, the maximum deviation Δ_{max} from the measured value x is defined as:

$$\begin{aligned} \Delta_{max} &= x_{max} - \hat{x} & , \quad \text{if} & \quad x_{max} - \hat{x} > \hat{x} - x_{min}, \\ \Delta_{max} &= \hat{x} - x_{min} & , \quad \text{if} & \quad x_{max} - \hat{x} < \hat{x} - x_{min}. \end{aligned}$$

Then the uncertainty of \hat{x} can be estimated conservatively as:

$$\sigma_{\hat{x}} = \Delta_{max} \cdot \frac{1}{\sqrt{3}}.$$

Appendix C

Relation between Width and Integrated Cross Section of J/ψ and $\psi(2S)$

The peaking structure of the charmonium resonances in the cross section as a function of the center-of-mass energy can be described with the Breit-Wigner-formula, which is given as [116]:

$$\sigma_{i \rightarrow f}(s) = 12\pi(\hbar c)^2 \cdot \frac{\Gamma_i \cdot \Gamma_f}{(s - M_\psi^2 c^4)^2 + M_\psi^2 c^4 \Gamma_{int}^2}. \quad (\text{C.1})$$

Γ_i is the partial width of the input channel and Γ_f the partial width of the resonance decay process. The total width is given as the sum of all partial widths for all possible fermion-antifermion decays. Integration over the cross section as a function of the effective CM $E_{CM} = \sqrt{s}$ leads to:

$$\sigma_{int} = \int_0^\infty d\sqrt{s} \sigma_{i \rightarrow f}(s) = A \cdot \int_0^\infty dx \frac{1}{(x^2 - B)^2 + 1} = A \cdot I, \quad (\text{C.2})$$

with

$$A = \frac{12\pi(\hbar c)^2 \Gamma_i \cdot \Gamma_f}{M_\psi^2 c^4 \Gamma_{tot}^2} \cdot \sqrt{M_\psi c^2 \Gamma_{tot}}, \quad B = \frac{M_\psi c^2}{\Gamma_{tot}}, \quad (\text{C.3})$$

$$(\text{C.4})$$

and

$$I = \int_0^\infty dx \frac{1}{(x^2 - B)^2 + 1}. \quad (\text{C.5})$$

The exact solution for the integral I as a function of B is plotted in Fig. C.1 and given as:

$$I = \frac{i \cdot \pi}{2} \left(\frac{1}{\sqrt{-i - B}} - \frac{1}{\sqrt{i - B}} \right). \quad (\text{C.6})$$

By Taylor expansion and the assumption $B \gg 1$, which translates into $M_\psi c^2 \gg \Gamma_{tot}$ the following solution for I is obtained:

$$\int_0^\infty dx \frac{1}{(x^2 - B)^2 + 1} \approx \frac{\pi}{2\sqrt{B}}. \quad (\text{C.7})$$

The approximation $M_\psi c^2 \gg \Gamma_{tot}$ is satisfied by the J/ψ and the $\psi(2S)$ ($M_{J/\psi} c^2 = 3097 \text{ MeV} \gg \Gamma_{J/\psi} = 0.09 \text{ MeV}$ and $M_\psi(2S) c^2 = 3686 \text{ MeV} \gg \Gamma_{J/\psi} = 0.32 \text{ MeV}$, parameters are taken from [111]). This approximate solution is also indicated in Fig. C.1.

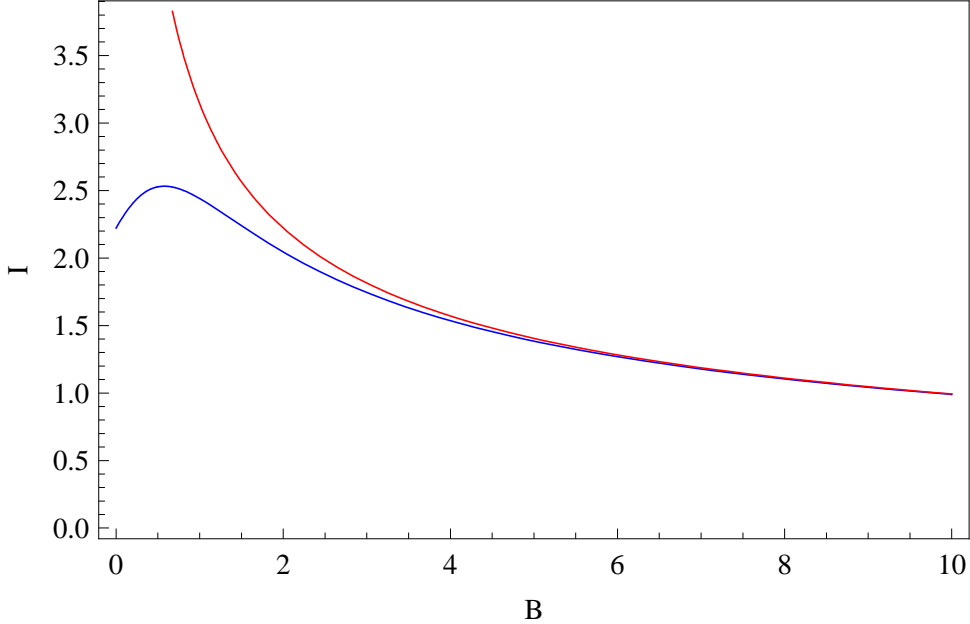


Figure C.1: The exact solution of the Integral I (blue line) as well as the approximate solution (red line).

The approximate solution for I leads to the following equation:

$$\int_0^\infty d\sqrt{s}\sigma_{i \rightarrow f}(s) = 6\pi(\hbar c)^2\Gamma_i\Gamma_f \frac{1}{M_\psi^2 c^4 \Gamma_{tot}}. \quad (\text{C.8})$$

The initial process i , corresponding to the $e^+e^- \rightarrow \psi$ production ($\Gamma_i = \Gamma_{ee}^\psi$), can be separated by eliminating the branching ratio $\mathcal{B}_{\psi \rightarrow f} = \frac{\Gamma_f}{\Gamma_{tot}}$ on the right hand side of the equation. This leads to the final result for the cross section σ_{int}^ψ :

$$\int_0^\infty d\sqrt{s}\sigma_{e^+e^- \rightarrow \psi}(s) = \sigma_{int}^\psi(s) = \frac{6\pi(\hbar c)^2\Gamma_{ee}^\psi}{M_\psi^2 c^4}. \quad (\text{C.9})$$

Appendix D

Comparison of PHOKHARA5 Simulation with Data

In Fig. 7.4 of Chapter 7 the intermediate resonances of the AFKQED simulation are compared to the intermediate resonances found in data. The AFKQED code is based on an early version of the PHOKHARA generator. PHOKHARA5 (Version 5) includes the same model for the intermediate resonances as AFKQED. Fig. D.1 shows invariant $\pi^+\pi^-\pi^\pm$ -mass and $\pi^+\pi^-$ -mass distributions for data and the standalone version of PHOKHARA5. The same features are seen as in the comparison between data and AFKQED including the *BABAR* detector simulation. Thus the efficiencies are rather flat as a function of the invariant $\pi^+\pi^-\pi^\pm$ -mass and $\pi^+\pi^-$ -mass for the five indicated $M_{4\pi}$ regions. This allows a comparison study of data with PHOKHARA7, including additional intermediate resonances.

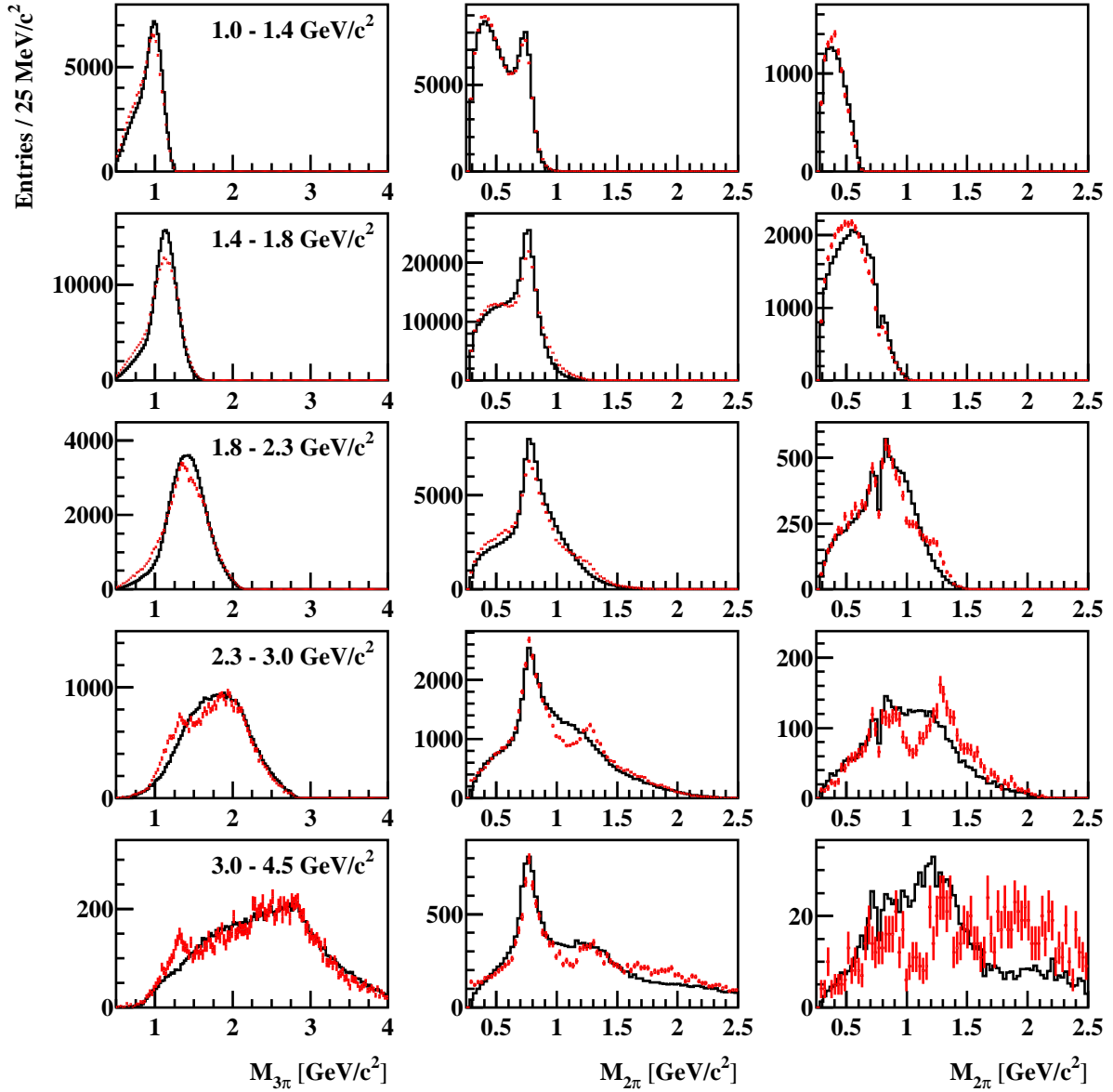


Figure D.1: Invariant mass distributions for data (red) and PHOKHARA5 simulation (black). Left: Invariant $\pi^+\pi^-\pi^\pm$ -mass (4 entries per event) for different regions in $M_{4\pi}$. Middle: Invariant $\pi^+\pi^-$ -mass distributions (4 entries per event). Right: Invariant $\pi^+\pi^-$ -mass distributions with another $\pi^+\pi^-$ mass in the $\rho(770)^0$ -mass region.

Bibliography

- [1] D. Hanneke, S. Fogwell, G. Gabrielse, Phys. Rev. Lett. **100**, 120801 (2008).
- [2] M. Davier, A. Hoecker, B. Malaescu, Z. Zhang, Eur. Phys. J. C **71**, 1515 (2011).
- [3] M. Steinhauser, Phys. Lett. B **429**, 158 (1998).
- [4] J. H. Kühn, M. Steinhauser, Phys. Lett. B **437**, 425 (1998).
- [5] F. Jegerlehner, Nucl. Phys. Proc. Suppl. **181-182**, 135 (2008).
- [6] F. Jegerlehner, talk presented at the *LC10 Workshop*, INFN/LNF Frascati, Italy, December (2010).
- [7] L. M. Barkov *et al.* [CMD Collaboration], Nucl. Phys. B **256**, 365 (1985).
- [8] R. R. Akhmetshin *et al.* [CMD2 Collaboration], Phys. Lett. B **527**, 161 (2002).
- [9] R. R. Akhmetshin *et al.* [CMD2 Collaboration], Phys. Lett. B **578**, 285 (2004).
- [10] M. N. Achasov *et al.* [SND Collaboration], Jour. Exp. Theor. Phys. **101**, 1053 (2005).
- [11] M. N. Achasov *et al.* [SND Collaboration], Jour. Exp. Theor. Phys. **103**, 380 (2006).
- [12] A. D. Martin, J. Outhwaite, M. G. Ryskin, Phys. Lett. B **492**, 69 (2000).
- [13] J. F. de Troconiz, F. J. Yndurain, Phys. Rev. D **71**, 073008 (2005).
- [14] H. Burkhardt, B. Pietrzyk, Phys. Rev. D **72**, 057501 (2005).
- [15] K. Hagiwara, A.D. Martin, D. Nomura, T. Teubner, Phys. Lett. B **649**, 173 (2007).
- [16] K. Hagiwara, R. Liao, A.D. Martin, D. Nomura, T. Teubner. KEK-TH-1458, LTH-913, IPPP-11-18, DCPT-11-36, TU-883, arXiv:1105.3149 (2011).
- [17] The LEP Electroweak Working Group (EWWG),
<http://lepewwg.web.cern.ch/LEPEWWG/>, status of 25th of July (2011).
- [18] A Generic Fitter Project for HEP Model Testing (Gfitter),
<http://gfitter.desy.de>, status of 25th of July (2011).
- [19] The ALEPH, DELPHI, L3, OPAL, SLD Collaborations, the LEP Electroweak Working Group, the SLD Electroweak and Heavy Flavour Groups, *Precision Electroweak Measurements on the Z Resonance*, Eprint hep-ex/0509008, CERN, (2005).

[20] R. Barate *et al.*, The ALEPH, DELPHI, L3 and OPAL Collaborations, and LEP Working Group for Higgs Boson Searches, Phys. Lett. B **565**, 61 (2003).

[21] The TEVNPH Working Group for the CDF and D \emptyset Collaborations, arXiv:0804.3423, FERMILAB-PUB-08-069-E (2008).

[22] G. Bernardi *et al.*, Tevatron New Phenomena Higgs Working Group, arXiv:0808.0534, FERMILAB-PUB-08-270-E (2008).

[23] H. Burkhardt, B. Pietrzyk, Phys. Rev. D **72**, 057501 (2005).

[24] S. Eidelman, F. Jegerlehner, Z. Phys.C **67**, 585 (1995).

[25] F. Jegerlehner, A. Nyffeler, Phys. Rept. 477, 1 (2009).

[26] J. Bailey *et al.* [CERN-Mainz-Daresbury Collaboration], Nucl. Phys. B **150**, 1 (1979).

[27] G. W. Bennett *et al.* [Muon g-2 Collaboration], Phys. Rev. D **73**, 072003 (2006).

[28] G. T. Danby *et al.*, Nucl. Instr. and Methods Phys. Res. A **457**, 151 (2001).

[29] Y. K. Semertzidis, Nucl. Instr. and Methods Phys. Res. A **503**, 458 (2003).

[30] E. Efstathiadis *et al.*, Nucl. Instr. and Methods Phys. Res. A **496**, 8 (2002).

[31] V. Bargmann, L. Michel, V. A. Telegdi, Phys. Rev. Lett. **2**, 435 (1959).

[32] L. H. Thomas, Phil. Mag. **3**, 1 (1927); B. W. Montague, Phys. Rept. **113**, 1 (1984); J. S. Bell, CERN-75-11, 38 (1975).

[33] R. Prigl *et al.*, Nucl. Instr. and Methods Phys. Res. A **374**, 118 (1996); X. Fei, V. Hughes, R. Prigl, Nucl. Instr. and Methods Phys. Res. A **394**, 349 (1997).

[34] W. Liu *et al.*, Phys. Rev. Lett. **82**, 711 (1999).

[35] T. Kinoshita, M. Nio, Phys. Rev. D **53**, 4909 (1996); M. Nio, T. Kinoshita, Phys. Rev. D **55**, 7267 (1997); T. Kinoshita, arXiv:hep-ph/9808351v1, (1998).

[36] A. Czarnecki, S. I. Eidelman, S. G. Karshenboim, Phys. Rev. D **65**, 053004 (2002); S. G. Karshenboim, V. A. Shelyuto, Phys. Lett. B **517**, 32 (2001).

[37] G. Charpak *et al.*, Phys. Rev. Lett. **6**, 128 (1961); G. Charpak *et al.*, Nuovo Cimento **22**, 1043 (1961).

[38] J. Bailey *et al.*, Phys. Lett. B **28**, 287 (1968); Nuovo Cimento A **9**, 369 (1972).

[39] R. M. Carey *et al.*, Phys. Rev. Lett. **82**, 1632 (1999).

[40] H. N. Brown *et al.* [Muon (g-2) Collaboration], Phys. Rev. D **62**, 091101 (2000).

[41] H. N. Brown *et al.* [Muon (g-2) Collaboration], Phys. Rev. Lett. **86**, 2227 (2001).

- [42] G. W. Bennett *et al.* [Muon g-2 Collaboration], Phys. Rev. Lett. **89**, 101804 (2002) [Erratum-*ibid.* **89**, 129903 (2002)].
- [43] G. W. Bennett *et al.* [Muon g-2 Collaboration], Phys. Rev. Lett. **92**, 161802 (2004).
- [44] C. M. Sommerfield, Phys. Rev. **107**, 328 (1957); Ann. Phys. (N.Y.) **5**, 26 (1958).
- [45] M. V. Terentev, Sov. Phys. JETP **16**, 444 (1963) [Zh. Eksp. Teor. Fiz. **43**, 619 (1962)].
- [46] J. A. Mignaco, E. Remiddi, Nuovo Cim. A **60**, 519 (1969); R. Barbieri, E. Remiddi, Phys. Lett. B **49**, 468 (1974); Nucl. Phys. B **90**, 233 (1975); R. Barbieri, M. Caffo, E. Remiddi, Phys. Lett. B **57**, 460 (1975); M. J. Levine, E. Remiddi, R. Roskies, Phys. Rev. D **20**, 2068 (1979); S. Laporta, E. Remiddi, Phys. Lett. B **265**, 182 (1991); S. Laporta, Phys. Rev. D **47**, 4793 (1993); Phys. Lett. B **343**, 421 (1995); S. Laporta, E. Remiddi, Phys. Lett. B **356**, 390 (1995).
- [47] S. Laporta, E. Remiddi, Phys. Lett. B **379**, 283 (1996).
- [48] T. Kinoshita, Phys. Rev. Lett. **75**, 4728 (1995).
- [49] R. Jackiw, S. Weinberg, Phys. Rev. D **5**, 2396 (1972); I. Bars, M. Yoshimura, Phys. Rev. D **6**, 374 (1972); G. Altarelli, N. Cabibbo, L. Maiani, Phys. Lett. B **40**, 415 (1972); W. A. Bardeen, R. Gastmans, B. Lautrup, Nucl. Phys. B **46**, 319 (1972); K. Fujikawa, B. W. Lee, A. I. Sanda, Phys. Rev. D **6**, 2923 (1972).
- [50] A. Czarnecki, W. J. Marciano, A. Vainshtein, Phys. Rev. D **67**, 073006 (2003).
- [51] J. Prades, E. de Rafael, A. Vainshtein, UG-FT-242-08, CAFPE-112-08, CPT-P092-2008, FTPI-MINN-08-41, UMN-TH-2723-08, arXiv:0901.0306 (2009).
- [52] F. Jegerlehner, R. Szafron, Eur. Phys. J. C **71**, 1632 (2011).
- [53] A. Hoecker, W. Marciano, “The Muon Anomalous Magnetic Moment”, in: Particle Data Group (K. Nakamura *et al.*), J. Phys. **G37**, 075021 (2010).
- [54] T. Teubner, Talk given at Tau 2010 Workshop, Manchester, UK, 13–17 Sep (2010).
- [55] M. Davier *et al.*, Eur. Phys. J. C **66**, 127 (2010).
- [56] M. Davier, A. Hoecker, B. Malaescu, C.Z. Yuan, Z. Zhang, Eur. Phys. J. C **66**, 1 (2010).
- [57] B. Aubert *et al.* [BABAR Collaboration], PRL **103**, 231801 (2009).
- [58] I. B. Vasserman *et al.* [TOF Collaboration], Sov. J. Nucl. Phys. **33**, 368 (1981).
- [59] L. M. Barkov *et al.* [OLYA and CMD Collaborations], Nucl. Phys. B **256**, 365 (1985).
- [60] I. B. Vasserman *et al.* [OLYA Collaboration], Sov. J. Nucl. Phys. **30**, 519 (1979).
- [61] R. R. Akhmetshin *et al.* [CMD2 Collaboration], Phys. Lett. B **578**, 285 (2004).

[62] V. M. Aulchenko *et al.* [CMD2 Collaboration], JETP Lett. **82**, 743 (2005); R. R. Akhmetshin *et al.* [CMD2 Collaboration], JETP Lett. **84**, 413 (2006); R. R. Akhmetshin *et al.* [CMD2 Collaboration], Phys. Lett. B **648**, 28 (2007).

[63] M. N. Achasov *et al.* [SND Collaboration], JETP Lett. **103**, 380 (2006).

[64] A. Quenzer *et al.* [DM1 Collaboration], Phys. Lett. B **76**, 512 (1978).

[65] D. Bisello *et al.* [DM2 Collaboration], Phys. Lett. B **220**, 321 (1989).

[66] F. Ambrosini *et al.* [KLOE Collaboration], Phys. Lett. B **700**, 102 (2011).

[67] F. Ambrosini *et al.* [KLOE Collaboration], Phys. Lett. B **670**, 285 (2009).

[68] F. Ambrosini *et al.* [KLOE Collaboration] Phys. Lett. B **606**, 12 (2005).

[69] B. Aubert *et al.* [BABAR Collaboration], Phys. Rev. D **70**, 072004 (2004).

[70] B. Aubert *et al.* [BABAR Collaboration], Phys. Rev. D **71**, 052001 (2005).

[71] B. Aubert *et al.* [BABAR Collaboration], Phys. Rev. D **73**, 052003 (2006).

[72] B. Aubert *et al.* [BABAR Collaboration], Phys. Rev. D **73**, 012005 (2006).

[73] B. Aubert *et al.* [BABAR Collaboration], Phys. Rev. D **76**, 092006 (2007).

[74] B. Aubert *et al.* [BABAR Collaboration], Phys. Rev. D **76**, 092005 (2007).

[75] B. Aubert *et al.* [BABAR Collaboration], Phys. Rev. D **76**, 012008 (2007).

[76] B. Aubert *et al.* [BABAR Collaboration], Phys. Rev. D **77**, 092002 (2008).

[77] A. Hafner [BABAR Collaboration], Nucl. Phys. B **207** (Proc. Suppl.) 207, 133 (2010).

[78] P. F. Harrison (ed.), H. R. Quinn (ed.), *The BABAR Physics Book: Physics at an Asymmetric B Factory*. Papers from Workshop on Physics at an Asymmetric B Factory(BABAR Collaboration Meeting), Rome, Italy, 11-14 Nov (1996), Princeton, NJ, 17-20 Mar (1997), Orsay, France, 16-19 Jun (1997) and Pasadena, CA, 22–24 Sep (1997).

[79] PEP-II: An asymmetric B Factory. Conceptual Design Report, SLAC-R-418 (1993).

[80] B. Aubert *et al.* [BABAR Collaboration], “The BABAR Detector,” Nucl. Instr. Meth. PR A **479**, 1 (2002).

[81] The BABAR Collaboration. *The Pub Board Page of Official Plots*, <http://www.slac.stanford.edu/BFROOT/www/Organization/PubBoard/OfficialPlots/index.html>, status of 25th of July (2011).

[82] The BABAR Collaboration. http://www.slac.stanford.edu/BFROOT/detector/online/archive/bbr-nfs01/www/babarrc/LumInt-Run_1-7.eps (2011).

[83] B. Aubert *et al.* [BABAR Collaboration], Nucl. Instr. Meth. A **538** (2005).

- [84] B. Aubert *et al.* [BABAR Collaboration], SLAC-pub-10170.
- [85] A. M. Ruland [BABAR calorimeter group], J. Phys.: Conf. Ser. **160**, 012004 (2009).
- [86] M. N. Achasov *et al.* [SND Collaboration], J. Exp. Theor. Phys. **96**, 789 (2003).
- [87] R. R. Akhmetshin *et al.* [CMD-2 Collaboration], Phys. Lett. B **595**, 101 (2004).
- [88] R. R. Akhmetshin *et al.* [CMD-2 Collaboration], Phys. Lett. B **475**, 190 (2000).
- [89] D. Bisello *et al.*, Nucl. Phys. (Proc. Suppl.) **21**, 111 (1991).
- [90] A. B. Arbuzov *et al.*, JHEP **9812**, 009 (1998).
- [91] S. Binner *et al.*, Phys. Lett. B **459**, 279 (1999); J. Kühn, Nucl. Phys. Proc. Suppl. **98**, 289-296 (2001).
- [92] M. Benayoun, S. I. Eidelman, V. N. Ivanchenko, Z. K. Silagadze. “Spectroscopy at B-factories using hard photon emission”, Mod. Phys. Lett. A **14**, 2605 (1999).
- [93] F. Jegerlehner *et al.*, <http://www-com.physik.hu-berlin.de/~fjeger/alphaQED.tar.gz>, status of 25th of July (2010).
- [94] V. P. Druzhinin, “Simulation of ISR processes with hard photon”, www.slac.stanford.edu/BFROOT/www/Physics/Tools/generators/AfkQed.ps, status of 25th of July (2011).
- [95] H. Czyż, J. H. Kühn, Eur. Phys. J C **18**, 497 (2000).
- [96] H. Czyż, J.H. Kühn, A. Wapienik, Phys. Rev. D **77**, 114005 (2008).
- [97] E. Barberio, B. van Eijk, Z. Was. Comput. Phys. Commun. **66**, 115 (1991).
- [98] S. Jadach, W. Placzek, B. F. L. Ward, Phys. Lett. B **390**, 298 (1997).
- [99] S. Jadach, B. F. L. Ward, Z. Was, Nucl. Phys. Proc. Suppl. **89**, 106 (2000).
- [100] G. Balossini, C. M. Carloni Calame, G. Montagna, O. Nicrosini, F. Piccinini, Nucl. Phys. B **758**, 227 (2006).
- [101] A. Hafner, Diplomarbeit, Institut für Experimentelle Kernphysik, KIT (2007).
- [102] S. Actis *et al.*, Working Group on Radiative Corrections and Monte Carlo Generators for Low Energies, Eur. Phys. J. C **66**, 585 (2010).
- [103] A. B. Arbuzov *et al.*, “Large angle QED processes at e^+e^- colliders at energies below 3 GeV”, JHEP 9710, 001 (1997).
- [104] M. Caffo, H. Czyz, E. Remiddi, Nuo. Cim. **110A**, 515 (1997); Phys. Lett. B **327**, 369 (1994).
- [105] R. R. Akhmetshin *et al.* [CMD-2 Collaboration], Phys. Lett. B **466**, 392 (1999).

- [106] A. Bondar *et al.*, Phys. Lett. B **466**, 403 (1999).
- [107] H. Czyż, J. H. Kühn, E. Nowak, G. Rodrigo, Eur. Phys. J. C **35**, 527 (2004).
- [108] H. Czyż, A. Grzelinska, J. H. Kühn, G. Rodrigo, Eur. Phys. J. C **39**, 411 (2005).
- [109] T. Sjostrand, Comput. Phys. Commun. **82**, 74 (1994).
- [110] S. Jadach, Z. Was, Comput. Phys. Commun. **85**, 453 (1995).
- [111] K. Nakamura *et al.* [Particle Data Group], J. Phys. G **37**, 075021 (2010).
- [112] H. Mendez *et al.* [CLEO Collaboration], Phys. Rev. D **78**, 011102R (2008).
- [113] B. Aubert *et al.* [BABAR Collaboration], Phys. Rev. Lett. **95**, 142001 (2005).
- [114] B. Aubert *et al.* [BABAR Collaboration], Phys. Rev. Lett. **98**, 212001 (2007).
- [115] M. Passera, W. J. Marciano, A. Sirlin, Phys. Rev. D **78**, 013009 (2008).
- [116] B. Povh, K. Rith, C. Scholz, F. Zetsche, *Teilchen und Kerne*, 3. Auflage, 147 (1995).